Extinction in Turbulent Swirling Non-premixed Flames

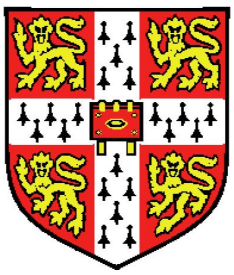

Huangwei Zhang

Churchill College

University of Cambridge

A thesis submitted for the degree of

Doctor of Philosophy

May 22, 2015

To my wife Ruiqin

Declaration

The research presented in this dissertation was conducted in Department of Engineering, University of Cambridge between October 2011 and May 2015.

They are from my own work and include nothing which is the outcome of work done in collaboration except where specifically indicated in the text.

No part of this dissertation has already been, or is being concurrently submitted for any other degree, diploma or qualification.This dissertation contains approximately 61,000 words, 136 figures and 6 tables.

Signature :

Name : Huangwei Zhang

Date : May 22, 2015

Acknowledgements

Studying abroad is an odyssey for me and it is full of surprise and depression. Fortunately, I was helped by many people throughout the way, thereby materializing this thesis.

First and foremost, I would like to express the most sincere gratitude to my supervisor, Professor Epaminondas Mastorakos, for his support, guidance and mentorship during my study in University of Cambridge. It is a great honor for me to become his Ph.D. student. His enthusiasm for scientific research, understanding of combustion theory and meticulous scholarship always inspire me. His influence will continue to nurture my personal and professional developments in the future.

I am also indebted to Professor N. Swaminathan and Dr. Salvador Navarro-Martinez for reading this thesis and providing lots of helpful suggestions. This thesis would not have been possible without the help of Drs. Artur Tyliszczak and Andrew Garmory. Their invaluable suggestions and insights gave me lots of guidance when I started to learn the CMC combustion model. I appreciate the discussions about combustion with Drs. Giulio Borghesi, James Kariuki, Andrea Giusti, Shaohong Ruan and Mr. Ivan Langella. In addition, the help from the anonymous repliers from CFD Online Forum played extremely important roles when I first used OpenFOAM.

Thanks also go to my friends and colleagues in the department and college. With them I can have a pleasant environment for my Ph.D. and, particularly, I wish to thank Ruoyang Yuan, Dave Farrow, Zhi Chen, Joe Hobbs and Elena Demosthenous.

Little would be achieved in this thesis without the high performance computing support and resources. I want to thank Mr. Peter Benie, for his continuous help with all the computer matters in the laboratory office. Dr. Stuart Rankin from High Performance Computing Service in University of Cambridge answered my every question about code compilations and always patiently responded to my complaints about the desperate long-waiting queue. Mr. Adrian Jackson from the Edinburgh Parallel Computing Centre (EPCC) provided me the important help with compiling the OpenFOAM package and also the CMC solver on ARCHER cluster of the UK National Supercomputing Service. Professor Nilanjan Chakraborty should also be thanked since part of the CPU hours used for this thesis were allocated by him under the project of the UK Consortium on Turbulent Reacting Flows (UKCTRF).

I am very much indebted to Professor Zheng Chen at Peking University, who is my advisor there and also one of my best friends. He led me into the fields of combustion theory and modelling. During my study at Cambridge, he still gave me lots of encouragements and support. What I learned during the two-year-long working at Peking University is significant in completion of this thesis.

I owe deep gratitude to my parents, Weilin Zhang and Tiaojuan Huang, for their unconditional love and support. It was my parents who first instilled in me the motivation for learning and their hard work made me have the chance for higher education. This thesis is dedicated to my wife, Ruiqin, for her endless love. She supported me through the entire process even when we lived separately for several years during my Ph.D. study. It is impossible for me to finish this thesis without her support, encouragement and sacrifice.

This work was funded by the Engineering and Physical Sciences Research Council (EPSRC) and Rolls-Royce in UK through a Dorothy Hodgkin Postgraduate Award (DHPA), and also the studentship from the Cambridge Commonwealth, European and International Trust.

Abstract

This thesis investigates the localized and global extinction in turbulent swirling non-premixed flames with Large Eddy Simulation (LES) and sub-grid scale Conditional Moment Closure (CMC) model.

The first part of this thesis describes the derivations of the three dimensional conservative CMC governing equations and their finite volume discretization for unstructured mesh. The parallel performance of the newly developed CMC code is assessed. The runtime data coupling interface between the 3D-CMC and LES solvers is designed and the different solvers developed during the course of this research are detailed.

The aerodynamics of two swirling non-reacting flows from the Sydney and Cambridge burners are first simulated. The main flow structures (e.g. the recirculating zones) in both cases are correctly predicted. The sensitivity analysis about the influences of turbulent inlet boundary, computational domain and mesh refinement on velocity statistics is conducted. This analysis acts as the preparatory investigation for the following flame simulations.

The Sydney swirl diluted methane flame, SMA2, is then simulated for validating the LES/3D-CMC solvers. Excellent agreements are achieved in terms of velocity and mixture fraction statistics, averaged reactive scalars in both physical and mixture fraction space. The local extinction level from the increased central fuel velocity is reasonably predicted. At the experimental blow-off point, the LES/3D-CMC modelling does not obtain the occurrence of complete extinction, but severe extinction occurs at the flame base, qualitatively in line with experimental observations.

Localized extinction features of a non-premixed methane flame in the Cambridge swirl burner are investigated and it is found that the occurrence of local extinction is typically manifested by low heat release rate and hydroxyl mass fraction, as well as low or medium temperature. It is also accompanied by high scalar dissipation rates. In mixture fraction space, the CMC cells undergoing local extinction have relatively wide scatter between inert and fully burning solutions. The PDFs of reactedness at the stoichiometric mixture fraction demonstrate some extent of bimodality, showing the events of local extinction and re-ignition and their relative occurrence frequency.

Local extinction near the bluff body in the Cambridge swirl burner is also studied. The convective wall heat loss is included as a source term in the conditionally filtered total enthalpy equation. It shows a significant influence on the mean flame structures, directly linked to the changes of the conditional scalar dissipation near the wall. Furthermore, the degree of local extinction near the bluff body surface is intensified because of the wall heat loss. However, the wall heat loss shows a relatively small influence on the statistics of lift-off height.

Finally, the blow-off conditions and dynamics in the Cambridge swirl burner are investigated. The blow-off critical air bulk velocity from LES/3D-CMC is over-predicted, greater than the experimental one by at most 25%. The predicted blow-off transient lasts finitely long duration quantified by the blow-off time, in good agreement with the experimental results. The reactive scalars in both physical and mixture fraction space demonstrate different transient behaviors during blow-off process. When the current swirling flame is close to blow-off, high-frequency and high-amplitude fluctuations of the conditionally filtered stoichiometric scalar dissipation rate on the iso-surfaces of the filtered stoichiometric mixture fraction are evident. The blow-off time from the computations is found to vary with different operating conditions.

Contents

List of Figures

List of Tables

Nomenclature

Acronyms

r.m.s. root-mean square

AMC amplitude mapping closure

CFD computational fluid dynamics

CFL Courant−Friedrichs−Lewy

CMC conditional moment closure

CNG compressed natural gas

CRZ corner recirculation zone

DLR German Aerospace Center

DNS direct numerical simulation

FDF filtered probability density function

FPV flamelet/progress variable

IRZ inner recirculation zone

ISR incompletely stirred reactor

LDV laser Doppler velocimetry

LES large eddy simulation

LHV lower heating value

LIF laser-induced fluorescence

MMC multiple mapping conditioning

MPI message passing interface

ODE ordinary differential equation

PDF probability density function

PISO pressure implicit with splitting of operator

PIV particle image velocimetry

PLIF planar laser-induced fluorescence

PSD power spectrum density

PSR perfectly stirred reactor

PVC precessing vortex core

RANS Reynolds-averaged Navier−Stokes

SIMPLE semi-implicit method for pressure linked equations

TDMA tri-diagonal matrix algorithm

TNF The International Workshop on Measurement and Computation of Turbulent Non-premixed Flames

Greek Symbols

α thermal diffusivity

Δ LES filter width

δ jet exit radius

ϵ dissipation rate of sub-grid kinetic energy

η sample space variable for mixture fraction

λ thermal conductivity

μ dynamic viscosity

ν kinematic viscosity

Ω computational domain

ω reaction rate, or vorticity

ϕ number ratio of LES cells to inter-processor faces

ρ density

Σ area of stoichiometric mixture fraction iso-surface

τ characteristic timescale, or blow-off time

θ vane angle of swirler

ϱ number of LES cells in one CMC cell

ξ mixture fraction

Non-dimensional Numbers

Da Damköhler number

Le Lewis number

Ma Mach number

Pr Prandtl number

Re Reynolds number

S_N swirl number

Sc Schmidt number

Operators

$(\cdot)^T$ transpose of a tensor

$\Gamma(\cdot)$ Gamma function

$\langle\cdot\rangle$ time averaged quantity

$\langle\cdot\rangle_\Sigma$ spatial averaging based on stoichiometric mixture fraction iso-surface

$\mathrm{tr}(\cdot)$ trace of a tensor

$\nabla\cdot(\cdot)$ divergence in physical space

$\nabla(\cdot)$ gradient in physical space

$\overline{(\cdot)}$ non-density-weighted filter, defined in Eq. (3.1)

$\|(\cdot)\|$ tensor module

$\widetilde{(\cdot)}$ density-weighted (Favre) filter, defined in Eq. (3.13)

$B(\cdot,\cdot)$ β-function

$\mathrm{erf}^{-1}(\cdot)$ inverse error function

Roman Symbols

B sub-grid stress tensor

b sub-grid scalar transport

D strain rate tensor

I unit tensor

j molecular scalar transport

L antisymmetric part of the velocity gradient tensor

n unit normal vector of LES or CMC faces

R Reynolds stress tensor

S viscous stress tensor

$\mathbf{U}$	velocity vector
$\mathcal{V}$	volume of LES or CMC cells
$\mathscr{N}$	number of processors, or LES cells, or CMC cells
A	pre-exponential factor
a	centerline velocity gradient of coutnerflow configuration
a_{ij}	Cholesky decomposition of the Reynolds stress tensor
b	reactedness of reactive scalars
c_k, c_ϵ	constants in Smagorinsky model
c_N	constant in sub-grid scalar dissipation model, i.e. Eq. (3.22)
c_V	constant in mixture fraction sub-grid variance model, i.e. Eq. (3.23)
D	species diffusion coefficient, or diameter
D_{hub}	diameter of swirler hub
D_{sw}	diameter of swirler
E	number of edges for one CMC cell
e_f	sub-grid conditional scalar flux
F	number of faces for one CMC cell
f	extinguished fraction
G	LES spatial filter function, or shape function in AMC model
H	heat transfer coefficient
h_L	lift-off height
K	turbulent kinetic energy of the resolved flows
k	sub-grid kinetic energy

L	integral length scale
M	fraction of residual kinetic energy
N	scalar dissipation rate, or number of vertices for one CMC cell
n	number of species
P	Filtered probability density Function (FDF)
p	pressure [Pa], or processor number
Q	conditionally filtered reactive scalars, or total heat release rate
$q_{W,\Omega}$	volumetric heat loss
$q_{W,S}$	surface heat flux
S_L	laminar burning velocity
T	temperature
t	time coordinate
T_a	activation temperature
T_f	adiabatic flame temperature
t_{wall}	wall clock time
T_W	wall temperature
U	streamwise velocity
V	radial velocity
W	swirl velocity, or chemical reaction term
w	molecular weight
x	spatial coordinate
Y	mass fraction

y^+ distance from the wall normalized by the viscous length scale

Superscripts

CMC quantity related to CMC

LES quantity related to LES

p quantity related to processor in parallel computations

Subscripts

α index for species

a quantity related to annular flow

b quantity related to bluff body

BO quantity related to blow-off

$chem$ quantity related to chemistry

dev deviatoric part of a tensor

e quantity related to co-flow

e quantity related to extinction

F quantity related to fuel

f quantity related to flows

h index for total enthalpy

i quantity related to ignition

j quantity related to jet exit

N quantities stored at the neighbor LES cell centroids

O quantity related to oxidizer

P quantities stored at the owner LES cell centroids

r	quantity related to radiation
res	quantity related to resolved field
s	quantity related to swirl flow
sgs	quantity related to sub-grid scale
st	quantity related to stoichiometric mixture fraction
t	quantity related to turbulence
x, y, z	Cartesian components of a vector

Chapter 1

Introduction

1.1 Motivation

Exploitation of fire and combustion witnesses the evolution history of human society since about 1.5 million year ago [James, 1989]. Fire and its god widely exist in the circulated myths and legends from the different cultures all over the world. For instance, it is well known from Greek mythology that Prometheus was the benefactor who brought fire to mankind from Apollo. Also, the Chinese ancestors struggled to spark the first fire through drilling the dry wood. With help of fire, early humans can cook food, obtain warmth as well as keep away from the attack by wild animals. These represent the most primitive energy utilizations in the human civilizations.

The Industrial Revolution originated from Great Britain between the mid-1700s and mid-1800s marked the starting of the age of machines, and, more importantly, marked the revolutionary change of the energy harnessing and conversion in the human life and industry. Specifically, the efficiencies of the water power and bio-fuel were considerably improved while the steam power and coal started to be extensively used by the various industrial sectors. Since then the total energy consumption on the planet gradually increased and around mid-1990s its exponential increase happened abruptly, caused by the simultaneous population expansion and new round of industrialization after World War II [Ehrlich et al., 2012]. Based on the statistics from International Energy Agency [IEA,

2014], by 2012, the chemical energy derived from fossil fuels (e.g. coal, natural gas and oil) still accounts for roughly 80% of the world energy demands although the emerging renewable ones, such as solar, wind and geothermal energy, have already been used over the recent years. Therefore, combustion is still the dominant technology for energy conversion in modern society.

Combustion occurs in domestic heating, industrial furnaces, internal combustion engines and gas turbine combustors for transportation vehicles, etc. The critical issues in the design and development of the above burners and combustors, particularly for industrial ones, are efficiency of energy conversion, safety and emissions. The last one becomes increasingly significant since the stringent regulations for pollutant emissions over the last few decades. In addition, new concepts of combustion modes are proposed to improve the combustion efficiency and reduce the pollutant emissions, e.g. stratified charged combustion and homogeneous charge compression ignition. All these are tightly related to the near-limit combustion phenomena, such as ignition, extinction and instability. Therefore, fundamental research focusing on the near-limit flame dynamics is required for designing the next-generation burners.

The topic of the thesis is local and global extinction in turbulent swirl-stabilized non-premixed flames. The swirling flow environment has been applied in many industrial combustion devices such as furnaces and gas turbine combustors. It can create complicated and unsteady flow structures, such as the recirculation zone, PVC and vortex breakdown [Syred, 2006]. Meanwhile, the strong tangential velocity component can make the turbulence more anisotropic and hence the flow transport can have more pronounced three dimensional effects than in relatively simpler flows, e.g. turbulent jet flows. It has been widely accepted that recirculating flows can enhance the mixing efficiency, stabilize the flame and also transport the hot products from the burned downstream regions, thereby making the combustor compact[Gupta et al., 1984]. It is also able to extend the stability or blow-off limits compared to the non-swirling flames, although the degree to which it can improve still depends on the particular fuel compositions, flow conditions and burner configurations [Feikema et al., 1990]. Current attention to investigations on turbulent swirling flames has shifted from simple flame configurations to prototype of industrial combustor or realistic gas

turbine burners and the reader can find the latest research progress from detailed reviews by Gicquel et al. [2012] and Candel et al. [2014]. However, studies on the extinction in swirling flames are still not common. Since many practical combustion technologies, such as in jet engines, are designed with high feeding rates of the fuel and oxidizer, whether the flame could experience unexpected extinction, is one of the core issues that the designers need to take into account. Therefore, fundamental research on extinction and resultant flame dynamics in swirl-stabilized non-premixed flames is necessary.

The strong turbulence−chemistry interaction can lead to local extinction. This phenomenon exists in both laboratory-scale and real burners. The local extinction on the flame front can have an important influence on the local velocity and mixing fields, whilst it may be re-ignited again when the extinction zones have favorable conditions or interact with the neighboring fluid parcels [Lignell et al., 2011]. The local extinction can also be responsible for pollutant formation which is always not desirable. For practical burners, severe local extinction would greatly reduce the energy conversion efficiency. In the present work, local extinction in laboratory-scale swirl-stabilized non-premixed flames will be investigated, to understand the different physical mechanisms for them.

Blow-off (interchangeable with *global extinction* in this thesis) is a limiting situation in which case the complete extinction of a flame occurs from its stable and strongly reactive conditions. Blow-off limits covering a wide range of operating conditions are one of the most important parameters of interest for real combustors [Lefebvre, 2005]. The occurrence of blow-off in operating combustion devices can result in disastrous consequences. Investigations on this problem can be dated back to the day when engines and combustors were initially used in practice, e.g. to understand the flame holding mechanism in afterburners [Gabriel et al., 1952; Hottel et al., 1963]. Recently, active research on the blow-off mechanism in different flame regimes is conducted [Al-Abdeli and Masri, 2003; Cavaliere, 2013; Chaudhuri et al., 2010; Feikema et al., 1991; Kariuki, 2012; Kariuki et al., 2012]. This experimental work measured the blow-off limits and/or dynamics based on laboratory-scale burners, providing insights of blow-off mechanisms and hence a reference for designing practical combustors. However, the limitations from diagnostic technologies prevent them to have the in-depth investigations about

the change of the flame reactivity during blow-off, which is linked to such flame dynamics as pollutant emission and re-ignition. Numerical simulations can provide more informative data and therefore are significant supplemental tools for blow-off studies, in both laboratory-scale and industrial burners. This is the second motivation for the present work. In addition, the accuracy in predicting the blow-off conditions for a range of conditions in numerical simulations will also be examined in this work.

1.2 Strategy

Numerical simulations will be the research strategy applied in the current work. The flow and conserved scalar fields will be solved by the LES whereas the reactive scalar fields will be solved by the first order sub-grid scale CMC model.

LES has already become a well-acknowledged computational tool in predicting both non-reacting and reacting flows since its governing equations were first formulated by Smagorinsky [1963] in the early 1960s. The small scales are active in dissipating the energy from the larger scales through the cascade process and are relatively uniform, based on the theory of Kolmogorov [Kolmogorov, 1991]. Instead of resolving all the turbulent scales (which is the philosophy of DNS), LES resolves the large scales of the motion, thereby leading to the significant dimension reduction in turbulence. The resolved flows contain most of the energy, are responsible for most of the transport and may be influenced by the boundary conditions. Models should be developed for the unresolved part and its effects on the large motions [Pope, 2000]. Through filtering the small scales, LES relaxes the stringent limits for computational cost and therefore it has become viable and affordable for simulating the combustion in both laboratory-scale and real engine combustors [Gicquel et al., 2012]. Typically, LES is expected to be more reliable and accurate than the RANS simulations, which is particularly true when the computed flow fields are strongly transient and complex with considerable separation, vortex breakdown and shedding.

In a turbulent non-premixed combustion system, LES has been proved to demonstrate substantial improvements in predicting the fuel and oxidizer mixing occurring at the molecular level, compared with RANS simulations [Pitsch, 2006].

A well-resolved LES for the velocity field may ensure that it can resolve most of the passive scalar fluctuations for the gaseous mixture with about unity Schmidt number (comparable Kolmogorov and Batchelor scales). In spite of the above benefits, LES is not able to resolve the chemical reactions in turbulent combustion and the filtered chemical source terms should be modelled. Therefore, sub-grid scale combustion models must be included for the LES of turbulent combustion.

The CMC model was derived independently by Bilger and Klimenko in the early 1990s [Bilger, 1993; Klimenko, 1990], with the assumptions of large Re and unity Le. The basis for CMC is that the correlation between reactive scalars and a single key quantity, the mixture fraction for non-premixed flames, is exploited and hence fluctuations in the mixture fraction space can be used for quantifying the fluctuations of conditional reactive scalars [Klimenko and Bilger, 1999]. It is expected that the fluctuations around the conditional mean are relatively small for the conditional reactive scalars and hence the first order model can apply. It can also be used for predictions of flames with strong turbulence−chemistry interactions, in which case the fluctuations around the conditional mean are significant. It is shown that the CMC model has the consistency with the frozen and fast chemistry limits, which correspond to the cases of $Da \to 0$ and $Da \to \infty$, respectively [Klimenko and Bilger, 1999].

The state of the art of the CMC model has been reviewed by Kronenburg and Mastorakos [2011]. The first order CMC model will be used in this thesis. Its applications in RANS simulations for turbulent non-premixed flames are extensive, in the aspects of theoretical development and also its applications, such as the work by Roomina and Bilger [1999, 2001], Fairweather and Woolley [2004], Kim and Mastorakos [2005], Cleary and Kent [2005], Kronenburg and Kostka [2005], Borghesi et al. [2011] and Buckrell and Devaud [2013], just to name a few. The sub-grid first order CMC model for LES has been derived with a fine-grained FDF [Bushe and Steiner, 1999; Navarro-Martinez et al., 2005; Triantafyllidis and Mastorakos, 2010]. LES/CMC is experiencing rapid development recently and demonstrates the capacity in predicting significant flame dynamics, such as auto-ignition [Stanković et al., 2011], forced ignition [Triantafyllidis et al., 2009], lift-off [Navarro-Martinez and Kronenburg, 2009], or spray combustion [Ukai et al., 2013, 2015]. The above applications show that the CMC model is also able to

describe the intermediate state between frozen and fast chemistry limits, which always occurs when finite-rate chemistry dominates. Studies with LES/3D-CMC concentrating on extinction are also available [Garmory and Mastorakos, 2011; Tyliszczak et al., 2014], but still not extensive.

The advantages of the LES with the sub-grid CMC model to predict the extinction for the present work are as follows. Firstly, the accurate mixing field from LES provides the significant premise for the modelling of the scalar dissipation rate. This is directly linked to the localized extinction in globally stable flames and the flame transients towards blow-off. As such, the improvement of the conditional scalar dissipation estimation in the CMC model could be achieved and the conditional reactive scalars in mixture fraction space can be accurately captured. Secondly, the CMC model includes the transport effects from both large scale resolved motions and also sub-grid scale fluxes on the conditional reactive scalars. The filtering operations applied in LES retain most of the large scale flow information that is critical in predicting the transport in the CMC model. Therefore, with the computed transient flow and conserved scalar fields, the CMC model can include the instantaneous influences of flow and mixing fields and also the scalar dissipation on extinction dynamics. Thirdly, detailed chemical mechanism can be included into the first order CMC model, which is important for the finite-rate chemistry effect dominated combustion phenomena (e.g. extinction).

The disadvantages of the sub-grid scale CMC model are also multi-fold. Firstly, the first order CMC model applied in this thesis neglects the conditional fluctuations of reactive scalars that may become significant when extinction occurs. Early efforts introducing second order closure for the chemical source term were made based on global chemistry and additional terms are needed to be closed [Kronenburg et al., 1998; Mastorakos and Bilger, 1998]. When detailed chemistry is used, modelling the conditional variance and co-variance in second order CMC becomes difficult [Klimenko and Bilger, 1999]. Secondly, since the CMC governing equations need to be solved on-the-fly with LES, the computational cost would be high when there are many species considered. Thirdly, the large scale computations with the CMC model are also expensive in terms of memory consumption, even if they run on the modern shared memory computing architectures. Fourthly, the instantaneous data coupling implementations are required

between LES and CMC solvers. Due to the high computational cost and relatively low spatial variations of conditional flame structures, the coarse CMC cells, different from the LES ones, can be used [Navarro-Martinez et al., 2005], and averaging over all the LES cells within one CMC cell filters some instantaneous information for both velocity and scalar dissipation fields.

1.3 Objective

The objectives of the research in this thesis include:

- Derive three dimensional conservative CMC governing equations that can be discretized on unstructured CMC meshes in the framework of finite volume method; develop computationally accurate and scalable parallel predictive tools with LES and CMC modelling for turbulent non-premixed flames, which extend the potential of the CMC model about simulating the combustion in real combustors.

- Assess the accuracy of LES modelling in simulations of aerodynamics in different swirling non-reacting flows; examine the ability of newly developed LES/3D-CMC solvers in correctly computing the velocity, conserved and reactive scalar fields in a laboratory-scale swirl flame with little extinction.

- Study the local extinction features in two laboratory-scale swirl-stabilized non-premixed flames, including the underlying physics for local extinction and the dynamics.

- Analyze the effects of convective wall heat loss from the bluff body on the near-wall localized extinction and lift-off.

- Investigate the blow-off dynamics in two laboratory-scale swirl non-premixed flames; evaluate the capacity of the LES/3D-CMC solver in capturing the critical conditions at blow-off over a range of operating conditions; analyze the evolutions of reactive scalars and scalar dissipation rate during the blow-off transients.

1.4 Structure of the thesis

The structure of the thesis is as follows. Chapter 2 reviews the fundamental theory for flame extinction and the previous investigations about the extinction in both laminar and turbulent non-premixed flames, in both computational and experimental aspects. Since the LES with CMC modelling is the main research tool for the present work, the recent development of the sub-grid CMC model in LES is also detailed. Chapter 3 describes the governing equations for both LES and CMC, their respective numerical discretizations with finite volume method, data transfer strategy and parallelization performance on the ARCHER clusters of the UK National Supercomputing Service.

The arrangement of the ensuing computations in the remaining part of the thesis is as follows: (i) first non-reacting flows, then reacting ones; (ii) first stable flames (relatively low turbulence−chemistry interaction), then flames with severe localized extinction or even blow-off and (iii) first Sydney swirl flame series (with Raman−Rayleigh−LIF measurements, jet-like flames, blow-off by increased fuel bulk velocity), then Cambridge swirl flame series (with OH-PLIF and OH* chemiluminescence measurements, gas-turbine-like flames, blow-off by increased air bulk velocity).

Prior to presenting the reacting flow results, the LES of non-reacting flows in the swirl burners respectively from the University of Sydney and University of Cambridge are studied first in Chapter 4. Their flow conditions are exactly the same as or close to those of the non-premixed flame cases in the following chapters. The general flow characteristics in both burners are identified. In addition, the sensitivity analysis for the numerics, including the LES grid dependence, computation domain and the inlet turbulence, are investigated in detail. Chapter 4 is viewed as the preparation work for Chapters 5−8.

In Chapter 5, the LES/3D-CMC model described in Chapter 3 is validated with the Sydney swirl flame cases. Meanwhile, the extinction features and their dynamics are analyzed. Chapters 6−8 are focused on the predictions of local extinction and blow-off in the swirl burner from University of Cambridge. Specifically, the local extinction and lift-off are discussed in Chapter 6, whilst the effects of convective wall heat loss from the bluff-off surface on the near-wall combustion

are investigated in Chapter 7. The computational efforts to predict the blow-off curves for a range of operating conditions are presented in Chapter 8. Meanwhile, the blow-off transients, blow-off time and evolutions of flame structures and scalar dissipations are studied.

A summary of the key conclusions from the investigations in the preceding Chapters of this thesis is presented in Chapter 9, and meanwhile some recommendations for the future work concerning the LES/CMC developments and the applications in turbulent combustion are provided.

Chapter 2

Literature Review

The phenomenological theories and previous investigations about extinction in non-premixed flames will be reviewed in this Chapter. In addition, the theoretical developments and applications of the CMC model in recent years will also be discussed.

2.1 Phenomenological description of extinction

Flames are sustained by both heat and mass transfer interacting with the immediate surroundings. As such, their extinction can occur through removing some amount of chain-carrying or chain-branching radicals, or some amount of heat [Law, 2006]. The mechanism causing both removals can be diverse, depending on the specific flame regimes and flow conditions. For instance, when the flame front approaches a solid wall, it may be quenched due to possible radical quenching [Poinsot and Veynante, 2005]. Extinction can also happen when some less reactive species or inert additives are added into the flame region, such as the fire suppression [Drysdale, 1999]. The heat removal can occur by unfavorable heat transfer with the immediate flow field or completely by the local physiochemical properties. The heat transfer that can result in extinction exists between the flame and the surrounding cold gas or cold surface. For radiative or sooty flames, excessive intrinsic heat loss may lead to extinction as well.

The early studies on characterizing the extinction resorted to the PSR, also

known as the Longwell jet-stirred reactor [Longwell and Weiss, 1955]. The reaction intensity in PSR can be controlled through adjusting the flow rate of the injected mixture and hence the flow residence time τ_f. The reactivity in PSR can be measured by the fields of temperature and species concentrations. As such, combustion within PSR depends on the mixture reactivity and also the flow residence time. The non-dimensional parameter, Damköhler number Da, is introduced based on the ratio of flow residence time τ_f and characteristic chemical time τ_{chem} as

$$Da = \frac{\tau_f}{\tau_{chem}}. \tag{2.1}$$

Larger Da corresponds to the stronger reaction and $Da \to 0$ means that the characteristic chemical time τ_{chem} becomes infinitely long, implying the nearly frozen chemistry.

For non-premixed flames with finite-rate chemistry, the dependence of heat release rate on the Damköhler number Da can be illustrated by the well-known S-shaped curve [Williams, 1985], shown in Fig. 2.1. When Da is increased from zero (chemically inert state) along the lower weakly burning branch, slow reactions with limited heat release rate can exist. The system jumps to the upper intensely reactive branch when $Da = Da_i$ and continuing increasing Da along the upper branch leads to the completely burning flame regimes with negligibly small heat release rate. This is the limiting case (i.e. the reaction-sheet limit with $Da \to \infty$ in non-premixed flames) shown in Fig. 2.1. If the initial state lies on the upper branch, reducing Da gradually increases the heat release rate and the system suddenly jumps to extinction when $Da = Da_e$. Another limiting case with $Da \to 0$ is reached and the heat release rate is reduced to zero again. Da_i and Da_e marked in Fig. 2.1 denote the critical ignition and extinction Damköhler number, respectively. The middle branch is not stable and physically not observable. As the appreciations about new fuel properties and combustion regimes are increasingly extended over these years, different extinction features from other forms of S-curves are obtained, e.g. stretched S-curve (for applications with high initial temperature [Law, 2006] or plasma assisted combustion [Ju and Sun, 2015]) and S-curve with multiple bifurcation points (for fuels with negative temperature coefficient behaviors [Shan and Lu, 2012]).

For infinitely fast chemistry, the dependence of heat release rate on Damköhler number Da is monotonic (shown as the dashed line in Fig. 2.1). For very large Da, it is close to zero heat release rate as the asymptote, similar to the finite-rate chemistry case. Nevertheless, for $Da \to 0$, the heat release becomes high without extinction (no critical extinction point Da_e).

2.2 Extinction in laminar non-premixed flames

2.2.1 Theoretical and computational studies

Theoretical investigations in laminar flame extinction can be traced back to the 1950s and Spalding [1957] developed a theory to account for the flammability limit with a one dimensional premixed flame close to a solid wall. The stability of two derived burning velocities due to the wall heat loss was analyzed and it was found that the flame speed is finite when flammability limit is reached and therefore the flame is quenched [Spalding, 1957]. For laminar non-premixed flames, Williams [1981] performed the theoretical analysis with the counterflow configuration and Arrhenius one-step chemistry with the overall reaction rate being $\omega = \rho A Y_O Y_F e^{-T_a/T}$. He proposed the following extinction criterion

$$Ae^{-T_a/T_f} = Fa(T_a/T_f)^3, \tag{2.2}$$

which describes the correlation between centerline velocity gradient a and flame temperature T_f. F in Eq. (2.2) is a non-dimensional function, depending on the mixture properties.

Two asymptotic limits parameterized by small and large Da were analyzed by Fendell [1965]. He also discussed the ability of Arrhenius kinetics in predicting ignition and extinction, which cannot be achieved with the Burke−Schumann kinetics. The latter corresponds to the curve of infinitely fast chemistry shown in Fig. 2.1. In the seminal paper by Liñán [1974], the matched asymptotic expansion method was applied for analyzing the laminar mixing zone in the non-premixed counterflow flame with an Arrhenius one-step irreversible reaction and in the limit of large activation energies. Different flame structures corresponding to the three

branches in S-curve were studied and, in particular, analytical expressions for ignition and extinction conditions were derived. Extension of the work by Liñán [1974] is for the extinction of non-premixed flame established close to a vaporizing fuel surface [Krishnamurthy et al., 1976], in which an explicit expression for critical extinction condition, in terms of a Damköhler number, was derived.

Sohrab et al. [1982] proposed the corrected extinction conditions considering the radiant-loss factor. However, based on his analysis, the radiation effect on extinction is only from temperature reduction. The relation between radiation induced extinction and stretch rate (and therefore Damköhler number) was quantified by the flammability map shown in Fig. 2.2, for small and large stretch rates in a condensed-fuel flame in the stagnation point region [T'ien, 1986]. From Fig. 2.2, one can see that when the radiation is considered, the flammable region is greatly reduced with the appearance of new branch (i.e. curve AB in Fig. 2.2) for radiation extinction at small stretch rate (corresponding to large but finite Da). Therefore, besides Da_e, there exists another critical Damköhler number $Da_{e,r}$. Da_e and $Da_{e,r}$ respectively correspond to the kinetic and radiative extinction limits, both of which are intrinsically induced by the reactant leakage at the flame front indicated by Liñán [1974]. The mechanism of radiation induced extinction at $Da_{e,r}$ can be justified by the dimension dependence of both radiation and Damköhler number [Chao et al., 1991]. Later, theoretical or numerical investigations on extinction are mainly motivated by micro-gravity combustion, exemplified by the work from Mills and Matalon [1998], and Wang and Chao [2011], just to name a few.

2.2.2 Experimental studies

Extinction experiments for laminar non-premixed flames were conducted based on different burners and flame configurations, e.g. counterflow and spherical flames. They are the important experimental methods for studying the fuel oxidation characteristics, including the structures and reaction mechanisms for non-premixed flames. In the counterflow experiments such as the Tsuji burner [Tsuji, 1982], extinction can be achieved by increasing the exit velocities of oxidant and/or fuel streams, U_O and U_F, or by dilution. Increased U_O and/or U_F

leads to increased strain rate, thereby reducing the flow characteristic time τ_f and hence rendering $Da < Da_e$. For the dilution induced extinction, varied fuel and oxidizer concentrations can result in different chemical characteristic time τ_{chem}. In addition, spherical burner-stabilized flames are used for the extinction in the micro-gravity condition [Chernovsky et al., 2007; Santa et al., 2007; Tse et al., 2001]. The radius of the spherical flame can be adjusted through controlling the flow rates from the burner. Two flow establishments can be made, i.e. by issuing the fuel into the ambient oxidizer or by issuing the oxidizer into the fuel environment. The dilution effects can also be investigated with some additives introduced into the streams [Tse et al., 2001].

2.3 Extinction in turbulent non-premixed flames

2.3.1 Experimental studies

2.3.1.1 Localized extinction

Single point Raman−Rayleigh−LIF measurements

The flame structures can be measured from single-point and planar imaging experiments using the Raman−Rayleigh−LIF diagnostic methods. When local extinction occurs, one can see that the data points representing the composition variables demonstrate large scatter approximately between the fully burning and frozen solution profiles predicted from the laminar flame calculations [Masri et al., 1996]. The bimodality of conditional PDFs of reactedness is also exhibited when the flame approaches blow-off.

Local extinction can be found when the fuel jet velocity is sufficiently high in jet or bluff body flames, such as the piloted jet and bluff body non-premixed flames summarized by Masri et al. [1996], DLR flames [Meier et al., 2000], Sandia flames D−F [Barlow and Frank, 1998] and also the bluff body and swirl-stabilized flame series measured by the researchers from University of Sydney [Dally et al., 1998]. For the bluff body flame measured by Dally et al. [1998], beyond some critical jet velocity local extinction occurs in the immediate downstream of the recirculation zone (also termed as the neck region) where intense mixing exists, consistent with the local extinction features in piloted flames [Barlow and Frank,

1998]. In fact, in some of the Sydney swirl-stabilized flames (i.e. SM and SMH series) with low swirl number, the earliest local extinction also occurs around the neck region, similar to the bluff body flames [Dally et al., 1998]. However, for high swirl number cases, when the fuel jet velocity is increased, the earliest local extinction appears at the flame base, which lies in the upstream of the RZ and near the bluff body. This may be related to the features of localized flow rotation, flow reversals and the velocity shear stresses [Masri et al., 2006].

Meier et al. [2006] measured three swirling methane/air non-premixed flames in a model gas turbine combustor with varying swirl numbers. The elements of this burner and illustrations of flow pattern as well as flame topology are shown in Fig. 2.3. In this burner, the swirling air is provided through the central and annular nozzles, while the fuel methane (CH_4) is fed from a series of circularly equipped injectors. It was found that at the considered axial locations there is considerable scattering for temperature and selected species mass fractions versus mixture fraction. In addition, the flame lift-off is also indicated by the appearance of immediate or low temperature close to the burner. Their measurements of major species concentrations, temperature and mixture fraction with laser Raman scattering provide a good database for modellers to evaluate their combustion models in simulating the gas-turbine-like and fuel lean combustion, if complete validations with the above mentioned simple flame configurations have been made.

Planar laser-induced fluorescence measurements

High speed PLIF technique can be used for imaging reactive radicals, such as hydroxyl (OH), formaldehyde (CH_2O) and methylidyne (CH). When it is combined with other diagnostic tools, such as PIV and Rayleigh imaging techniques, more informative data can be acquired, for instance, velocity and derived strain rate fields, as well as the temperature field.

The local extinction and re-ignition in the DLR-B turbulent non-premixed flame from the database of the TNF workshop were studied by Hult et al. [2005] and the correlations between them and the strain rate and temperature fields were analyzed with OH-PLIF imaging, stereoscopic PIV and Rayleigh imaging techniques. Furthermore, the dissipative scales in both DLR-A and DLR-B were

also investigated by Kaiser and Frank [2009] and the analysis about the statistics of number and size of flame holes (corresponding to possible instantaneous local extinction events) identified from OH-PLIF indicates that the DLR-B has more pronounced streamwise varying hole numbers than DLR-A but its hole sizes are more uniform. The mechanisms for re-ignition in flame holes of DLR-B were studied by Steinberg et al. [2011] and based on their analysis the flame hole can be re-ignited predominantly by edge-flame propagation and also flow transport in some circumstances. This is different from the findings by Hult et al. [2005], in which the roles of local vortical structures are fairly emphasized.

Juddoo and Masri [2011] also used the OH-PLIF imaging techniques to study a range of turbulent non-premixed piloted jet flames and the selected fuel compositions are CNG, CNG/air and CNG/hydrogen (H_2). The former two fuels respectively correspond to the Sydney flames L, B, M and Sandia flames D and E. The time sequence analysis was made for all the flames and three dynamically evolving structures were identified, i.e. breaks, closures and growing kernels. Juddoo and Masri [2011] analyzed the individual rates of breaks and closures and found that the breakage rate is faster than the closure rate. Similar to what was found by Steinberg et al. [2011], they also acknowledged the contributions from growing kernels in flame hole re-ignition, particularly when the flame is very close to blow-off.

The scalar dissipation rate has a significant influence on reaction rates of turbulent non-premixed flames [Bilger, 1976]. Recently, Sutton and Driscoll [2007] measured the mixture fraction, scalar dissipation, temperature, and fuel consumption rate simultaneously in a turbulent non-premixed carbon monoxide (CO) flame with nitric oxide (NO) PLIF and Rayleigh scattering diagnostics [Sutton and Driscoll, 2006]. It was found that the strong scalar dissipation close to the regions with stoichiometric mixture fraction may lead to the occurrence of local extinction, visualized by the low fuel consumption rate. With the two dimensional imaging technique for mixture fraction and scalar dissipation, they also compared the distinctions of scalar dissipation structures for two turbulent CO flames with varying jet velocities [Sutton and Driscoll, 2013]. When the jet exit velocity is closer to blow-off point, more local extinction occurs and the scalar dissipation structures exhibit more discernable isotropy, similar to those in turbu-

lent non-reacting flows [Su and Clemens, 2003]. To examine the relation between the scalar dissipation conditioned on mixture fractions and local extinction level, Sutton and Driscoll [2013] also compared the results from their CO flames with those from Sandia flames D and E [Karpetis and Barlow, 2005], as well as the H_2/CO_2 flames [Kelman and Masri, 1998]. It was shown that the peak value of mean dissipation rate is smaller for the flames closer to blow-off, but their reduction magnitudes are different in the above three groups of flames.

The local extinction during blow-out process was visualized by Stöhr et al. [2011] with simultaneous PIV and OH-PLIF measurements in the same model gas turbine combustor investigated by Meier et al. [2006] (cf. Fig. 2.3), which clearly indicates the intrinsic blow-out mode. Specifically, the flame root is quenched first and the flame can survive for a finite duration downstream along the PVC until complete blow-out. More recently, the local extinction characteristics in stable and blow-off cases of a different prototype of gas turbine combustor were studied by Cavaliere et al. [2013] with 5 kHz OH-PLIF. Different from the observations of Stöhr et al. [2011], during the blow-off transients, the instantaneous extinction level becomes increasingly severe, leading to the gradual flame fragmentation and shrinking towards bluff body where the recirculating flows dominate. The long-lasting re-ignition and local extinction process there considerably delays the blow-off conditions. In addition, measuring the flame holes in swirl flows is not as straightforward as in jet flames [Juddoo and Masri, 2011; Steinberg et al., 2011]. This is because the strong tangential velocities may lead to the significant out-of-plane motions, which makes the motions of flame holes and their edges difficult to be predicted unless accurate flow measurements are provided. Furthermore, even if the clear-cut signals can be discerned from OH-PLIF images, the locations of the flame fronts and therefore the flame holes are still difficult to be determined, due to the high distortion of the actual reaction zones.

2.3.1.2 Global extinction

The early work on blow-out in turbulent non-premixed jet flames is always linked to the lift-off and stabilization, due to their essential physical correspondence. Rich experimental data were measured and empirical or semi-empirical correla-

tions for lift-off and blow-off were derived, such as by Kalghatgi [1984], Broadwell et al. [1985], Pitts [1989] and Dahm and Mayman [1990], just to name a few. One can refer to the review papers by Lyons [2007] and Lawn [2009] for more details. Recently, the OH-PLIF technique was applied by Wu et al. [2006] to visualize the blow-out transients for turbulent non-premixed jet flames. The critical position along the stoichiometric mixture fraction iso-lines is identified, beyond which the flame would step into the pulsating and unstable stage, towards the possible blow-out. Meanwhile, based on the images from OH-PLIF, the flame root is first lifted with the local extinction occurring there, then pulsates downstream around 20 times the jet exit diameters and ultimately blows out.

To the author's knowledge, the first systematic investigations about the blow-out in turbulent swirling non-premixed flames were conducted in University of Michigan by Feikema et al. [1990] and Feikema et al. [1991]. The burner for the swirl-stabilized methane flame experiments is schematically shown in Fig. 2.4. The swirling motion is generated with four tangential air inlets connected to an axial air inlet. The central fuel jet is surrounded by the swirling air. As shown in Fig. 2.4, the diverging wall section has a inclination angle of 30° and is designed for improving recirculating strength and flame stability. Feikema et al. [1990] measured the blow-out curves for a range of operating conditions (i.e. fuel bulk velocity versus air bulk velocity) and examined the effects of swirl velocity, burner size and fuel composition (i.e. H_2 addition) through comparing their blow-out diagrams. The blow-off modes are different for fuel-rich and fuel-lean limits: at fuel-lean limit only short and recirculating flames can be observed, without pronounced lift-off. The envelops for stable flames are extended with increased swirl number, particularly for the fuel-rich conditions. Moreover, the stable regions strongly depend on the burner size. In the investigated smallest size, the stable regions are not disjoined with isolated regions for lifted flames. Feikema et al. [1991] also compared the flame shapes without and with swirl and it was found that the existence of coaxial velocity would shorten the flame but the ratio of fuel velocity to fuel tube diameter should be reduced to prevent the blow-out. Furthermore, the correlation between fuel and air velocities for blow-out limits was also presented by Feikema et al. [1990], with help of the Damköhler number derived by Broadwell et al. [1985]. They estimated the characteristics

flow time scale and chemical time scale as $\tau_f = U_F/d_F$ and $\tau_{chem} = S_L^2/\alpha_F$, respectively. d_F is the jet exit diameter. It is still questionable about whether these estimations are reliable for swirling flows, although their measured blow-off conditions do collapse to that correlation line.

In the swirl burner from University of Michigan, the recirculating motion is created only by the swirling motion [Feikema et al., 1990, 1991]. The researchers from University of Sydney developed a swirl burner, as a simple extension from the bluff-body burner [Dally et al., 1998]. Al-Abdeli and Masri [2003] measured the blow-off limits for different operating conditions with three fuel compositions (i.e. SM−pure CH_4, SMA−air diluted CH_4 and SMH−H_2 added CH_4), and different flame shapes were also recorded schematically. Based on the results by Al-Abdeli and Masri [2003], it is unambiguous that blow-off limits (i.e. central fuel jet bulk velocity versus the swirl number) depend on the swirl number, Reynolds number and also the fuel composition. As mentioned above, two blow-off modes, base and neck blow-off, can be observed for SM and SMH flame series, while only the base blow-off can be seen in SMA series. In their work, base and neck indicate the positions where the earliest localized extinction occurs during the blow-off transients [Al-Abdeli and Masri, 2003].

Blow-off of non-premixed, premixed and also spray flames in a confined swirl burner was experimentally investigated by Cavaliere et al. [2013]. The elongated IRZ in the chamber are generated by the bluff body and dominantly by the swirling air from the annulus. Due to the existence of chamber walls, the CRZ is also observable, which does not appear in the Michigan and Sydney burners [Al-Abdeli and Masri, 2003; Feikema et al., 1990]. For the methane non-premixed flames, Cavaliere et al. [2013] used the 5 kHz OH* chemiluminescence and 5 kHz OH-PLIF to record the blow-off transients. The blow-off durations τ_{BO} estimated from the area integrated OH* chemiluminescence signals were presented. The localized extinction and complete blow-off process were visualized resorting to the images acquired with combined OH* chemiluminescence and OH-PLIF. For blow-off of non-premixed flames in this swirl burner, no continuous lift-off can be observed, similar to mode of the fuel-lean swirling flames studied by Feikema et al. [1991], and alternate local extinction and re-burning appear in the IRZ close to the bluff body until complete extinction.

Blow-out dynamics in another gas turbine model combustor shown in Fig. 2.3 were investigated by Stöhr et al. [2011]. The roles of both helical flame zone, where the PVC exists, and flame root in flame stabilization are emphasized. The blow-out starts when the extinction state at the flame root lasts exceeding a critical duration, followed by the expanded extinction in the helical flame zone until the global extinction happens. During the blow-out process, the re-ignition in the flame root is inhibited by the intermittent fluctuations of local strain rate [Stöhr et al., 2011]. This is in contrast to what was observed by Cavaliere et al. [2013], in which case the re-ignition at the flame near the bluff body persists even near the blow-off point.

2.3.2 Computational studies

2.3.2.1 Localized extinction

DNS

Extinction and re-ignition in non-premixed combustion of isotropic decaying turbulence were studied by Sripakagorn et al. [2004] with three dimensional DNS. The different mechanisms for re-ignition, i.e. independent flamelet, edge flame propagation and engulfment, were identified and the evolutions of the flame elements were tracked with a Lagrangian approach. However, they used single step chemistry and did not account for the density variation. Lately, the planar non-premixed ethylene jet flames (with $Re = 5120$) were studied with compressible DNS and detailed chemistry by Lignell et al. [2011], concentrating on the Da effect on extinction and re-ignition therein. It was found that the flow development, including the scalar dissipation rate, stoichiometric surface area, and heat release rate evolution, strongly depend on the extinction level. However, due to the relatively high computational cost, DNS still limits itself towards the computations of more realistic flow condition and intricate fuel chemistry.

Transported PDF model

The capacity of a joint velocity−composition−turbulence frequency PDF model in RANS was tested for predicting the local extinction and re-ignition in Sandia flames D, E and F [Xu and Pope, 2000]. The extensive comparisons for profiles of

velocity means and variances, conditional statistics and conditional PDF indicate that the levels of local extinction in the simulated flames are correctly predicted. However, the local extinction in Sandia flame F is under-predicted. In addition, the accuracy of local extinction prediction, particularly in flame F, is shown to greatly depend on the mixing model, particularly the velocity-to-scalar timescale ratio.

Sandia flames D, E and F were also selected for testing the capability of the filtered probability density function/stochastic field method in LES [Jones and Prasad, 2010]. The increased levels of local extinction caused by the increased jet velocities of flames D, E and F were well reproduced by the simulations, but similar to the work by Xu and Pope [2000], the localized extinction in flame F was also under-predicted. It may be attributed to the selected chemical kinetics [Jones and Prasad, 2010].

Flamelet model

There are also many efforts made to develop the ability of the flamelet model in combustion with local extinction and re-ignition. For instance, the Lagrangian unsteady flamelet governing equations were solved to study the CO production in the methane non-premixed flame close to extinction [Mauss et al., 1991]. Additionally, a stochastic, interacting flamelet model was developed to extend the ability of the unsteady flamelet model to predict re-ignition [Pitsch and Fedotov, 2001; Pitsch et al., 2003].

The FPV model was proposed by Pierce and Moin [2004] based on the steady flamelet model. The progress variable predicted from reactive scalars was introduced, thereby accounting for the local extinction and re-ignition. The assumptions in FPV model (e.g. steady flamelet and single flamelet closure) were assessed by Ihme et al. [2005] against the DNS results of decaying isotropic turbulence with a one-step reversible chemical reaction at different levels of local extinction and re-ignition. The models for the presumed PDFs for conserved and reactive scalars were studied further and a statistically most likely distribution was applied [Ihme and Pitsch, 2008b]. Based on the work by Ihme and Pitsch [2008b], the reactive scalar distributions can be accurately represented when more than two moments were taken into account. This FPV model was

applied in LES for predicting the local extinction and re-ignition in Sandia flames D and E [Ihme and Pitsch, 2008a] and good results were observed for statistical flow field quantities and conditional data in mixture fraction space.

CMC model

The investigations on local extinction in turbulent non-premixed flames with the CMC model can also be found, which can be dated back to the 2000s. The doubly-conditional moment closure approach was developed by Cha et al. [2001], with the scalar dissipation rate as the second conditioning variable. This approach can capture the local extinction, but predict the occurrence of re-ignition too early. Furthermore, the fluctuations around the conditional mean are still significant. Meanwhile, the higher order CMC model directly for the chemical source term itself was investigated by Cha and Pitsch [2002], but closure of the transport equations for higher moments was still a challenge in their work. The second order correction was also made to the conditional reaction term with both the assumed conditional joint PDF method and the Taylor expansion method [Kim et al., 2002]. With the latter method, the onset of re-ignition was not correctly predicted. Later, Kronenburg [2004] and Kronenburg and Papoutsakis [2005] introduced sensible enthalpy as the second conditioning variable to account for the reactive scalar fluctuations around their singly conditioned means. The same modelling strategies were used to simulate the Sandia flames D, E and F [Kronenburg and Kostka, 2005]. Excellent agreements of major species and intermediate were achieved for flames D and E, while for flame F the conditional temperature is over-predicted.

The CMC equations has been derived for LES [Bushe and Steiner, 1999; Navarro-Martinez et al., 2005; Triantafyllidis and Mastorakos, 2010], and the first order CMC model with detailed chemistry has been applied for predicting the local extinction in turbulent non-premixed flames. The inclusion of detailed chemistry is helpful in analyzing the chemical kinetics during the extinction events. The Delft III non-premixed jet flames were simulated by LES/CMC modelling with GRI 3.0 mechanism [Smith et al., 2000] and localized extinction and re-ignition were demonstrated, with the strong fluctuations for the conditional reactive scalars in the mixture fraction space for the upstream streamwise loca-

tions [Ayache and Mastorakos, 2012]. The similar LES/CMC models were also used by Garmory and Mastorakos [2011] with ARM2 mechanism [Sung et al., 1998] for Sandia flames D and F. In their work, the model constant for the sub-grid scale scalar dissipation rate was tuned compared with the conditional scalar dissipation behaviors for Sandia flame D, and based on new constant the extent of local extinction in flame F was correctly captured. This explicitly implies that when strong finite-rate chemistry effect dominates (such as in Sandia flame F), contributions to the total scalar dissipation rate from the sub-grid scale component may become significant. The LES/CMC models developed for turbulent non-premixed flames [Ayache and Mastorakos, 2012; Garmory and Mastorakos, 2011] were also extended to spray combustion approaching blow-off, assuming the mixture fraction framework for non-premixed flame can still apply for the spray flame regime [Tyliszczak et al., 2014].

MMC model

A stochastic implementation of the MMC approach in RANS was applied to Sandia flame D with "Interaction by Exchange with the Mean"(IEM) as the sub-grid mixing model [Vogiatzaki et al., 2011] and it was observed that whether the MMC-IEM model can correctly predict the level of localized extinction depends on the parameter of "minor dissipation time scale". Ge et al. [2013] performed the Sparse-Lagrangian MMC simulations for Sandia flames D, E and F. Their results show that the increased level of local extinction was correctly predicted but for Sandia flame F, an early prediction of re-ignition was observed. It was also shown that the characteristic distance in mixture fraction space between mixing particles directly influences the occurence of extinction in Sandia flame F with their MMC model [Ge et al., 2013]. The hybrid binomial Langevin−MMC model was developed by Wandel and Lindstedt [2013], which is expected to combine the benefits for both binomial Langevin model and the MMC model. The results from simulations of Sandia flame E show that the the local extinction is predicted better than the MMC model with the Euclidean minimum spanning tree mixing model, which leads to very little local extinction.

2.3.2.2 Global extinction

As far as the author is aware, the computational studies on blow-off or blow-out in turbulent non-premixed flames are comparatively limited. Some mathematical modelling efforts about the blow-off critical conditions have been made, typically extended from the investigations of lifted flames [Bradley et al., 1998]. However, LES or RANS with advanced combustion models is still not common.

2.3.3 Summary

The understanding on local and global extinction in turbulent non-premixed flames is increasingly profound with help of the state-of-the-art diagnostic techniques. The flame structures can be measured with the Raman−Rayleigh−LIF diagnostic methods and therefore the extinction events can be quantified by their evolutions. Meanwhile, the PLIF diagnostic technique provides the significant tool to visualize the local extinction and blow-off transients.

In terms of computational modelling, different levels of success in local extinction predictions using the above mentioned combustion models have been achieved. Although their mathematical principles and characterizations are different, however, all these combustion models should have the capacity to accurately simulate or model the mixing fields, PDF, scalar dissipation rate, and/or the flow transport effects on the local flame structures, if the local extinction dynamics aim to be predicted by them correctly. For instance, the correctness of the mixing model in transported PDF and also in MMC is an important concern, as indicated by Xu and Pope [2000] and Wandel and Lindstedt [2013]. However, for CMC model, the mixing fields are solved, instead of being modelled, but how to model the scalar dissipation rate needs delicate efforts [Garmory and Mastorakos, 2011]. For flamelet model, their early studies are concentrated on how to incorporate the flamelet interaction [Pitsch and Fedotov, 2001; Pitsch et al., 2003] and lately about how to accurately describe the transient intermediate state between burning and quenched flamelets [Pierce and Moin, 2004]. In this sense, one can see that these different aspects are equally important in predicting the local extinction, but with different levels of concern for different models. Additionally, the computational studies on global extinction are limited. This topic will be one

of the objectives in this thesis using LES and multi-dimensional CMC model.

2.4 State of the art of the CMC model

Although the studies on extinction predictions with the CMC combustion model have been reviewed in Sub-section 2.3.2, it seems still necessary to appreciate its latest developments and applications in broader dimensions in this Section. The derivations, main features, closures/assumptions and some applications are discussed in-depth in the comprehensive reviews by Klimenko and Bilger [1999]. Recently, the theoretical developments and the applications to flows of engineering interest achieved in the decade of 2000−2010 are reviewed by Kronenburg and Mastorakos [2011]. Therefore, for simplicity, in this Section the progress of the CMC model made roughly from 2010 till now (2015) will be mainly focused, on the aspects of modelling and implementation, applications to near-limit gaseous flame dynamics, and applications to multiphase combustion.

2.4.1 Modelling

The conditional scalar dissipation in the micro-mixing term in the CMC governing equations is one of the unclosed quantities. Different from widely adopted scalar dissipation model from homogeneous mixing assumption, the one from inhomogeneous mixing model, proposed by Devaud et al. [2004], was introduced and its influences on the auto-ignition predictions in high pressure methane jets were studied. It was found that the inhomogeneous mixing model has a significant improvement about the ignition delay and ignition kernel evolutions [Milford and Devaud, 2010]. Devaud et al. [2013] applied the MMC model to calculate the turbulent mixing field and the conditionally filtered scalar dissipation rate in the Cabra lifted hydrogen flames. In addition, the differential diffusion effect (and therefore the assumption of unity Le is relaxed) was incorporated into the CMC model for both conditional mass fraction and enthalpy governing equations [Ma and Devaud, 2015]. For the conditional reaction term, the tabulated chemistry was developed for both first and second order closures [Colin and Michel, 2015] and their accuracy and computational cost were analyzed with a lifted

methane/air flame. The results show that the computational cost of tabulated chemistry is less than ten times that of the flamelet model. Also, the Lagrangian CMC method was proposed by Han and Huh [2015] where multiple Lagrangian fuel groups are identified according to injection sequence or residence time.

2.4.2 Implementation of conservative CMC

The finite volume discretizations for the two dimensional CMC equations were implemented with RANS by Cleary and Kent [2005] in predicting CO in hood fires. The three dimensional conservative CMC model for an unstructured-grid finite volume method was developed to simulate the complex, turbulent non-premixed syngas/air flames by Kim et al. [2008]. They also demonstrated the advantages of finite volume CMC model in improving the robustness and accuracy for the boundary treatment of CMC-related numerical fluxes. The flux conservation idea was also applied by Mobini and Bilger [2009] to investigate the CO and NO in an ISR. Thornber et al. [2011] discretized the CMC governing equations for LES of premixed flames and demonstrated the numerical flux predictions in the framework of finite volume method. Recently, the finite volume discretization for the conservative CMC governing equations was implemented by Siwaborworn and Kronenburg [2013] and validated with Sandia flames D−F. The different approaches for predicting the convective fluxes were also discussed. Meanwhile, the finite volume discretization on unstructured meshes was implemented by Garmory and Mastorakos [2015] and the reconstruction of polyhedral CMC cells was applied. Nevertheless, an oxy-fuel jet flame was simulated by them and the focus is about correct predictions of the scalar fields with different compositions in oxidiser and fuel streams. Applications of the conservative CMC model in predicting near-limit flame dynamics such as extinction are still not common. In this work, the three dimensional conservative CMC model will be discretized on unstructured meshes with finite volume method, and its applications in extinction of turbulent swirling non-premixed flames will be investigated.

2.4.3 Applications to near-limit gaseous flame dynamics

In recent years, the CMC model has been extensively used for simulating the near-limit dynamics of turbulent non-premixed flames. Prediction of extinction in turbulent non-premixed flames has been reviewed in Sub-section 2.3.2 and therefore will not be repeated again. Triantafyllidis et al. [2009] applied LES with the sub-grid scale CMC model to simulate the spark ignition in a non-premixed bluff body methane flame, comfirming the ability of the CMC model in forced ignition prediction. Also, ignition of lean *n*-heptane/air and *iso*-octane/air mixtures with various levels of thermal stratification was investigated by Salehi et al. [2015] and the advanced ignition from their computations was related to the level of ignition delay time fluctuations. The lifted flames and their stabilization mechanisms were studied by Navarro-Martinez and Kronenburg [2009] and Navarro-Martinez and Kronenburg [2011]. An extinction model has been incorporated into the first-order CMC to improve its predictions of lift-off height for a turbulent lifted methane/air flame issuing in a vitiated coflow [Roy et al., 2014]. LES with the first order CMC model was used by Stanković et al. [2013] for simulating the auto-ignition regimes in the lifted hydrogen flame in hot turbulent air coflow and all the auto-ignition regimes (i.e. no ignition, random spots, flashback and lifted flame) were reproduced. These successful applications of the CMC model in studying the near-limit flame dynamics can be attributed to its intrinsic ability in predicting different effects, such as scalar dissipation, convection and sub-grid scale diffusion, which are expected to have significant influences on the above flame phenomena.

2.4.4 Applications to multiphase combustion

Significant progress has been made about applications of the CMC model in multiphase combustion in recent years. The governing equations for spray combustion were first derived by Mortensen and Bilger [2009]. As the first work introducing the evaporation source terms in CMC, the two dimensional, first order CMC model was used for simulations of an *n*-heptane spray auto-ignition under a diesel engine condition [Borghesi et al., 2011]. The conditional evaporation term is closed assuming interphase exchange to occur at the droplet saturation

mixture fraction values only. LES with sub-grid scale CMC model for turbulent acetone spray flame was conducted and the relevant modelling issues, particularly concerning the conditional evaporation terms, were examined by Ukai et al. [2013]. The same author also introduced the two-conditional moment method to account for the existence of pre-evaporated fuel by introducing two sets of conditional moments based on different mixture fractions [Ukai et al., 2014], in order to overcome the limitations of upper limit in mixture fraction space in their previous work [Ukai et al., 2013]. The blow-off in a swirl heptane spray flame was investigated and the blow-off transients and duration are reasonably reproduced by Tyliszczak et al. [2014]. In addition, the soot formation of n-heptane auto-igniting spray in a constant volume vessel under diesel engine conditions was predicted with two-dimensional, first order CMC model [Bolla et al., 2013]. The transport equations for soot mass fractions and soot number density were solved. The above efforts with the CMC model developments in spray combustion are encouraging and provide a foundation for the continued research in the future.

2.4.5 Summary

The CMC combustion model has been developed in the aspects of modelling and implementation and been applied to simulate the near-limit phenomena in turbulent non-premixed flames and multiphase combustion recently. One of the objectives in this thesis is to derive the conservative governing equations and implement the CMC model in the finite volume discretization. This is a development for the CMC model discretization and also a step towards extending the CMC model in simulating the realistic burners with complex geometries and boundaries, such as gas turbine combustors.

2.5 Conclusions

This Chapter first describes the phenomenological theories for extinction based on the S-shaped curve. Then both theoretical and computational studies about local and global extinction in laminar non-premixed flames are discussed. For local extinction in turbulent non-premixed flames, the progress in experimen-

tal and computational investigations are reviewed. However, limited studies on global extinction are available. In addition, the state of the art of the CMC combustion model is also reviewed in the aspects of modelling and implementation, applications to near-limit gaseous flame dynamics and multiphase combustion.

2.6 Figures for Chapter 2

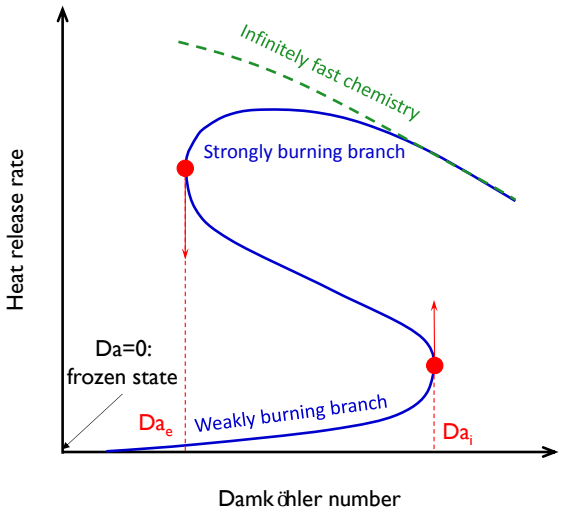

Figure 2.1: Schematic of S-curve [Williams, 1985].

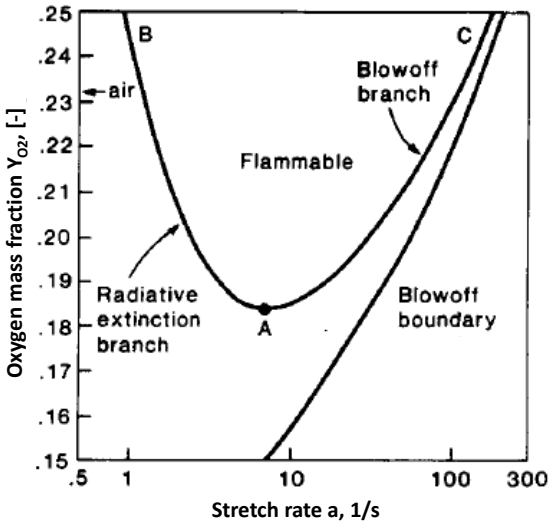

Figure 2.2: Flammability map parameterized by oxygen mass fraction and stretch rate for a stagnation flame near the condensed fuel surface [T'ien, 1986].

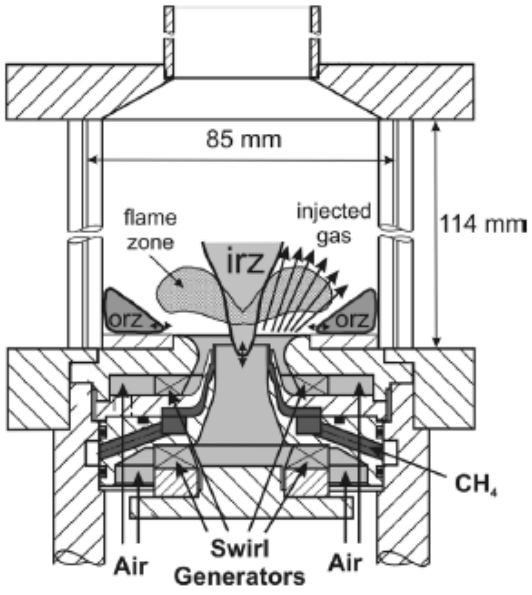

Figure 2.3: Schematic of the dual swirl burner and combustion chamber investigated by Meier et al. [2006].

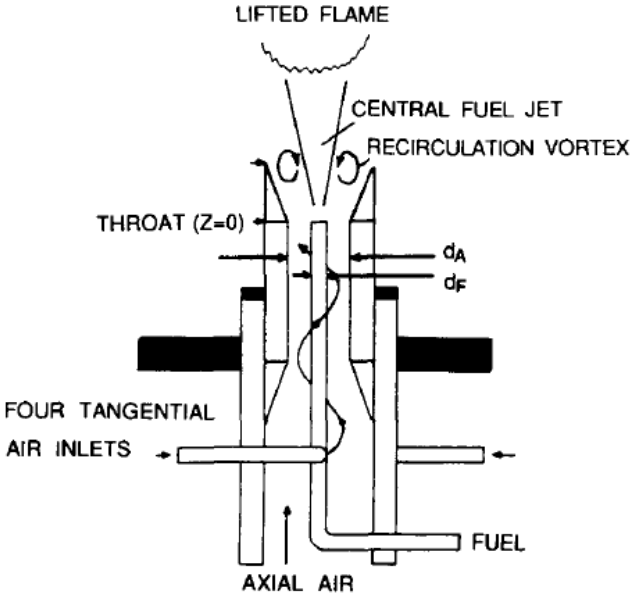

Figure 2.4: Schematic of swirl burner from University of Michigan [Feikema et al., 1990].

Chapter 3

Governing Equations and Numerical Discretizations

3.1 Large eddy simulation

In LES, the large-scale energy containing flows are resolved while the small, sub-grid ones and their effects on the resolved flows are modelled. The decomposition of resolved and sub-grid scales are performed through introducing the spatial filter function G [Leonard, 1975], which is defined as

$$\bar{f}(x) = \int \bar{f}(x')G(x - x', \Delta(x))dx', \tag{3.1}$$

in which the integral is over the flow domain and x denotes the coordinate in the LES computational domain Ω^{LES}. f is the function to which G is applied and Δ is the filter width and here it is estimated as $\Delta = \sqrt[3]{\mathcal{V}^{LES}}$, where $\mathcal{V}^{LES}$ is the volume of LES cells. The filter function G satisfies the normalization condition

$$\int G(x - x', \Delta(x))dx' = 1. \tag{3.2}$$

3.1.1 Isothermal incompressible flows

The filtered governing equations for isothermal incompressible flows can be derived when the filter function, i.e. Eq. (3.1), is applied to the corresponding

instantaneous mass and momentum equations. They are formulated as [Poinsot and Veynante, 2005]

$$\nabla \cdot \bar{\mathbf{U}} = 0, \tag{3.3a}$$

$$\frac{\partial \bar{\mathbf{U}}}{\partial t} + \nabla \cdot (\bar{\mathbf{U}}\bar{\mathbf{U}}) = -\frac{1}{\rho}\nabla \bar{p} + \nabla \cdot (\bar{\mathbf{S}} - \mathbf{B}), \tag{3.3b}$$

in which $\bar{\mathbf{S}} = 2\nu\mathbf{D}$ is the viscous stress tensor and the strain rate tensor $\mathbf{D}$ is

$$\mathbf{D} = \frac{1}{2}\left(\nabla \bar{\mathbf{U}} + \nabla \bar{\mathbf{U}}^T\right), \tag{3.4}$$

which is the symmetric part of the velocity gradient. Furthermore, $\mathbf{B}$ is the sub-grid scale stress tensor and reads

$$\mathbf{B} = \overline{\mathbf{U}\mathbf{U}} - \bar{\mathbf{U}}\bar{\mathbf{U}}, \tag{3.5}$$

which represents the contributions of momentum from sub-grid scales to the resolved scales.

In this thesis, the linear eddy-viscosity model for $\mathbf{B}$ is applied and it is assumed that the deviatoric part of $\mathbf{B}$ is aligned with the resolved deviatoric part of strain rate tensor $\mathbf{D}$, i.e.

$$\mathbf{B} = \frac{2}{3}k\mathbf{I} - 2\nu_{sgs}\bar{\mathbf{D}}_{dev}, \tag{3.6}$$

while the normal stress of $\mathbf{B}$ is related to the sub-grid scale kinetic energy k with

$$k = \frac{1}{2}\mathrm{tr}(\mathbf{B}). \tag{3.7}$$

The deviatoric part of resolved strain rate tensor is

$$\bar{\mathbf{D}}_{dev} = \bar{\mathbf{D}} - \frac{1}{3}\mathrm{tr}(\bar{\mathbf{D}})\mathbf{I}. \tag{3.8}$$

The Smagorinsky model is used here to close the sub-grid scale viscosity ν_{sgs} and kinetic energy k in Eq. (3.6) [Lilly, 1965], i.e.

$$\nu_{sgs} = c_k \Delta k^{1/2}, \tag{3.9}$$

$$k = 2\frac{c_k}{c_\epsilon}\Delta^2\|\bar{\mathbf{D}}\|^2, \tag{3.10}$$

in which $\|\bar{\mathbf{D}}\|$ is the magnitude of the filtered strain rate tensor and here defined as $\|\bar{\mathbf{D}}\| = \sqrt{\bar{\mathbf{D}} : \bar{\mathbf{D}}}$. The model constants c_k and c_ϵ in Eqs. (3.9) and (3.10) are respectively 0.094 and 1.048 [Fureby, 1996]. The underlying assumptions for Eqs. (3.9) and (3.10) are that the small scales are in equilibrium and instantaneously dissipate all the energy received from the large-scale flows [Smagorinsky, 1963].

The consistency between the current model (i.e. Eqs. 3.9 and 3.10) and Smagorinsky model with one constant C_S can be demonstrated if Eq. (3.10) is substituted into Eq. (3.9)

$$\nu_{sgs} = c_k\sqrt{2\frac{c_k}{c_\epsilon}}\Delta^2\sqrt{\bar{\mathbf{D}} : \bar{\mathbf{D}}} = (C_S\Delta)^2\sqrt{2\bar{\mathbf{D}} : \bar{\mathbf{D}}}. \tag{3.11}$$

Therefore, the original "Smagorinsky constant" C_S takes the following form

$$C_S = \sqrt{c_k\sqrt{\frac{c_k}{c_\epsilon}}}, \tag{3.12}$$

and hence $C_S = 0.168$.

3.1.2 Reacting flows

For variable-density flows such as reacting flows, it is advantageous to use density-weighted (Favre) filtered quantities, i.e.

$$\tilde{f} = \frac{\overline{\rho f}}{\bar{\rho}}, \tag{3.13}$$

instead of those from Eq. (3.1), since with it the covariance of density and other quantity fluctuations would not appear and the resulting equations are closer to the original instantaneous equations [Poinsot and Veynante, 2005]. The LES governing equations for mass, momentum and mixture fraction are derived through applying Eq. (3.13) to their corresponding instantaneous equations and

read [Poinsot and Veynante, 2005]

$$\frac{\partial \bar{\rho}}{\partial t} + \nabla \cdot \left(\bar{\rho} \tilde{\mathbf{U}} \right) = 0, \tag{3.14a}$$

$$\frac{\partial \bar{\rho} \tilde{\mathbf{U}}}{\partial t} + \nabla \cdot \left(\bar{\rho} \tilde{\mathbf{U}} \tilde{\mathbf{U}} \right) = -\nabla \bar{p} + \nabla \cdot \left(\tilde{\mathbf{S}} - \mathbf{B} \right), \tag{3.14b}$$

$$\frac{\partial \bar{\rho} \tilde{\xi}}{\partial t} + \nabla \cdot \left(\bar{\rho} \tilde{\mathbf{U}} \tilde{\xi} \right) = \nabla \cdot \left(\tilde{\mathbf{j}} - \mathbf{b} \right), \tag{3.14c}$$

in which $\tilde{\mathbf{S}} = 2\mu \tilde{\mathbf{D}}_{dev}$ is the filtered stress tensor and $\tilde{\mathbf{j}} = \bar{\rho} D \nabla \tilde{\xi}$ is the molecular scalar transport by assuming a Fick's diffusion law. The molecular viscosity μ and scalar diffusivity D are given by $\mu = \rho\nu$ and $D = \nu/Sc$, respectively. In the low Ma number approximation, the pressure $\bar{p}$ in Eq. (3.14b) is decoupled with the thermodynamic pressure, and its variations do not directly affect the changes of density and temperature [Law, 2006].

In Eq. (3.14b), $\mathbf{B} = \bar{\rho} \left(\widetilde{\mathbf{U}\mathbf{U}} - \tilde{\mathbf{U}}\tilde{\mathbf{U}} \right)$ is the sub-grid scale stress tensor. The constant Smagorinsky model is used to close the deviatoric part of the sub-grid stress tensor $\mathbf{B}$, i.e.

$$\mathbf{B} - 2\bar{\rho} k \mathbf{I}/3 = -2\mu_{sgs} \tilde{\mathbf{D}}_{dev}. \tag{3.15}$$

Here the expression for $\tilde{\mathbf{D}}_{dev}$ has been given in Eq. (3.8). Similar to the estimation for ν_{sgs} in Eq. (3.9), the sub-grid scale viscosity μ_{sgs} is modelled as

$$\mu_{sgs} = c_k \Delta \bar{\rho} k^{1/2}, \tag{3.16}$$

where the constant $c_k = 0.02$ is used [Fureby, 1996]. It should be highlighted here that c_k in Eq. (3.16) does not equal that for Eq. (3.9) in the isothermal flow situation. Based on the local equilibrium (i.e. production equals dissipation) assumption, the algebraic relation is obtained for the sub-grid scale kinetic energy k [Fureby, 1996]

$$\mathbf{B} : \tilde{\mathbf{D}} + \bar{\rho}\epsilon = 0, \tag{3.17}$$

in which the symbol ":"denotes the double inner product of two tensors and the

dissipation rate ϵ is modelled as

$$\epsilon = c_\epsilon \frac{k^{3/2}}{\Delta} \tag{3.18}$$

with the constant $c_\epsilon = 1.048$ [Fureby, 1996].

With Eq. (3.17), one can obtain

$$\frac{2}{3}k\mathbf{I} - 2c_k\Delta k^{1/2}\tilde{\mathbf{D}}_{dev} + \frac{c_\epsilon k^{3/2}}{\Delta} = 0. \tag{3.19}$$

The analytical expression for k can be obtained further from Eq. (3.19), i.e.

$$\begin{aligned} k^{1/2} &= \frac{-\frac{2}{3}\tilde{\mathbf{D}} : \mathbf{I} + \sqrt{\left(\frac{2}{3}\tilde{\mathbf{D}} : \mathbf{I}\right)^2 + 8c_k c_\epsilon \tilde{\mathbf{D}}_{dev} : \tilde{\mathbf{D}}}}{2c_\epsilon/\Delta} = \\ &\frac{-\frac{2}{3}\mathrm{tr}\left(\tilde{\mathbf{D}}\right) + \sqrt{\left[\frac{2}{3}\mathrm{tr}\left(\tilde{\mathbf{D}}\right)\right]^2 + 8c_k c_\epsilon \tilde{\mathbf{D}}_{dev} : \tilde{\mathbf{D}}}}{2c_\epsilon/\Delta}. \end{aligned} \tag{3.20}$$

In the LES equation for filtered mixture fraction, i.e. Eq. (3.14c), $\mathbf{b} = \bar{\rho}\left(\widetilde{\mathbf{U}\xi} - \tilde{\mathbf{U}}\tilde{\xi}\right)$ represents the scalar transport caused by the sub-grid scale fluctuations. It can be modelled similarly to the term $\mathbf{B}$ in Eq. (3.14b), assuming that the sub-grid scale flux is proportional to the gradient of resolved mixture fraction, i.e.

$$\bar{\rho}\left(\widetilde{\mathbf{U}\xi} - \tilde{\mathbf{U}}\tilde{\xi}\right) = -\bar{\rho}D_t\nabla\tilde{\xi}. \tag{3.21}$$

Here the sub-grid scale diffusivity D_t is modelled as $D_t = \nu_{sgs}/Sc_t$ and the sub-grid scale kinematic viscosity ν_{sgs} is calculated as $\nu_{sgs} = \mu_{sgs}/\bar{\rho}$.

The filtered scalar dissipation rate $\tilde{N}$ is determined from both resolved and sub-grid contributions (i.e. N_{res} and N_{sgs}) as [Pera et al., 2006]

$$\tilde{N} = \tilde{N}_{res} + \tilde{N}_{sgs} = \underbrace{D\nabla\tilde{\xi}\cdot\nabla\tilde{\xi}}_{resolved} + \underbrace{\frac{c_N}{2}\frac{\mu_t}{\bar{\rho}\Delta^2}\widetilde{\xi''^2}}_{sub-grid}. \tag{3.22}$$

For the sub-grid scalar dissipation model in Eq. (3.22), the assumption has been made that a characteristic mixing time scale $\widetilde{\xi''^2}/\tilde{N}_{sgs}$ is proportional to

a characteristic velocity time scale ν_{sgs}/Δ^2 [Jiménez et al., 2001; Pera et al., 2006]. In Eq. (3.22), $c_N = 42$ is used, a constant determined through matching the computational and experimental results in Sandia flame D [Garmory and Mastorakos, 2011]. This has given good results for the statistics of local extinction in Sandia flame F [Garmory and Mastorakos, 2011] and for capturing the global extinction of a spray swirl flame [Tyliszczak et al., 2014].

In Eq. (3.22), $\widetilde{\xi''^2}$ is the sub-grid variance of mixture fraction and is modelled with the following scaling law

$$\widetilde{\xi''^2} = c_V \Delta^2 \nabla\tilde{\xi} \cdot \nabla\tilde{\xi}, \tag{3.23}$$

where the constant c_V is 0.1 [Pierce and Moin, 1998]. The models in Eqs. (3.22) and (3.23) and the constants therein, i.e. c_N and c_V, are used for all the LES computations in this thesis.

3.2 Conditional moment closure modelling

In this work, the *conservative* CMC governing equations are derived for finite volume discretizations. We start from the following CMC equation for conditionally filtered mass fraction for α-th species $Q_\alpha \equiv \widetilde{Y_\alpha|\eta}$, which is derived with a fine grained FDF [Navarro-Martinez et al., 2005; Triantafyllidis and Mastorakos, 2010]

$$\frac{\partial Q_\alpha}{\partial t} + \widetilde{\mathbf{U}|\eta} \cdot \nabla Q_\alpha = \widetilde{N|\eta} \frac{\partial^2 Q_\alpha}{\partial \eta^2} + \widetilde{W_\alpha|\eta} + e_f. \tag{3.24}$$

Equation (3.24) has been used for finite difference formulation, such as in the studies by Navarro-Martinez and Kronenburg [2009], Triantafyllidis et al. [2009] and Ayache and Mastorakos [2012]. $\widetilde{\mathbf{U}|\eta}$, $\widetilde{N|\eta}$ and $\widetilde{W_\alpha|\eta}$ are the conditionally filtered velocity, scalar dissipation rate and rate of formation of α-th species per unit mass of mixture, respectively. In Eq. (3.24), the transport in physical space by molecular diffusion is neglected because of the large Re assumption [Klimenko and Bilger, 1999]. The sub-grid scale conditional scalar flux term e_f in Eq. (3.24)

accounts for the conditional transport in physical space. It can be written as

$$e_f = -\frac{1}{\overline{\rho_\eta}\tilde{P}(\eta)}\nabla\cdot\left[\overline{\rho_\eta}\tilde{P}(\eta)\left(\widetilde{\mathbf{U}Y_\alpha|\eta}-\widetilde{\mathbf{U}|\eta}Q_\alpha\right)\right], \tag{3.25}$$

where $\overline{\rho_\eta} \equiv \widetilde{\rho|\eta}$ is the conditional density. The FDF $\tilde{P}(\eta)$ in Eq. (3.25) is modelled with β-function based on the filtered mixture fraction $\tilde{\xi}$ and its sub-grid variance $\widetilde{\xi''^2}$ [Cook and Riley, 1994], i.e.

$$\tilde{P}(\eta) = \frac{\eta^{s-1}(1-\eta)^{t-1}}{B(s,t)}, \tag{3.26}$$

in which the β-function $B(s,t)$ takes the following expression

$$B(s,t) = \frac{\Gamma(s)\Gamma(t)}{\Gamma(s+t)}. \tag{3.27}$$

Here $\Gamma(s)$ is the Gamma function. The quantities s and t are functions of $\tilde{\xi}$ and $\widetilde{\xi''^2}$, i.e.

$$s = \tilde{\xi}\left[\frac{\tilde{\xi}\left(1-\tilde{\xi}\right)}{\widetilde{\xi''^2}}-1\right], \tag{3.28}$$

$$t = \frac{s\left(1-\tilde{\xi}\right)}{\tilde{\xi}}. \tag{3.29}$$

The term e_f in Eq. (3.25) is calculated with the usual gradient model [Kim and Pitsch, 2006; Navarro-Martinez et al., 2005]

$$\widetilde{\mathbf{U}Y_\alpha|\eta}-\widetilde{\mathbf{U}|\eta}Q_\alpha = -D_t\nabla Q_\alpha, \tag{3.30}$$

in which the turbulent diffusivity D_t is considered to be equal for all the species and is the same as the one used for sub-grid scalar flux of mixture fraction in Eq. (3.21). Then e_f in Eq. (3.24) can be re-formulated as

$$e_f = \frac{1}{\overline{\rho_\eta}\tilde{P}(\eta)}\nabla\cdot\left[\overline{\rho_\eta}\tilde{P}(\eta)D_t\nabla Q_\alpha\right]. \tag{3.31}$$

Neglecting the variation of $\overline{\rho_\eta}\tilde{P}(\eta)$ in the gradient operator in Eq. (3.31), and then substituting e_f into Eq. (3.24) yield

$$\frac{\partial Q_\alpha}{\partial t} + \widetilde{\mathbf{U}|\eta} \cdot \nabla Q_\alpha = \widetilde{N|\eta}\frac{\partial^2 Q_\alpha}{\partial \eta^2} + \widetilde{W_\alpha|\eta} + \nabla \cdot (D_t \nabla Q_\alpha). \tag{3.32}$$

The second term of LHS of Eq. (3.32) can be expanded into the following form

$$\widetilde{\mathbf{U}|\eta} \cdot \nabla Q_\alpha = \nabla \cdot \left(\widetilde{\mathbf{U}|\eta} Q_\alpha\right) - Q_\alpha \nabla \cdot \widetilde{\mathbf{U}|\eta}. \tag{3.33}$$

Substituting Eq. (3.33) into Eq. (3.32) yields the following five dimensional equation for Q_α

$$\frac{\partial Q_\alpha}{\partial t} + \nabla \cdot \left(\widetilde{\mathbf{U}|\eta} Q_\alpha\right) = Q_\alpha \nabla \cdot \widetilde{\mathbf{U}|\eta} + \widetilde{N|\eta}\frac{\partial^2 Q_\alpha}{\partial \eta^2} + \widetilde{W_\alpha|\eta} + \nabla \cdot (D_t \nabla Q_\alpha). \tag{3.34}$$

It should be reminded that the conditional density $\overline{\rho_\eta}$ does not explicitly appear in Eq. (3.34) due to the removal of $\overline{\rho_\eta}\tilde{P}(\eta)$ for e_f. Integrating Eq. (3.34) over each CMC cell Ω^{CMC}, one can obtain

$$\begin{aligned} &\underbrace{\int_{\Omega^{CMC}} \frac{\partial Q_\alpha}{\partial t} d\Omega}_{T_0} + \underbrace{\int_{\Omega^{CMC}} \nabla \cdot \left(\widetilde{\mathbf{U}|\eta} Q_\alpha\right) d\Omega}_{T_1} = \\ &\underbrace{\int_{\Omega^{CMC}} Q_\alpha \nabla \cdot \widetilde{\mathbf{U}|\eta} d\Omega}_{T_2} + \underbrace{\int_{\Omega^{CMC}} \widetilde{N|\eta}\frac{\partial^2 Q_\alpha}{\partial \eta^2} d\Omega}_{T_3} + \underbrace{\int_{\Omega^{CMC}} \widetilde{W_\alpha|\eta} d\Omega}_{T_4} + \\ &\underbrace{\int_{\Omega^{CMC}} \nabla \cdot (D_t \nabla Q_\alpha) \, d\Omega}_{T_5}. \end{aligned} \tag{3.35}$$

The physical interpretations of the individual terms in Eq. (3.35) are as follows. Term T_0 denotes the unsteadiness, Term T_1 is the conditional convection, Term T_2 is the conditional dilatation, Term T_3 is the micro-mixing related to the scalar dissipation, and Term T_4 is the conditional reaction rate for α-th species and the last one, T_5, is the sub-grid scale conditional scalar flux.

In Eq. (3.35), Terms T_3 and T_4 are in mixture fraction space, whilst Terms T_1, T_2 and T_5 are in physical space. Equations (3.34) or (3.35) are termed as

the *conservative* CMC governing equations since the finite volume discretization with Gauss divergence theorem can be employed for the terms in physical space, i.e. T_1, T_2 and T_5 and therefore the numerical scalar fluxes related to Q_α across the CMC cell faces can be conserved. The details about the discretization of Eq. (3.35) can be found in Sub-section 3.3.2. Another form of conservative CMC governing equations for LES is also derived and has been listed in Appendix A.

In this work, the CMC governing equation for conditionally filtered total enthalpy $Q_h \equiv \widetilde{h|\eta}$ in an adiabatic system is also solved and the integrated form is

$$\begin{aligned} \int_{\Omega^{CMC}} \frac{\partial Q_h}{\partial t} d\Omega + \int_{\Omega^{CMC}} \nabla \cdot \left(\widetilde{\mathbf{U}|\eta} Q_h \right) d\Omega = \\ \int_{\Omega^{CMC}} Q_h \nabla \cdot \widetilde{\mathbf{U}|\eta} d\Omega + \int_{\Omega^{CMC}} \widetilde{N|\eta} \frac{\partial^2 Q_h}{\partial \eta^2} d\Omega + \int_{\Omega^{CMC}} \nabla \cdot \left(D_t \nabla Q_h \right) d\Omega, \end{aligned} \tag{3.36}$$

which has the same form as Eq. (3.35) without the conditional reaction term.

Compared to Eq. (3.24), the conditional dilatation effect has been decomposed from the conditional convection term in Eqs. (3.35) and (3.36), which are similar to the conservative CMC equations for premixed combustion [Thornber et al., 2011]. The variables $\overline{\rho_\eta}$ and $\tilde{P}(\eta)$ do not appear in the above CMC equations since the simplified model for e_f is used in Eq. (3.31). The grouped variables of $\overline{\rho_\eta}\tilde{P}(\eta)$ are retained in the CMC governing equations solved by Kim et al. [2008] and Siwaborworn and Kronenburg [2013]. This can be useful to predict the variations of Q_α and Q_h when the FDF has considerable spatial variations. However, they assume that $\overline{\rho_\eta}\tilde{P}(\eta)$ does not change with the time. In Appendix A, the CMC governing equations considering the temporal and spatial variations of $\overline{\rho_\eta}\tilde{P}(\eta)$ are derived but quantitative studies concerning their performance in predicting the flame dynamics (such as extinction) in non-premixed flames have not been performed yet, which may be a topic for future work.

In Eqs. (3.35) and (3.36), $\widetilde{\mathbf{U}|\eta}$, $\widetilde{N|\eta}$ and $\widetilde{W_\alpha|\eta}$ need to be modelled and their respective models in the framework of finite difference method still apply here. The conditional velocities are assumed to be equal to the filtered velocity

[Navarro-Martinez et al., 2005], i.e.

$$\widetilde{\mathbf{U}|\eta} \approx \tilde{\mathbf{U}}. \tag{3.37}$$

The AMC model [Chen et al., 1989; Oboukhov, 1962; O'Brien and Jiang, 1991] derived from homogeneous turbulence is used here to calculate conditional scalar dissipation $\widetilde{N|\eta}$, i.e.

$$\widetilde{N|\eta} = N_0 G(\eta), \tag{3.38}$$

where N_0 and $G(\eta)$ are

$$N_0 = \frac{\tilde{N}}{\int_0^1 G(\eta)\,\tilde{P}(\eta)\,d\eta} \tag{3.39}$$

and

$$G(\eta) = \exp\left\{-2\left[\mathrm{erf}^{-1}(2\eta - 1)\right]^2\right\}. \tag{3.40}$$

The filtered scalar dissipation rate $\tilde{N}$ in Eq. (3.39) is determined from Eq. (3.22). In the AMC model, the conditional scalar dissipation rate profiles have the shape of $G(\eta)$ in mixture fraction space and are scaled based on N_0 (corresponds to the scalar dissipation at $\eta = 0.5$) and therefore $\tilde{N}$. Swaminathan and Mahalingam [1996] conducted the simulations of an inhomogeneous layer and compared the AMC model with the conditional scalar dissipation model also from homogeneous turbulence, which was developed by Girimaji [1992] based on a β-function for mixture fraction. Based on their results, the model by Girimaji [1992] only gave slightly better results than AMC model initially and at the later stage when the mixing field becomes homogeneous, the profiles of conditional scalar dissipation is almost the same. The inhomogeneous models for the scalar dissipation, derived from the PDF transport equation, were compared with the AMC and Girimaji's model in the case of autoignition of high pressure methane jets [Milford and Devaud, 2010]. It was found that the improvement from their models is relatively small in predicting the ignition delay and Milford and Devaud [2010] attribute this to the inaccurate turbulence description in their RANS simulations.

The first order CMC model, which neglects the sub-grid fluctuations around the conditionally filtered on $\widetilde{W_\alpha|\eta}$, is applied for the conditional chemical source

terms such that

$$\widetilde{W_\alpha|\eta} = W_\alpha\left(Q_1, \ldots, Q_n, Q_T\right), \tag{3.41}$$

where $Q_T \equiv \widetilde{T|\eta}$ is the conditionally filtered temperature.

The unconditionally filtered quantities $\tilde{f}$ (including $\bar{\rho}$, $\tilde{T}$ and other reactive scalars) are obtained through

$$\tilde{f} = \int_0^1 \widetilde{f|\eta}\tilde{P}\left(\eta\right) d\eta, \tag{3.42}$$

in which $\widetilde{f|\eta}$ is the conditionally filtered scalars (e.g. $\overline{\rho_\eta}^{-1}$, Q_T and Q_α).

3.3 Numerical discretizations

3.3.1 LES discretizations

The finite volume discretizations are applied for both isothermal incompressible flows (i.e. Eqs. 3.3a and 3.3b) and reacting flows (i.e. Eqs. 3.14a, 3.14b and 3.14c). The relevant numerical algorithms can be found in the books by Patankar [1980] and Versteeg and Malalasekera [1995]. Therefore, only the pressure Poisson equation for compressible flows and the velocity−pressure coupling are presented in this Sub-section. These algorithms have existed in the LES solver (OpenFOAM®, see Sub-section 3.4.1), and inclusion of this Sub-section is merely for completeness.

Discretizing momentum equation, Eq. (3.14b), leads to the following quasi-algebraic form [Jasak, 1996]

$$a_P\tilde{\mathbf{U}}_P = \mathbf{H}(\tilde{\mathbf{U}}) - \nabla\bar{p}, \tag{3.43}$$

in which $\tilde{\mathbf{U}}_P$ is the velocity vector that needs to be solved while a_P is the coefficient resulting from the explicit discretizations of such terms as convection and diffusion. The pressure gradient $\nabla\bar{p}$ is retained in Eq. (3.43), following the strategy by Rhie and Chow [1983]. The term $\mathbf{H}(\tilde{\mathbf{U}})$ in Eq. (3.43) takes the following

expression

$$\mathbf{H}(\tilde{\mathbf{U}}) = \underbrace{-\sum_{N} a_N \tilde{\mathbf{U}}_N}_{Transport\ Terms} + \underbrace{\frac{\tilde{\mathbf{U}}^o}{\Delta t}}_{Source\ Terms} . \tag{3.44}$$

Equation (3.44) indicates two contributions to $\mathbf{H}(\tilde{\mathbf{U}})$: one is from the discretizations of transport terms and the other is from source terms [Jasak, 1996]. Δt in Eq. (3.44) is the time step.

Explicitly expressing $\tilde{\mathbf{U}}_P$ based on Eq. (3.43) yields

$$\tilde{\mathbf{U}}_P = \frac{\mathbf{H}(\tilde{\mathbf{U}})}{a_P} - \frac{\nabla \bar{p}}{a_P} \tag{3.45}$$

After substituting Eq. (3.45) into the filtered mass conservation equation, i.e. Eq. (3.14a), one can obtain

$$\frac{\partial \bar{\rho}_P}{\partial t} + \nabla \cdot \bar{\rho}_P \left[\frac{\mathbf{H}(\tilde{\mathbf{U}})}{a_P} - \frac{\nabla \bar{p}}{a_P} \right] = 0. \tag{3.46}$$

For isothermal incompressible flows, Eq. (3.46) is reduced to

$$\nabla \cdot \left[\frac{\mathbf{H}(\tilde{\mathbf{U}})}{a_P} - \frac{\nabla \bar{p}}{a_P} \right] = 0. \tag{3.47}$$

Equations (3.46) and (3.47) are the pressure Poisson equations with respect to $\bar{p}$ for compressible and incompressible flows, respectively, used in the current computations. Theoretically, satisfying the pressure Poisson equations is equivalent to the fact holds that the divergence-free velocity fields are always divergence-free [Pope, 2000].

As shown in Eqs. (3.43), (3.46) or (3.47), the velocity $\tilde{\mathbf{U}}$ and pressure $\bar{p}$ are coupled. In this work, the coupled method is applied to solve the LES equations, with the hybrid PISO [Issa, 1986] and SIMPLE [Patankar, 1980] algorithms. Specifically, the time marching is performed by the outer SIMPLE loops, while within each time step the inner PISO iteration is utilized. This treatment allows to use large time step without destabilizing the computations.

3.3.2 CMC discretizations

The numerical discretizations of the individual terms in Eq. (3.35) are discussed as follows.

- Term T_0

$$\int_{\Omega^{CMC}} \frac{\partial Q_\alpha}{\partial t} d\Omega \approx \frac{\partial}{\partial t} \int_{\Omega^{CMC}} Q_\alpha d\Omega \approx V^{CMC} \frac{\partial Q_\alpha}{\partial t}, \tag{3.48}$$

  where it is assumed that the CMC cell of interest Ω^{CMC} does not change with respect to time and V^{CMC} is the volume of the CMC cells.

- Term T_1

$$\int_{\Omega^{CMC}} \nabla \cdot \left(\widetilde{\mathbf{U}|\eta} Q_\alpha \right) d\Omega = \oint_{\partial\Omega^{CMC}} \left(\widetilde{\mathbf{U}|\eta} Q_\alpha \right) \cdot \mathbf{n} dS, \tag{3.49}$$

  in which $\partial\Omega^{CMC}$ denotes all the faces of each CMC cell. The discrete form of RHS in Eq. (3.49) is as follows:

$$\begin{aligned} \oint_{\partial\Omega^{CMC}} \widetilde{\mathbf{U}|\eta} Q_\alpha \cdot \mathbf{n} dS \approx \sum_{m=1}^{F^{CMC}} \left(\widetilde{\mathbf{U}|\eta} Q_\alpha \cdot \mathbf{n} \right)_m \Delta S_m = \\ \sum_{m=1}^{F^{CMC}} \left(\widetilde{U_x|\eta} Q_\alpha n_x + \widetilde{U_y|\eta} Q_\alpha n_y + \widetilde{U_z|\eta} Q_\alpha n_z \right)_m \Delta S_m \end{aligned} \tag{3.50}$$

  where n_x , n_y and n_z are the Cartersian components of the CMC face normal vectors $\mathbf{n}$. ΔS_m is the area of the CMC face. $\widetilde{U_x|\eta}$, $\widetilde{U_y|\eta}$ and $\widetilde{U_z|\eta}$ are the Cartersian components of the conditionally filtered velocity $\widetilde{\mathbf{U}|\eta}$. F^{CMC} is the number of the faces surrounding one CMC cell.

- Term T_2

$$\begin{aligned} \int_{\Omega^{CMC}} Q_\alpha \nabla \cdot \widetilde{\mathbf{U}|\eta} d\Omega = \\ Q_\alpha \int_{\Omega^{CMC}} \nabla \cdot \widetilde{\mathbf{U}|\eta} d\Omega = Q_\alpha \oint_{\partial\Omega^{CMC}} \widetilde{\mathbf{U}|\eta} \cdot \mathbf{n} dS, \end{aligned} \tag{3.51}$$

in which we assume that Q_α is constant within one CMC cell Ω^{CMC}. For $\oint_{\partial\Omega^{CMC}} \widetilde{\mathbf{U}|\eta} \cdot \mathbf{n} dS$, if we assume that $\widetilde{\mathbf{U}|\eta} \approx \widetilde{\mathbf{U}}$, i.e. Eq. (3.37), then

$$\oint_{\partial\Omega^{CMC}} \widetilde{\mathbf{U}|\eta} \cdot \mathbf{n} dS \approx \oint_{\partial\Omega^{CMC}} \widetilde{\mathbf{U}} \cdot \mathbf{n} dS \approx \sum_{m=1}^{F^{CMC}} \left(\tilde{U}_x n_x + \tilde{U}_y n_y + \tilde{U}_z n_z \right)_m \Delta S_m, \tag{3.52}$$

in which $\tilde{U}_x$, $\tilde{U}_y$ and $\tilde{U}_z$ are the Cartesian components of the filtered velocity $\tilde{\mathbf{U}}$.

- Term T_3

$$\int_{\Omega^{CMC}} \widetilde{N|\eta} \frac{\partial^2 Q}{\partial \eta^2} d\Omega \approx V^{CMC} \widetilde{N|\eta} \frac{\partial^2 Q}{\partial \eta^2}. \tag{3.53}$$

  Here we apply the assumption that $\widetilde{N|\eta}$ and $\partial^2 Q/\partial \eta^2$ are constant within each CMC cell.

- Term T_4

$$\int_{\Omega^{CMC}} \widetilde{W_\alpha|\eta} d\Omega \approx V^{CMC} \widetilde{W_\alpha|\eta}, \tag{3.54}$$

  in which we assume that $\widetilde{W_\alpha|\eta}$ is constant in each CMC cell, and hence can be moved out of the volume integration.

- Term T_5

$$\oint_{\Omega^{CMC}} \nabla \cdot (D_t \nabla Q_\alpha) \, d\Omega = \oint_{\partial\Omega^{CMC}} (D_t \nabla Q_\alpha) \cdot \mathbf{n} dS. \tag{3.55}$$

  We further write Eq. (3.55) into the following discrete form

$$\begin{aligned} \oint_{\partial\Omega^{CMC}} (D_t \nabla Q_\alpha) \cdot \mathbf{n} dS \approx \sum_{m=1}^{F^{CMC}} \left(D_t \nabla Q_\alpha \cdot \mathbf{n} \right)_m \Delta S_m = \\ \sum_{m=1}^{F^{CMC}} D_{t,m} \left(\frac{\partial Q_\alpha}{\partial x} n_x + \frac{\partial Q_\alpha}{\partial y} n_y + \frac{\partial Q_\alpha}{\partial y} n_y \right)_m \Delta S_m. \end{aligned} \tag{3.56}$$

  The derivatives $\partial Q_\alpha/\partial x$, $\partial Q_\alpha/\partial y$, and $\partial Q_\alpha/\partial z$, are the Cartesian components of ∇Q_α.

The discretizations for the terms in the CMC equation for total enthalpy Q_h, Eq. (3.36), are identical and therefore not repeated here.

The Operator Splitting (OS) method is used to update Q_α from the above terms and the following steps are executed once from *Step 1* to *Step 3* within each time step:

- *Step 1*: $T_0 = -T_1 + T_2 + T_5$
  The terms in physical space, T_1, T_2 and T_5, are solved in this step and the first order explicit Euler scheme is used for temporal discretization.

- *Step 2*: $T_0 = T_3$
  The micro-mixing term in mixture fraction space, T_3, is solved using the TDMA method.

- *Step 3*: $T_0 = T_4$
  The chemical source term in mixture fraction space, T_4, is calculated with the stiff ODE solver VODPK [Brown and Hindmarsh, 1989].

3.4 LES and CMC solvers

3.4.1 Introduction to LES and CMC solvers

There are totally four independent solvers applied for the computations in this thesis and they are 0D-CMC, LES (isothermal flows), LES/0D-CMC and LES/3D-CMC solvers. The LES/3D-CMC solver is the major computational tool for this work and the previous three ones provide some preliminary computations for the LES/3D-CMC.

The LES governing equations are solved by the open source object-oriented CFD library, OpenFOAM® (version 2.1.1) [Weller et al., 1997], which can be downloaded online (http://www.openfoam.com/). The three dimensional CMC governing equations are solved by the in-house code developed and improved during the course of this research based on the ground by Garmory and Mastorakos [2015]. The four solvers will be briefly introduced in this Sub-section.

3.4.1.1 0D-CMC solver

In the 0D-CMC solver, the governing equations for conditional mass fractions for α-th species Q_α and total enthalpy Q_h are solved without the terms in physical space, i.e.

$$\frac{\partial Q_\alpha}{\partial t} = N|\eta \frac{\partial^2 Q_\alpha}{\partial \eta^2} + W_\alpha|\eta, \tag{3.57}$$

$$\frac{\partial Q_h}{\partial t} = N|\eta \frac{\partial^2 Q_h}{\partial \eta^2}. \tag{3.58}$$

In 0D-CMC solver Q_α and Q_h are $Y_\alpha|\eta$ and $h|\eta$, respectively. Equations (3.57) and (3.58) are virtually identical to the transient laminar flamelet model with unity Lewis number [Peters, 1984]. Q_α and Q_h are functions of the scalar dissipation rate, besides the mixture fraction. The AMC model (cf. Eq. 3.38) is applied for $N|\eta$ and therefore Eqs. (3.57) and (3.58) are parameterized by the peak scalar dissipation value N_0. The results from the 0D-CMC solver can be used to initialize the flame structures in individual CMC cells for LES/3D-CMC.

3.4.1.2 LES solver (isothermal flows)

In the LES solver (isothermal flows), the LES governing equations for isothermal incompressible flows, Eqs. (3.3a) and (3.3b), are solved. It corresponds to the OpenFOAM solver *pisoFOAM*. This solver is used for investigating the aerodynamics of the non-reacting flows, typically as the preparation work for turbulent flame simulations.

3.4.1.3 LES/0D-CMC solver

In the LES/0D-CMC solver, the LES governing equations correspond to the filtered momentum and mixture fraction, i.e. (3.14b) and (3.14c). The sub-grid variance of mixture fraction is modelled with Eq. (3.23). The LES solver is developed from *fireFOAM* with low Ma number assumption.

It should be clarified that the 0D-CMC equations, i.e. Eqs. (3.57) and (3.58), are not solved in this solver; instead, Eq. (3.42) is applied to calculate the filtered density $\bar{\rho}$ and temperature $\tilde{T}$ from pre-calculated $\overline{\rho_\eta}$ and Q_T from the 0D-CMC solver. The former two quantities are provided to the LES solver. In

addition, other reactive scalars are also able to be predicted from their respective conditional counterparts Q_α. Here $\overline{\rho_\eta}$, Q_T and Q_α are obtained from Eq. (3.57) with specified N_0.

This solver can be employed for studying the flow and mixing fields for flames far from extinction [Ayache and Mastorakos, 2013]. In the present work, its results provide the initial fields of velocities and mixture fraction for LES/3D-CMC.

3.4.1.4 LES/3D-CMC solver

In this solver, the LES implementations are exactly the same as those in the LES/0D-CMC solver. However, the three dimensional CMC governing equations, i.e. Eqs. (3.35) and (3.36), are solved here, with the required sub-models detailed in Section 3.2. Note that the filtered mass continuity equation, Eq. (3.14a), is not solved in both LES/0D-CMC and LES/3D-CMC solvers, since the density is updated from its conditional solution in the CMC solver, as will be shown in Subsection 3.4.3. Theoretically, the mass conservation is ensured through solving the pressure Poisson equation, Eq. (3.46), in the LES/0D-CMC and LES/3D-CMC solvers. This solver is the computational tool that is developed to predict the extinction in turbulent swirling non-premixed flames.

3.4.2 CMC cell reconstruction

The LES solvers based on OpenFOAM® can solve the flow fields with polyhedral unstructured meshes [Jasak, 1996]. In the LES/3D-CMC solver, the LES equations and three dimensional CMC equations are discretized on separate meshes, specifically, fine and coarse meshes respectively. In this work, the coarse CMC cells are reconstructed from the fine LES meshes with its initially provided CMC nodes. Figure 3.1 schematically shows the CMC cell reconstruction based on the unstructured LES mesh. The relevant algorithms have also been introduced elsewhere [Garmory and Mastorakos, 2015] and will be explained as follows for completeness.

- *Step 1*: Aggregation
  For each LES cell, find its closest CMC cell based on the minimal distance

between its centroid and CMC nodes. The found CMC cell is termed as the host CMC cell for the considered LES cell.

- *Step 2*: Demarcation
  For each LES face, examine the host CMC cells for its owner and neighbor cells, i.e. N and P in Fig. 3.1, respectively. If the host CMC cells of the owner and neighbor cells are different, then this LES face is selected as the CMC face (the dashed lines in Fig. 3.1). In addition, if the LES computational domain is exactly consistent with the CMC one, all the LES boundary faces are inherited as the CMC boundary faces. If the CMC domain is smaller than the LES domain, the CMC boundary faces should be selected from the internal LES faces, while if the CMC domain is larger than the LES domain, the original CMC boundary faces with the initial CMC nodes can be used.

- *Step 3*: Enclosure
  Each CMC node, such as N_{CMC1} and N_{CMC2} in Fig. 3.1, is enclosed by a series of CMC faces selected from the LES faces. The LES cells enclosed by the CMC faces (in the same color in Fig. 3.1) belong to the same CMC cells and therefore now the new CMC cells are reconstructed.

The above strategy provides the CMC cells used for discretizing the CMC governing equations, Eqs. (3.35) and (3.36). Kim et al. [2008] solved the CMC equations on the tetrahedral CFD mesh, and therefore the numerical flux calculations and other discretizations were performed on the CFD cells. However, there are several disadvantages for their implementation. First, this would be prohibitively expensive when fine CFD meshes are used, such as in LES. Second, the refinement of the CFD meshes in the computational domain may not be necessary for CMC equations. In other words, the zones requiring mesh refinements for CFD and CMC may not coincide. Third, the spatial variations of Q_α and Q_h typically are small compared to the CFD quantities [Navarro-Martinez et al., 2005] and hence employing the same resolution for CFD and CMC may be not necessary. Siwaborworn and Kronenburg [2013] solved the conservative CMC equations on structured hexahedral cells, limiting the applications in computations with complex domains and boundaries.

The topological features of the reconstructed CMC cells in this implementation are worth further discussing. First, the CMC cells can be arbitrary polyhedrons. The initial CMC nodes are not necessarily the CMC cell centroids, and therefore the discretization of CMC terms in physical space cannot be performed on them. In this work, the numerical fluxes on the CMC faces are predicted based on the LES cell stencil, e.g. N and P for their shared CMC face in Fig. 3.1. The topology (e.g. non-orthogonality and skewness) of reconstructed CMC cells would not constitute the mesh-induced error source. Second, the completeness of the reconstructed CMC cells is of great significance for finite volume method based on the Gauss divergence theorem. The completeness of each CMC cell can be examined resorting to the quantity of Euler characteristic χ^{CMC} from the classical theory of algebraic topology [Richeson, 2008]

$$\chi^{CMC} = N^{CMC} - E^{CMC} + F^{CMC}, \tag{3.59}$$

in which N^{CMC}, E^{CMC} and F^{CMC} respectively denote the numbers of vertices, edges and faces in one CMC cell. That the Euler characteristic $\chi^{CMC} = 2$ holds for a reconstructed polyhedral CMC cell indicates its geometrical completeness. Conversely, any individual CMC cells with missing one or multiple faces (i.e. that cell is not closed) would lead to $\chi^{CMC} = 1$.

3.4.3 Data runtime coupling

Since the LES and CMC governing equations are solved on different meshes the runtime data coupling between them must be conducted. In LES/3D-CMC modelling, the data coupling has two levels of implications: data averaging and transfer.

3.4.3.1 Data averaging

The unclosed quantities, e.g. $\widetilde{N|\eta}$, and $\tilde{P}(\eta)$, must be modelled on the reconstructed CMC mesh. Specifically, the conditionally filtered scalar dissipation rate for Eqs. (3.35) and (3.36) in the CMC resolution, $\widetilde{N|\eta}^{CMC}$, is estimated through FDF weighted integrating the conditional scalar dissipation, $\widetilde{N|\eta}$, over each LES

cell constituting the host CMC cell [Triantafyllidis and Mastorakos, 2010]

$$\widetilde{N|\eta}^{CMC} = \mathscr{L}_{FDF}\left(\widetilde{N|\eta}\right). \tag{3.60}$$

For the CMC cells, $\tilde{\xi}^{CMC}$ and $\widetilde{\xi''^2}^{CMC}$ are necessary to calculate their β-function FDF $\tilde{P}^{CMC}(\eta)$, i.e. Eqs. (3.26). They are estimated based on $\tilde{\xi}$ and $\widetilde{\xi''^2}$ from the contained LES cells [Triantafyllidis and Mastorakos, 2010]

$$\tilde{\xi}^{CMC} = \mathscr{L}\left(\tilde{\xi}\right), \tag{3.61a}$$

$$\widetilde{\xi''^2}^{CMC} = \mathscr{L}\left(\tilde{\xi}^2\right) + \mathscr{L}\left(\widetilde{\xi''^2}\right) - \mathscr{L}^2\left(\tilde{\xi}\right). \tag{3.61b}$$

In Eqs. (3.60) and (3.61), $\mathscr{L}_{FDF}(x)$ and $\mathscr{L}(x)$ are respectively defined as

$$\mathscr{L}_{FDF}(x) = \frac{\int_{\Omega^{CMC}} \bar{\rho}\tilde{P}(\eta)\, x d\Omega}{\int_{\Omega^{CMC}} \bar{\rho}\tilde{P}(\eta)\, d\Omega} \tag{3.62a}$$

and

$$\mathscr{L}(x) = \frac{\int_{\Omega^{CMC}} \bar{\rho} x d\Omega}{\int_{\Omega^{CMC}} \bar{\rho} d\Omega}, \tag{3.62b}$$

which denote the FDF weighted Favre averaging and Favre averaging operators, respectively.

3.4.3.2 Data transfer

The bidirectional data transfer has been illustrated in Fig. 3.2 and is executed within each time step. It aims to make the CMC solver receive $\widetilde{N|\eta}^{CMC}$, $\tilde{P}^{CMC}(\eta)$, interpolated velocity $\widetilde{\mathbf{U}}$ and sub-grid mass diffusivity D_t on CMC faces, and make the LES solver have $\bar{\rho}$ and $\tilde{T}$.

Quantities from LES to CMC solvers

$\widetilde{N|\eta}^{CMC}$ and $\tilde{P}^{CMC}(\eta)$ are calculated with Eqs. (3.60) and (3.61). The volume fluxes $\tilde{\mathbf{U}} \cdot \mathbf{n}dS$ ($\mathbf{n}dS$ is the CMC face normal vectors) and the sub-grid scale diffusivity D_t at the CMC faces are required in Eqs. (3.50) and (3.56), to predict the numerical fluxes from the convection and sub-grid scale diffusion terms. In

the current implementation, they are interpolated based on the instantaneous flow and sub-grid properties at their neighbour and owner LES cells, e.g. N and P marked in Fig. 3.1. As mentioned in Sub-section 3.4.2, the interpolations and flux predictions are performed based on the LES cell centroids (solid circles in Fig. 3.1). The flux conservation for the CMC cells can be ensured since the current strategy does not introduce any kind of averaging for $\tilde{\mathbf{U}}$ and D_t like what was performed previously, e.g. using $\mathscr{L}\left(\tilde{\mathbf{U}}\right)$ and $\mathscr{L}\left(D_t\right)$ by Triantafyllidis et al. [2009] and Triantafyllidis and Mastorakos [2010]. The flux conservation is advantageous in accurately predicting the transport between CMC cells in physical space. The quantitative studies about the difference between the current implementation for $\tilde{\mathbf{U}}$ and D_t and the averaging for them have not been conducted and will be a future topic.

Quantities from CMC to LES solvers

The filtered density $\bar{\rho}$ and temperature $\tilde{T}$ are required for each LES cell and are predicted using Eq. (3.42). The conditional quantities $\widetilde{f|\eta}$ are obtained from the corresponding host CMC cell for the LES cell of interest, and the FDF $\tilde{P}\left(\eta\right)$ is calculated using the β-function with filtered mixture fraction $\tilde{\xi}$ and its sub-grid variance $\widetilde{\xi''^2}$ at LES resolution. The other filtered scalars at the LES fields, such as $\tilde{Y}_\alpha$, can also be calculated from their respective conditional quantities with Eq. (3.42), as also demonstrated in Fig. 3.2.

3.4.4 Chemical mechanism

The ARM2 mechanism by Sung et al. [1998] is included into the CMC model for the methane oxidization in this work. It consists of 19 species and 15 lumped elementary reactions. The ARM2 mechanism has been used, e.g. by Xu and Pope [2000] and Garmory and Mastorakos [2011], for Sandia flames D and F and reasonable levels of local extinction were captured.

In the CMC model, the ability of ARM2 in predicting extinction in mixture fraction can be examined by the response of flame structures to a varying scalar dissipation rate. Plotted in Fig. 3.3 are the conditional temperatures at stoichiometry, $T|\xi_{st}$, as the function of peak values of conditional scalar dissipation rate, N_0. Two compositions (tabulated in Fig. 3.3) are taken into consideration,

corresponding to the Sydney swirl flame SMA series [Masri et al., 2004] and Cambridge swirl non-premixed flames [Cavaliere et al., 2013] studied in this work. One can see that for both situations, with the increased N_0, $T|\xi_{st}$ decreases sharply for $0 < N_0 < 25$ 1/s, and then gradually becomes small. At the respective critical scalar dissipation rate, flames are quenched suddenly with finite temperature and the flame structures tend to be frozen state. This critical scalar dissipation rate is parameterized by $N_{0,e}$, which is roughly 298 1/s and 174 1/s for the compositions in Sydney and Cambridge swirl flames. $N_{0,e}$ is of great importance and will be used as a reference when studying the transient extinction in single CMC cells in LES/3D-CMC.

3.4.5 Parallelization

For the LES/3D-CMC modelling, both solvers are parallelized using the MPI library, but the decompositions for LES and CMC domains in physical space are performed separately. The mixture fraction space for the CMC solver will not be decomposed particularly and is affiliated to the CMC cell in the current implementation.

3.4.5.1 LES and CMC parallelization

Parallelization of the LES solver is realized resorting to the implementation of OpenFOAM®. The domain decomposition is conducted with *PT-Scotch* method [Pellegrini, 2006] which is expected to minimize the communication overhead.

The CMC cells in the physical domain are decomposed using the *round-robin* method. Specifically, the processor number p ($1 \leq p \leq \mathscr{N}^p$) is designated to the n-th CMC cell ($1 \leq n \leq \mathscr{N}^{CMC}$) as

$$p = \mathrm{mod}\,(n-1, \mathscr{N}^p) + 1, \tag{3.63}$$

in which $\mathscr{N}^p$ is the total processor number and $\mathscr{N}^{CMC}$ is total number of CMC cells. The advantage for the *round-robin* method is that the perfectly balanced load for the CMC cells can be obtained among all the processors. Nevertheless, since it is not straightforward to ensure that the spatially close CMC and LES

cells belong to the same processor, global MPI reducing, collecting and scattering are required for each time step in order to perform the LES and CMC coupling described in Sub-section 3.4.3.

3.4.5.2 Scalability and computational cost

The parallel scalability of LES solver (isothermal flows), LES/0D-CMC and LES/3D-CMC solvers is assessed on the ARCHER (Cray XC30) clusters of the UK National Supercomputing Service. Each node on ARCHER clusters contains two 2.7 GHz, 12-core E5-2697 v2 (Ivy Bridge) series processors, with 64 GB of memory shared by the two processors. The Cray Aries interconnect links all compute nodes in a *Dragonfly* topology, and within the node, the two processors are connected by two QuickPath Interconnect (QPI) links.

The tested cases are the non-reacting flow N16S159 for LES solver (isothermal flows), and the swirl non-premixed flames SMA2 for LES/0D-CMC and LES/3D-CMC solvers. The total LES cell number is around 8,400,000 and the CMC cell number is 120,000. Irrespective of processor number, the ratio of CFD to CMC cells on each processor, ϱ^{CMC}, is about 70. 51 nodes are used to discretize mixture fraction space. The chemical mechanism is ARM2 with 19 species described in Sub-section 3.4.4. As such, the total number of ODEs that needed to be solved for each time step is roughly 120 million. More information about the two test cases can be found in Chapters 4 and 5.

Plotted in Fig. 3.4 is the wall clock time for each time step, t_{wall}, as a function of the processor number $\mathscr{N}^p$. At each time step from $t = 1$ to $\mathscr{N}^t$ ($\mathscr{N}^t = 800-1000$ in these tests) of a simulation on $\mathscr{N}^p$ processors, the overall wall clock time spent $t^{t,p}_{wall}$ for p-processor is computed. The cumulative wall clock time T_{wall} for p-processor and each run is

$$T^p_{wall} = \sum_{t=1}^{\mathscr{N}^t} t^{t,p}_{wall}. \tag{3.64}$$

Since the LES solvers are synchronized among all the processors at the end of each time step, T^p_{wall} is roughly the same on all the processors and hence t_{wall} in

Fig. 3.4 is estimated from the first processor, i.e.

$$t_{wall} \approx t^1_{wall} = \frac{T^1_{wall}}{\mathscr{N}^t}. \tag{3.65}$$

The number ratio of the LES cells to inter-processor faces in the local processors, ϕ, is also explicitly marked in Fig. 3.4, which is an indicator for the balance of local computations and MPI communications. About t_{wall} for LES of N16S159, it decreases until $\mathscr{N}^p = 960$, and then increasing $\mathscr{N}^p$ leads to the increased t_{wall}. However, the maximum $\mathscr{N}^p$ for linear speedup in this case is about 480 based on the results in Fig. 3.4. For LES/0D-CMC, the tendency that t_{wall} first decreases and then increases is still observable. Due to the extra overhead for predicting $\bar{\rho}$ and $\tilde{T}$, t_{wall} is consistently higher than that in LES of N16S159 for the presented processor number. However, their difference is gradually minimized with increased $\mathscr{N}^p$. The maximum $\mathscr{N}^p$ for linear speedup is extended to about 960. The reader should be reminded that the comparison of t_{wall} between LES of N16S159 and LES/0D-CMC results is not accurate; after all, the LES solvers are different as described in Sub-section 3.4.1. The long t_{wall} indicates the expensive computational cost of the LES/3D-CMC computations. Quantitatively, t_{wall} from LES/3D-CMC is 20−25 times higher than that from LES/0D-CMC. A particular feature for the LES/3D-CMC case is that t_{wall} monotonically decreases as $\mathscr{N}^p$ increases over the range of the tested processor numbers, although the maximum $\mathscr{N}^p$ for linear speedup is still about 960 beyond which t_{wall} does not change much. The scaling is extended from LES (isothermal) to the LES/3D-CMC solvers. The accuracy of LES/0D-CMC and LES/3D-CMC solvers in predicting local extinction will be compared in Sub-section 6.3.2.

Figure 3.5 shows the wall clock time t_{wall} from different operations in the 3D-CMC solver as a function of the number of processor $\mathscr{N}^p$. Four individual operations are considered here, including the MPI communications (collecting and scattering Q_α, Q_h and other quantities), data averaging over all the LES cells for each CMC cell, computations of the CMC terms in physical space (i.e. T_1, T_2 and T_5) as well as the CMC terms in mixture fraction space (i.e. T_3 and T_4). Here t_{wall} for individual operation is estimated with averaging through the cumulative wall clock time of the corresponding operation for N_t time steps and

all the $\mathscr{N}^p$ processors, i.e.

$$T_{wall} = \sum_{p=1}^{\mathscr{N}^p} \sum_{t=1}^{\mathscr{N}^t} t_{wall}^{t,p}. \tag{3.66}$$

One can see from Fig. 3.5 that t_{wall} for data averaging and MPI communications demonstrates limited variations as N_p increases. However, the wall clock time used for the terms in physical space shows a linear speedup until $\mathscr{N}^p$ reaches 1920, beyond which it still slightly decreases with the increase of $\mathscr{N}^p$. Over the entire range of $\mathscr{N}^p$ shown in Fig. 3.5, t_{wall} for the terms in mixture fraction space has a linear speedup. This feature confirms the good scaling for the VODPK ODE solver T_4 and the TDMA algorithms for T_3.

The fact that the scaling of total wall clock time t_{wall} plotted in both Figs. 3.5 and 3.4 deteriorates may result from the unsatisfactory scalability of MPI communication and data averaging overheads. Figure 3.6 presents the percentages for the operations in the 3D-CMC solver as shown in Fig. 3.5. For clarity, the corresponding wall time t_{wall} values for each operation with each $\mathscr{N}^p$ are also marked. The costs for data averaging and MPI communications become increasingly dominant when $\mathscr{N}^p$ is increased and when $\mathscr{N}^p \geq 1920$, they account for over a half of the total t_{wall}. The percentage for the terms in physical space maintains 15% or so, irrespective of $\mathscr{N}^p$. For the terms in mixture fraction, their cost is gradually minimized and when $\mathscr{N}^p = 7680$, t_{wall} becomes less than 10%.

Finally, the generality of the scaling results presented in Figs. 3.4−3.6 should be taken into consideration, i.e. how the scaling curves could be affected by the simulated turbulent flame configurations and by the computer architecture. First, the scale of 3D-CMC computations jointly depends on the numbers of species, CMC cells in physical space and CMC nodes in mixture fraction space. The specifications for these numbers in the present tests basically take the full advantage of the memory on ARCHER cluster (3−4 GB per processor), assuming that the interfaced LES solver is memory-saving. The memory consumption does not change with increased $\mathscr{N}^p$ since global arrays are needed for both Q_α and Q_h. In addition, the stiffness of the selected mechanism would also change its contribution to the total wall clock time. The variation of flame reactivity may

also lead to change of the overhead for the chemical source terms. Second, the implementation of MPI in 3D-CMC solver is general and it is anticipated that the scaling results in Figs. 3.4−3.6 do not have the significant sensitivity to different computing platforms. Nevertheless, one cannot neglect the influence from the inter-node and inter-processor physical connections of different clusters on MPI communications; after all, this limits the scaling of LES/3D-CMC when $\mathscr{N}^p$ is close to $O(10^3)$.

3.5 Summary

In this Chapter, the LES governing equations for isothermal incompressible and reacting flows are presented. The conservative governing equations for the three dimensional sub-grid scale CMC model are derived, which can be discretized on the unstructured meshes with the finite volume method. Based on them, the in-house unstructured CMC solver is developed. The CMC cell reconstruction approach is proposed, with which the CMC cells are generated from the LES cells and can be arbitrarily polyhedral. The numerical flux conservation in physical space in this implementation is significant in predicting the large variations of conditional mass fractions that may exist in extinction of turbulent non-premixed flames. The data transfer interface between the CMC and LES solvers is designed and the MPI based parallelization is realized in the 3D-CMC solver with round-robin algorithm, which can ensure the perfect load balancing among all the processors. The solvers used in different occasions of this thesis are also introduced in this Chapter. The scalability of the solvers is assessed on the ARCHER (Cray XC30) clusters of the UK National Supercomputing Service and, particularly, the LES/3D-CMC solver can have a linear speedup until $\mathscr{N}^p$ is close to $O(10^3)$. Through the computational cost analysis, one can see that the MPI communications become the limiting factor for the LES/3D-CMC solver to have a linear speedup with higher processor numbers.

3.6 Figures for Chapter 3

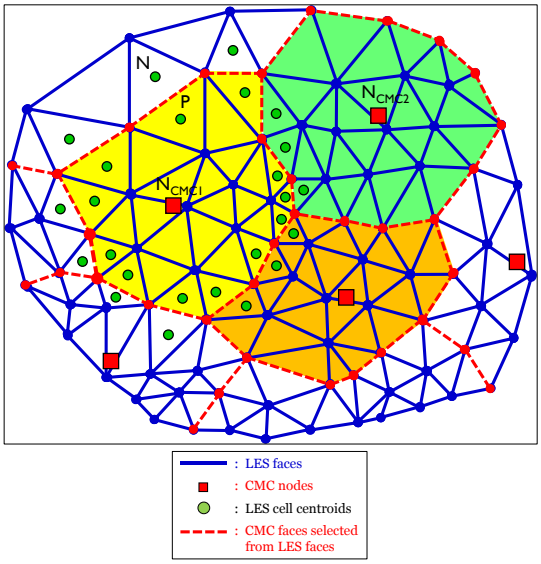

Figure 3.1: Schematic of CMC cell reconstruction from unstructured LES mesh. The symbols "N" and "P" denote the neighbor and owner LES cells for a LES and CMC inter-cell face, while "N_{CMC1}" and "N_{CMC2}" the CMC nodes.

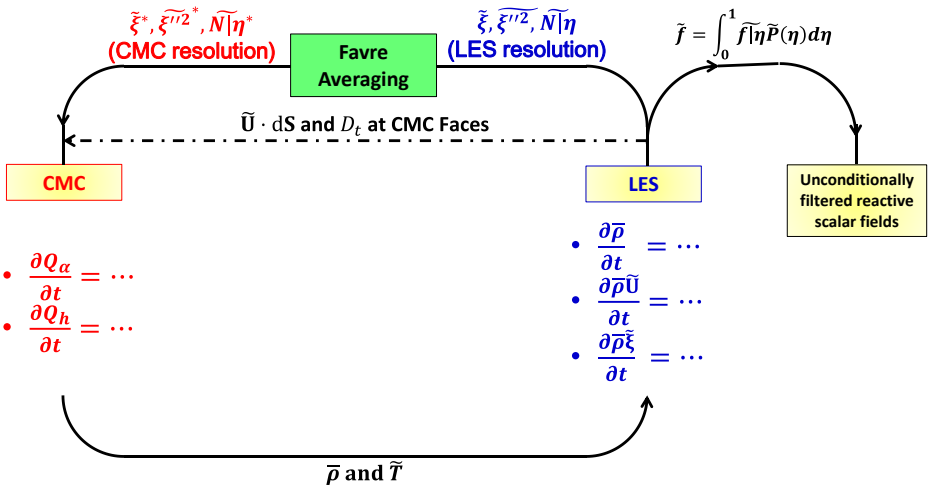

Figure 3.2: Schematic of data coupling between the LES and CMC solvers.

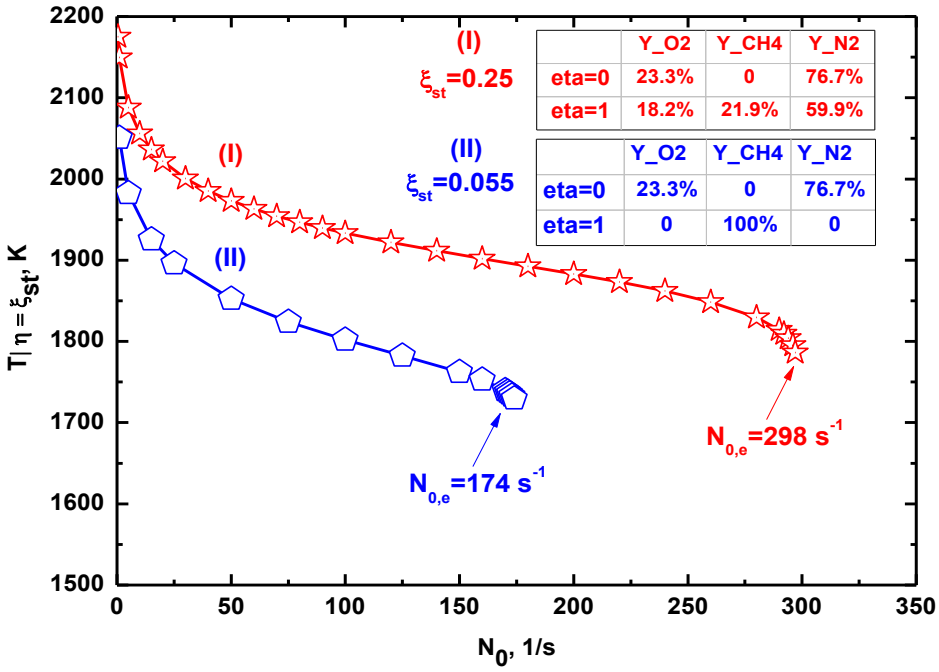

Figure 3.3: Conditional temperature at stoichiometry $T|\eta = \xi_{st}$ as a function of peak value of conditional scalar dissipation rate N_0 from the 0D-CMC solver. Curve I corresponds to the compositions in Sydney swirl flames (SMA series) [Masri et al., 2004], while Curve II those in Cambridge swirl flames [Cavaliere et al., 2013]. The species mass fractions at oxidizer and fuel streams are listed in the inset tables. $N_{0,e}$ is the critical N_0 for extinction.

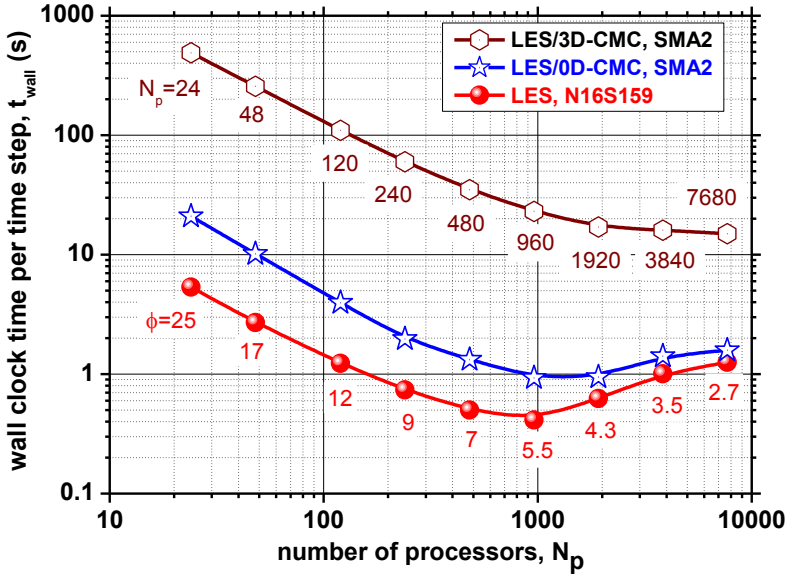

Figure 3.4: Wall clock time per time step t_{wall} as a function of processor number N_p for LES of N16S159, LES/0D-CMC and LES/3D-CMC of SMA2. The quantity ϕ is the number ratio of LES cells to inter-processor faces in the local processors.

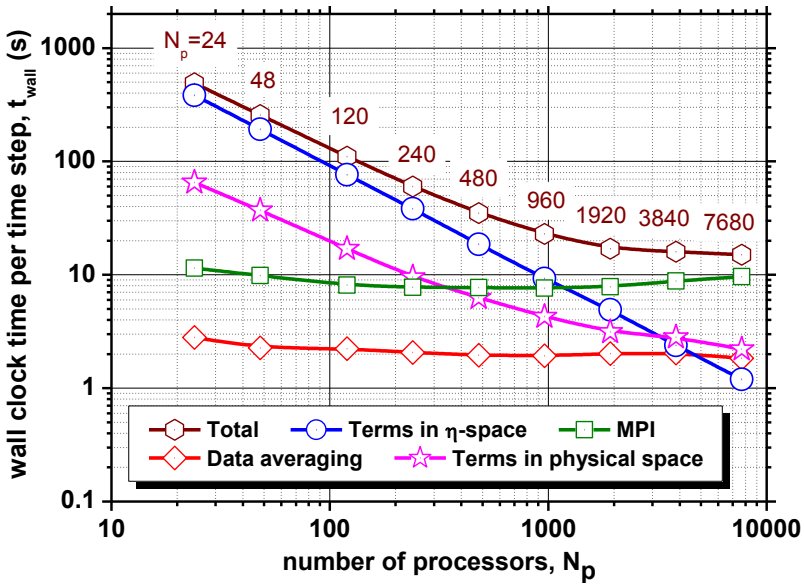

Figure 3.5: Wall clock time per time step t_{wall} as a function of processor number $\mathcal{N}^p$ for different operations in the 3D-CMC solver.

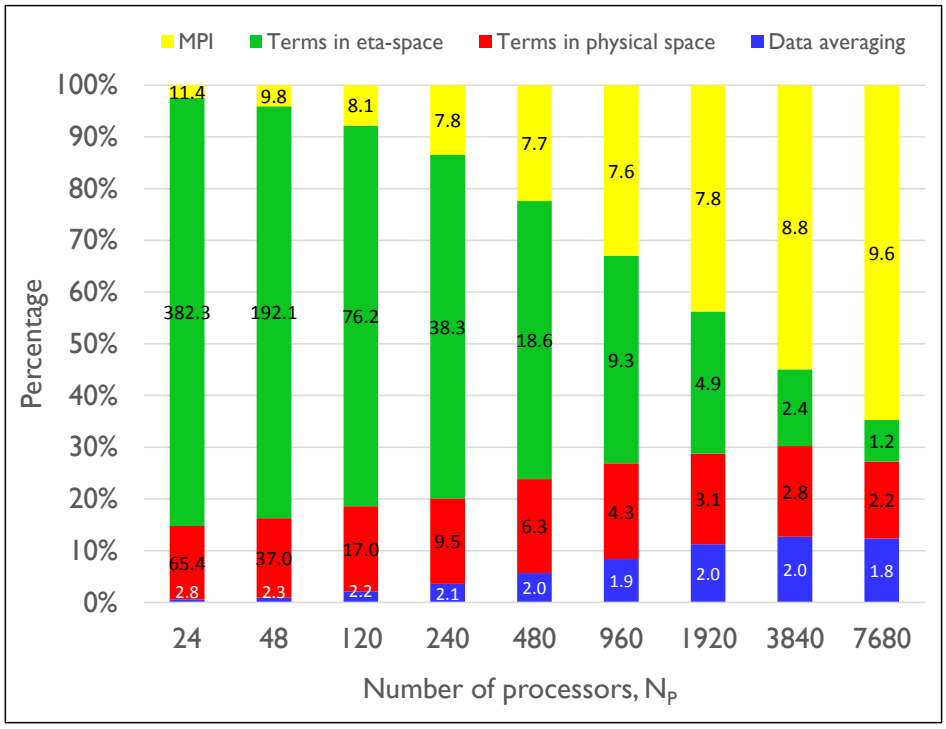

Figure 3.6: Percentage of wall clock time t_{wall} for individual operations in the 3D-CMC solver. The numbers on the histograms are t_{wall} (in unit of s) corresponding to the marked operations.

Chapter 4

Swirl Non-reacting Flows

4.1 Introduction

The swirling non-premixed flames investigated experimentally in University of Sydney [Masri et al., 2004] and University of Cambridge [Cavaliere et al., 2013] are selected as target flames in this thesis. The localized and global extinction in both types of flames will be studied with LES and sub-grid scale CMC model in Chapters 5−8. As a preparatory study for the following combustion simulations, this Chapter aims to examine the ability of the current LES solver to correctly predict the instantaneous and time averaged features of aerodynamics in the non-reacting flows, which have been measured by Al-Abdeli and Masri [2004] and Cavaliere [2013] respectively for both burners. In addition, the numerics (mesh, boundary condition and computational domain) relevant to LES in non-reacting flows will be studied, and the findings from the sensitivity analysis are references for the LES/3D-CMC computations in the following Chapters. The burner configurations, LES numerics, flow information and simulated cases are detailed in Section 4.2. The results about the flow fields predicted by LES will be discussed and the sensitivity analysis about the mesh, boundary condition and the computational domain will be conducted in Section 4.3. This Chapter closes by the conclusion section.

4.2 Modelling

4.2.1 LES modelling

The filtered governing equations for mass and momentum equations for isothermal incompressible flows have been presented in Sub-section 3.1.1, i.e. Eqs. (3.3a) and (3.3b). The Smagorinsky model detailed in Sub-section 3.1.1 is used here to close the sub-grid scale viscosity.

4.2.2 Experimental setup and flow information

4.2.2.1 Sydney swirl burner and flow information

Figures 4.1 and 4.2 show the configuration of Sydney swirl burner [Masri et al., 2004]. This burner is extended from a bluff-body burner [Dally et al., 1998] also from the University of Sydney and designed for investigating turbulence−chemistry interactions and blow-off limits in swirl stabilized non-premixed flames [Al-Abdeli and Masri, 2003; Al-Abdeli et al., 2006; Masri et al., 2004]. It has a bluff body with diameter $D_b = 50$ mm. For the investigations of non-reacting flows, air with bulk velocity U_j is injected through the jet exit with diameter $D_j = 3.6$ mm, which is located in the center of the bluff body. The primary swirling air with axial bulk velocity U_s and swirl bulk velocity W_s is fed through the annular gap ($D_a = 60$ mm), which concentrically surrounds the bluff body. The axial streams of air are injected from two diametrically opposed ports as explicitly marked in Fig. 4.1(b). In the Sydney swirl burner, the swirling flows are induced into the primary axial streams via three inclined (15° to the horizontal plane) tangential swirl ports (each 7 mm in diameter), circumferentially 120° to each other and 300 mm upstream of the burner exit plane as shown in Fig. 4.1(b). Clearly, three tangential swirl ports are located downstream of the diametrically opposed ones. The burner is positioned in a secondary axial (coflow) square wind tunnel (130 mm × 130 mm) with constant air bulk velocity U_e of 20 m/s and turbulence level of around 2%. More information about the Sydney swirl burner can be found elsewhere [Al-Abdeli and Masri, 2003, 2004; Al-Abdeli et al., 2006; Masri et al., 2004] and will not repeated here.

A series of non-reacting flows and flames varied by different bulk velocities and/or fuel compositions in this burner were measured. The data are currently archived in the database by TNF workshop (http://www.sandia.gov/TNF). LDV is applied to measure all the velocity statistics while Raman−Rayleigh−LIF technique is used for the scalar measurements. Contributions from the Sydney swirl burner include characterization of the swirl-induced aerodynamics [Al-Abdeli and Masri, 2004], detailed measurements of the flame structures [Masri et al., 2004], blow-off limits [Al-Abdeli and Masri, 2003] and the time varying flame behaviors [Al-Abdeli et al., 2006], etc. The detailed operating conditions (parameterized by U_s, W_s, U_j and U_e) and the measured data have been freely available on the web (http://sydney.edu.au/engineering/aeromech/thermofluids/swirl.htm).

The non-reacting case, N16S159, is selected. For the primary air flows in the annulus, the axial and swirl bulk velocities are $U_s = 16.3$ m/s and $W_s = 25.9$ m/s, respectively. The air bulk velocity in the central jet is $U_j = 66.3$ m/s. Following the same formula used by Masri et al. [2004], we predict the swirl number S_N as the ratio of swirl bulk velocity to primary air axial bulk velocity at the burner exit, i.e.

$$S_N = \frac{W_s}{U_s}, \tag{4.1}$$

to quantitatively represent the swirl intensity and hence for this case S_N is 1.59. All the streams are under ambient conditions (i.e. 1 atm and 298 K). The Reynolds numbers for the primary air stream ($Re_s = D_a U_s/\nu$) and central jet ($Re_j = D_j U_j/\nu$) are approximately $Re_s = 62{,}300$ and $Re_j = 15{,}200$, respectively. The above mentioned operating conditions (i.e. U_s, W_s, U_j and U_e) are exactly the same as the swirl non-premixed flame case, SMA2, studied in Chapter 5 in which case the air-diluted methane, rather than air, is fed through the central jet. Therefore, the LES of N16S159 in this Chapter is viewed as the prerequisite step towards correctly understanding its aerodynamics and the relevant LES methodology needed for the flame simulations in Chapter 5.

4.2.2.2 Cambridge swirl burner and flow information

The configurations and dimensions of the Cambridge swirl burner can be found in Figs. 4.3 and 4.4. This burner is developed from a previous setup used for

studying lean turbulent flames with oscillating inlet conditions [Balachandran et al., 2005], spark ignition in both non-premixed flames [Ahmed et al., 2007] and in spray flames [Marchione et al., 2009]. As shown in Figs. 4.3 and 4.4, a glass enclosure (95 mm × 150 mm) made of synthetic optical-quality quartz is fitted at the burner exit. Its outlet is open to the atmospheric surroundings. The confinement resulting from the enclosure walls is expected to considerably affect the flow fields (e.g. RZ pattern and the air entrainment) [Cavaliere, 2013].

The Cambridge swirl burner consists of a 350 mm long annulus with inner diameter $D_a = 37$ mm, fitted with a concentric bluff body, as marked in Fig. 4.4. Close to burner exit, the bluff body has a wedged top (cf. Fig. 4.3c) with the radius being increased to give a diameter $D_b = 25$ mm, which is expected to result in a sudden acceleration of the swirling air stream. The bluff body surface has a central fuel exit with diameter $D_j = 4$ mm. Swirl motion of the air in the annular gap (with axial bulk velocity U_s) is generated when it passes a static swirler which has six guide vanes (the constant vane angle is $\theta = 60°$ with respect to the streamwise direction) and is located 41.6 mm upstream of burner exit. The configurations of bluff body and swirler can be seen in Fig. 4.4(c). Following the same formula used in the experiment by Cavaliere et al. [2013], the swirl number S_N for the Cambridge swirl burner is predicted using Beer and Chigier's method [Beer and Chigier, 1971] originating from purely geometrical consideration

$$S_N = \frac{2}{3}\frac{1-(D_{hub}/D_{sw})^3}{1-(D_{hub}/D_{sw})^2}\tan\theta. \tag{4.2}$$

For this burner, the swirler hub diameter D_{hub} and the swirler diameter D_{sw} are 11 mm and 37 mm respectively, and hence the swirl number for the Cambridge buner is $S_N = 1.23$.

The additional comments about the swirl generation method and the swirl number for the Sydney and Cambridge facilities are made here. As mentioned above, the tangential velocity component is imparted into the flow in the Sydney and Cambridge swirl burners using aerodynamic and geometric approaches respectively: axial-plus-tangential entry swirler and guide vane swirler [Gupta et al., 1984]. Both devices are commonly found in practice: the former was also used by Martinelli et al. [2007] for a swirling jet and the latter technique

was applied in the work by Holäpfel et al. [1996] and in the TECFLAM burner [Schmittel et al., 2000], to name a few. The efficiency of swirl generation (i.e. the ratio of kinetic energy of swirling flow to the pressure drop between air inlet and burner throat) for the axial-plus-tangential entry swirler is high for small S_N, while the axial-plus-tangential entry swirler is less efficient than guide vane swirler for large S_N (e.g. > 1.0) [Gupta et al., 1984]. Principally, S_N is dependent on both the Reynolds number and vane angle [Sheen et al., 1996]. However, for high S_N, it is negligibly influenced by the Reynolds number and hence Eq. (4.2) is valid. In addition, although the same symbol S_N is used for swirl numbers of the Sydney and Cambridge burners, however, they are respectively calculated through different formulas, i.e. Eqs. (4.1) and (4.2). In the Sydney swirl burner, the mass flow rates of axial and tangential ports can be modulated to achieve the varying S_N while S_N for Cambridge swirl burner is fixed as long as the vane angle θ does not change. It is not straightforward to directly compare the values of S_N for the current two burners because they are expected to generate non-equivalent flow fields downstream even if they have the same S_N. Equations. (4.1) and (4.2) are appealing since measurements of axial and tangential velocity profiles at the swirler outlet are not necessary. The comparisons of S_N from different formulas were made by Candel et al. [2014] and it was found that S_N from algebraic formulas, e.g. Eqs. (4.1) and (4.2), is typically larger than those with measured velocity and integration using the ratio of swirl and axial momenta.

The Cambridge swirl burner has been used to experimentally investigate the spark ignition in spray flames [Letty et al., 2012] and, more recently, local extinction and blow-off in premixed, non-premixed and spray flames [Cavaliere et al., 2013; Yuan et al., 2015a,b]. For the extinction studies, a series of flames for each regime are systematically studied by Cavaliere et al. [2013] and the contributions include studying the flame behaviors approaching blow-off, blow-off limits as well as blow-off transient and its duration in premixed, non-premixed and spray flames under gas-turbine-like conditions. Besides the LDV used to measure the velocity fields, 5 kHz OH* chemiluminescence and 5 kHz OH-PLIF are applied in order to image the transients of localized extinction and blow-off.

In this Chapter, the non-reacting case from the Cambridge swirl burner, CSWH1, is selected for investigation of flow fields using LES. Here the nam-

ing for this case exactly follows what is adopted by Cavaliere [2013]. The axial bulk velocity for swirling air stream is $U_s = 14.3$ m/s (The corresponding mass flow rate at the burner exit is 500 L/min). The air stream is under ambient conditions, i.e. 1 atm and 298 K. As such, the Reynolds number Re_s for the swirling stream is about 23,000. In the CSWH1 case, no flows are injected through the central jet exit. Furthermore, the operating conditions of CSWH1 are not exactly identical to those of the non-premixed flames simulated in Chapters 6, 7 and 8. It was observed experimentally that the basic flow structures of the Cambridge swirl burner do not change qualitatively with the varying air mass flow rate [Cavaliere, 2013]. Hence, it is still meaningful to select CSWH1 as the non-reacting case to first investigate the aerodynamics characteristics before we proceed to study the non-premixed flames in Chapters 6, 7 and 8.

4.2.3 Numerics

4.2.3.1 Numerical implementations

The LES solver (isothermal flows) introduced in Sub-section 3.4.1 will be applied for the computations in this Chapter. Second order implicit backward scheme is used for time discretization in Eqs. (3.3a) and (3.3b). Second order central differencing is applied for discretizing the convection and diffusion terms. The velocity−pressure coupling is performed by the hybrid SIMPLE and PISO method [Issa, 1986] and the Rhie−Chow strategy is used to avoid the spurious oscillations [Rhie and Chow, 1983], which have been described in Sub-section 3.3.1. The time step is 1×10^{-6} s for LES of non-reacting flows in both Sydney and Cambridge burners. In the LES solver, the CFL number for each cell is estimated as

$$CFL = \frac{1}{2}\Delta t \frac{\sum_{m=1}^{F^{LES}} \rho_m \tilde{\mathbf{U}}_m \cdot \mathbf{n}_m \Delta S_m}{\rho \mathcal{V}^{LES}}. \tag{4.3}$$

Here F^{LES} is the number of faces for the considered LES cell and the density is constant in incompressible flows. The above time step can ensure the CFL number from Eq. (4.3) is less than unity over the entire computational domain. Parallel computations (32 processors) are performed on the Cambridge High Performance Computing Cluster *Darwin*, and 0.001 s physical time needs approximately 20

minutes wall clock time. The total simulated physical time for both burners is 0.15 s.

In LES, generating the inflow turbulence is of great importance and may have an influence on the downstream turbulence evolutions. The state-of-the-art approaches to specify the inlet turbulence for LES have been reviewed and summarized by Tabor and Baba-Ahmadi [2010] and include the precursor calculation method [Lund et al., 1998], digital filter method [Klein et al., 2003] and its variant [di Mare et al., 2006], as well as synthesised turbulence method [Jarrin et al., 2006; Kornev and Hassel, 2007], just to name a few. Two types of synthesised turbulent inlet methods are used in this and the following Chapters: white-noise random fluctuation method and synthetic eddy method. Their algorithms will be briefly introduced as follows.

White-noise random fluctuation method

In this method white noise random fluctuations are imposed to the mean velocity profiles at the inlet, however, they do not have the required features of the turbulent flows, i.e. no spatially or temporally coherent structures, and hence would be destroyed by the LES solver. Its drawbacks in generating the realistic inlet turbulence have been extensively investigated [Klein et al., 2003]. However, since one only needs to specify the mean velocity profiles over the inlets, which to some degree reduces the uncertainty, it is still adopted in some computations of this and following Chapters.

Synthetic eddy method

The synthetic eddy method is more sophisticated than the white-noise random fluctuation method. The inlet turbulence in this method is generated with the temporally and spatially evolving distributions of Lagrangian vortices [Jarrin et al., 2006; Kornev and Hassel, 2007], i.e.

$$\mathbf{U}_{rms} = \sum_{k=1}^{N} \mathbf{c}^k f\left(\mathbf{x} - \mathbf{x}^k\right), \tag{4.4}$$

in which N is the number of vortices and $\mathbf{x}^k$ is the locations of k-th vortex. The amplitudes $\mathbf{c}^k$ are given by

$$c_i^k = a_{ij}\epsilon_i^k. \tag{4.5}$$

Here a_{ij} is the Cholesky decomposition of the Reynolds stress tensor $\mathbf{R}$, i.e.

$$\begin{bmatrix} \sqrt{R_{11}} & 0 & 0 \\ R_{21}/a_{11} & \sqrt{R_{22}-a_{21}^2} & 0 \\ R_{31}/a_{11} & (R_{32}-a_{21}a_{31})/a_{22} & \sqrt{R_{33}-a_{31}^2-a_{32}^2} \end{bmatrix}. \tag{4.6}$$

ϵ_i^k in Eq. (4.5) are random variables and the function f is the spatial distribution of velocity at location of $\mathbf{x}^k$. These Lagrangian vortices are transported by the bulk flows from the inlet into the computational domain. The quantities that should be provided include the length scale and Reynolds stress tensor, besides the mean velocity distributions for the inlets.

4.2.3.2 Computational domain, boundary condition and mesh

Sydney swirl burner

The computational domain for the Sydney swirl burner is illustrated in Fig. 4.5. The origin of Cartesian coordinate system lies at the center of fuel jet exit on the bluff body surface, as marked in Fig. 4.2. x is aligned with the streamwise direction, while y and z denote the spanwise coordinates. As shown in Fig. 4.5, the computational domain is composed of three parts: the pipe leading to jet exit, annulus carrying the swirling air stream and cylindrical downstream domain. The streamwise length of both pipe and annulus are 50 mm, while the extent of the cylindrical downstream domain is 300 mm $\times$ 150 mm $\times$ 2π (in streamwise, radial and azimuthal directions, respectively).

The velocity and pressure fields are initialized by the results from a RANS simulation with RNG k-ϵ model conducted beforehand. The boundaries for the computational domain except walls are marked explicitly in Fig. 4.5. Here the size of the coflow inlet is greater than that of the wind tunnel cross-section (130 mm $\times$ 130 mm) since the investigations in this Chapter are made as close as possible to the LES in Chapter 5. The scalar measurements for the flames were made in the wind tunnel with 310 mm $\times$ 310 mm in Sandia National Laboratories. The uniform velocity distribution $U_e = 20$ m/s imposed by 2% turbulent intensity is applied for it. Since there is no measurements available for the velocities exactly at the burner exit, the one-seventh power law is assumed for the axial velocity in

the central jet, following what was adopted by Masri et al. [2000]

$$\langle U \rangle = 1.218 U_j \left(1 - \frac{|r|}{1.01\delta}\right)^{1/7}, \tag{4.7}$$

in which the mean air bulk velocity U_j is 66.3 m/s for N16S159 case. $r = \sqrt{y^2 + z^2}$ is the distance to the jet exit center while $\delta = D_j/2 = 1.8$ mm. In Eq. (4.7), the factor 1.01 is introduced to ensure that the velocity gradient at the walls is finite [Masri et al., 2000]. For the axial and swirl velocities at the annular air inlets (25 mm $< r <$ 30 mm), the one-seventh power law, i.e. Eq. (4.7), is applied as well. In these cases, $\delta = 2.5$ mm and U_j in Eq. (4.7) should be replaced by U_s or W_s. r is the distance to the radial center of the annulus, i.e. $(D_a - D_b)/4$. Equation (4.7) is also adopted for the swirling air inlet by Malalasekera et al. [2007], Dinesh and Kirkpatrick [2009] and Yang and Kær [2012] for their LES of the N16S159 and other non-reacting cases and very good agreement of velocity fields with the measurements was achieved, confirming its validity. However, strictly, the profiles of axial and swirl velocities are far from symmetry with respect to the geometric center (which characterizes the profile from Eq. 4.7) and typically their peaks are shifted off the center due to the centrifugal effect, which is particularly true when S_N is high [Gupta et al., 1984]. The radial velocity component is set to be zero for the swirling air inlets, considering its relatively small magnitude compared to other two components. Zero pressure gradient conditions are enforced for all the inlets. For the lateral boundary open to the atmosphere and downstream outlet, the velocity is specified with zero gradient condition while the pressure is atmospheric. The walls (the bluff body, pipe as well as the annulus) have nonslip condition for velocity and zero pressure gradient. The wall function developed by Spalding [1961] is applied for the above mentioned solid walls.

The two dimensional slice of the mesh distribution for the downstream domain is schematically demonstrated in Fig. 4.6. Purely tetrahedral cells are used to discretize the whole domain shown. Three regions are refined and roughly correspond to the central air jet (refinement zone 1 in Fig. 4.6), recirculation zone (refinement zone 2) and its immediate downstream (refinement zone 3) based on the flow pattern observed in the experimental measurements by Al-Abdeli and

Masri [2003]. The minimal cell size gradually increases from refinement zone 1 to refinement zone 3. For the bluff body, annulus as well as the pipe walls, the mean values of y^+ vary between 20 and 80.

Cambridge swirl burner

Figure 4.7 demonstrates the computational domain of the Cambridge swirl burner. It should be mentioned here that a large hemispherical far-field is also included in the computational domain but not shown in Fig. 4.7. It aims to include the complete CRZ which extends beyond the combustion chamber shown from the experiments [Cavaliere, 2013] and also to minimize the effects of potential numerical pressure perturbations at the chamber exit on the upstream flow fields [Escudier et al., 2006]. Similar to the Sydney swirl burner, the origin of the Cartesian coordinate system is located in the center of the jet exit (cf. Fig. 4.4). x-axis is parallel to the streamwise direction while y- and z-axes are perpendicular to the chamber walls. The computational domain for Cambridge swirl burner include rectangular chamber and annulus, which are shown in Fig. 4.7. Different from the domain for the Sydney burner in Fig. 4.5, the swirler with six guide vanes is also included.

With CSWH1 operating conditions, a RANS simulation with RNG k-ϵ model is first performed using the complete geometry (i.e. including the annnulus and swirler). The velocity and pressure fields from RANS are used for initializing the LES fields. The boundaries except the solid walls are marked in Fig. 4.7. The mean velocity distributions at the annular air inlet are interpolated from the RANS and the zero gradient pressure is specified there. For the boundaries of the far-field, the velocity has the zero gradient condition and the pressure is fixed to atmospheric, mimicking the open surroundings near the chamber exit. For all the walls, including the chamber walls, annulus, swirler hub and vanes as well as bluff body, nonslip condition is enforced for velocity and zero gradient for pressure. For all the walls, the wall function by Spalding [1961] is used.

The mesh distribution of the combustion chamber visualized on the two dimensional slice is shown in Fig. 4.8. In the current investigations, purely tetrahedral cells are used to discretize the computational domain for Cambridge swirl burner. Although the IRZ is long, however, considerable shear and hence the

induced turbulent flows are confined to $x < 75$ mm [Cavaliere, 2013]. Therefore, the mesh in the bowl-like regions highlighted in Fig. 4.8 are refined (marked as refinement zone 1) and its downstream is refined as well (marked as refinement zone 2 in Fig. 4.8). The mean values of y^+ for the chamber walls are roughly 20−50.

4.2.3.3 Simulated cases

For the non-reacting flows N16S159 in the Sydney swirl burner, five cases are simulated and their details about the computational domain, inlet boundary specification and mesh number have been tabulated in Table 4.1. Case N16S159 is viewed as the base one in the current investigations and its computational domain starts at the burner exit and the white noise is specified at the swirling inlets and central jet exit. Its total LES cell number is around 8.4 millions. The other cases in Table 4.1 are grouped with N16S159 for the following comparisons:

1. mesh refinement effect: N16S159, N16S159-c, N16S159-f
2. turbulent inlet effect: N16S159, N16S159-ti
3. computational domain effect: N16S159, N16S159-fl

For the Cambridge swirl burner, the similar comparative studies are conducted and the five cases are listed in Table 4.2. Case CSWH1 is selected as the base simulation. The computational domain starts at the burner exit and the white noise method is used at the inlet boundaries. Its total LES cell number is approximately 8.2 millions. The influences of mesh refinement, turbulent inlet and computational domain are investigated with the following groups of simulations:

1. mesh refinement effect: CSWH1, CSWH1-c, CSWH1-f
2. turbulent inlet effect: CSWH1, CSWH1-ti
3. computational domain effect: CSWH1, CSWH1-fl

For all the cases for both Sydney and Cambridge swirl burners shown in Tables 4.1 and 4.2, the time duration used for compiling the velocity statistics is approximately 0.1 s after the initial period of 0.05 s.

4.3 Results and discussion

4.3.1 Sydney swirl burner

4.3.1.1 General characteristics

The two dimensional contours from $x-y$ plane for the base case, N16S159, are shown in Fig. 4.9. The filtered axial and swirl velocities ($\tilde{U}$ and $\tilde{W}$) as well as z-vorticity ($\tilde{\omega}_z$) are plotted in Figs. 4.9(a)−4.9(c) while the mean axial and swirl velocities ($\langle\tilde{U}\rangle$ and $\langle\tilde{W}\rangle$) in Figs. 4.9(d) and 4.9(e). The RZ is observable in Fig. 4.9(a), which is enclosed by the iso-lines of zero axial velocity, and extends from the immediate downstream of bluff body to $x/D_b \approx 2.5$. The non-swirling air jet penetrates into RZ along the centerline and there are also reverse flows downstream of the jet tip based on Fig. 4.9(a). In Fig. 4.9(b), the strong swirl velocity exists immediately from the ring inlets of the swirling air to $x/D_b = 1.0$ downstream and the regions with peak $\tilde{W}$ are roughly cylindrical with the radius $0.5D_b$, which completely confine the RZ. The time averaged distributions of axial and swirl velocities are presented in Figs. 4.9(d) and 4.9(e). Here the mean shape of RZ shown in Fig. 4.9(d) is slightly asymmetric which is different from the experimental findings [Al-Abdeli and Masri, 2003]. Furthermore, although the length of instantaneous RZ in Fig. 4.9(a) is very close to the experimental counterpart, i.e. $2D_b$ [Al-Abdeli and Masri, 2003], the length of mean RZ (around $1.4D_b - 1.6D_b$ based on Fig. 4.9d) is under-predicted. Also, the RZ surrounding the air jet is radially wider than the experimental results, particularly close to the waist of the jet, e.g. $x/D_b = 0.8$. For $\langle\tilde{W}\rangle$ demonstrated in Fig. 4.9(e), no considerable swirl motions exist around the jet exit and the magnitude of $\langle\tilde{W}\rangle$ in the RZ is relatively uniform.

The distribution of z-vorticity $\tilde{\omega}_z$ for N16S159 is shown in Fig. 4.9(c). The strongest vorticity is generated upstream of the air jet, resulting from the shearing between the jet and RZ. Further downstream, say $x/D_b = 1-1.5$, the distribution of z-vorticity is not continuous and shows streak structures with appreciable inhomogeneity. In addition, the swirling air is also responsible for the considerable z-vorticity, which extends from the ring inlet until $x/D_b = 2.5$. The generation of the vortices is mainly in the RZ, although upstream close to the bluff body

surface (e.g. $x < D_b$ and $-0.5D_b < y < 0$), $\tilde{\omega}_z$ is comparatively small as shown in Fig. 4.9(c).

The statistics of axial and swirl velocities at eight streamwise positions (from $x = 6.8$ mm to 125 mm) from N15S159 case are shown in Figs. 4.10 and 4.11, respectively. The mean axial velocity $\langle\tilde{U}\rangle$ from the computations agrees well with the experimental data. One discrepancy that needs to be pointed out is that the LES over-predicts $\langle\tilde{U}\rangle$ along the centerline at the streamwise positions $x = 20$ mm, 30 mm and 40 mm. At $x = 40$ mm, $\langle\tilde{U}\rangle$ is lower in LES, thereby over-predicting the intensity of recirculation close to the RZ center. The axial velocity *r.m.s.* in the jet flow regions is under-predicted at $x = 6.8$ mm, 10 mm, 20 mm. This is expected to be affected by the white noise inlet since no real turbulence is injected through central jet. Further downstream ($x \geq 30$ mm) shown in Figs. 4.10(d)−4.10(h), the computation predicts the *r.m.s.* very well.

The mean swirl velocities from the N16S159 case in Fig. 4.11 also demonstrate excellent agreements with the measurement results. Nevertheless, the computation fails to predict the swirling motion immediately around the jet exit. Specifically, at $x = 6.8$ mm and 10 mm, $\langle\tilde{W}\rangle$ over 3 mm $< r <$ 15 mm from LES is lower than that from the measurements. This can be found as well in the two dimensional contours of $\langle\tilde{W}\rangle$ in Fig. 4.9(e). The highly swirling zone around the base of the non-swirling jet is an important aerodynamic feature in the N16S159 case and also observed in the Sydney swirl flame cases [Al-Abdeli and Masri, 2003], such as SMA2. This under-prediction may result from the fact that no real and accurate turbulence is specified for both fuel and swirling inlets, which is expected to affect obtaining the correct radial pressure gradient near the bluff body. Similar to the upstream axial velocity *r.m.s.*, the swirl velocity *r.m.s.* at $x = 6.8$ mm and 10 mm is also smaller than the experimental results. The statistics of swirl velocity are well reproduced at $x \geq 40$ mm, as demonstrated in Figs. 4.11(e)−4.11(h).

The PSD functions of axial velocity at different locations are calculated and plotted in Fig. 4.12. The probed locations, $C1$−$C8$, have been marked explicitly in Fig. 4.9(e) and $C1$−$C4$ are exactly on the centerline while $C5$−$C8$ are 15 mm radially away from the centerline. As shown in Fig. 4.12(a), the axial velocity PSDs from the centerline probed locations do not manifest any dominant

frequency over the entire calculated frequency range. Similar observations are made for the probed locations $C5-C8$ based on the results in Fig. 4.12(b). In addition, the slopes of PSD curves for all the shown locations change at high frequency range ($f \geq 10,000$).

Figure 4.9(a) shows the penetration of the central jet which basically follows the centerline. To elucidate the transient characteristics of the air jet, the pressure distributions overlaid by the streamlines on the $y-z$ slice with $x = 50$ mm are presented in Fig. 4.13. The sub-figures respectively correspond to four time instants separated by 0.01 s. From Fig. 4.13(a), one can see that the pressure is relatively low in the RZ and large scale vortical structures can be found on the periphery of the low pressure regions. However, in the RZ there are no pronounced large vortices and instead only small ones exist. Meanwhile, the positions of the low pressure pockets do not show the consistency with vortices. This is quite different from the situations when the PVC exists, in which case the large scale vortex with low pressure can be seen off the central axis of symmetry [Syred, 2006]. The flow structures within the RZ at other three instants as shown in Figs. 4.13(b)−4.13(d) do not show any hints for the appearance of PVCs either. As such, based on Figs. 4.12 and 4.13, no PVC phenomenon and dominant frequency appear in the N16S159 case. This is consistent with the experimental measurements in which no characteristic frequency was detected [Al-Abdeli and Masri, 2004]. Accurately predicting the transient behaviors in the RZ is of great importance since the flows there are expected to directly influence the local mixing rates in turbulent non-premixed flames.

4.3.1.2 Sensitivity analysis

Grid sensitivity

The effects of grid refinement on the velocity statistics will be examined here. Three case with coarse, intermediate and fine meshes are used here and correspond to N16S159-c, N16S159, and N16S159-f listed in Table 4.1. The nominal cell sizes in refinement zones 1, 2 and 3 marked in Fig. 4.6 are shown in Table 4.3 and the total cell number can be found in Table 4.1. Figures 4.14(a)−4.14(c) present the fractions of residual kinetic energy $\langle M \rangle$ for the N16S159, N16S159-c, and

N16S159-f cases, respectively. The instantaneous M is calculated as follows

$$M = \frac{k}{K + k}, \tag{4.8}$$

in which the turbulent kinetic energy of the resolved flows, K, is predicted with

$$K = \frac{1}{2}\left\langle \left(\tilde{\mathbf{U}} - \langle\tilde{\mathbf{U}}\rangle\right) \cdot \left(\tilde{\mathbf{U}} - \langle\tilde{\mathbf{U}}\rangle\right) \right\rangle. \tag{4.9}$$

The sub-grid scale kinetic energy k is modelled with Eq. (3.10). Based on Eq. (4.8), M should vary between 0 and 1, corresponding to the DNS and RANS as the limiting cases. $M \leq 0.2$ is a widely accepted criterion for a well resolved LES, corresponding to the resolution of 80% of kinetic energy in LES [Pope, 2004]. As such, $\langle M \rangle$ in Fig. 4.14 is clipped to 0−0.2. One can see from Fig. 4.14(a) that in the RZ $\langle M \rangle$ is relatively small and in most of the refinement zone 2 it is less than 0.06. For the refinement zone 3, $\langle M \rangle$ is close to 0.1. The coarse mesh leads to the slightly larger $\langle M \rangle$ in the refinement zone 1 as shown in Fig. 4.14(b) and no obvious changes in other two zones. In the fine mesh case in Fig. 4.14(c), the time averaged fractions of residual kinetic energy in the zones 1 and 2 become smaller, indicating more kinetic energy is resolved in the fine mesh case. However, the fractions of the residual kinetic energy in the regions $0.5D_b$ downstream of the jet exit are greater than 0.2 (approximately 35%, 29% and 25% for the coarse, base and fine cases) in all the three cases due to the large jet exit velocity. This leads to the possibility that the turbulence near the jet exit would not be well resolved.

The comparisons of the statistics of axial velocities at four streamwise locations (x = 10 mm, 30 mm, 70 mm and 100 mm) from the above three meshes are made in Fig. 4.15. It is shown that the mean axial velocity from the current three meshes has negligible difference, with an exception being the mean profiles close to the centerline at x = 30 mm and 70 mm. For the $r.m.s.$, noticeable difference due to the mesh resolution exists close to the centerline at all shown locations in Fig. 4.15. In particular, the $r.m.s.$ from the base and fine meshes are closer to the experimental results than that from coarse mesh at x = 30 mm and 70 mm. The comparisons of the swirl velocity statistics are made in Fig. 4.16. The

mean swirl velocities from the three meshes agree with measurements very well, whereas the $r.m.s.$ from the base and fine meshes is much closer to the centerline. Therefore, the mean axial velocity and the $r.m.s.$ of axial and swirl velocities at the centerline are considerably influenced by the mesh resolutions in the current LES.

Effect of computational domain

Figures 4.17 and 4.18 show the statistics of axial and swirl velocities from N16S159-fl which has the full geometry, including the fuel pipe, annulus as well as cylindrical downstream domain as illustrated in Fig. 4.5. The mean axial velocities shown for four streamwise locations are reasonably predicted based on the results in Fig. 4.17 but at $x = 20$ mm in Fig. 4.17(a), the mean axial velocity close to the centerline is under-predicted. The *r.m.s.* of the axial velocity close to the centerline is better captured in N16S159-fl, compared to the results for the cases of N16S159 in Fig. 4.10 and N16S159-ti in Fig. 4.19. Nevertheless, over the entire radius range there are still pronounced differences between the results from N16S159-fl and the measured data. For the swirl velocity statistics at the same streamwise locations in Fig. 4.18, the mean shows a good agreement with the experimental data but the *r.m.s.* is not well predicted. These differences may result from the fact that the flows in the upstream annulus and pipe are not accurately computed, which makes the results from N16S1569-fl not superior to those from N16S159 and N16S159-ti.

Effect of turbulent inlet boundary condition

For the synthetic eddy boundary condition, in addition to the mean velocity profiles at the inlets, one also needs to specify the length scale L and Reynolds stress tensor $\mathbf{R}$. Since the measurements at both central jet exit and circular swirling air inlet are not available, the estimated values are specified in the present investigations exactly following the strategy by Masri et al. [2000]. For the central air jet, the length scale is assumed to be $L = 0.1D_j = 0.00036$ m. The components of $\mathbf{R}$ are given as follows

$$\langle vv \rangle = \langle ww \rangle = 0.5\langle uu \rangle, \tag{4.10}$$

$$\langle uv \rangle = 0.5 \frac{r}{D_j/2} \langle uu \rangle, \tag{4.11}$$

$$\langle uw \rangle = \langle vw \rangle = 0. \tag{4.12}$$

In the current simulation, $\langle uu \rangle$ is taken from the experimental data at $x = 6.8$ mm. In the swirling air inlets, the length scale is $L = 0.1(D_a - D_b)/2 = 0.0005$ m. The *r.m.s.* of axial and swirl velocities are assumed to linearly increase with radius from the center of circular inlets to the walls. At the center, u and w are assumed to be 3.0 m/s and 2.0 m/s, respectively, while at the walls, they are 6.3 m/s and 7.1 m/s, respectively. These values are estimations from the measurements at $x = 6.8$ mm. Linear variations across the circular swirling air inlets are assumed for $\langle uv \rangle$ and $\langle vw \rangle$. At the walls, $\langle uv \rangle_w = 0.0025 U_0^2$ and $\langle vw \rangle_w = 0.0025 W_0^2$ are assumed [Masri et al., 2000]. As such, $\langle uv \rangle$ and $\langle vw \rangle$ vary from $-\langle uv \rangle_w$ and $-\langle vw \rangle_w$ at the inner walls to $+\langle uv \rangle_w$ and $+\langle vw \rangle_w$ at the outer walls. Here U_0 and W_0 are the mean axial and swirl velocities at the center, respectively. In addition, $\langle uw \rangle$ is assumed to be zero in this case.

The velocity statistics from N16S159-ti case with synthetic eddy boundary condition can be found in Figs. 4.19 and 4.20. Based on Fig. 4.19, the mean axial velocity $\langle \tilde{U} \rangle$ is in line with the experimental results at both upstream ($x \leq$ 20 mm) and downstream ($x \geq 100$ mm) locations. However, discrepancies exist at $x = 30$ mm, 40 mm and 70 mm. The mean axial velocity is under-predicted over the radial ranges of $r < 15$ mm, which is completely converse compared to the results from the LES with white noise inlets (i.e. N16S159) as showed in Figs. 4.10(d)−4.10(f). At $x = 70$ mm, $\langle \tilde{U} \rangle$ is slightly negative, indicating the appearance of reverse flows along the centerline. This is different from the LES results with white noise boundary conditions in Fig. 4.10(f) and the experimental observations by Al-Abdeli and Masri [2004]. The axial velocity *r.m.s.* close to the fuel jet exit, such as $x = 6.8$ mm, 10 mm and 20 mm in Figs. 4.19(a)−4.19(c), is improved to some degree compared to the results with white noise inlets in Figs. 4.10(a)−4.10(c), but it is still lower than the measured results. Meanwhile, this under-prediction lasts until $x = 70$ mm while in the same streamwise locations the *r.m.s.* from LES with white noise inlet boundary conditions are closer to the

experimental data.

The radial profiles of swirl velocity statistics from N16S159 case at the same streamwise positions are plotted in Fig. 4.20. The mean swirl velocity $\langle \tilde{W} \rangle$ agrees with the experimental results very well and the only point that needs to be improved is the under-calculation of $\langle \tilde{W} \rangle$ close to the central air jet exit, say at $x = 6.8$ mm and 10 mm in Figs. 4.20(a) and 4.20(b). This discrepancy indicates that the current specifications for synthetic eddy method, Eqs. (4.10)−(4.12), may be still not accurate and hence do not fully mimic the realistic turbulence at the inlet, compared to the results with white noise boundary conditions. The comparisons of *r.m.s.* between the LES with synthetic eddy method and experimental results show that the noticeable difference exists at the upstream of RZ, i.e. from $x = 6.8$ mm to 40 mm.

The evolutions of mean and *r.m.s.* of axial velocity along the centerline are further compared between the cases with white noise (N16S159) and synthetic eddy (N16S159-ti) specifications for the inlets in Fig. 4.21. One can find that $\langle \tilde{U} \rangle$ in N16S159 is considerably over-predicted but at $x = 60$ mm afterwards, the experimental data are well reproduced. Although there are still some differences shown in Fig. 4.19, the decay rate of $\langle \tilde{U} \rangle$ and therefore the jet penetration into the RZ are greatly improved in N16S159-ti due to the imposed temporally and spatially correlated turbulent inlet conditions. In Fig. 4.21(b), it is shown that the axial velocity *r.m.s.* is close to the experimental data starting from $x = 30$ mm and at the upstream regions ($x \leq 30$ mm) the simulation results are much smaller. In N16S159-ti, the *r.m.s.* is much closer to the experimental data but still lower, as demonstrated in Fig. 4.19. Therefore, the inclusion of synthetic eddy inlet boundary conditions improves the penetration of central air jet and the *r.m.s.* close to the jet exit. However, at 30 mm $< x <$ 85 mm, both mean and *r.m.s.* are slightly smaller than the measured data when synthetic eddy method is used. The influences from different specifications of turbulent inlet boundary conditions are not observable when $x > 85$ mm.

4.3.2 Cambridge swirl burner

4.3.2.1 General characteristics

Figure 4.22 shows the velocity and z-vorticity distributions on the $x-y$ plane from the base case, CSWH1. From Figs. 4.22(a) and 4.22(b), the swirling air stream entres the combustion chamber with an angle of roughly 30° with respect to the streamwise direction. They impinge on the chamber lateral walls at around $x/D_b = 1.0$ and then flow towards the chamber exit. This is quite different from results of the Sydney swirl flows (i.e. N16S159) in Fig. 4.9, in which case the swirling air remains cylindrical after leaving the annular air inlets. This discrepancy leads to different aerodynamic characteristics in two burners. In the flame cases it is also responsible for the quite different flame shapes and behaviors that will be discussed in detail in Chapters 5 and 6. In particular, the IRZ confined by the swirling air streams (marked by the iso-lines of zero axial velocity in Fig. 4.22a) is long and extends beyond the chamber that is 0.15 m long. In addition, there are also small CRZ due to the confinement of the chamber walls. The distributions of time averaged axial and swirl velocities are shown in Figs. 4.22(d) and 4.22(e). The IRZ and CRZ are basically symmetric, although the slight asymmetry of IRZ at the downstream still exists in the computational results, which may be due to the fact that the time used for statistics calculation is still not long enough for the flows near the chamber exit. The z-vorticity in the CSWH1 case mainly exists along the shear layers between the swirling air and the IRZ as well as CRZ. Since there is no central jet from the bluff body in CSWH1, it is not able to examine the velocity and vorticity distributions for it in this study. Nevertheless, they will be discussed in the LES/3D-CMC of the Cambridge swirl non-premixed flames in Chapters 6 and 7.

The flow patterns can be understood further when the streamlines based on the filtered and time averaged velocities in Fig. 4.23 are analyzed. In CRZ, one can observe the counter-clockwise and clockwise rotating vortices in the LHS and RHS, respectively. Close to the swirling air in the IRZ, there are some small vortices, whereas further downstream two large scale vortex structures rotating in the opposite directions can be found. Their cores are on the iso-lines of zero axial velocity and near the points where the swirling air impinges on the walls. Near

the chamber exit, the flows are still turbulent, characterized by the appearance of small vortices. This implies the necessity of including the sufficiently large far-fields to accurately simulate the highly swirling flows like CSWH1. Besides the above structures, the IRZ is basically dominated by the reverse flow, from the chamber exit towards the bluff body. This can be further confirmed by the streamlines predicted from the time averaged velocities components in Fig. 4.23(b). Similar to Fig. 4.22(d), the slight asymmetry is also observed in Fig. 4.23(b) although essentially the flows in the CSWH1 case are symmetric based on the measurements [Cavaliere, 2013].

The radial profiles of statistics of the axial, swirl and radial velocity components are presented in Figs. 4.24−4.27. The mean axial velocities $\langle \tilde{U} \rangle$ show good agreement with the experimental results, from $x = 8$ mm to $x = 117$ mm in Fig. 4.24. About the axial velocity $r.m.s.$ in Fig. 4.25, the LES results are close to the measured ones, except at $x = 8$ mm, 13 mm and 23 mm. The peaks of axial velocity $r.m.s.$ at these locations are under-calculated. This may be caused by the white noise inlet which does not have the spatially and temporally correlated turbulence. The mean swirl and radial velocities in Figs. 4.26 and 4.27 also agree with experimental data well. The only difference is about the mean radial velocity in the CRZ at $x = 8$ mm shown in Fig. 4.27(a), which is slightly lower than the experimental results. At the locations of $x = 8$ mm, 13 mm and 18 mm, the peak $r.m.s.$ of swirl and radial velocities are clearly smaller compared to the experimental data, similar to the situations for $r.m.s.$ of axial velocity. Since these peak locations spatially correspond to the shear layers between the swirling streams and chamber flows, this implies that the $r.m.s.$ in the shear layers is under-predicted. This may be due to the not enough mesh resolution, making the velocity field under-resolved there.

4.3.2.2 Sensitivity analysis

Grid sensitivity

The influence of mesh resolution on the velocity statistics is examined here with three sets of meshes, i.e. CSWH1-c (coarse mesh), CSWH1 (intermediate mesh) and CSWH1-f (fine mesh). Their cell sizes of refinement zone 1 and zone 2 are

tabulated in Table 4.4 and the total cell numbers in Table 4.2. The LES with the intermediate mesh has been analyzed in Figs. 4.22−4.27. Figure 4.28 shows the contours of time averaged fraction of residual kinetic energy, $\langle M \rangle$, for the above mentioned three cases. The instantaneous fraction, M, is calculated using Eq. (4.8). In Fig. 4.28(a), in the refinement zone 1 where the strong shearing occurs, $\langle M \rangle$ is below 0.2 and, more specifically, it varies around 0.1 over the shown domain. In addition, $\langle M \rangle$ is larger than 0.2 immediately downstream of the annulus air inlets. There is also large fraction of residual kinetic energy near the bottom and lateral walls of the combustor chamber. They may respectively affect the prediction of the turbulence near the inlet as well as the chamber walls but these influences are expected to be small since most of the turbulence in this burner is generated by the strong shearing within the chamber. About the coarse mesh case (CSWH1-c), in the refinement zone 1, $\langle M \rangle$ is noticeably larger compared to the counterpart from CSWH1 in Fig. 4.28(a), but is still less than 0.2. Close to the chamber walls, there are large areas with $\langle M \rangle > 0.2$. When the cell is refined further compared to the intermediate case CSWH1, $\langle M \rangle$ is reduced to below 0.04 over most of the refinement zone 1, indicating the fairly small residual kinetic energy in the CSWH1-f case.

The statistics of axial and swirl velocities at three streamwise locations ($x =$ 8 mm, 13 mm and 33 mm) from CSWH1-c, CSWH1 and CSWH1-f cases are presented in Fig. 4.29. About the mean axial velocity, the results from CSWH1-c and CSWH1 are close to each other, whilst those from CSWH1-f are slightly better in predicting the reverse flows in IRZ, e.g. at $x = 13$ mm and 33 mm. This slight improvement is also observed in the results of swirl velocity in IRZ at $x =$ 33 mm. The location and magnitude of peak mean axial and swirl velocities are accurately calculated for all the three cases. Generally, the mesh resolution does not have obvious influence on the mean axial and swirl velocities. However, the *r.m.s.* is considerably affected as shown in Fig. 4.29. In particular, in the shear layers and/or also in the CRZ (e.g. $|y|/D_b \geq 0.5$), higher *r.m.s.* of axial velocity is predicted as the mesh is finer. This finding also exists for the *r.m.s.* of swirl velocity. The velocity fields are resolved more in this case from the Cambridge swirl burner if the mesh is finer, thereby leading to more accurate *r.m.s.* results in the CSWH1-f case. Combining the current results and those from the mesh

resolution studies in Figs. 4.15 and 4.16, one can see that the mesh resolution effects on the resolved and residual fields are not general and, instead, they are specific to the investigated flow features, the sub-grid scale model and the extent to which the studied fields are sensitive to the small scale dynamics, which was also observed by Boudier et al. [2008].

Effect of computational domain

Here the CSWH1-fl case with the complete computational domain (i.e. annulus, swirler, combustion chamber shown in Fig. 4.7 and also hemisphereical far-field) is simulated and the emphasis will be laid on the influence of annulus and swirler on the velocity statistics. In Fig. 4.30, the filtered and mean axial and swirl velocities on the two dimensional $x-y$ cutting plane are presented. One can clearly see that the flow becomes complex after they pass the angled guide vanes and the toroidal recirculating regions appear spanning from the swirler hub to the whole bluff body lateral surfaces based on Figs. 4.30(a) and 4.30(b). Meanwhile, the rotating motion is generated characterized by the considerable swirl velocity component downstream of the swirler presented in Figs. 4.30(c) and 4.30(d). When it comes to the flows in the combustion chamber, they have qualitatively similar features (say, CRZ and IRZ) to the results in Fig. 4.22 which is predicted without the annulus and swirler. However, the radii of the IRZ are slightly smaller in Fig. 4.30 than those shown in Fig. 4.22.

The second invariant of the velocity gradient tensor, $\mathscr{Q}$, is calculated from

$$\mathscr{Q} = \frac{1}{2}\left(\mathbf{LL} - \mathbf{DD}\right), \tag{4.13}$$

in which $\mathbf{L}$ is the antisymmetric part of the velocity gradient tensor, i.e.

$$\mathbf{L} = \frac{1}{2}\left(\nabla\bar{\mathbf{U}} - \nabla\bar{\mathbf{U}}^T\right), \tag{4.14}$$

and the symmetric part of the velocity gradient tensor, $\mathbf{D}$, is from Eq. (3.4). $\mathscr{Q} > 0$ is a necessary condition for the existence of thin, convex low-pressure tubes and its iso-suface can be used for visualizing the vortex [Lesieur et al., 2005]. Figure 4.31 plots the iso-surfaces of $\mathscr{Q} = 1.5 \times 10^7$ $1/\mathrm{s}^2$ coloured by the vorticity

magnitude. The strong vorticity is generated in the annulus after the swirler. The vortices visualized by the $\mathscr{Q}$ iso-surfaces in the annulus extend into the combustor, with the streak-like structures normal to or inclined to the longitudinal direction. Therefore, inclusion of the swirler and annulus is expected to accurately simulate the generation of the swirling flows and the spatial evolution of the vortices. Meanwhile, this also imposes the challenge for the LES of complex flows in the swirler and the near-wall turbulence in the annulus.

The comparisons of axial and swirl velocities between the current cases and the experimental results at the selected streamwise positions are made in Fig. 4.32. For the axial velocity, excellent agreement is achieved at all the three locations, although two points should be pointed out. First, the recirculation in the IRZ at $x = 13$ mm and 33 mm is over-predicted, with stronger magnitudes of axial velocities compared to the measured ones. Second, for the axial velocity $r.m.s.$ at $x = 8$ mm and 13 mm, the LES results are roughly symmetric and the peak positions are different from the experimental counterparts although the peak $r.m.s.$ values are close to the experimental results as shown in Fig. 4.32. For the swirl velocity statistics, at $x = 8$ mm, the mean swirl velocity from the LES with annulus and swirler is generally in line with the experimental data. Nevertheless, at $x = 13$ mm and 33 mm, some discrepancies exist. Specifically, the LES over-predicts the swirl velocity within the RZ (i.e. $-0.5D_b < y < 0.5D_b$) at the $x = 13$ mm and over the entire spanwise range at $x = 33$ mm. This directly indicates that the swirling motion at these locations is not accurately captured. This is also relevant to the over-predictions of the recirculation at these two locations discussed above: qualitatively, the stronger swirling, the larger radial and axial pressure gradients, and hence the larger intensity of the recirculating flows. In addition, the current simulation gives better results of swirl velocity $r.m.s.$ at $x = 8$ mm and 13 mm compared to those from the simulation excluding the annulus and swirler (cf. Fig. 4.25). This improvement can be expected since the white noise imposed on the mean inlet velocity profiles does not contain the spatial and temporal correlation information and therefore decays quickly.

Some additional comments are made here concerning the over-calculations of the mean swirl velocities in LES including the annulus and swirler. First, this problem does not arise in the LES without annulus and swirler (cf. Fig. 4.25),

which shares the identical mesh (for the combustor chamber and far-field) and the LES sub-grid scale modelling. This implies that the flows in the upstream annulus section may not be accurately simulated. Second, a RANS simulation with RNG $k-\epsilon$ model is conducted as mentioned in Sub-section 4.2.3.2, which includes the annulus and swirler in the computational domain. The mean axial and swirl velocities are plotted in Fig. 4.32. The RANS results agree fairly well with the measured data and this is also the case for the more downstream locations not given in Fig. 4.32. Therefore, the conclusion can be made tentatively that the current LES modelling do not perform well in the annulus and swirler. As shown in Fig. 4.30, the wall confined turbulence and severe separations as well as recirculation characterize the complexity of the flows within the annulus. Systematic investigations of the near-wall treatment in LES modelling is beyond the scope of the thesis but the author acknowledges its importance in simulating the turbulence and also the combustion near walls, which will be part of the future work.

Both of the computational domains with and without the annulus are used for the non-premixed flame simulations in Chapters 6−8 since they have respective advantages in predicting the velocity statistics based on the analysis for Figs. 4.24−4.27 and 4.32. Particularly, for the LES/3D-CMC computations without annulus in Chapter 8, the mean velocity profiles at the swirling air inlet (i.e. the annulus exit) are interpolated from the RANS results since the experimental data are not available at the inlet whilst the RANS results show the excellent agreement with the measured velocity data in the chamber plotted in Fig. 4.32. This will be detailed in Sub-section 8.2.3.

Effect of turbulent inlet boundary condition

The effect of turbulent inlet boundary conditions on the velocity statistics in the combustion chamber will be studied here. The geometry with no annulus and swirler is used and therefore the inlet boundary corresponds to the chamber at $x = 0$. The Reynolds stress $\mathbf{R}$ imposed on the swirling air inlets is interpolated from the LES with the complete computational domain, i.e. CSWH1-fl. The above *ad hoc* specifications are based on that speculation that the *r.m.s.* from the LES with annulus agrees well with the experimental close to the inlet, say,

$x = 8$ mm in Fig. 4.32, and hence the turbulence exactly at the inlet should also be not far from the experimental ones. The integral length scale L is assumed to be uniform over the inlet and is estimated as $L = 0.1(D_a - D_b)/2 = 0.006$ m. Possible uncertainties may exist about if they accurately mimic the real turbulence at the air inlets. However, it will be still meaningful to examine the influence of turbulent inlet boundary on the flow fields in the Cambridge swirl burner.

Figure 4.33 shows the comparisons of axial and swirl velocity related Reynolds stress components, i.e. $\langle uu \rangle$, $\langle ww \rangle$ and $\langle uw \rangle$, close to the air inlet ($x = 1$ mm, 3 mm and 8 mm) from the two LES cases with the white noise and synthetic eddy inlet conditions, respectively. Three observations can be made. First, the LES with synthetic eddy inlet boundary conditions indeed introduces pronounced turbulence at the upstream locations, e.g. at $x = 1$ mm. Second, the difference between the LES with synthetic eddy inlet and white noise inlet is only limited to the shear layers between swirling air stream and IRZ as well as CRZ, respectively. Within the IRZ and CRZ, no obvious distinctions can be found for all the demonstrated streamwise locations. Third, in spite of the above improvements, the Reynolds stress from the LES with annulus is still lower than its experimental counterparts in Fig. 4.33(c). Therefore, one can see that the synthetic eddy method greatly improves the velocity statistics near the swirling air inlet but careful specifications are needed for the integral length scale and Reynolds stress tensor.

4.4 Conclusions

The swirl non-reacting flows from the Sydney and Cambridge swirl burners are simulated using LES. The parameters of both experimental setup and flow information are introduced first. The general features about the flow structures are analyzed based on the LES results and the velocity statistics are compared with the measurements. For the non-reacting flows in the Sydney burner, the RZ is reasonably captured although its mean length is slightly smaller than the measured results. For the non-reacting flows in the Cambridge burner, the IRZ and CRZ are correctly predicted. Generally, the current LES modelling can accu-

rately predict the swirl non-reacting flows in both burners. In addition, influences of LES grid refinement, extent of the computational domain and turbulent inlet boundary condition on the swirl flow fields are investigated. The mesh refinement has an important influence on the decay of mean axial velocity along the centerline and also on the $r.m.s$. Inclusion of the annulus and swirler can simulate the generation of the swirling motion and upstream turbulence, but also poses a challenge in correctly simulating the complex flows therein. The synthetic eddy method shows the improvements in computing the jet penetration and velocity $r.m.s$. near the inlets, but accurate specifications are needed to mimic the realistic inlet turbulence.

The studies in this Chapter serve as a preliminary preparation for the following chapters on LES/3D-CMC simulations of turbulent non-premixed flames. The numerics (domain, boundary condition and mesh) used in Chapters 5−8 are listed briefly as follows. The details for them are presented in Tables 4.1 and 4.2.

- Chapter 5 (Sydney swirl flames): N16S159 for SMA2, N16S159-ti for SMA3 and SMA4.
- Chapters 6 and 7 (Cambridge swirl flames): CSWH1-fl.
- Chapter 8 (Cambridge swirl flames): CSWH1.

4.5 Tables for Chapter 4

Table 4.1: Simulated cases of the Sydney swirl burner

Cases	Computational domain *	Inlet boundary	Total cells
N16S159	Cylindrical domain	White noise method	8.4 M
N16S159-c	Cylindrical domain	White noise method	4.3 M
N16S159-f	Cylindrical domain	White noise method	16.1 M
N16S159-ti	Cylindrical domain	Synthetic eddy method	8.4 M
N16S159-fl	Fuel pipe, annulus, cylindrical domain,	White noise method	15.0 M

* The individual parts of the computational domain for the Sydney swirl burner have been marked in Fig. 4.5.

Table 4.2: Simulated cases of the Cambridge swirl burner

Cases	Computational domain †	Inlet boundary	Total cells
CSWH1	combustor, far-field	White noise method	8.2 M
CSWH1-c	combustor, far-field	White noise method	3.1 M
CSWH1-f	combustor, far-field	White noise method	15.0 M
CSWH1-ti	combustor, far-field	Synthetic eddy method	8.2 M
CSWH1-fl	swirler/annulus, combustor, far-field	White noise method	10.2 M

† The individual parts of the computational domain for the Cambridge swirl burner have been marked in Fig. 4.7.

Table 4.3: Cell size in N16S159, N16S159-c and N16S159-f cases

Cases	cell size in Zone 1 (mm)	cell size in Zone 2 (mm)	cell size in Zone 3 (mm)
N16S159	0.3	0.4	1.0
N16S159-c	0.39	0.52	1.3
N16S159-f	0.23	0.31	0.77

Table 4.4: Cell size in CSWH1, CSWH1-c and CSWH1-f cases

Cases	cell size in Zone 1 (mm)	cell size in Zone 2 (mm)
CSWH1	0.4	0.75
CSWH1-c	0.6	1.1
CSWH1-f	0.3	0.5

4.6 Figures for Chapter 4

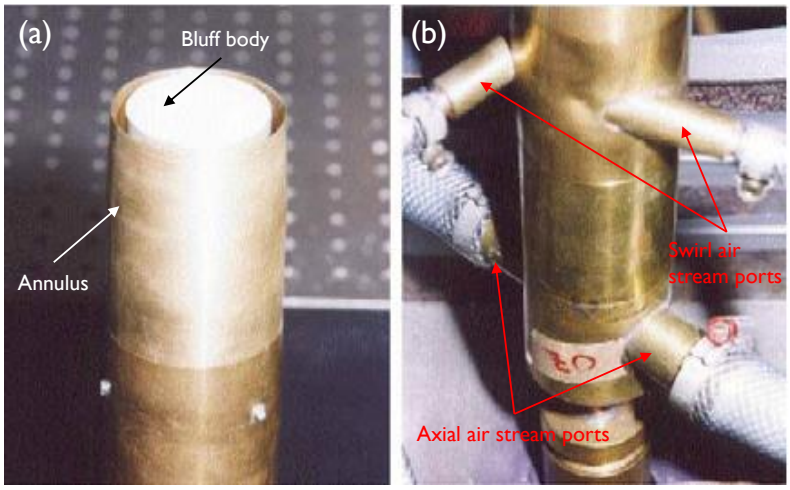

Figure 4.1: Photos of the Sydney swirl burner configuration [Al-Abdeli et al., 2006]: (a) bluff body and annulus; (b) axial and swirl stream ports.

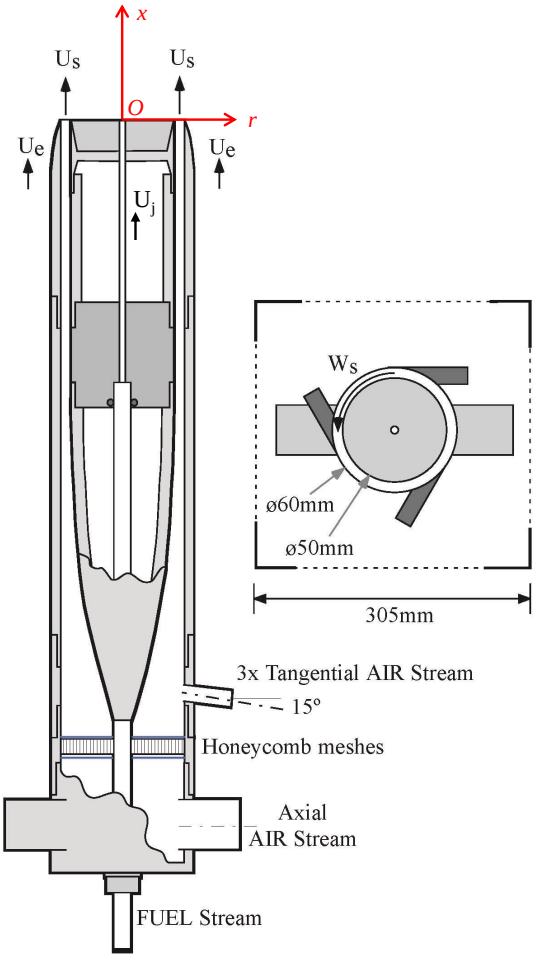

Figure 4.2: Schematic of the Sydney swirl burner [Masri et al., 2004].

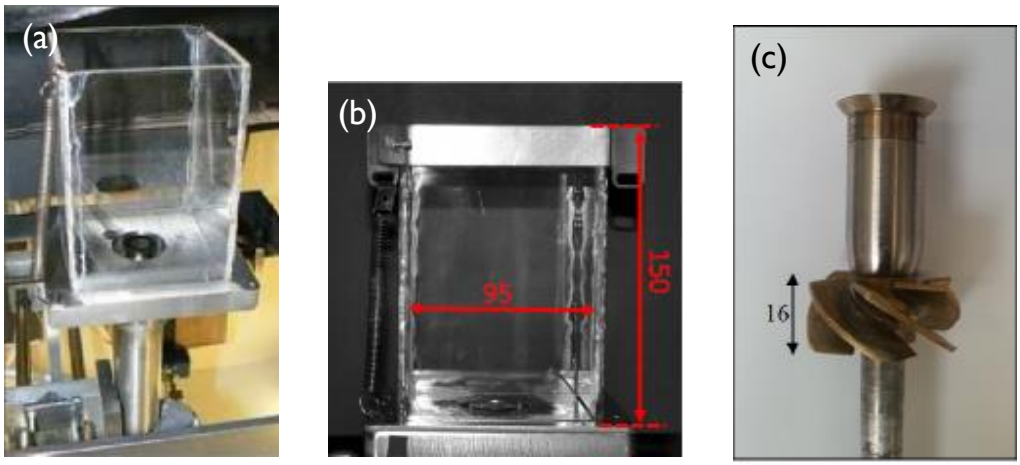

Figure 4.3: Photos of the Cambridge swirl burner [Cavaliere, 2013]: (a) combustor; (b) enclosure; (c) bluff body with swirler. All units in mm.

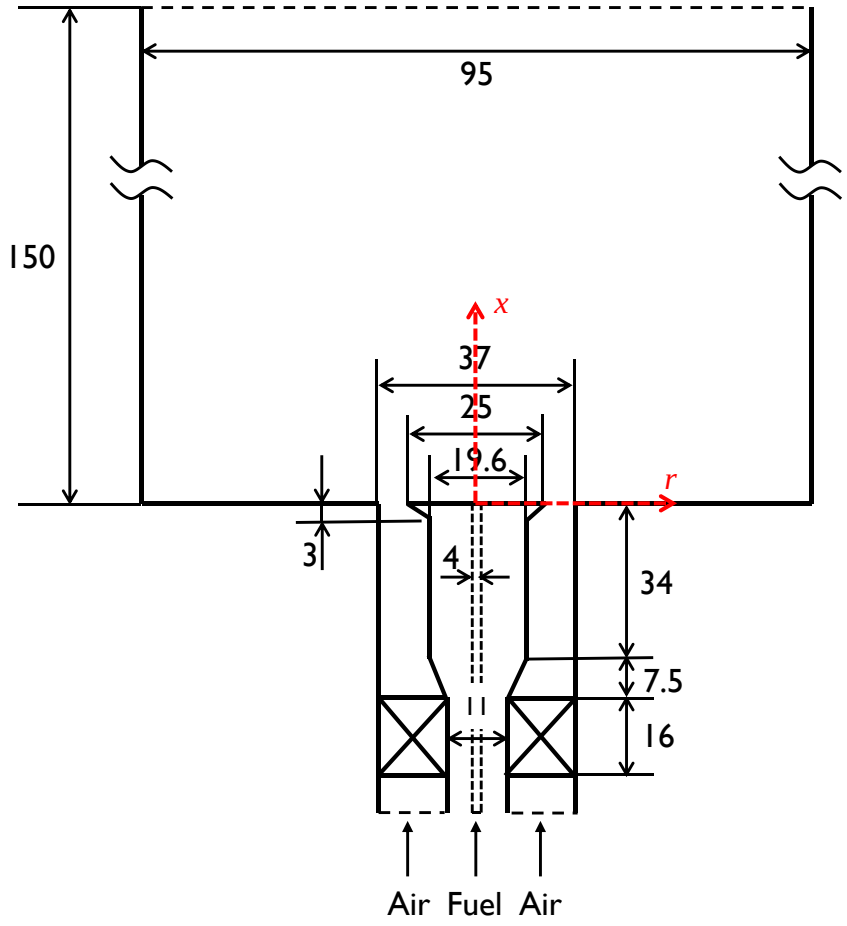

Figure 4.4: Schematic of the Cambridge swirl burner [Cavaliere, 2013]. All units in mm.

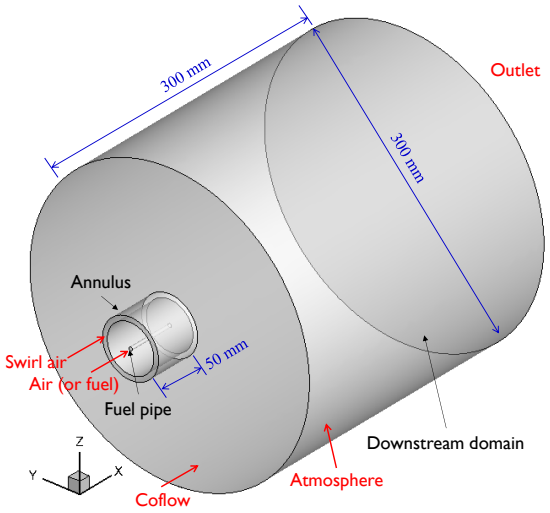

Figure 4.5: Computational domain of the Sydney swirl burner. The black notations are for parts of computational domains while the red for boundaries.

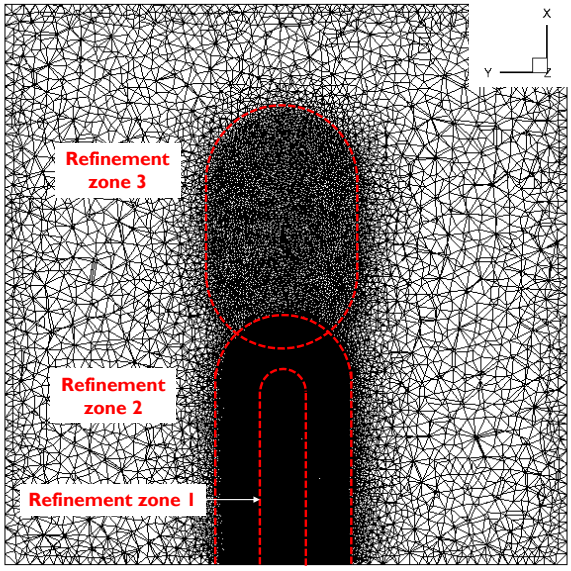

Figure 4.6: Schematic of mesh distribution in the downstream domain ($x-y$ slice with 300 mm $\times$ 300 mm) for the Sydney swirl burner.

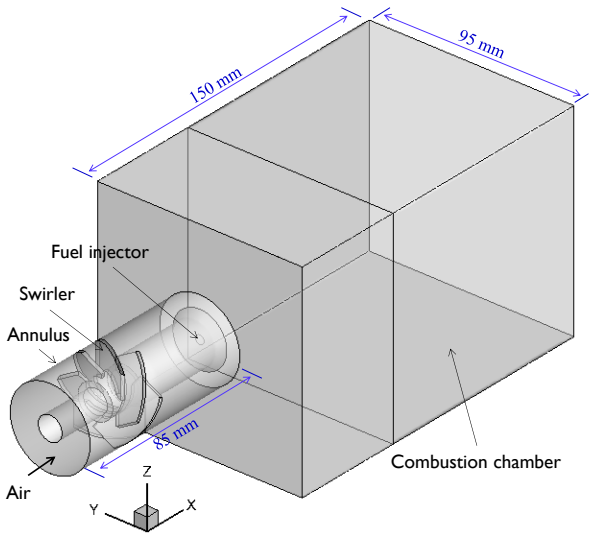

Figure 4.7: Computational domain of the Cambridge swirl burner.

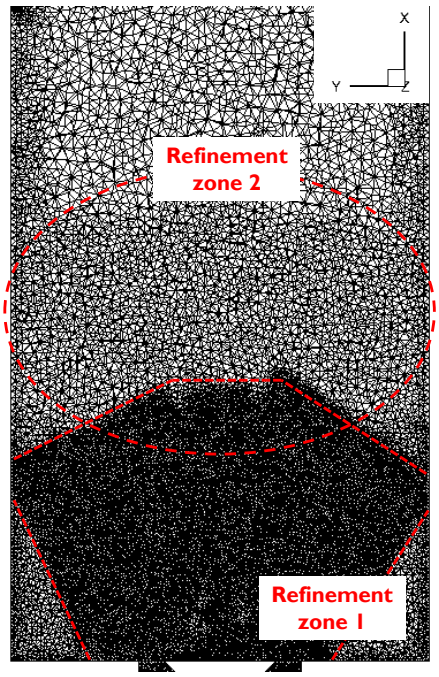

Figure 4.8: Schematic of mesh distribution in the combustion chamber ($x-y$ slice with 90 mm $\times$ 150 mm) for the Cambridge swirl burner.

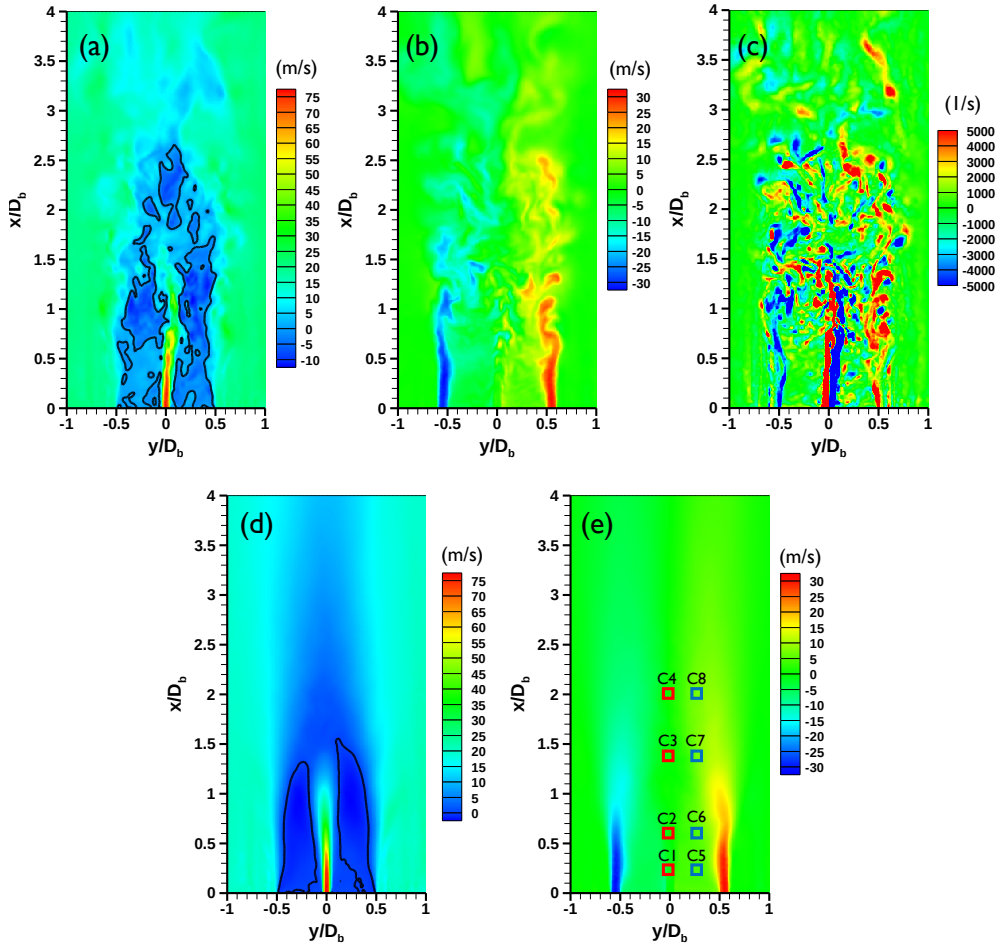

Figure 4.9: Two dimensional distributions ($x-y$ plane) of instantaneous (a) axial velocity, (b) swirl velocity, (c) z-vorticity, time averaged (d) axial velocity and (e) swirl velocity for N16S159. The solid lines in (a) and (d) denote the zero axial velocity iso-lines. The symbols denoted by $C1-C8$ in (e) are the LES probing locations.

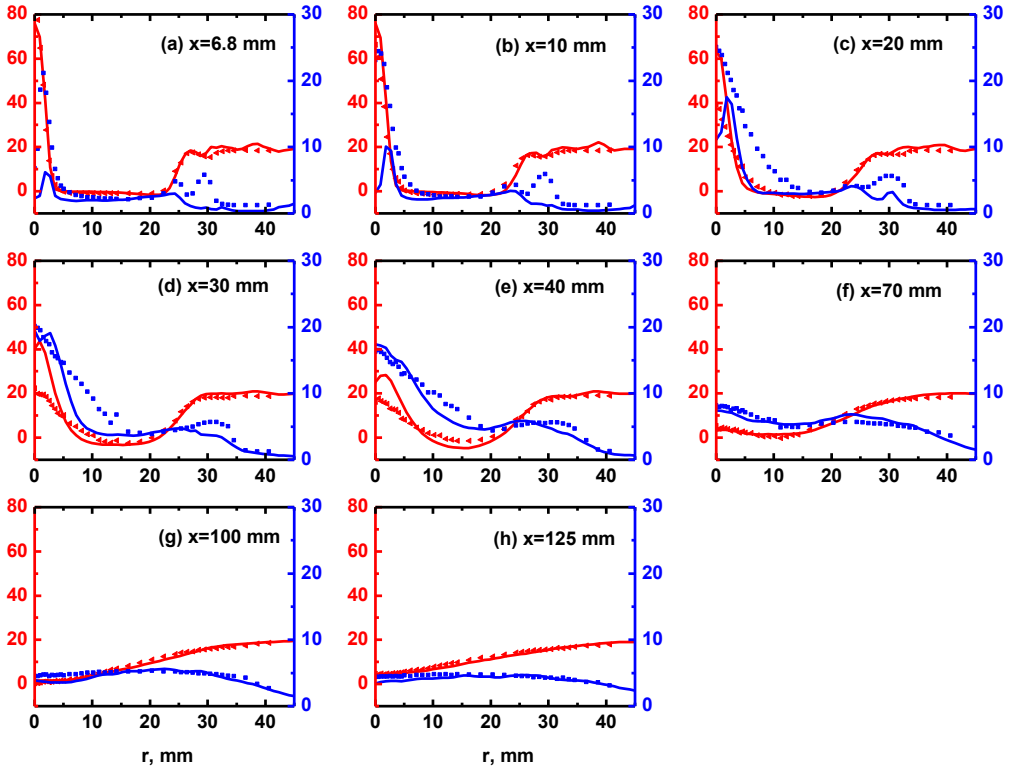

Figure 4.10: Radial profiles of mean (red) and *r.m.s.* (blue) of axial velocity at different streamwise locations for N16S159. Lines: LES; symbols: experiment. Simulation results are from LES with white noise inlets. The left and right ordinates (units in m/s) are for mean and *r.m.s.*, respectively.

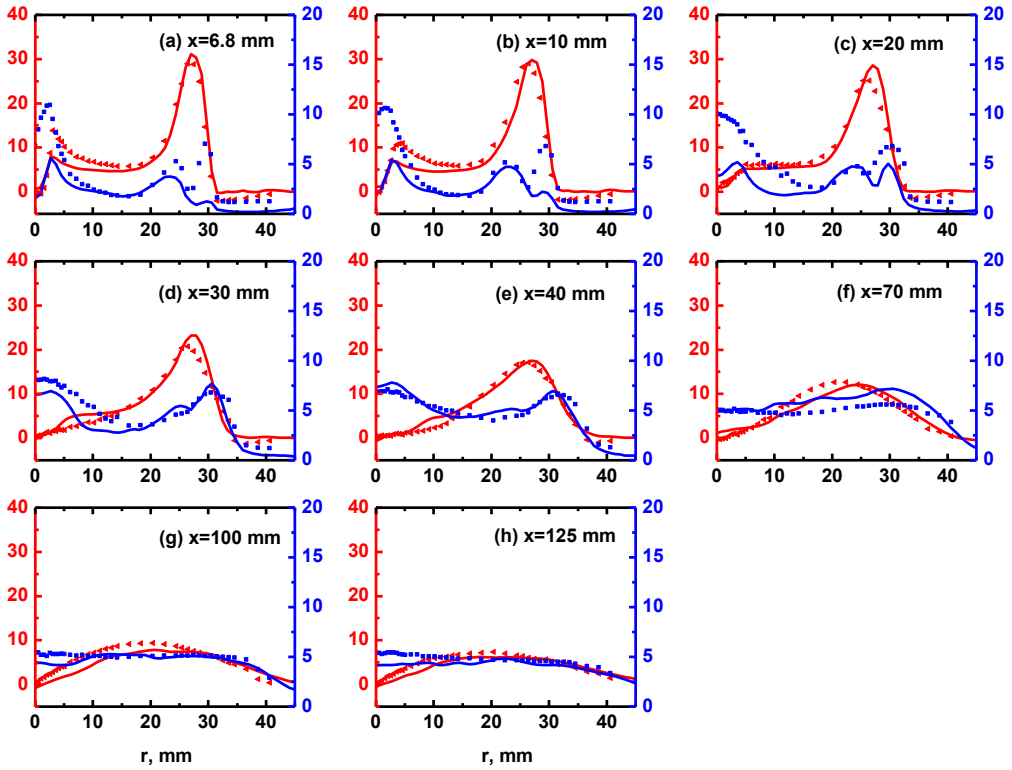

Figure 4.11: Radial profiles of mean (red) and *r.m.s.* (blue) of swirl velocity at different streamwise locations for N16S159. Lines: LES; symbols: experiment. Simulation results are from LES with white noise inlets. The left and right ordinates (units in m/s) are for mean and *r.m.s.*, respectively.

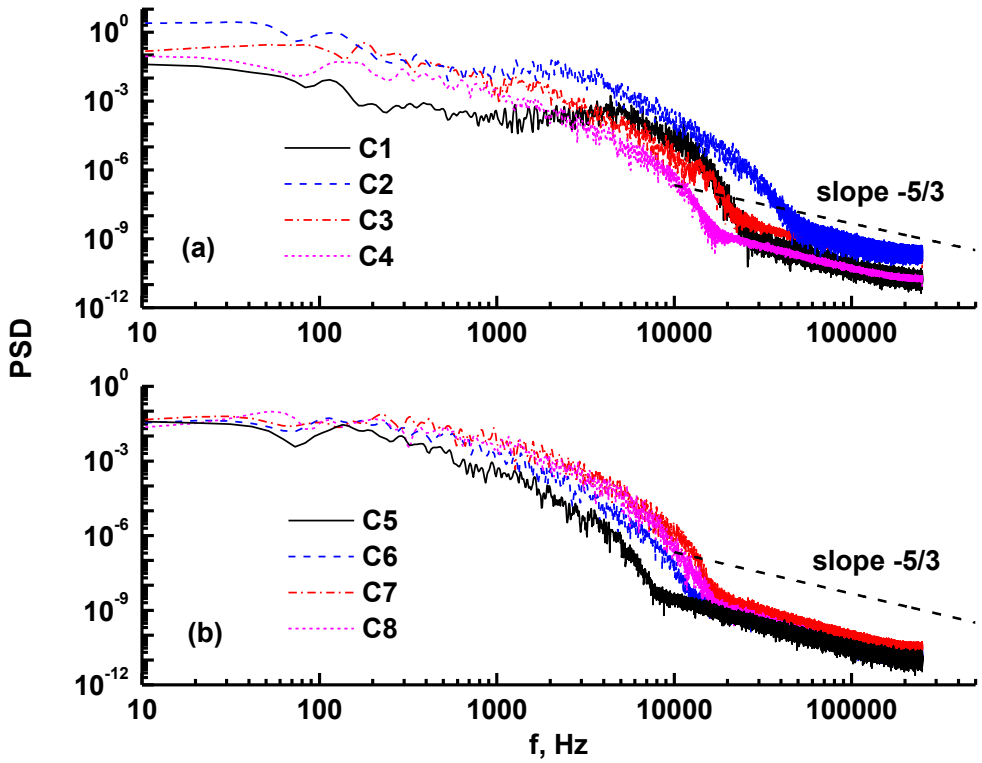

Figure 4.12: Spectra of the axial velocity with the different locations (a) along the centerline and (b) with $y = 0.015$ mm and $z = 0$. The positions for $C1-C8$ are marked in Fig. 4.9(e).

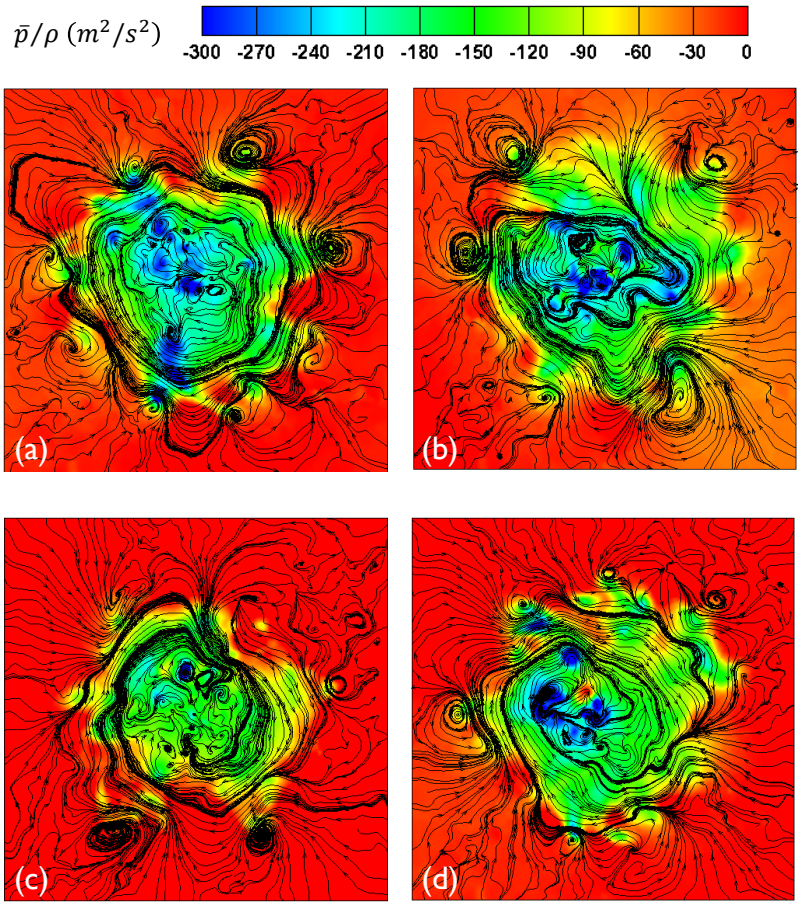

Figure 4.13: Distributions of kinematic pressure $\bar{p}/\rho$ on the $y-z$ plane ([-50 mm, 50 mm] $\times$ [-50 mm, 50 mm], x = 50 mm) overlaid by the streamlines at four different time instants.

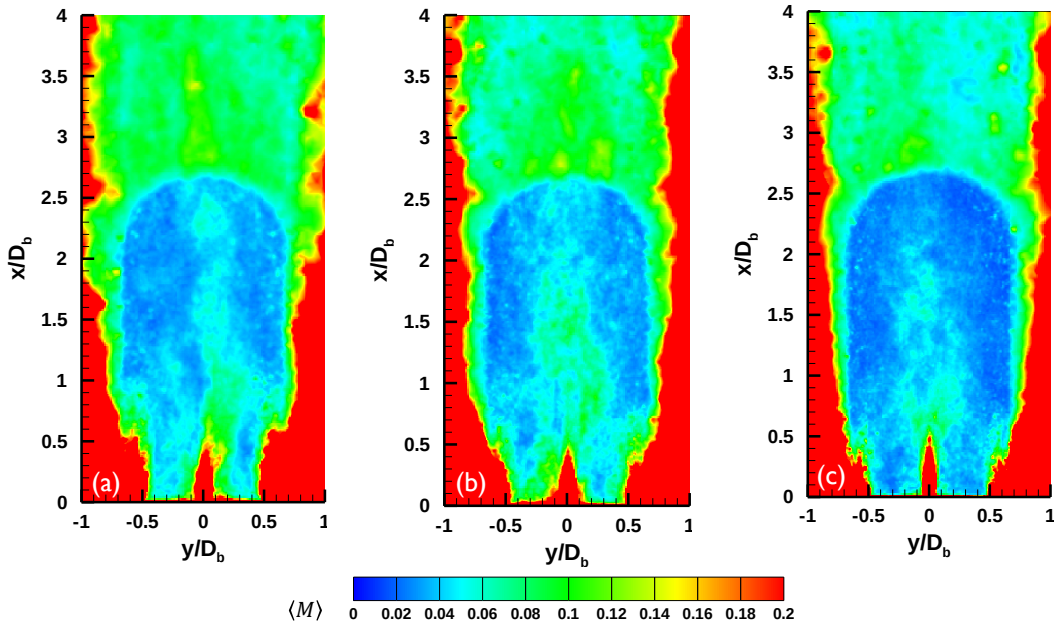

Figure 4.14: Time averaged fractions of residual kinetic energy $\langle M \rangle$ with (a) base (N16S159), (b) coarse (N16S159-c) and (c) fine (N16S159-f) meshes.

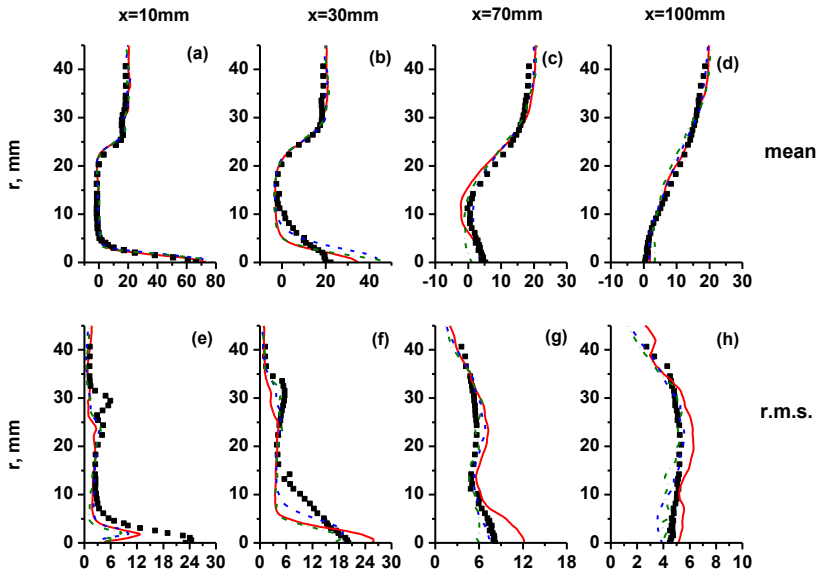

Figure 4.15: Radial profiles of mean (first row) and *r.m.s.* (second row) of axial velocity from LES with base (dashed), coarse (solid) and fine (dash-dotted) meshes. The symbols denote the experimental data.

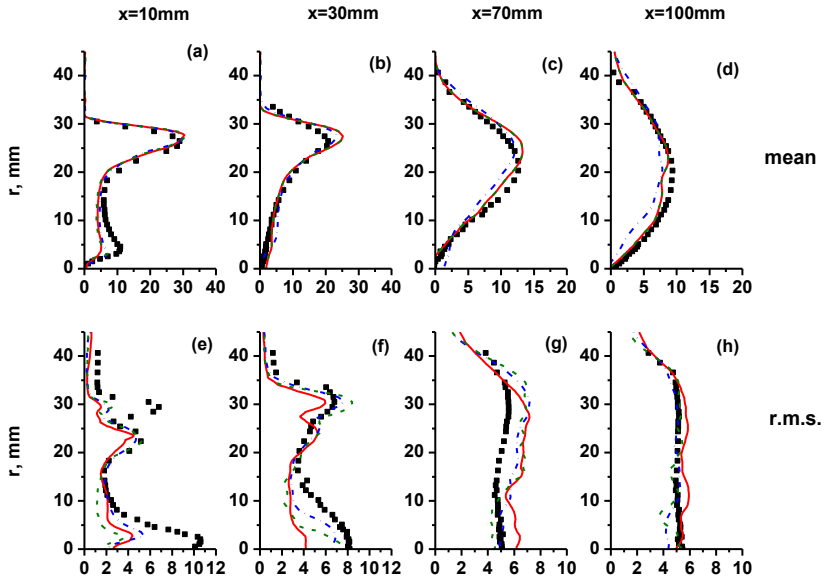

Figure 4.16: Radial profiles of mean (first row) and *r.m.s.* (second row) of swirl velocity from LES with base, coarse and fine meshes. The legend same as that in Fig. 4.15.

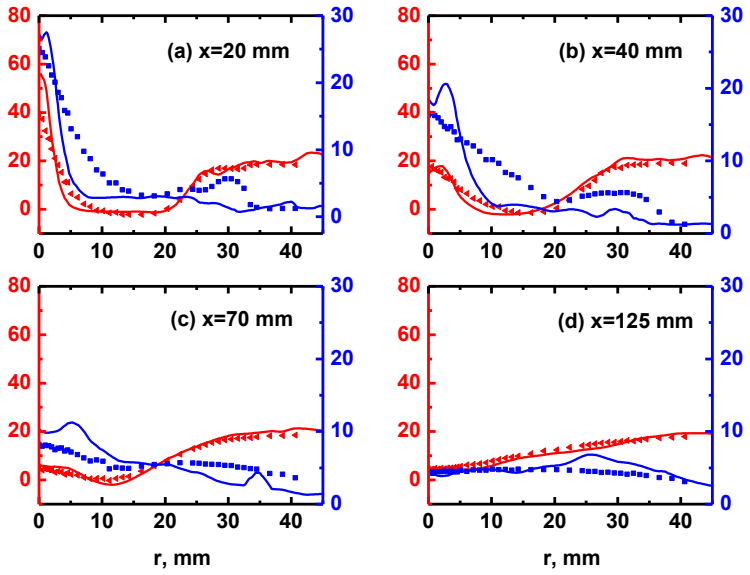

Figure 4.17: Radial distributions of mean and *r.m.s.* of axial velocity at four streamwise locations from N16S159-fl. Lines: LES results; symbols: measurements.

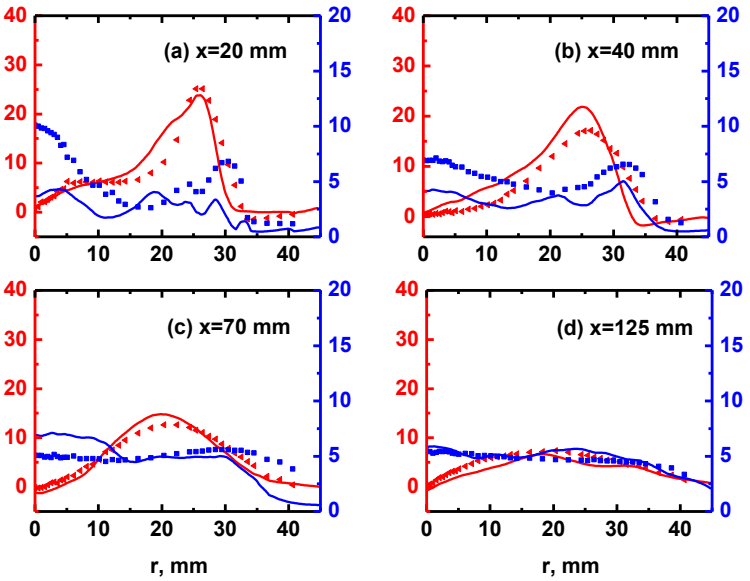

Figure 4.18: Radial distributions of mean and *r.m.s.* of swirl velocity at four streamwise locations from N16S159-fl. The legend same as that in Fig. 4.17.

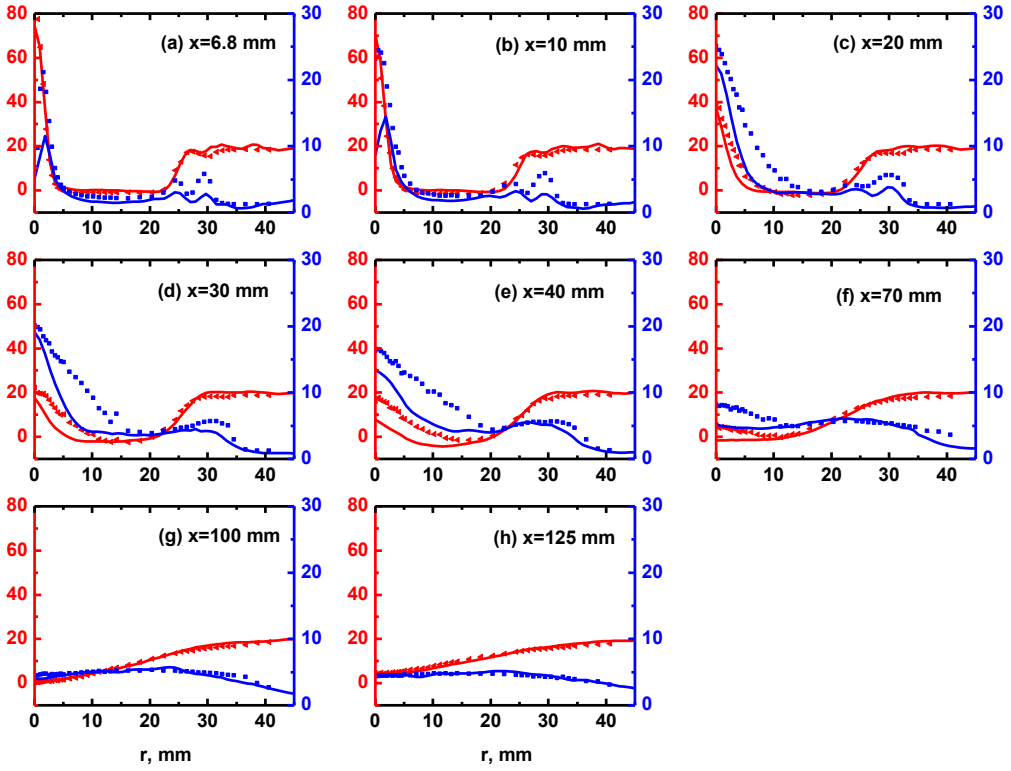

Figure 4.19: Radial profiles of mean (red) and *r.m.s.* (blue) of axial velocity at different streamwise locations from N16S159-ti. Lines: LES; symbols: experiment. The left and right ordinates (units in m/s) are for mean and *r.m.s.*, respectively.

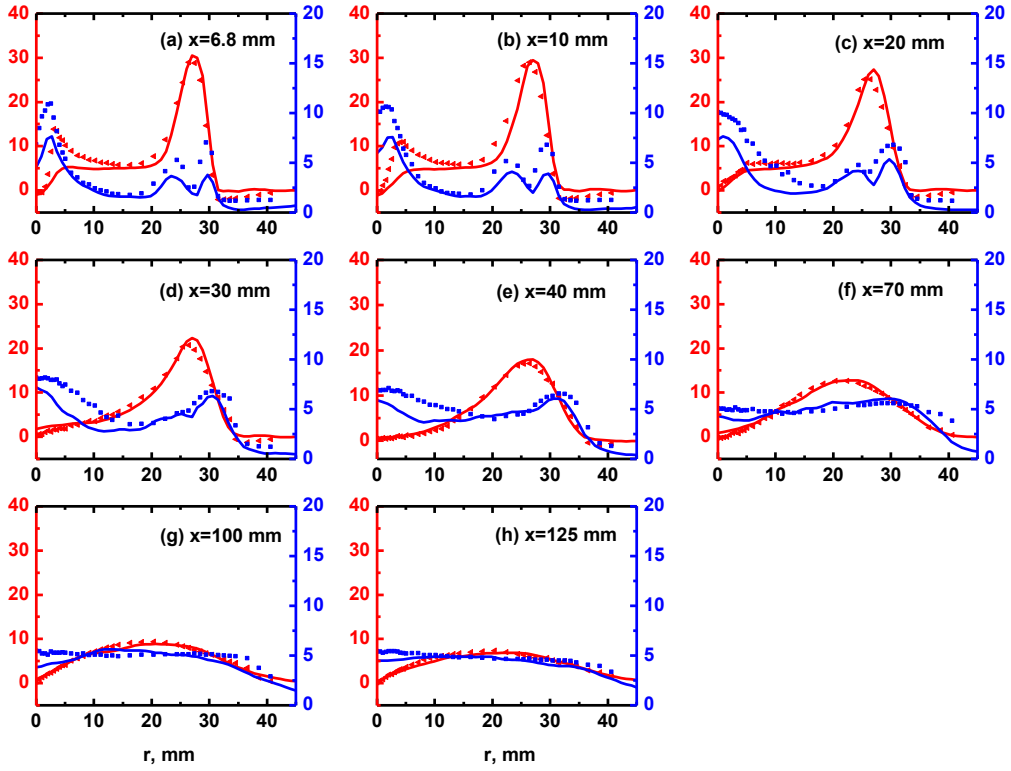

Figure 4.20: Radial profiles of mean (red) and *r.m.s.* (blue) of swirl velocity at different streamwise locations from N16S159-ti. Lines: LES; symbols: experiment. The left and right ordinates (units in m/s) are for mean and *r.m.s.*, respectively.

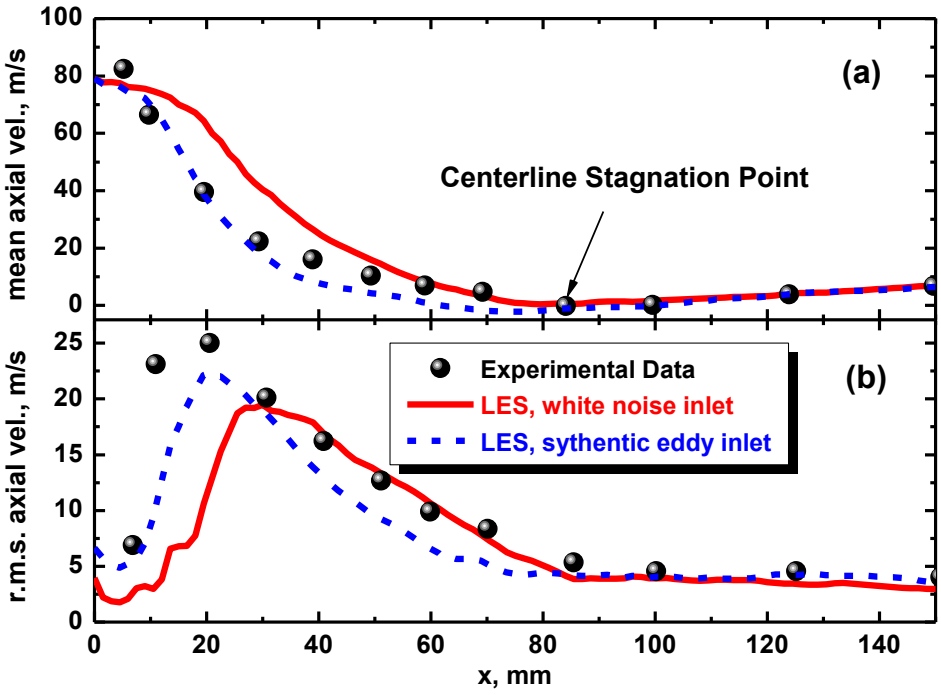

Figure 4.21: Centerline distributions of (a) mean and (b) *r.m.s.* of axial velocity from LES with white noise inlet (N16S159) and synthetic eddy method (N16S159-ti).

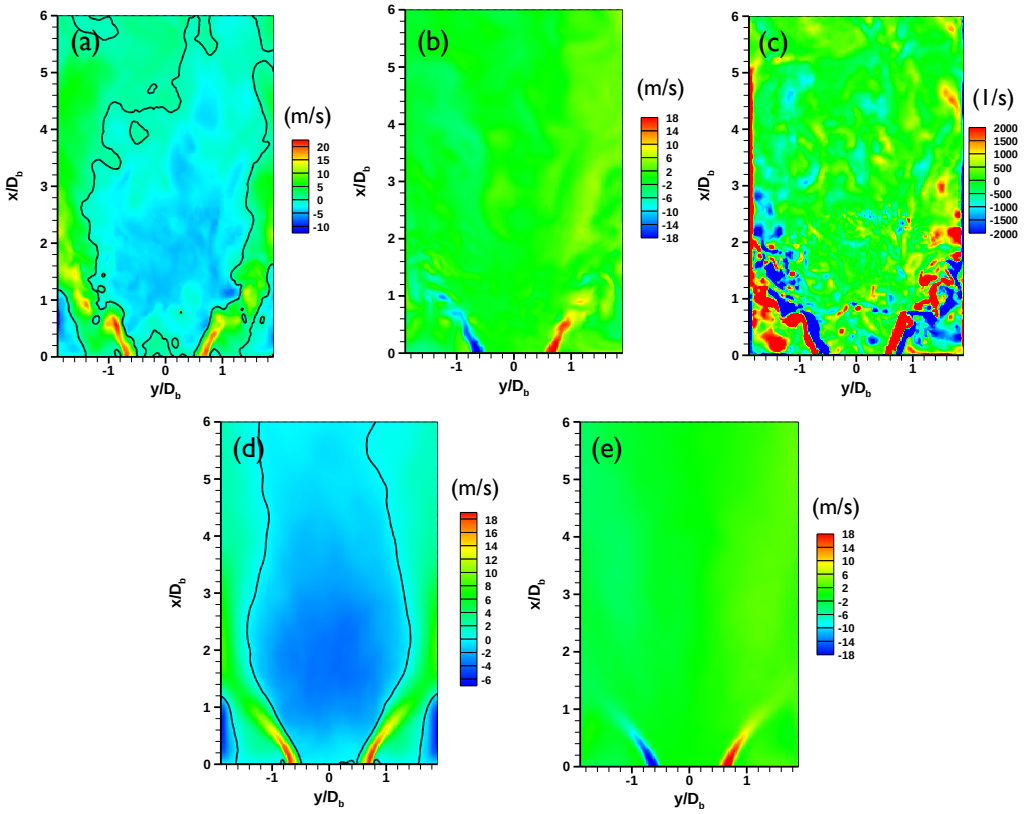

Figure 4.22: Two dimensional distributions ($x-y$ plane) of instantaneous (a) axial velocity, (b) swirl velocity, (c) z-vorticity, time averaged (d) axial velocity and (e) swirl velocity for CSWH1. The solid lines in (a) and (d) denote the zero axial velocity iso-lines.

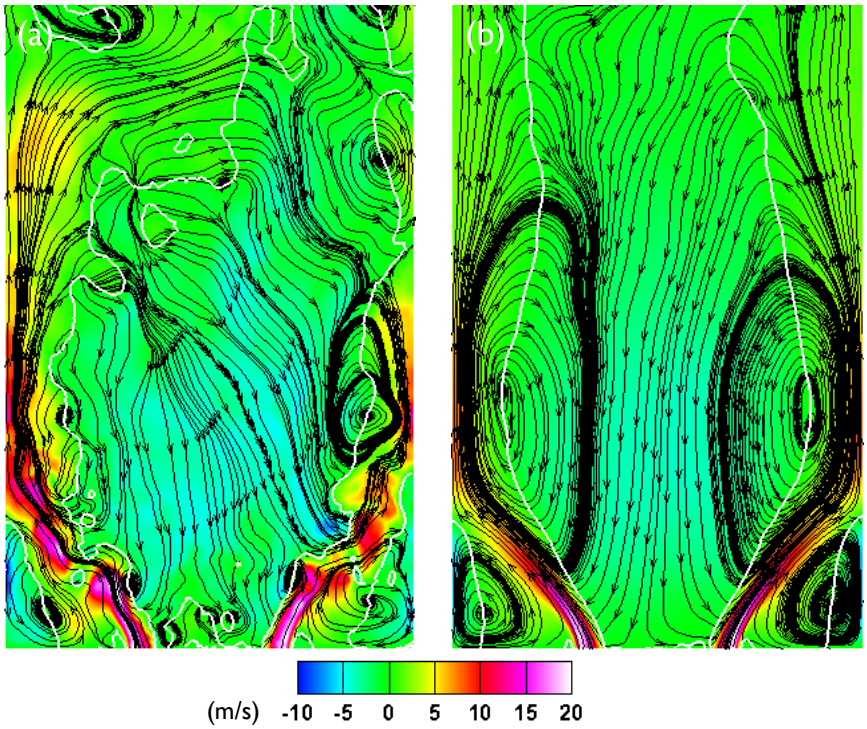

Figure 4.23: Streamlines on the $x-y$ plane based on (a) filtered velocity and (b) time averaged velocity. The image size is 95 mm $\times$ 150 mm. The background contours in (a) and (b) correspond to the filtered and time averaged axial velocities, respectively. White lines denote the zero axial velocity iso-lines.

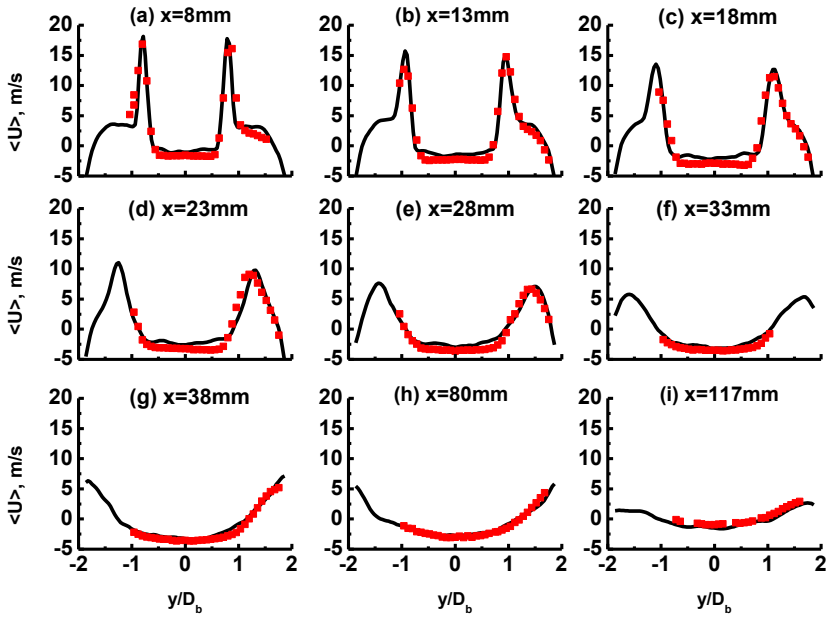

Figure 4.24: Radial profiles of mean axial velocity for different streamwise locations from CSWH1. Solid lines: LES; symbols: measurements [Cavaliere, 2013].

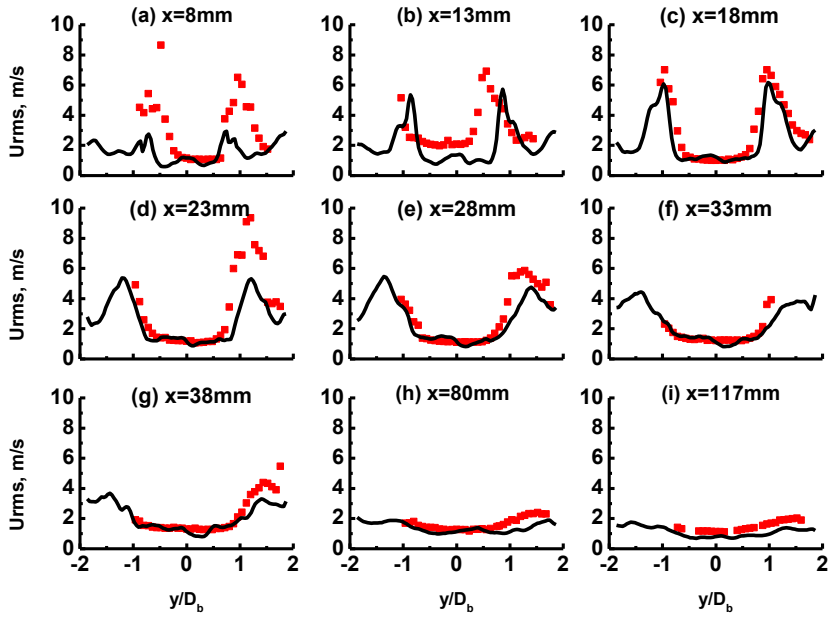

Figure 4.25: Radial profiles of axial velocity *r.m.s.* for different streamwise locations from CSWH1. The legend same as that in Fig. 4.24.

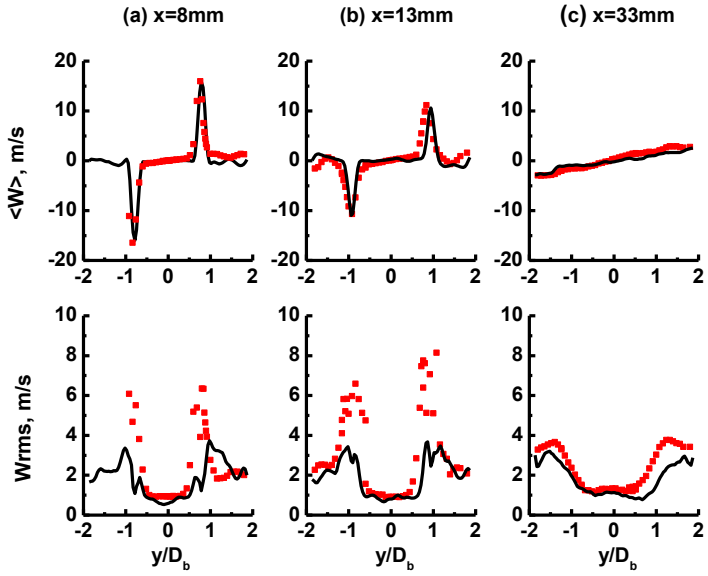

Figure 4.26: Radial profiles of mean (first row) and *r.m.s.* (second row) of swirl velocity for different streamwise locations from CSWH1. The legend same as that in Fig. 4.24.

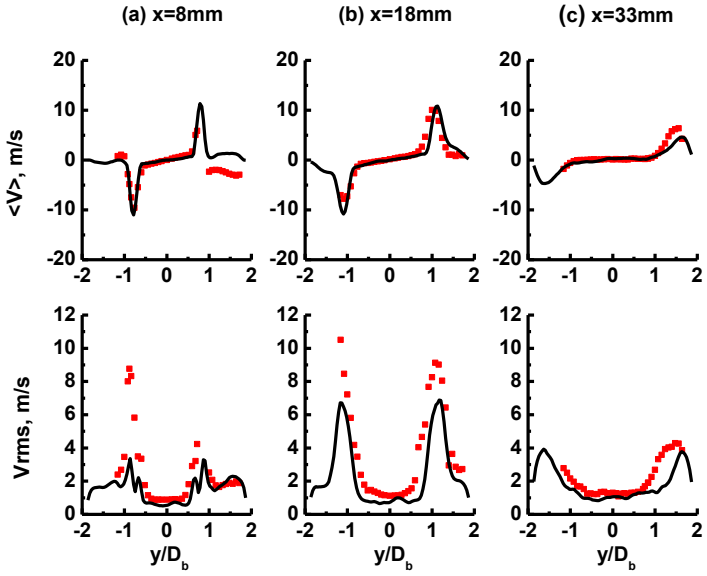

Figure 4.27: Radial profiles of mean (first row) and *r.m.s.* (second row) of radial velocity for different streamwise locations from CSWH1. The legend same as that in Fig. 4.24.

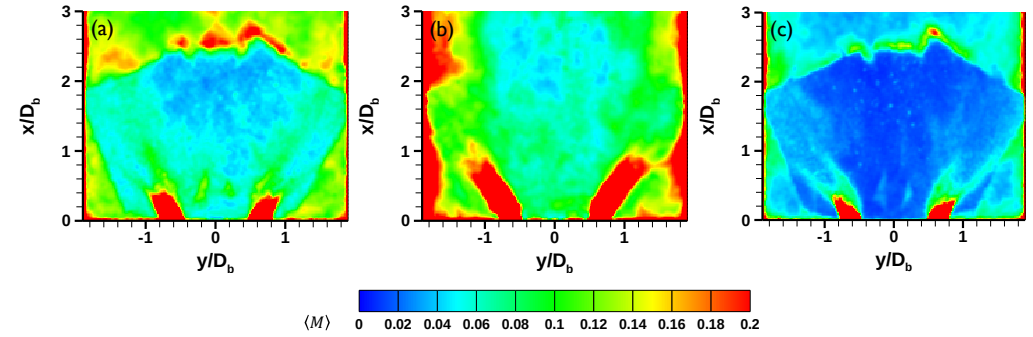

Figure 4.28: Time averaged fractions of residual kinetic energy $\langle M \rangle$ with (a) base (CSWH1), (b) coarse (CSWH1-c) and (c) fine (CSWH1-f) meshes.

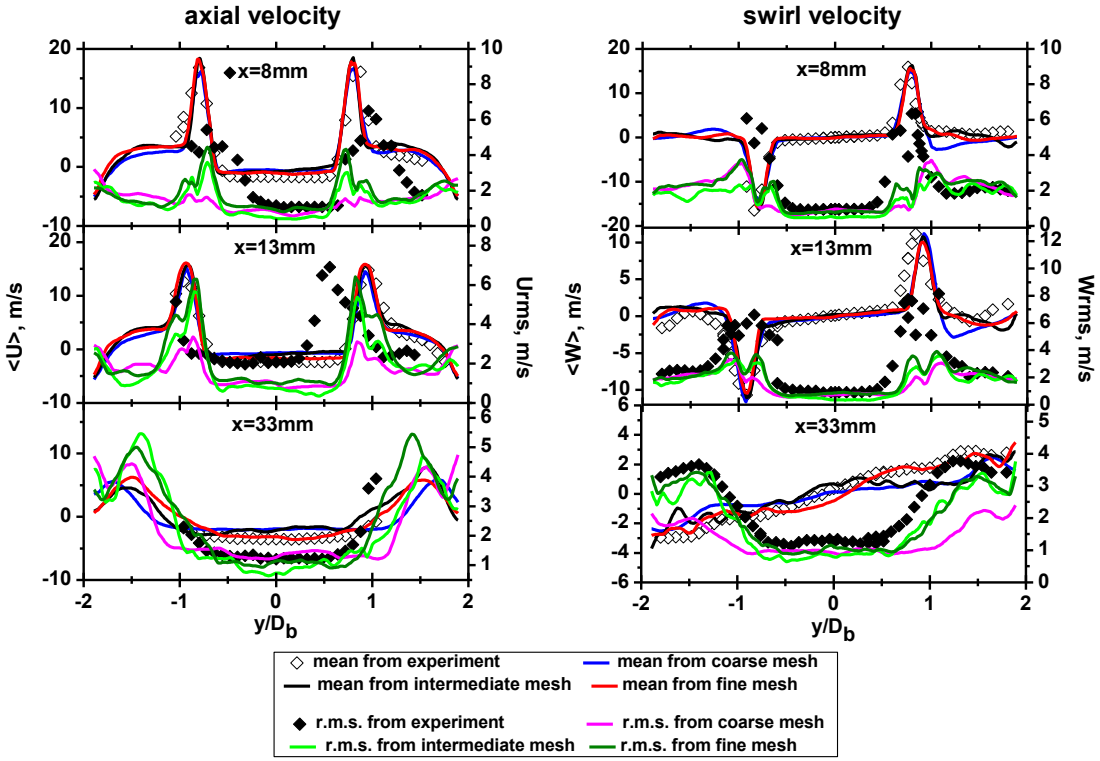

Figure 4.29: Comparisons of statistics of axial (left column) and swirl (right column) velocities from coarse, base and fine meshes.

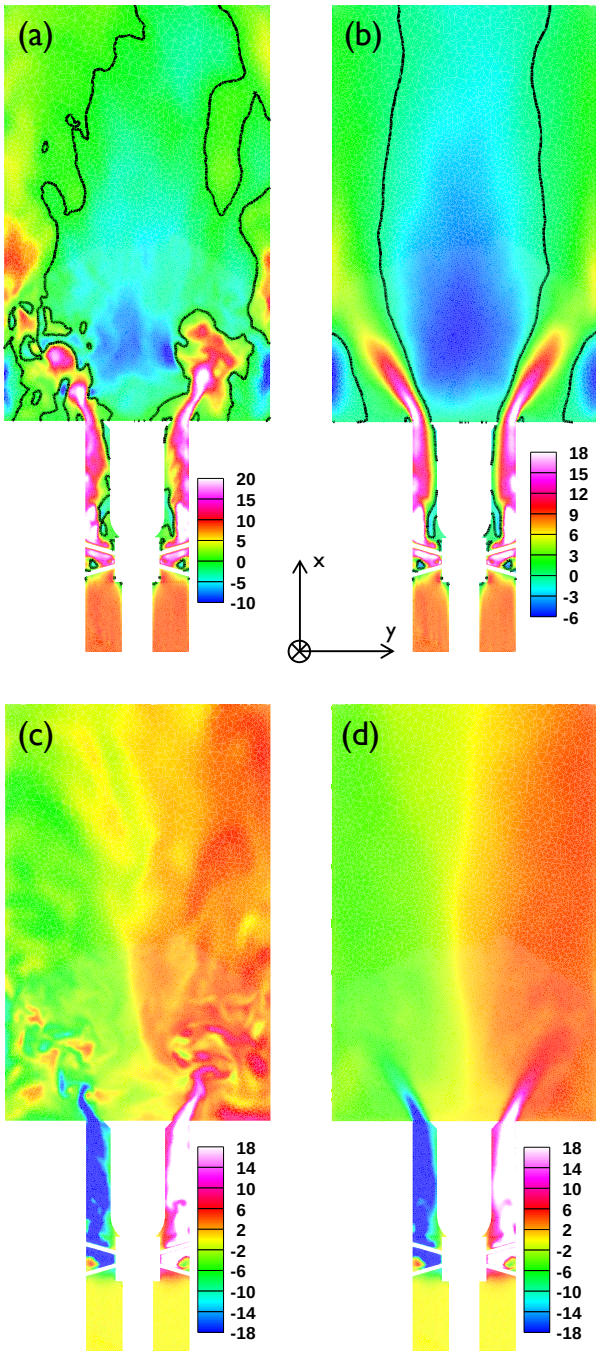

Figure 4.30: Distributions of (a, b) axial and (c, d) swirl velocities (units in m/s) on the $x-y$ plane from CSWH1-fl. Filtered velocity: first column; mean velocity: second column. Solid lines in (a) and (b): zero axial velocity.

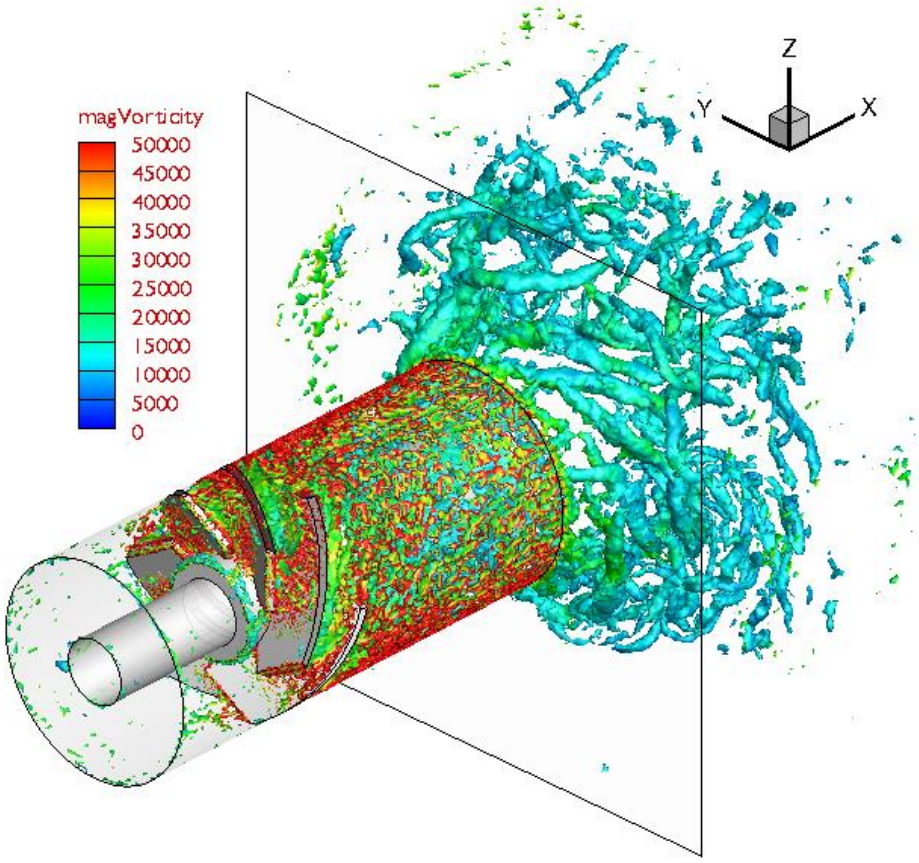

Figure 4.31: Instantaneous iso-surfaces of the second invariant of velocity gradient tensor from CSWH1-fl, $\mathscr{Q} = 1.5 \times 10^7$ 1/s^2, coloured by the magnitude of vorticity (unit in 1/s).

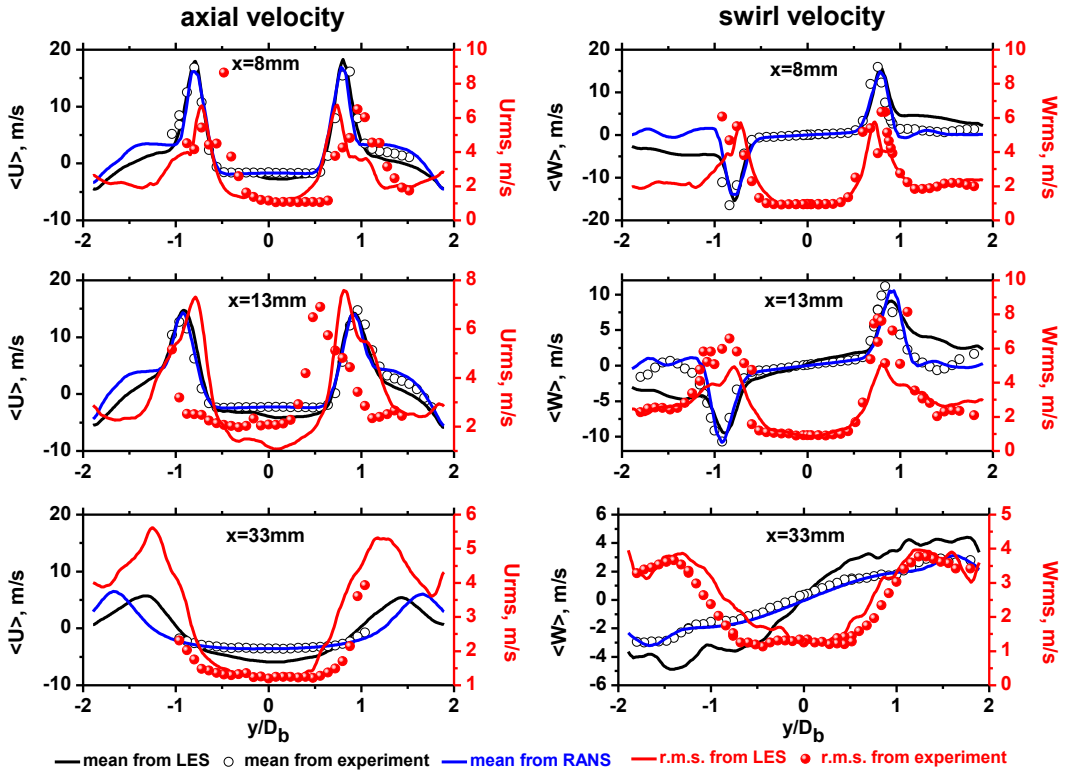

Figure 4.32: Radial profiles of statistics of axial (left column) and swirl (right column) velocities at $x = 8$ mm, 13 mm and 33 mm from CSWH1-fl. Black and red lines: LES; blue lines: RANS; symbols: experiment [Cavaliere, 2013].

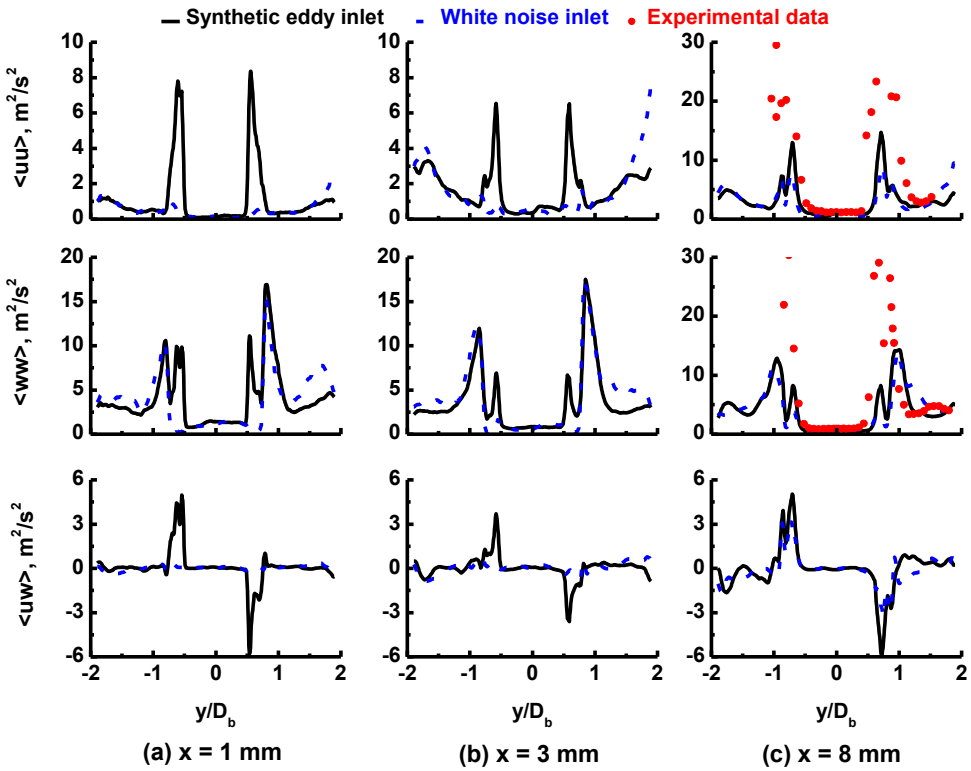

Figure 4.33: Radial profiles of axial and swirl velocity related Reynolds stress from the LES with the synthetic eddy (CSWH1-ti) and white noise (CSWH) inlet conditions at three streamwise locations: (a) $x = 1$ mm (left column), (b) $x = 3$ mm (middle column) and (c) $x = 8$ mm (right column).

Chapter 5

Local Extinction in Sydney Swirl Flames

5.1 Introduction

In terms of turbulent combustion modelling using the sub-grid scale CMC model, the local extinction features in Sandia flame F have been successfully predicted [Garmory and Mastorakos, 2011], using the constant for the sub-grid scalar dissipation rate model calibrated with Sandia flame D. Bearing in mind that the current LES/3D-CMC will be extended to simulation of local and global extinction in swirling turbulent flames, one would be naturally driven to see first if the CMC sub-grid model with its sub-models can accurately predict the extinction in laboratory scale swirl flames with simple geometry and boundary. In light of this motivation, the Sydney swirl flames are the ideal candidates since they still demonstrate the jet flame characteristics but with a cone-shaped RZ enclosing the flame base [Masri et al., 2004]. The RZ leads to the distinctive mixing field and its dissipation behaviors, thereby making the Sydney swirl flames show different stability characteristics compared to the simple and piloted jet flames[Al-Abdeli and Masri, 2003]. The previous LES investigations on the Sydney swirl flames were mainly to validate their combustion models in terms of the velocity fields and compositional structures, such as the work by El-Asrag and Menon [2007], James et al. [2007], Kempf et al. [2008] and Olbricht et al. [2010], and very limited

computational attempts were made to study the extinction characteristics for the swirl flames in this burner.

The objectives of this Chapter are two-fold. First, a detailed comparison between the current LES/3D-CMC and experimental data will be made for a flame case with little localized extinction (i.e. SMA2) in terms of the velocity, mixing and reactive scalar fields, providing the validation for the current implementations for the 3D-CMC model. Second, the extinction characteristics will be studied with increased fuel bulk velocities (i.e. SMA3 and SMA4). This Chapter is structured as follows. The modelling and numerics will be briefly introduced in Section 5.2, and the results and discussion for the three cases will be given in Section 5.3. Section 5.4 presents the conclusions that are made based on the studies in this Chapter.

5.2 Modelling

5.2.1 LES and CMC modelling

The filtered velocity and mixture fraction, $\tilde{\mathbf{U}}$ and $\tilde{\xi}$, are solved and their corresponding LES governing equations have been listed in Chapter 3. The Smagorinsky model and other models adopted have been detailed in Sub-section 3.1.2. The variance of filtered mixture fraction, $\widetilde{\xi''^2}$, is estimated with Eq. (3.23). The filtered scalar dissipation rate $\tilde{N}$ is the sum of the resolve and sub-grid parts ($\tilde{N}_{res}$ and $\tilde{N}_{sgs}$), as presented in Eq. (3.22).

The conditionally filtered mass fractions and total enthalpy, Q_α and Q_h, are solved with the three dimensional CMC governing equations, Eqs. (3.35) and (3.36). The models used for the unclosed terms in the CMC equations are presented in Section 3.2. Particularly, the laminar Schmidt number used in this Chapter is $Sc = 0.7$, while the sub-grid one is $Sc_t = 0.4$ [Pitsch and Steiner, 2000b], which is expected to be reasonable for predicting the scalar behaviors in turbulent jet and jet-like flames.

5.2.2 Numerics

The experimental setup and dimensions of the Sydney swirl burner have been demonstrated in Figs. 4.1 and 4.2 and introduced in Sub-section 4.2.2.1. More information concerning this burner can be found elsewhere [Al-Abdeli and Masri, 2003; Masri et al., 2004]. The flow in this burner is characterized by the external ambient coflow velocity (U_e), the axial annular velocity (U_s), the swirl annular velocity (W_s) and the fuel jet velocity (U_j). The coflow velocity U_e is 20 m/s with around 2% free stream turbulence. The SMA series is selected here and the fuel stream is CNG/air (1:2 by volume) with the temperature of 298 K and the pressure of 1 atm [Masri et al., 2004]. In the simulations, pure methane is used instead of CNG, consistent with the fuel for composition measurements in Sandia National Laboratories, allowed by the negligible influence that exists on the stability features and blow-off limits of the flame in this burner [Masri et al., 2004]. The stoichiometric mixture fraction for SMA is $\xi_{st} = 0.25$.

For the simulations in this Chapter, the LES computational domain is exactly the same as the one for N16S159 shown in Fig. 4.5. The domain starts at the burner exit plane and hence the annulus as well as the fuel pipe are excluded here. The scale for the LES domain is $6D_b \times 3D_b \times 2\pi$ ($D_b = 0.05$ m) in the longitudinal, radial and azimuthal directions, respectively. The origin of the Cartesian coordinate system lies at the center of the fuel jet exit and x is the axial coordinate while y and z the spanwise ones. The computational domain is discretized by approximately 8,400,000 tetrahedral cells illustrated in Fig. 4.6, which are also used for the LES of N16S159 case in Chapter 4. The mesh refinement information can be found in Table 4.3. The boundaries are also explicitly marked in Fig. 4.5. The velocity at the coflow inlet is set to be uniformly 20 m/s, imposed by the white noise of 2% intensity. The axial velocity at the fuel jet as well as both axial and swirl velocities profiles are specified using the one-seventh power law, i.e. Eq. (4.7), based on their individual bulk velocities. The 5% white noises are added to the swirling air inlet, with the above mentioned mean velocity profiles. This choice is based on the speculation that the turbulence immediately downstream of the air inlet is mainly caused by the swirling motion and therefore the inlet turbulence has a comparatively small contribution. The fuel jet exit boundary conditions

should be clarified here. The synthetic eddy method discussed in Chapter 4 is used for fuel jet exit for SMA2. For mean velocity profiles, the one-seventh profiles are applied while for the Reynolds stress components the measurements at $x = 6.8$ mm downstream are employed at the jet exit. For SMA3 and SMA4, there are no measurements for either mean velocities or Reynolds stress tensor at the jet exit or immediate downstream. In light of this, the white noise method is applied for the jet exit in both SMA3 and SMA4 in the LES/3D-CMC computations. Zero radial velocity is given in the current computations for the annulus air inlet. At the side and outflow boundaries, zero gradient conditions for the velocities are assumed. In addition, zero pressure gradient is enforced for all the inlets and the bluff body wall. The mixture fraction is unity at the central fuel jet exit while it is zero for both annulus air inlet and coflow. Its values at the side and outflow boundaries are extrapolated from the neighboring internal fields. The initial fields of the filtered velocity and mixture fraction in LES are obtained from a previous simulation with LES/0D-CMC solver (introduced in Sub-section 3.4.1) in which case a single flamelet solution ($N_0 = 150$ 1/s) is adopted for all the LES cells.

The mixture fraction space (i.e. η-space) for CMC is discretized by 51 nodes, refined around $\xi_{st} = 0.25$. At the boundary of $\eta = 0$, the mass fractions of O_2 and N_2 are 23.3% and 76.7%, respectively, while at $\eta = 1$, those of O_2, N_2 and CH_4 are 18.2%, 59.9% and 21.9%, respectively. The temperatures for both boundaries are 298 K. The total enthalpy in η-space is linear, assuming the adiabaticity of the current SMA flames. The conditional flame structures predicted using a stand-alone 0D-CMC solver (introduced in Sub-section 3.4.1) with the above boundary conditions and intermediate scalar dissipation rate (parameterized by $N_0 = 150$ 1/s) are used for initializing all the individual CMC cells.

The computational domain for CMC in physical space is identical to the one for LES. About 120,000 polyhedral CMC cells are re-generated from LES cells to discretize the domain. The Euler characteristic $\chi^{CMC} = 2$, calculated using Eq. (3.59), holds for each CMC cell, indicating the cell completeness. A schematic of the CMC cells is demonstrated in Fig. 5.1(a). Similar to the LES mesh, the refinement is also made in the zones 1−3, explicitly marked in Fig. 4.6. One should bear in mind that the mesh in Fig. 5.1(a) is merely illustrated for

CMC cell distribution and does not represent the actual one used for solving the CMC governing equations since the reconstructed CMC cells are polyhedral and difficult to visualize. In addition, Fig. 5.1(b) shows the number of LES cell within each CMC cell ϱ^{CMC}, which depends on the ratio of local LES and CMC cell distributions. Within the fuel jet, ϱ^{CMC} is less than 75. It increases to more than 200 in the surrounding of the fuel jet (red region in Fig. 5.1b) due to the coarse CMC cells there. Downstream of the jet (green region), ϱ^{CMC} is relatively uniform, approximately 100. One also needs to specify the boundary conditions (cf. Fig. 4.5) for Q_α and Q_h. Specifically, the inert mixing solutions with the above mentioned boundary conditions at $\eta = 0$ and $\eta = 1$ in η-space are assumed at all the inlets. For the bluff body wall, and lateral and outflow boundaries, zero gradient conditions for Q_α and Q_h are applied.

The LES/3D-CMC solver introduced in Sub-section 3.4.1 is applied for the computations in this Chapter. For the LES solver, second order implicit backward scheme is used for time discretization. The central differencing scheme is used for the diffusion and convection terms in the momentum equation as well as for the diffusion term in the filtered mixture fraction equation. The TVD scheme is adopted for the convection term in the filtered mixture fraction equation, ensuring the boundedness of the mixture fraction. The first order upwind scheme and second order central differencing are used for the conditional convection and diffusion terms. The data coupling between the LES and CMC solvers has been introduced in Sub-section 3.4.3 and will not be repeated here.

5.2.3 Simulated cases

Three cases, i.e. SMA2, SMA3 and SMA4, are selected. The velocity, mixture fraction and compositions were measured by Masri et al. [2004] and Al-Abdeli and Masri [2003] for SMA2 and SMA3. Nevertheless, the SMA4 has no measurements and is proposed particularly for the current LES/3D-CMC to examine the ability of the sub-grid scale CMC model for blow-off predictions. Their detailed information has been tabulated in Table 5.1. The three cases have the same bulk axial and swirl bulk velocities at the annulus air inlet, i.e. $U_s = 16.3$ m/s and $W_s = 25.9$ m/s and hence the same swirl number $S_N = 1.59$, predicted based on

Eq. (4.1). The bulk velocities for the fuel jet are progressively increased from SMA2 to SMA4, i.e. $U_j = 66.3$ m/s, 132.6 m/s and 225 m/s, respectively. Based on the LHV of the fuel, the heat release of the three cases are $\dot{W} = 11.5$ kW, 23.0 kW and 39.0 kW, respectively. The three fuel jet velocities respectively correspond to the 31%, 63% and 104% of the blow-off limit for $U_s = 16.3$ m/s and $W_s = 25.9$ m/s ($U_{BO} = 216$ m/s) measured by Al-Abdeli and Masri [2003]. The reader should be reminded that the experimental blow-off limits are determined when the earliest occurrence of visible flame extinction at the neck or base is observed. Based on the experimental measurements, SMA2 has little local extinction, while SMA3 some extinctions and the flame in SMA4 critically blows off [Masri et al., 2004].

To ensure the CFL numbers (see Eq. 4.3) of all the LES cells are less than unity in LES, the time step for SMA2, SMA3 and SMA4 are 2×10^{-6} s, 1×10^{-6} s and 0.6×10^{-6} s, respectively. The same time steps are used for the CMC solver. All the three simulations are performed on the Cray XC30 clusters of the ARCHER UK National Supercomputing Service. 480 processors (20 nodes) are used for both LES and CMC solvers. 100 time steps needs roughly 1 hour wall time. All the simulations run about 20 flow-through times τ, which is estimated from $\tau = L_\xi/U_j$. Here L_ξ is the centerline location of ξ_{st} and is about 0.12 m based on the measured results for SMA2 and SMA3 [Masri et al., 2004]. As such, their respective flow-through time τ is 0.0018 s and 0.0009 s. The statistics of SMA2 and SMA3 cases are compiled between $10\tau \leq t \leq 20\tau$ so that fields of LES and CMC are fully developed.

5.3 Results and discussion

5.3.1 SMA2 case

5.3.1.1 General flame characteristics

The general flame characteristics of the SMA2 case will be presented first, including contours of filtered and time averaged velocities, mixture fraction, temperature and some selected mass fractions. Figure 5.2 shows the contours of the filtered and mean axial and swirl velocities on the $x-y$ plane. The basic flow

structures for SMA2, including the RZ shape and swirling motion distribution, are qualitatively similar to those for the non-reacting flow case, N16S159, which are demonstrated in Fig. 4.9. Nevertheless, there are some differences between SMA2 and N16S159 cases. First, the length of the fuel jet is increased. Second, the RZ existing immediately downstream of the fuel jet in Fig. 4.9(a) is not pronounced in Fig. 5.2(a). The above two differences can be attributed to the thermal expansion effects from the reactions. Third, the RZ length in N16S159 plotted in Fig. 4.9(d) is less than experimental values, around 0.1 m. However, in the SMA2 results it is accurately captured (roughly 0.1 m as well, fairly close to the experimental results [Al-Abdeli and Masri, 2003]). Fourth, in LES of SMA2, swirling motion immediately around the base of the central jet is strong, quantified by the localized pockets with large swirl velocity demonstrated in Figs. 5.2(c) and 5.2(d). These are not observed in the computational results of N16S159 case. Actually, in the measurements, the highly swirling zones circumambulating the jet base are present in both reacting and non-reacting flows [Al-Abdeli and Masri, 2003]. This and the third points imply that in SMA2 the LES performs better than in N16S159 in terms of predicting the flows near the fuel jet tip and the swirling motion around the fuel jet base.

The filtered and mean mixture fraction contours are demonstrated in Figs. 5.3(a) and 5.3(b). One can clearly see that the mixture fraction fields are similar to those of the jet flame. Compared to the simple jet flame [Meier et al., 2000] or piloted jet flames [Barlow and Frank, 1998], the significant difference is that there is a cylindrical domain (roughly $1.0D_b$ long) enclosing the flame base, with considerable mixture fraction close to ξ_{st}. The recirculating flows after the bluff body surface leads to the strong mixing. The resolved scalar dissipation rate and its mean are presented in Figs. 5.3(c) and 5.3(d). For clarity, $\log_{10}N_{res}$ is visualized, rather than N_{res}. The scalar dissipation is high along the ξ_{st} iso-lines for $x \leq 0.7D_b$ due to the shearing between the injected jet and the RZ fluid. In the downstream region within the ξ_{st} iso-lines, say $0.7D_b < x < 1.5D_b$, the layer-like scalar dissipation structures become short and inhomogeneous. Beyond $x = 1.5D_b$, the scalar gradients dissipate mainly along the ξ_{st} iso-lines and N_{res} is reduced compared to the upstream counterparts. The scalar dissipation rates beyond the ξ_{st} iso-lines and in the cylindrical domain are weaker than those along

the ξ_{st} iso-lines, and their structures are not continuous.

The contours of filtered temperature $\tilde{T}$, heat release rate $\tilde{\dot{q}}$ and mass fractions of selected species $\tilde{Y}_\alpha$ for SMA2 are shown in Fig. 5.4. The instantaneous heat release rate $\tilde{\dot{q}}$ is calculated from

$$\tilde{\dot{q}} = \int_0^1 \widetilde{\dot{q}|\eta} \tilde{P}(\eta)\, d\eta, \tag{5.1}$$

where $\widetilde{\dot{q}|\eta} = \sum_{\alpha=1}^{n} w_\alpha h_\alpha \widetilde{W_\alpha|\eta}$ and w_α and h_α are the molecular weight and specific enthalpy of the α-th species, respectively. From Fig. 5.4(a), one can observe that high $\tilde{T}$ results in a hot RZ which is expected to stabilize the flame. Another section with high $\tilde{T}$ is at the downstream of the ξ_{st} iso-lines, i.e. $x \geq 1.5D_b$, where the scalar dissipation rate is comparatively small based on Fig. 5.3(c). For the middle section ($0.7D_b < x < 1.5D_b$), $\tilde{T}$ is lower, accompanied by higher N_{res}. These features on the reactivity of different flame sections can also be confirmed by $\tilde{\dot{q}}$ and $\tilde{Y}_{OH}$ in Figs. 5.4(b) and 5.4(c). Strong heat release rate and low OH mass fraction can be seen for $0.7D_b < x < 1.5D_b$. In addition, the OH concentration is large in the upstream of RZ. Figures 5.4(d)−5.4(f) show the contours of $\tilde{Y}_{CH4}$, $\tilde{Y}_{H2}$ and $\tilde{Y}_{CH2O}$, respectively. The radicals, H_2 and CH_2O, are basically confined within the ξ_{st} iso-lines. The peak H_2 concentration is found at the downstream section of flame while that of CH_2O occurs in the middle. Weak CH_2O concentration and heat release rate near the shear layer between RZ and swirling air streams in Figs. 5.4(b) and 5.4(f) may be caused by their different responses to the local finite scalar dissipation rate as presented in Fig. 5.3(d). The mass fractions of CO and NO, as the major pollutants from this gaseous flame, are demonstrated in Figs. 5.4(g) and 5.4(h), respectively. The considerable CO is emitted from the downstream while for NO its formation is mainly concentrated in both upstream and downstream of the flame, loosely consistent with high $\tilde{T}$ regions. Based on the results shown in Fig. 5.4, very little localized extinction is observable and this is also the case for the other instants for SMA2. This is in line with the experimental observations made by Masri et al. [2004].

5.3.1.2 Velocity and mixing fields

The comparison of axial velocity statistics between the results from LES/3D-CMC and the experimental data are made in Fig. 5.5. The mean axial velocity $\langle \tilde{U} \rangle$ is correctly predicted for all the presented streamwise locations. The least satisfactory location is $x/D_b = 1.0$, where $\langle \tilde{U} \rangle$ is slightly over-predicted for $r/D_b \leq 0.5$. The fuel jet penetration is examined in Fig. 5.5(h) through the centerline decay of mean axial velocity. The computational results have stronger mean axial velocity for $0.5 < x/D_b < 1.75$, e.g. around 25% higher for $x/D_b = 1.0$. Overall, the accuracy for the mean axial velocity is satisfactory. Some differences in the axial velocity *r.m.s.* between the computational and experimental results exist. At $x/D_b = 0.4-1.4$, the LES under-predicts the *r.m.s.* close to the fuel jet, but the qualitative tendencies of individual *r.m.s.* radial profiles are captured. It is worth noting that the axial velocity *r.m.s.* at $x/D_b = 0.136$ and 0.2 is predicted fairly well, which may be attributed to the spatially and temporally correlated inlet turbulence constructed with the synthetic eddy method for the SMA2 case.

The statistics of swirl velocity at the same locations are shown in Fig. 5.6 and are compared with the measured data. In the current computations, the strong rotation immediately around the central fuel jet is under-predicted, except at the most upstream location $x/D_b = 0.136$ in Fig. 5.6(a). A similar situation also occurs in Fig. 4.20 for the non-reacting case N16S159. The swirl velocity *r.m.s.* is well reproduced in the LES as presented in Fig. 5.6 and, particularly at the upstream locations, the swirl velocity *r.m.s.* in the jet shows a good agreement with the experimental data.

Figures 5.7(a)−5.7(f) show radial profiles of mixture fraction mean and *r.m.s.* for SMA2, while Fig. 5.7(g) shows the centerline decay of the mean. Both mean and *r.m.s.* of mixture fraction demonstrate excellent agreement with the measured data for all the shown longitudinal locations and also along the centerline. The only discrepancy that needs to be pointed out is that $\langle \tilde{\xi} \rangle$ is lower than the experimental data for $0.1 < |r|/D_b < 0.4$ at the upstream locations, i.e. $x/D_b = 0.2$ and 0.4 in Figs. 5.7(a) and 5.7(b). The RZ in the experiment at these locations is mixed with mean mixture fraction merely slightly less then $\xi_{st} = 0.25$, while the LES gives lower mean mixture fraction of about 0.2. In addition, based on

Fig. 5.7(g), the flame length along the centerline (i.e. the stoichiometric mixture fraction position) is around 0.125 m from the LES which is close to the measured one, 0.12 m [Masri et al., 2004]. In the current LES of SMA2, the fact that the mixture fraction can still achieve satisfactory mean and *r.m.s.* even if those of the velocity field are not very accurately predicted implies that the contribution from the sub-grid scale turbulence towards the mixing of conserved scalar may be small and the latter is expected to be affected dominantly by the large scale vortical structures resolved by LES.

The radial profiles of mean and *r.m.s.* of the resolved scalar dissipation rate $\tilde{N}_{res}$, which is calculated as $D\nabla\tilde{\xi}\cdot\nabla\tilde{\xi}$ shown in Eq. (3.22), are demonstrated in Fig. 5.8. The corresponding experimental data are not available. From Fig. 5.8(a), one can see that the mean of the resolved scalar dissipation rate is very narrow at $x/D_b = 0.2$ and the peak value location spatially coincides with the shear layer of the fuel jet where the strong turbulence is expected to intensify the gradient of the conserved scalar. Further downstream, say $x/D_b = 0.4$ and 0.6, the peaks still exist but their values are greatly relaxed. This behavior is very similar to the scalar dissipation features in the piloted turbulent jet flames, e.g. Sandia flames C, D and E [Barlow and Karpetis, 2004]. Beyond $x/D_b = 1.0$, the spikiness of mean scalar dissipation rate distributions cannot be observed and the mean is small (below 20 1/s) and relatively uniform within the entire radii. This is completely different from the above mentioned Sandia flame series, in which case the spikiness still exists at $x/D_j = 30$ ($D_j = 0.0072$ m for the piloted flame burner, the corresponding normalized locations here is $x/D_b = 4.32$). In fact, the distinctive distributions of the mean of $\tilde{N}_{res}$ can be found as well in Fig. 5.3(d), with the $x/D_b = 1.0$ being the rough demarcation. This may be affected by the local recirculation zone (shown in Fig. 5.2b), which enhances the mixing there. The profiles of the *r.m.s.* in Fig. 5.8(b) vary qualitatively following those of the respective means. At the upstream locations, e.g. $x/D_b = 0.4$, 0.6 and 1.0, the *r.m.s.* is strong and even larger than their means, whilst it is greatly reduced for $x/D_b \geq 1.0$.

5.3.1.3 Scalar fields in physical space

Figure 5.9 presents the radial distributions of the temperature statistics at eight locations and a comparison with the experimental data is made. The measured temperature *r.m.s.* is only available at $x/D_b = 0.4$, 0.6, 1.0 and 2.0. The mean temperature field is correctly predicted in the LES, including the peak value magnitudes and their locations. Nevertheless, in the upstream region of the RZ (e.g. $x/D_b = 0.4$ and 0.6), the mean temperature is slightly lower than the experimental data. The *r.m.s.* at both $x/D_b = 0.4$ and 0.6 is over-predicted, but generally results of both the temperature fluctuations and the locations are satisfactory based on Fig. 5.9.

The radial profiles of mean mass fractions of selected species (CH_4, OH, H_2, CO and NO) at $x/D_b = 0.4$, 0.6, 1.0 and 1.4 are demonstrated in Figs. 5.10 and 5.11. The mean CH_4 mass fractions agree with the experimental data very well at the upstream two locations, but are under-predicted to a small extent at $x/D_b = 1.0$ and 1.4. The noticeable differences can be seen for the mean OH and H_2 mass fractions at $x/D_b = 0.4$ and 0.6. In the simulation, considerable OH is produced immediately around the fuel jet while it is gradually decreased to zero near the jet based on the experimental data. However, for the mean H_2 mass fraction at $x/D_b = 0.4$ and 0.6, the under-prediction occurs in most of the RZ but the values just around the jet is correctly captured. In fact, the mean and *r.m.s.* of the mixture fraction at these two locations have good agreements with the measured data, which has already been shown in Figs. 5.7(b) and 5.7(c). These discrepancies presumably result from the errors of their conditional mass fractions Q_α, affected by the local scalar dissipation rates in both physical and mixture fraction space. In addition, individual species have the different responses to the variations of the dissipation in the mixture fraction space and therefore even for the same local mixing state, their differences compared to the experimental data could have different magnitudes. Both CH_4 and H_2 mean mass fractions are reasonably reproduced at the downstream locations, $x/D_b = 1.0$ and 1.4.

The mean mass fractions of CO and NO are shown in Fig. 5.11 at the same four streamwise locations. In the LES, CO mean mass fractions at $x/D_b = 0.4$ and 0.6 are greater than the counterparts from the experiments and are improved

at the downstream two locations in Figs. 5.11(c) and 5.11(d). Conversely, the peak values of NO at $x/D_b = 0.4$ and 0.6 are roughly 20% lower than the measured results but their profiles over the entire radii are reasonably obtained. The differences of both CO and NO at the upstream locations may affect or be affected by the temperature. Specifically, the higher CO accumulation means that less CO oxidization to CO_2 can proceed and hence lower temperature (shown in Fig. 5.9) since this conversion releases considerable heat [Law, 2006]. In addition, since the temperature is high in the upstream of RZ (shown in Fig. 5.2a), the formation of NO may be dominated by the thermal mechanism and therefore local temperature differences can lead to the errors in the NO predictions.

5.3.1.4 Scalar fields in mixture fraction space

In Figs. 5.12–5.15, comparisons of mean conditional temperature and species mass fractions in mixture fraction space from the computational and measured results are made. Note that the experimental data of conditional NO mass fractions are not available. They respectively correspond to four axial locations, i.e. $x/D_b = 0.4, 1.0, 1.4$ and 2.0. The means from the computations are calculated with both time and space averaging. For the latter, the conditional quantities, Q_α and Q_T, in the CMC cells with the radii being $|r|/D_b \leq 0.5$ (which is consistent with the measured range [Masri et al., 2004]) and the specific axial locations are averaged to obtain the space averaged Q_α and Q_T. The number of the extracted CMC cell corresponding to the above four axial locations is roughly 300, which helps the statistical convergence.

Plotted in Fig. 5.12 are the mean conditional temperature and mass fractions at $x/D_b = 0.4$. The mean conditional temperature and the product (CO_2 and H_2O) mass fractions in the LES are lower, whilst O_2, OH and CO mass fractions are over-predicted. This implies that the instantaneous extinctions at $x/D_b = 0.4$ may be over-predicted. However, conditional CH_4 mass fraction shows good agreement with the measured data. Further downstream at $x/D_b = 1.0$ in Fig. 5.13, the mean conditional temperature and the mass fractions are correctly predicted, except that of OH. The mean conditional OH mass fraction is greatly over-predicted (about 100% higher in the peak) in the current LES. The above

mentioned differences between the computational and experimental results also apply to the the comparisons at $x/D_b = 1.4$ and 2.0 demonstrated in Figs. 5.14 and 5.15. The over-prediction of conditional OH mass fraction also exists in the LES/3D-CMC of Sandia flame F by Garmory and Mastorakos [2011] where it was attributed to the occurrence frequency of intermediate OH mass fraction in mixture fraction space, a transient between fully reactively state to inert one, and its sustainability under some critical scalar dissipation rates and turbulence fields. Essentially this is related to the response to the variations of conditional scalar dissipation or the transport between the neighboring CMC cells. Also, the nonlinearity of reactants and major products (e.g. CH_4, O_2, CO_2 and H_2O) for $\eta > \xi_{st}$ may be caused by the flow transport between neighboring CMC cells in physical space.

In addition, based on the results in Figs. 5.12−5.15, the mean flame structures at all the four axial locations are basically in the fully burning state and the turbulence−chemistry effects are not outstanding for SMA2. In fact, in the computations the conditional reactive scalars at the above mentioned streamwise locations (results not presented here) demonstrate very little instantaneous localized extinction in mixture fraction space and Q_α as well as Q_T have small fluctuations around the burning solutions. These observations are in line with the measured mass fractions versus mixture fraction for SMA2 [Masri et al., 2004].

5.3.2 SMA3 and SMA4 cases

5.3.2.1 Velocity and scalar fields for SMA3

Similar to what is analyzed for SMA2, the velocity, mixture fraction and reactive scalars in both physical and mixture fraction space from SMA3 will be compared with the measurements [Al-Abdeli and Masri, 2003; Masri et al., 2004] in Figs. 5.16−5.26.

The axial velocity statistics at different streamwise locations are shown in Fig. 5.16. The mean axial velocities close to the centerline are over-predicted, although the experimental data at the fuel jet are not available at $x/D_b = 0.104, 0.2, 0.6$ and 1.0. The *r.m.s.* in the RZ ($0.17 \leq r/D_b \leq 0.5$) are lower than the measured results, which is particularly obvious at $x/D_b = 0.6, 1.0, 1.4$ and 2.0. The discrep-

ancies for the $r.m.s.$ are more pronounced than those for SMA2, shown in Fig. 5.5. The mean swirl velocities at the shown axial locations in Fig. 5.17 are correctly predicted, except for the rotation around the central fuel jet at $x/D_b = 0.4$ and 0.6, which is also the situation for the SMA2 results in Fig. 5.6. The swirl velocity $r.m.s.$ in the central fuel jet is slightly higher than the experimental data at $x/D_b = 0.6, 1.0$ and 1.4.

Different from the mixture fraction statistics for SMA2 in Fig. 5.7, the corresponding results for SMA3 in the upstream part of the RZ ($x/D_b = 0.2, 0.4$ and 0.6) are under-predicted, as shown in Fig. 5.18. This directly leads to the fact that the upstream spreading of the mean mixture fraction field is radially smaller. At the downstream locations of $x/D_b = 0.2, 0.4$ and 0.6, both mean and $r.m.s.$ are greatly improved. Based on the results in Fig. 5.18(g), the centerline distributions of mean mixture fraction agree with the experimental data very well, except the slight over-prediction between $x/D_b = 0.3$ and 0.6.

Additional comments are made here about the mixture fraction statistics. In fact, the results for SMA2 in Fig. 5.7 are excellent, for all the upstream and downstream locations. The different performances in SMA2 and SMA3 may be attributed to the turbulent inlet boundary conditions for the central fuel jet exit, i.e. synthetic eddy method. For SMA2, the measured Reynolds stress components (i.e. at $x = 6.8$ mm) are provided for the fuel jet. However, for SMA3, the measurements in the upstream fuel jet were not made and therefore white noise method with 5% intensity is applied. The inaccurate inlet turbulence may be directly responsible for the turbulence near the jet exit, around 5 to 10 times jet diameter [Lund et al., 1998]. Another cause may be the mesh resolution $5-10D_j$ downstream of the jet exit. The same LES meshes are used for SMA2 and SMA3, but U_j for SMA3 is twice higher than that for SMA2. As such, it is likely that in SMA3, the turbulence in the upstream shear layer between the fuel jet and RZ is not well resolved. Therefore, accurately predicting the turbulence in the upstream of the jet is important to obtain the mixture fraction field in the upstream part of the RZ.

Plotted in Figs. 5.19−5.22 are the mean reactive scalar fields, including the temperature and selected species mass fractions, at $x/D_b = 0.2, 0.3$ and 0.6. There are differences with the experimental results, due to the under-prediction

of the mixture fraction fields there. They are reasonably computed at the shown downstream locations, i.e. $x/D_b = 1.0, 1.4$ and 2.0.

The mean conditional reactive scalars at $x/D_b = 0.4, 1.0, 1.4$ and 2.0 are shown in Figs. 5.23−5.26. At $x/D_b = 0.4$, the mean flame structures from the computations have greater finite-rate chemistry effect than the experimental results. For instance, fuel leakage occurs at $\xi_{st} = 0.25$ and higher O_2 mass fraction appears there. But the mean OH and H_2O conditional mass fraction and temperature agree with the experimental profiles very well. At $x/D_b = 1.0, 1.4$ and 2.0, the mean conditional flame structures are reasonably reproduced by the LES/3D-CMC. Comparisons of mean conditional flame structures for SMA2 and SMA3 in Figs. 5.12−5.15 and 5.23−5.26 also indicate that the present LES/3D-CMC has the ability to capture the flame structure evolutions under different jet bulk velocities.

5.3.2.2 Extinction features in SMA3 and SMA4

Figure 5.27 shows three dimensional iso-surfaces of stoichiometric mixture fraction coloured by instantaneous OH mass fraction from SMA2, SMA3 and SMA4 cases. First, the longitudinal distances in SMA2 and SMA3 are correctly computed, i.e. around 0.125 m. This has also been shown in the centerline profiles of mean mixture fraction in Figs. 5.7 and 5.18. Second, comparing the ξ_{st} iso-surfaces, one can clearly find that the flame shape in SMA2 ($U_j = 66.3$ m/s) is more broad radially than SMA3 ($U_j = 132.6$ m/s). This may be caused by the stronger mixing in the RZ of SMA3. The differences of flame shape between SMA3 and SMA4 are not obvious. Third, in SMA2, very little local extinction can be found in Fig. 5.27(a). However, with increased U_j in SMA3, more extinction regions (in blue) can be seen on the ξ_{st} iso-surfaces, particularly at the flame base near the jet exit and also some pockets between $x = 0.06$ m and 0.1 m, illustrated in Fig. 5.27(b). In SMA4, the local extinction degree is more severe and the quenched fractions on the iso-surfaces expand downstream.

The two dimensional contour ($x-y$ plane) of instantaneous OH mass fraction $\tilde{Y}_{OH}$ from SMA3 is shown in Fig. 5.28(a). For $x \geq 0.5D_b$, $\tilde{Y}_{OH}$ is high along most of the iso-lines of instantaneous stoichiometric mixture fraction. Numbers 1−4

marked in Fig. 5.28(a) correspond to the regions along the ξ_{st} iso-lines with low $\tilde{Y}_{OH}$. Low $\tilde{Y}_{OH}$ in Region 1 has also been demonstrated in the results from Fig. 5.27(b). The distribution of resolved dissipation rate plotted in logarithmic scale is presented in Fig. 5.28(b). One can see that at $0 \leq x/D_b \leq 0.5$, the $\tilde{N}_{res}$ along the ξ_{st} iso-lines is high, which is directly responsible for the extinguishment in Region 1, shown in Fig. 5.28(a). However, for $0.5 \leq x/D_b \leq 1.25$, the structures of scalar dissipation become more anisotropic than those at $0 \leq x/D_b \leq 0.5$. Figures 5.28(c)−5.28(f) shows the contours of instantaneous temperature, heat release rate, temperature and scalar dissipation rate for Region 3, which is marked with dashed lines in Fig. 5.28(a). Based on Fig. 5.28(c), one can see that for the right branch of ξ_{st} iso-lines basically no $\tilde{Y}_{OH}$ can be observed, whereas for the left one, $\tilde{Y}_{OH}$ is high, close to a value representing a fully burnt state. For the left branch, very limited heat is released. Instead, at the regions close to or along the right ξ_{st} iso-line branch, the heat release is relatively high. If Fig. 2.1 is re-visited, one can explicitly see that the combustion along the right and left branches in Fig. 5.28(d) respectively is close to the two limiting cases in non-premixed flames, i.e. chemically frozen (small Da) and fully burning (large Da) situations. This can be confirmed by the distributions of instantaneous temperature and scalar dissipation, shown in Figs. 5.28(e) and 5.28(f). In particular, the right branch with low OH is experiencing the strong scalar dissipation, indicating a small Da, while for the left one, $\tilde{N}_{res}$ is almost zero with a large Da.

The time evolutions of instantaneous OH mass fraction $\tilde{Y}_{OH}$ with the ξ_{st} iso-lines are presented in Fig. 5.29, covering about 0.0105 s long since the initial field. At $t = 0$ s, the extinction along the ξ_{st} iso-lines mainly occurs for $x/D_b \leq 0.7$. Beyond that, very little extinction exists. At $t = 0.0015$ s and $t = 0.003$ s, more downstream fractions of the ξ_{st} iso-lines experience the extinguishment. Meanwhile, the length of the iso-lines slightly shrinks longitudinally. The local extinction reaches the strongest degree over the entire iso-lines at $t = 0.0075$ s for all the shown shapshots. However, at $t = 0.009$ s and $t = 0.0105$ s, most of the stoichiometric mixture fraction iso-lines are re-ignited. Since the OH* or OH-PLIF measurements were not made by the investigators in University of Sydney, comparisons concerning the dynamics of blow-off or flames approaching blow-off limits cannot be conducted.

5.4 Conclusions

Large eddy simulations with the sub-grid scale CMC combustion model discretized by finite volume method are applied to simulate three Sydney swirling flames (i.e. SMA2, SMA3 and SMA4) with fixed swirl number but gradually increased central fuel bulk velocity.

The detailed comparisons are made with SMA2 measurements in terms of the statistics of axial and swirl velocities as well as mixture fraction. The temperature and mass fractions of selected species in both physical and mixture fraction space are also compared with the Raman−Rayleigh−LIF data. The above comparisons for SMA2 demonstrate excellent agreement, thereby providing the validations for the implementations of LES/3D-CMC detailed in Chapter 3. The flow, mixing and scalar fields are not well predicted for the upstream part of the RZ ($x \leq 0.6D_b$) in SMA3, which may be related to the inaccurate specification of turbulence boundary conditions, first order CMC model and the applied submodels.

Extinction trend from the computations qualitatively agrees with the experimental observations, i.e. increased localized extinction from SMA2 to SMA4. In the measurements, base blow-off mode was observed for the SMA flame series, and the current LES/3D-CMC modelling correctly predicts this mode.

5.5 Tables for Chapter 5

Table 5.1: Information of simulated cases: SMA2, SMA3 and SMA4

Cases	U_s (m/s)	W_s (m/s)	U_j (m/s)	U_j/U_{BO}[1]	$\dot{W}$[2](kW)	Re_s[3]	Re_j[4]
SMA2	16.3	25.9	66.3	31%	11.5	32400	15400
SMA3	16.3	25.9	132.6	62%	23.0	32400	30800
SMA4	16.3	25.9	225.0	104%	39.0	32400	52300

[1] The blow-off limit of central fuel jet, U_{BO}, measured by Al-Abdeli and Masri [2003] for $U_s = 16.3$ m/s and $W_s = 25.9$ m/s (or equivalently $S_N = 1.59$) is 216 m/s.

[2] The heat release $\dot{W}$ is estimated for stoichiometric combustion based on the LHV of CNG/air (1:2 by volume), which is approximately 16672 kJ/kg [Al-Abdeli and Masri, 2003].

[3] The Reynolds number for the swirling air, Re_s, is predicted based on the radius of the burner annulus (0.03 m) and the primary (bulk) axial velocity U_s.

[4] The Reynolds number for the central fuel jet, Re_j, is predicted based the diameter of the jet exit (0.0036 m) and the bulk jet velocity U_j.

5.6 Figures for Chapter 5

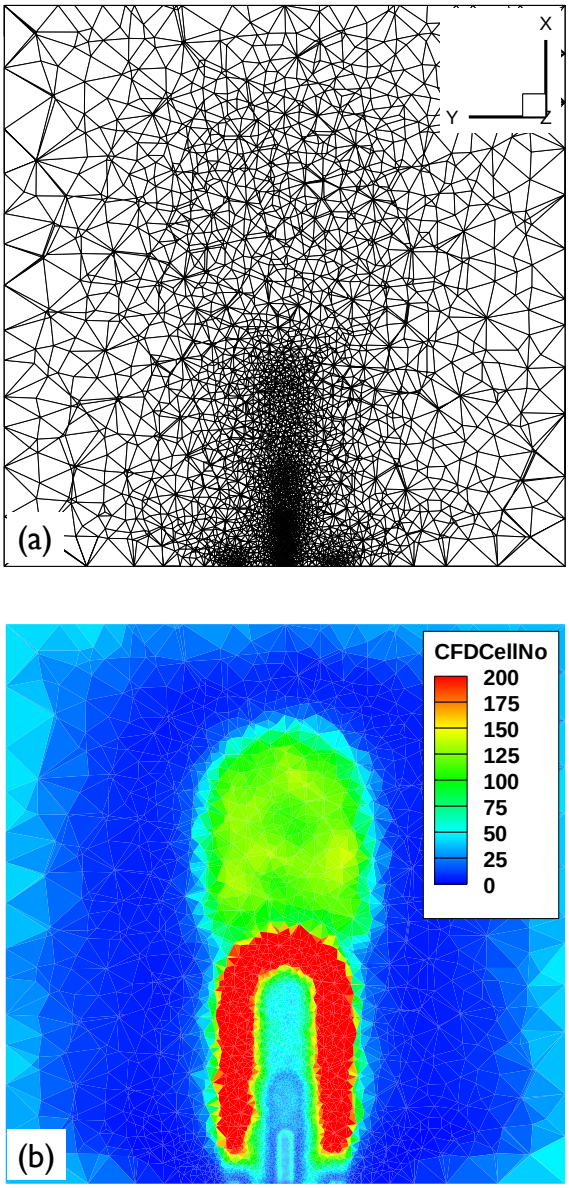

Figure 5.1: (a) Schematic of the CMC mesh distribution on the $x-y$ slice, and (b) contour of the LES cell number in each CMC cell. Note that the cells and their topology in (a) do not reflect the actual one used for the computations.

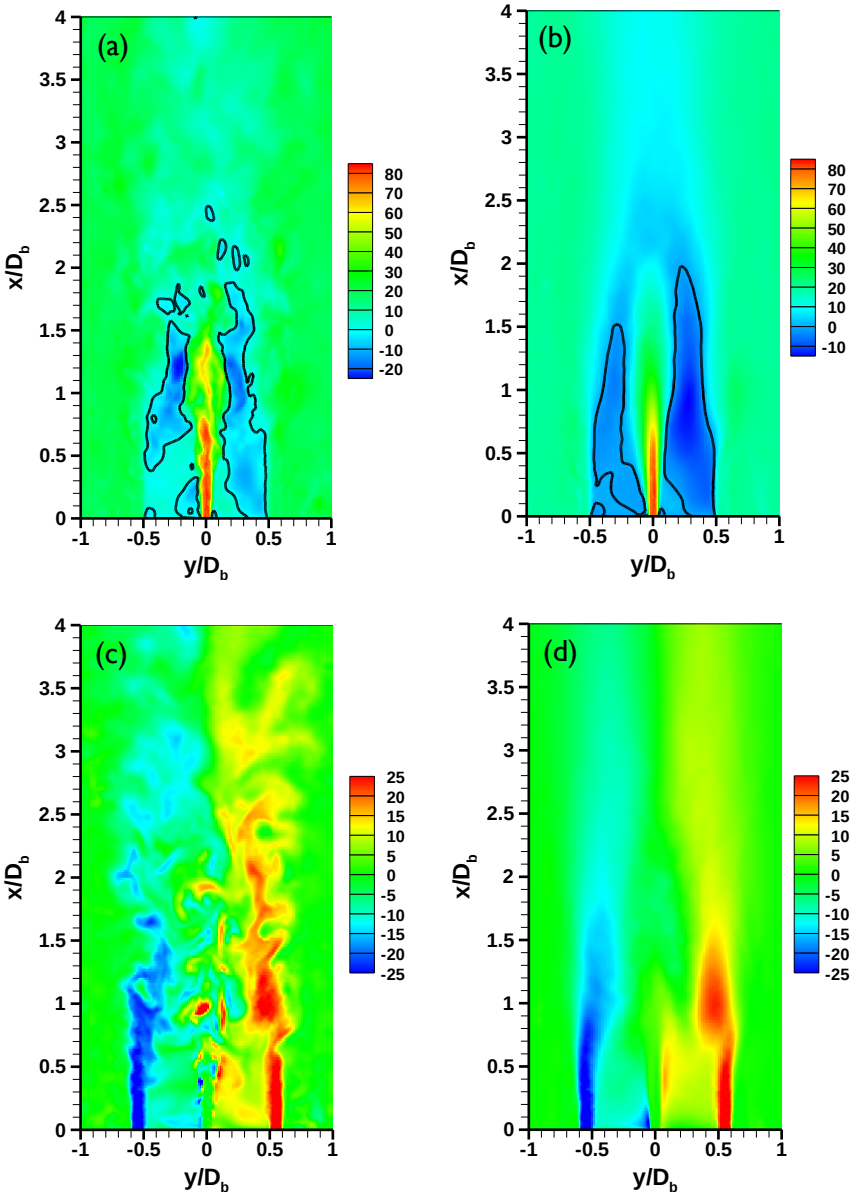

Figure 5.2: Contours of (a) filtered and (b) mean axial velocity as well as (c) filtered and (d) mean swirl velocity from SMA2. The units are m/s.

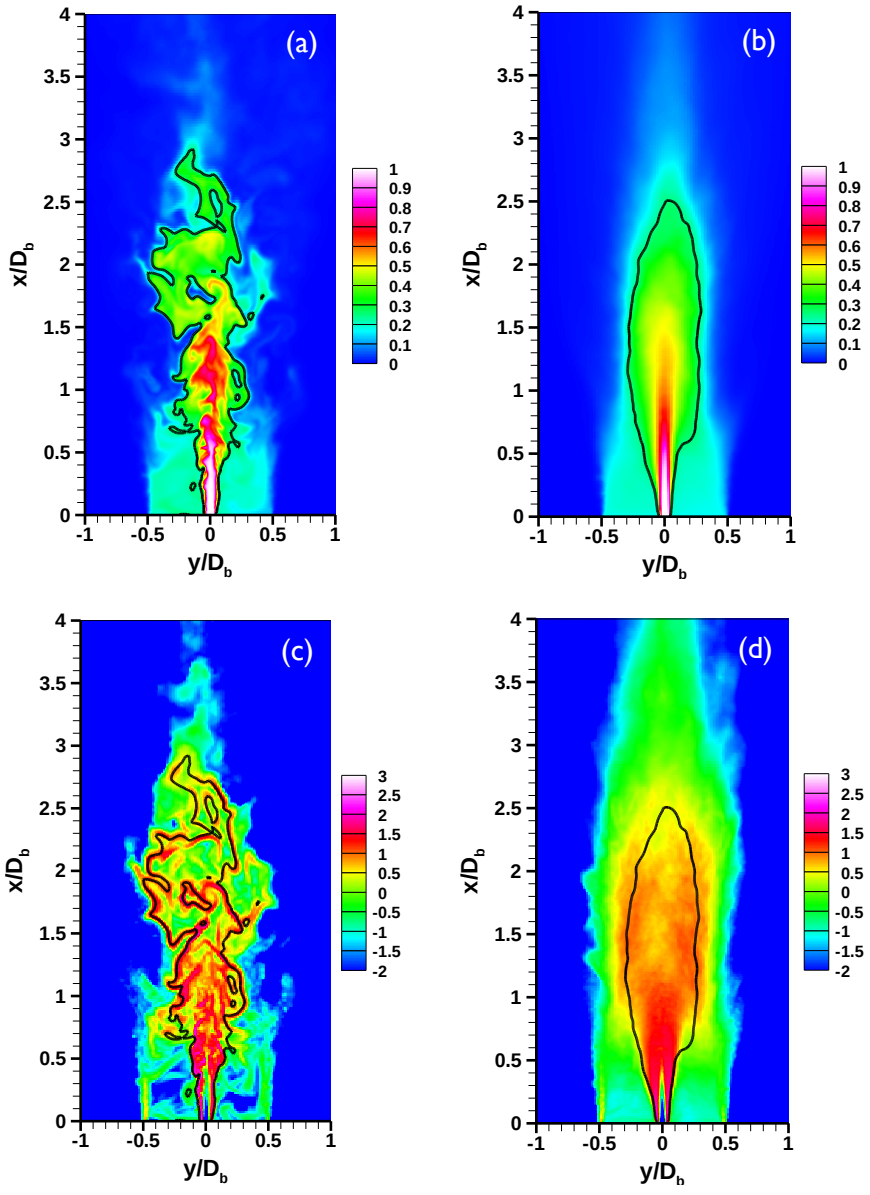

Figure 5.3: Contours of the (a) filtered and (b) mean mixture fraction as well as (c) resolved and (d) mean scalar dissipation rate (plotted in logarithmic scale) from SMA2. Unit for scalar dissipation rate is 1/s. Black lines: stoichiometric mixture fraction.

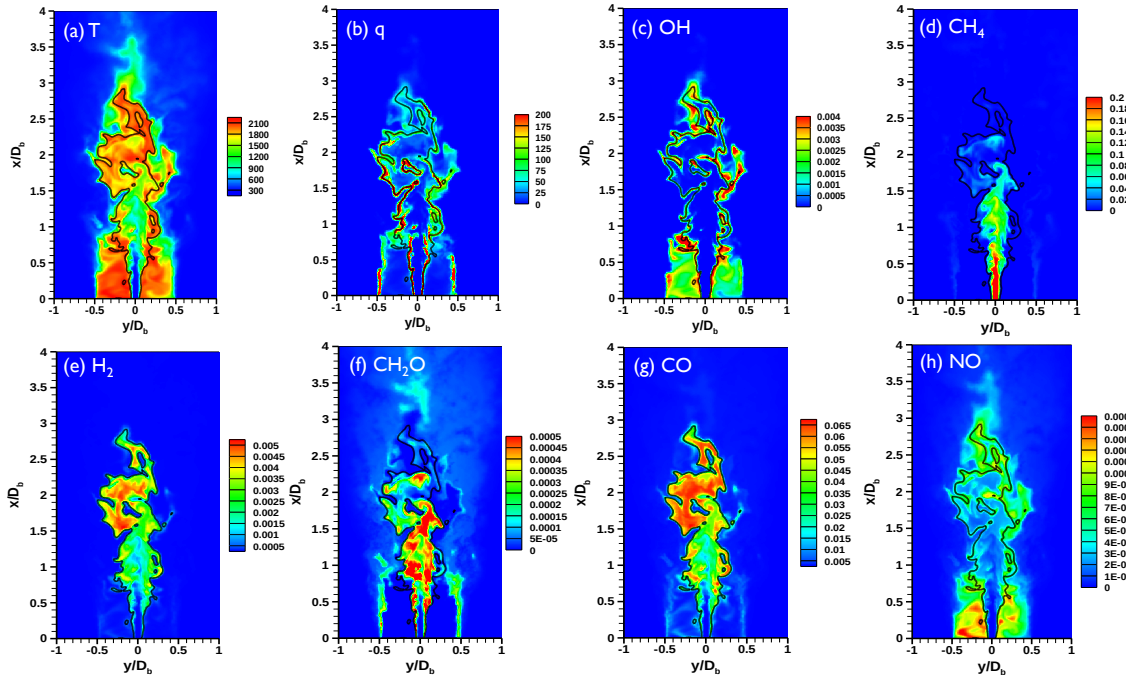

Figure 5.4: Contours of filtered (a) temperature (in K), (b) heat release rate (in MJ/m^3s) and (c−h) indicated mass fractions from SMA2. Black lines: stoichiometric mixture fraction.

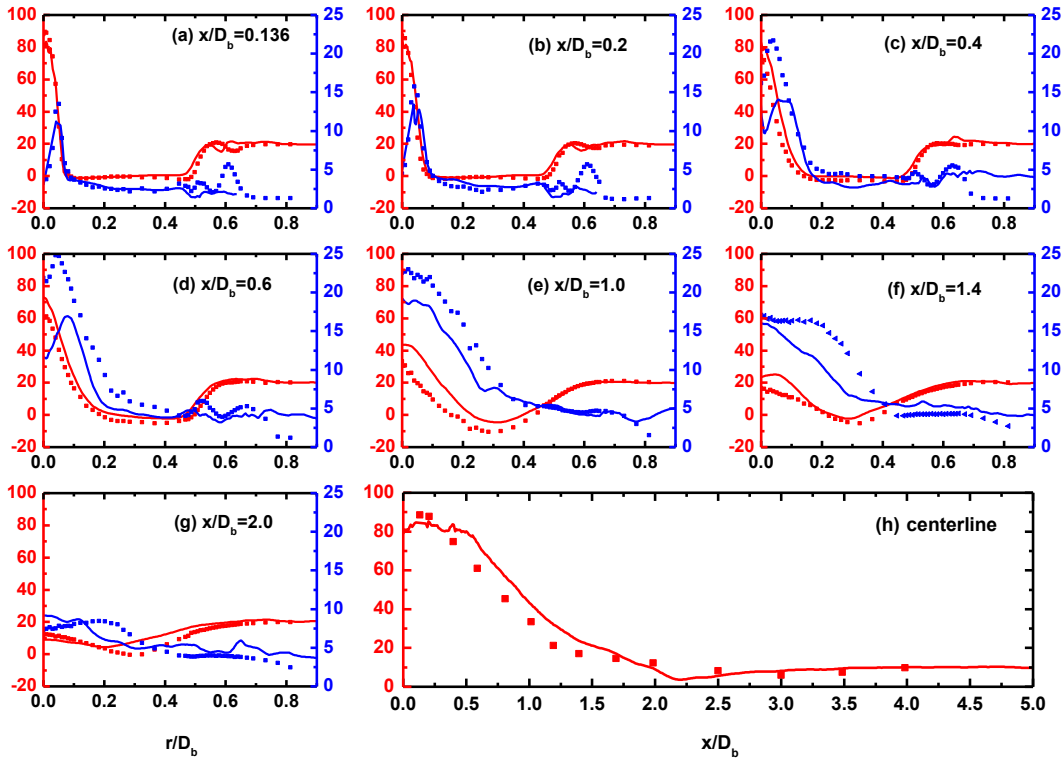

Figure 5.5: (a−g) Radial distributions at different streamwise locations and (h) centerline profile of axial velocity statistics from SMA2. Left ordinate: mean; right ordinate: *r.m.s.* The units for ordinates are m/s. Solids lines: computational results; symbols: experimental data.

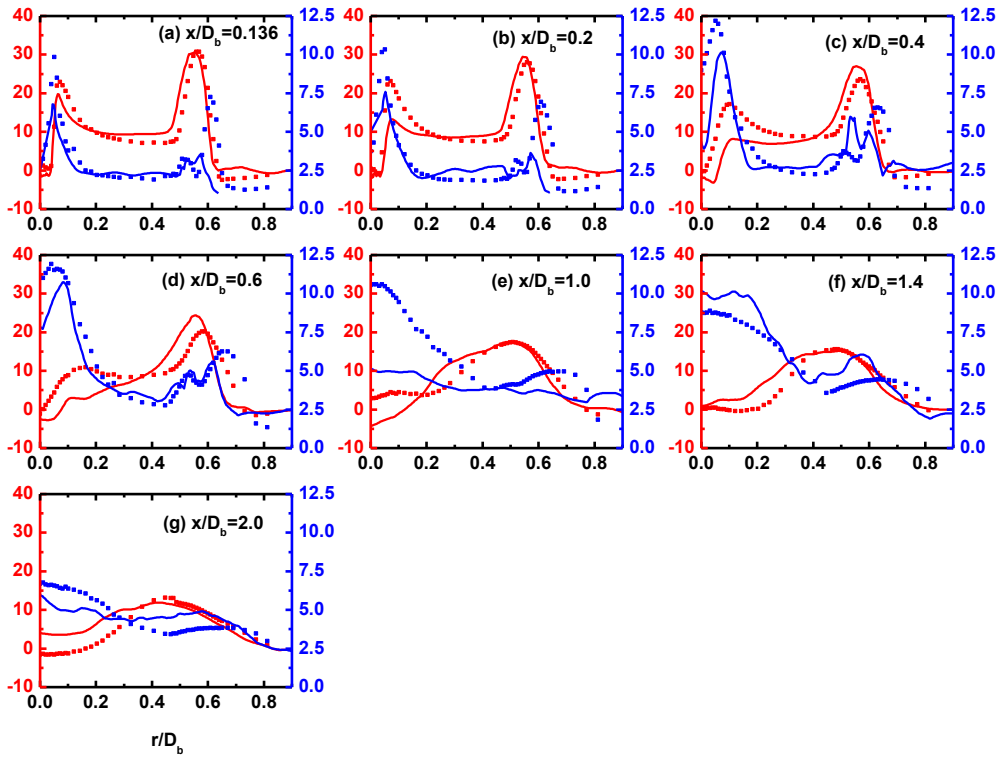

Figure 5.6: Radial distributions of mean and *r.m.s.* of swirl velocity at different streamwise locations from SMA2. Left ordinate: mean; right ordinate: *r.m.s.* The units for ordinates are m/s. Legend same as in Fig. 5.5.

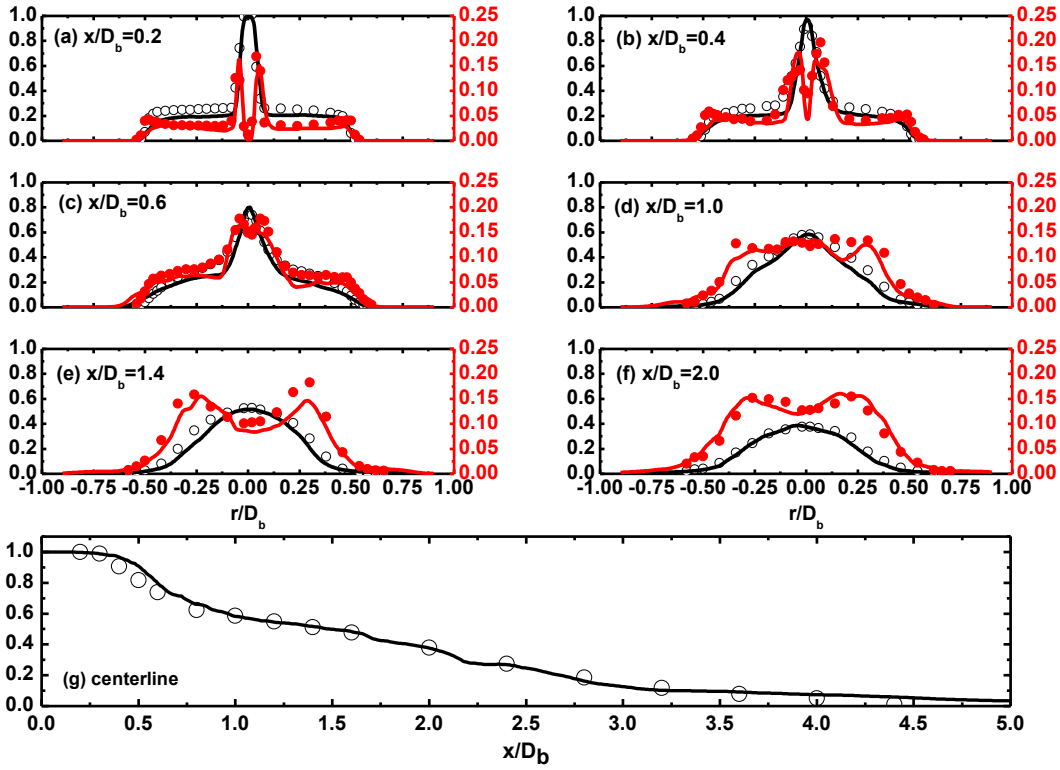

Figure 5.7: (a−f) Radial profiles at different streamwise locations and (g) centerline profile of mixture fraction statistics from SMA2. The left ordinate is for mean mixture fraction while the right one is for *r.m.s.* Solid lines: computational results; symbols: experimental data.

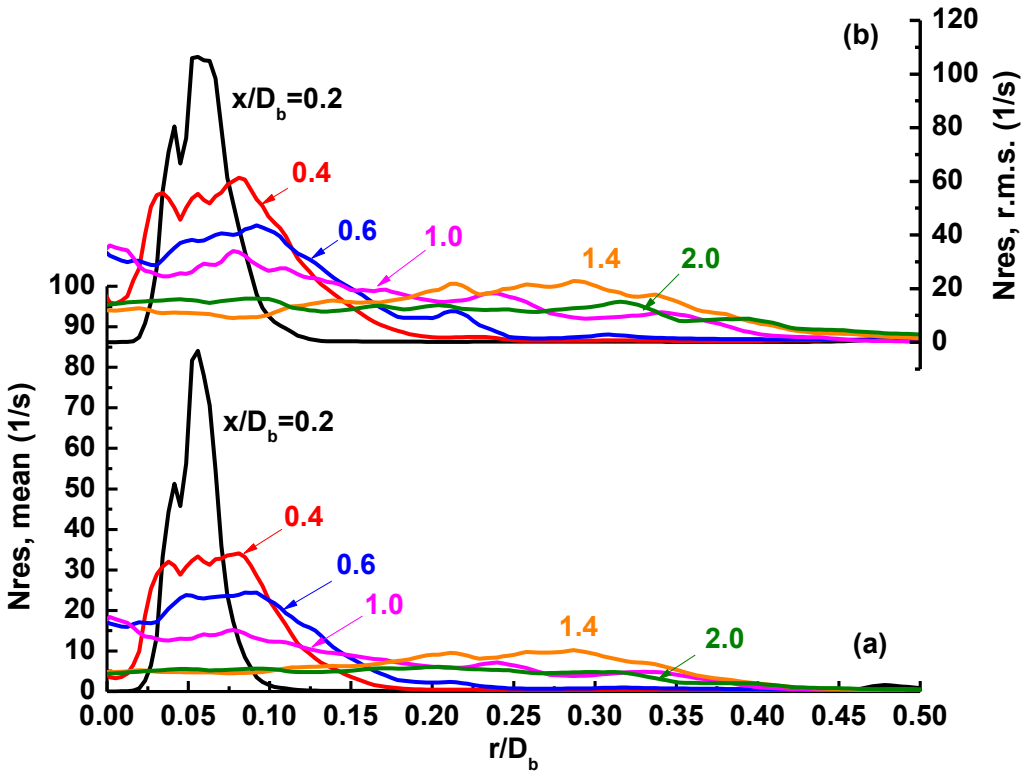

Figure 5.8: Radial profiles of (a) mean and (b) *r.m.s.* of resolved scalar dissipation rate from SMA2.

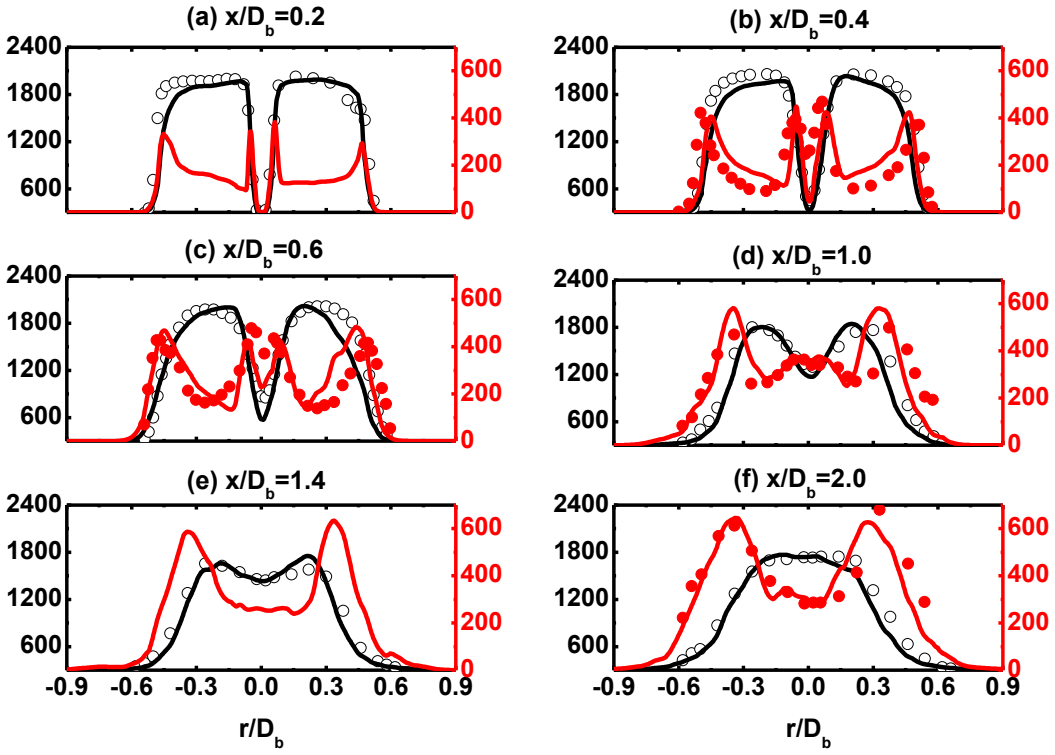

Figure 5.9: Radial profiles of temperature statistics from SMA2 at different streamwise locations. The left ordinate is for mean temperature while the right one is the *r.m.s.* Their unit is K. Lines: computational results; symbols: experimental data.

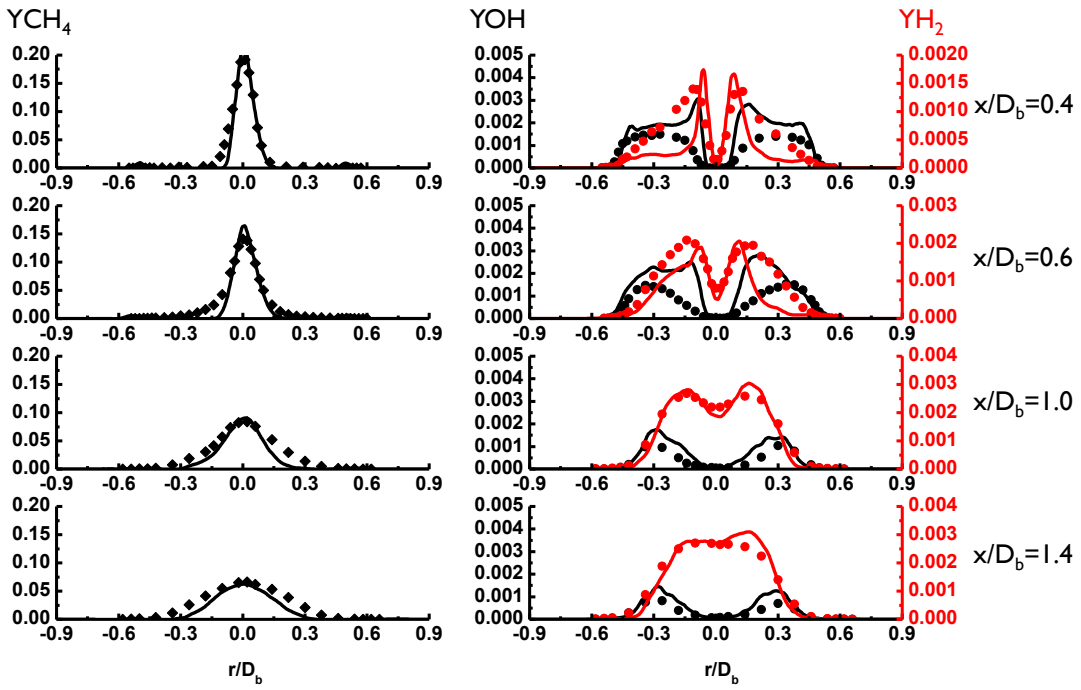

Figure 5.10: Radial profiles of mean mass fractions of CH_4, OH and H_2 from SMA2 at four streamwise locations. Lines: computational results; symbols: measurements.

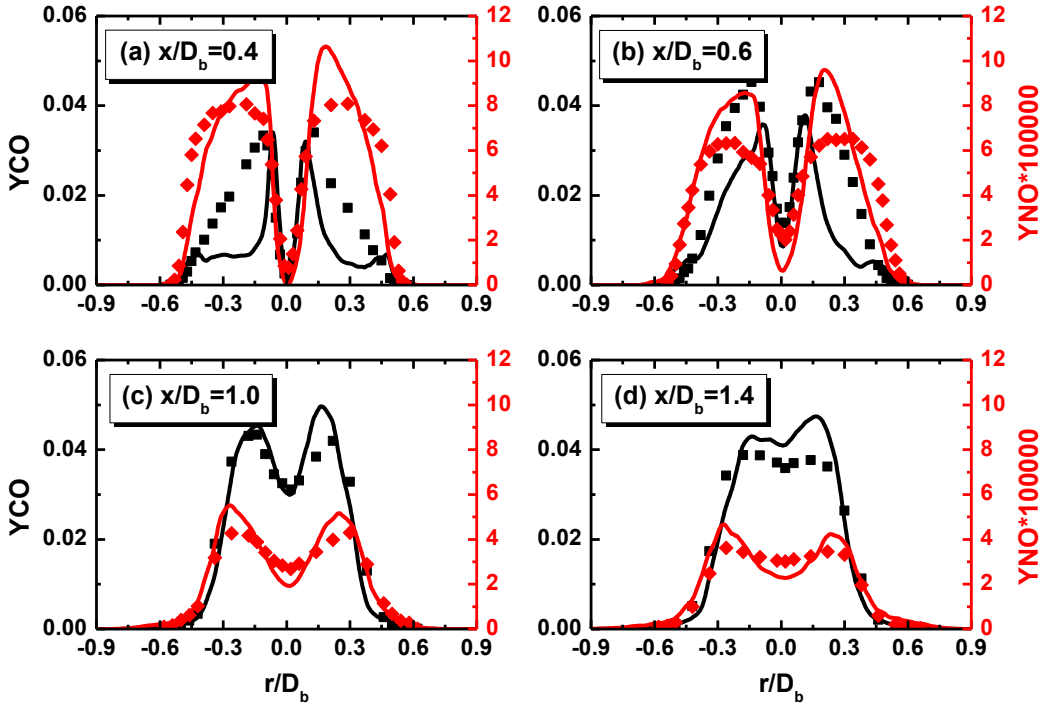

Figure 5.11: Radial profiles of mean mass fractions of CO and NO from SMA2 at four streamwise locations. Lines: computational results; symbols: measurements.

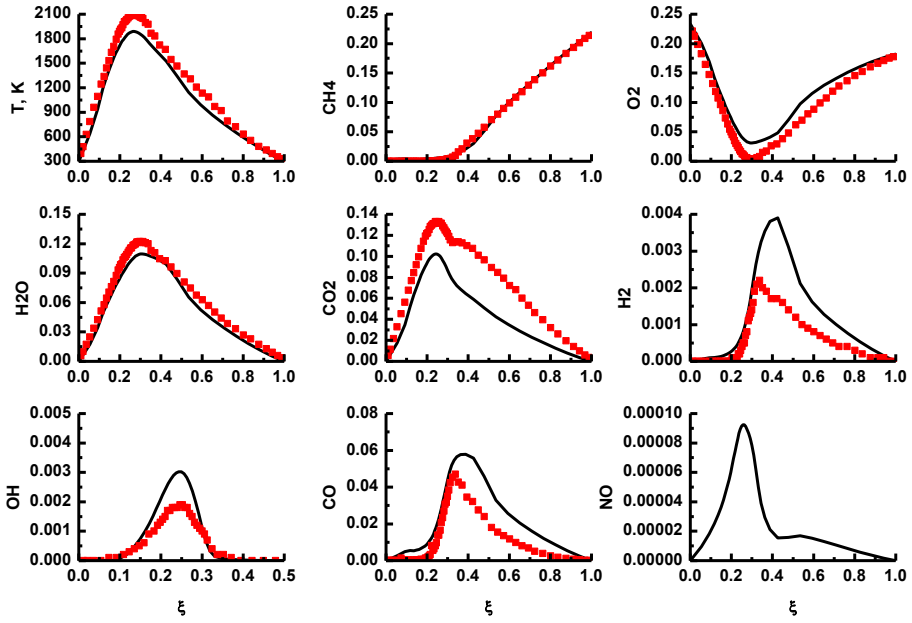

Figure 5.12: Mean conditional temperature and mass fractions at $x/D_b = 0.4$ from SMA2. Lines: computational results; symbols: measurements.

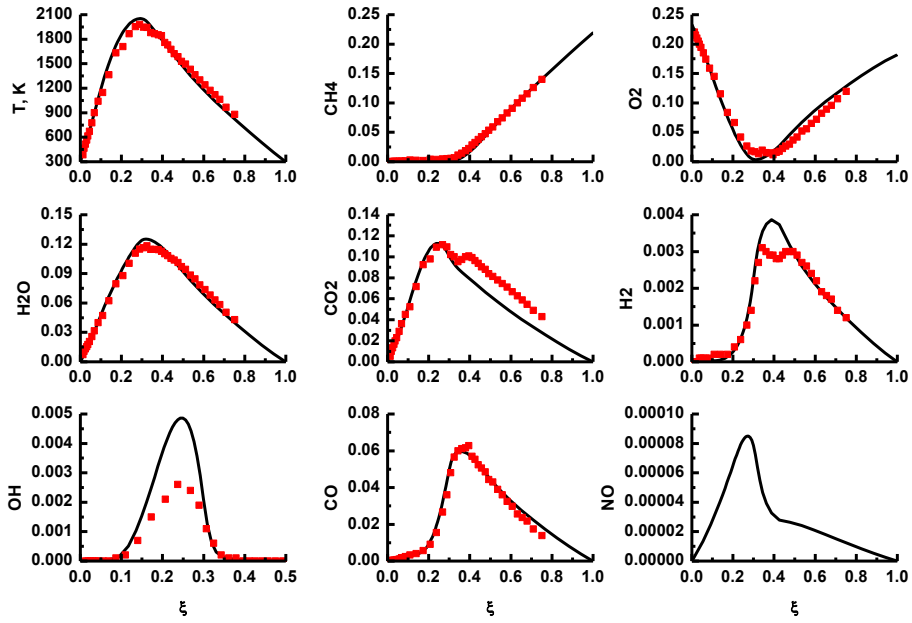

Figure 5.13: Mean conditional temperature and mass fractions at $x/D_b = 1.0$ from SMA2. Lines: computational results; symbols: measurements.

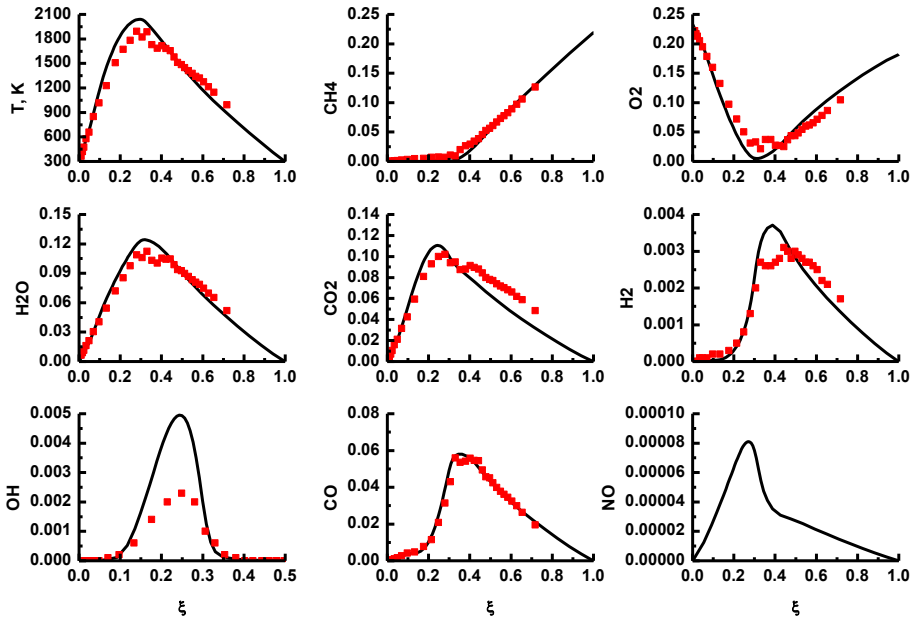

Figure 5.14: Mean conditional temperature and mass fractions at $x/D_b = 1.4$ from SMA2. Lines: computational results; symbols: measurements.

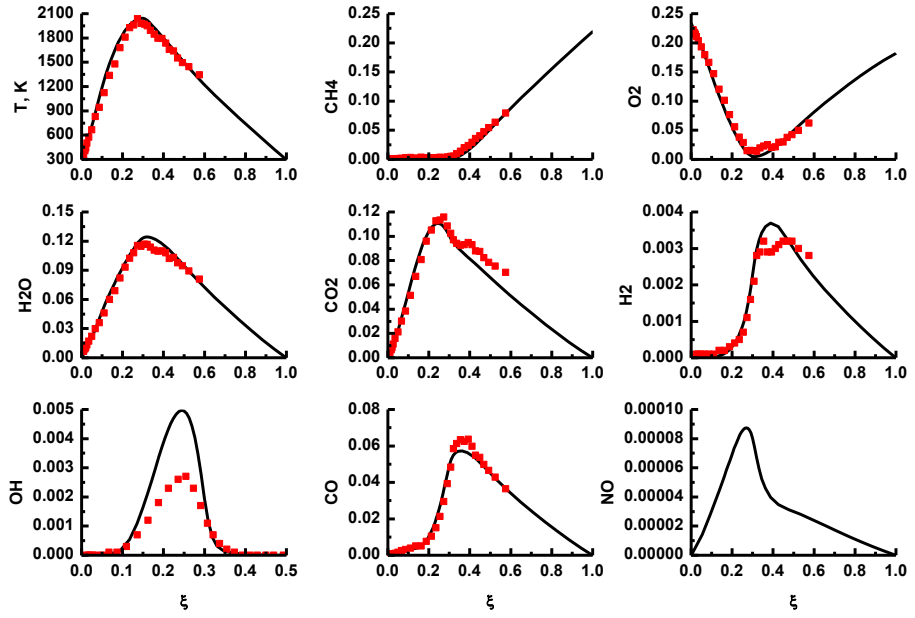

Figure 5.15: Mean conditional temperature and mass fractions at $x/D_b = 2.0$ from SMA2. Lines: computational results; symbols: measurements.

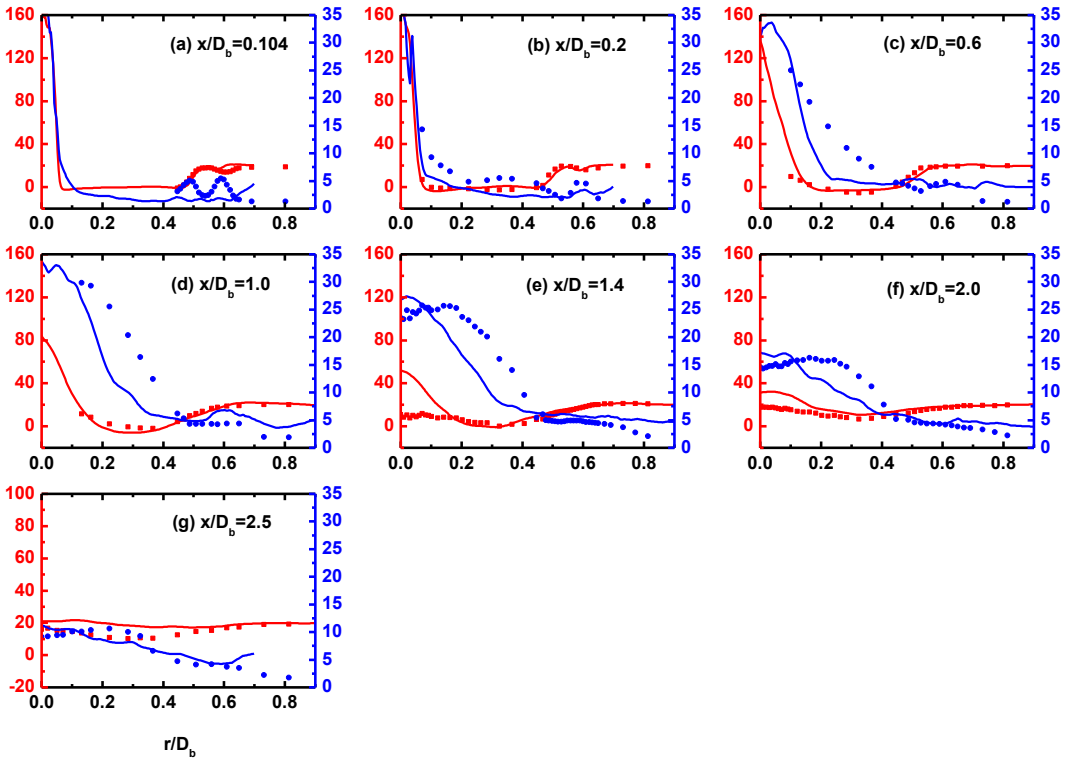

Figure 5.16: Radial distributions of mean and *r.m.s.* of axial velocity at different streamwise locations from SMA3. Left ordinate: mean; right ordinate: *r.m.s.* The unit for ordinates is m/s. Solids lines: computational results; symbols: experimental data.

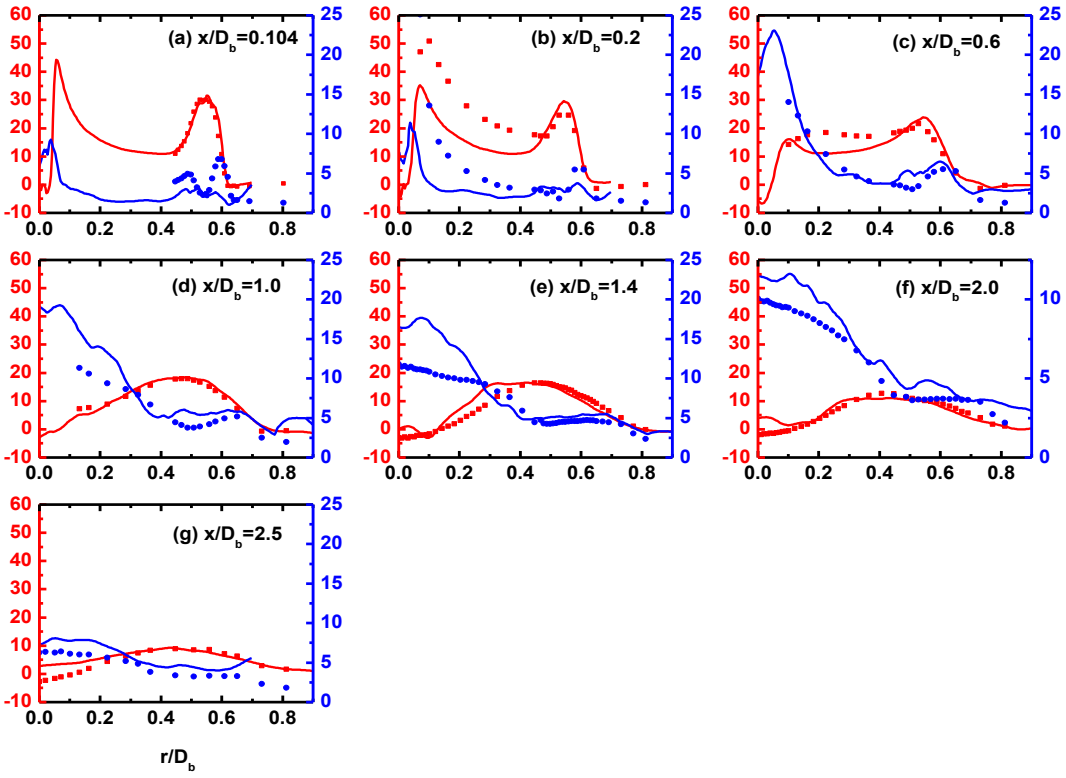

Figure 5.17: Radial distributions of mean and *r.m.s.* of swirl velocity at different streamwise locations from SMA3. Left ordinate: mean; right ordinate: *r.m.s.* The unit for ordinates is m/s. Legend same as in Fig. 5.16.

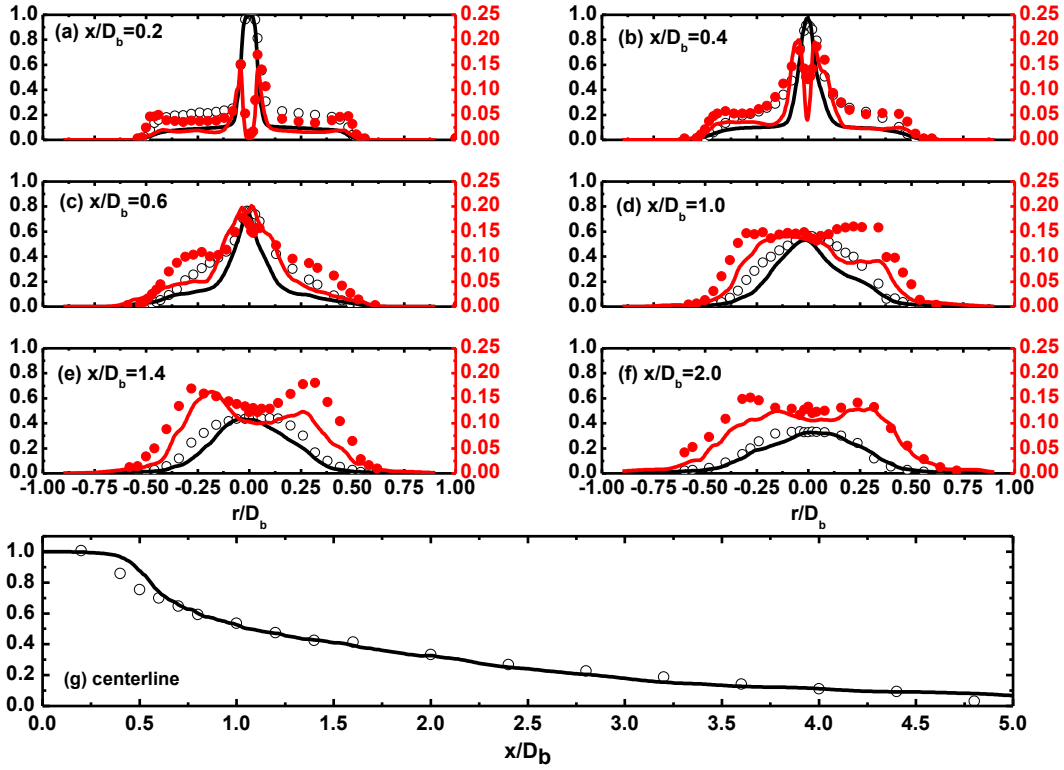

Figure 5.18: (a–f) Radial profiles at different streamwise locations and (g) centerline profile of mixture fraction statistics from SMA3. The left ordinate is for mean mixture fraction while the right ordinate is for *r.m.s.* Solid lines: computational results; symbols: experimental data.

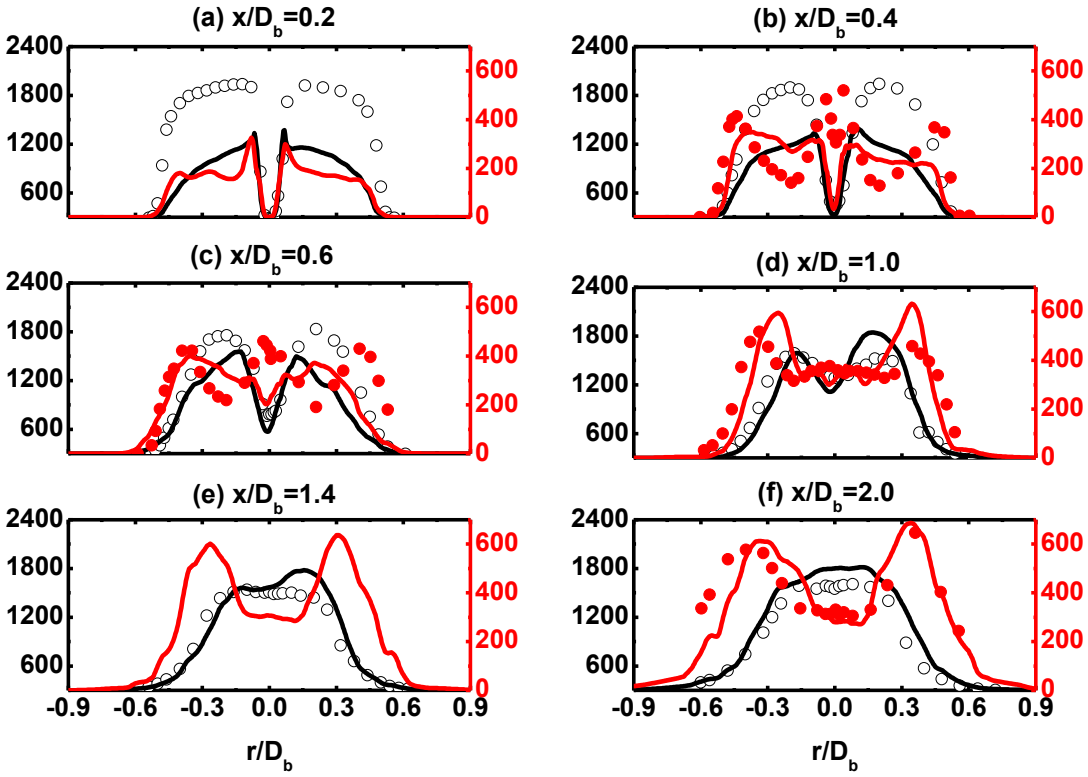

Figure 5.19: Radial profiles of temperature statistics from SMA3 at different streamwise locations. The left ordinate is for mean temperature while the right ordinate is for the *r.m.s.* Their unit is K. Lines: computational results; symbols: experimental data.

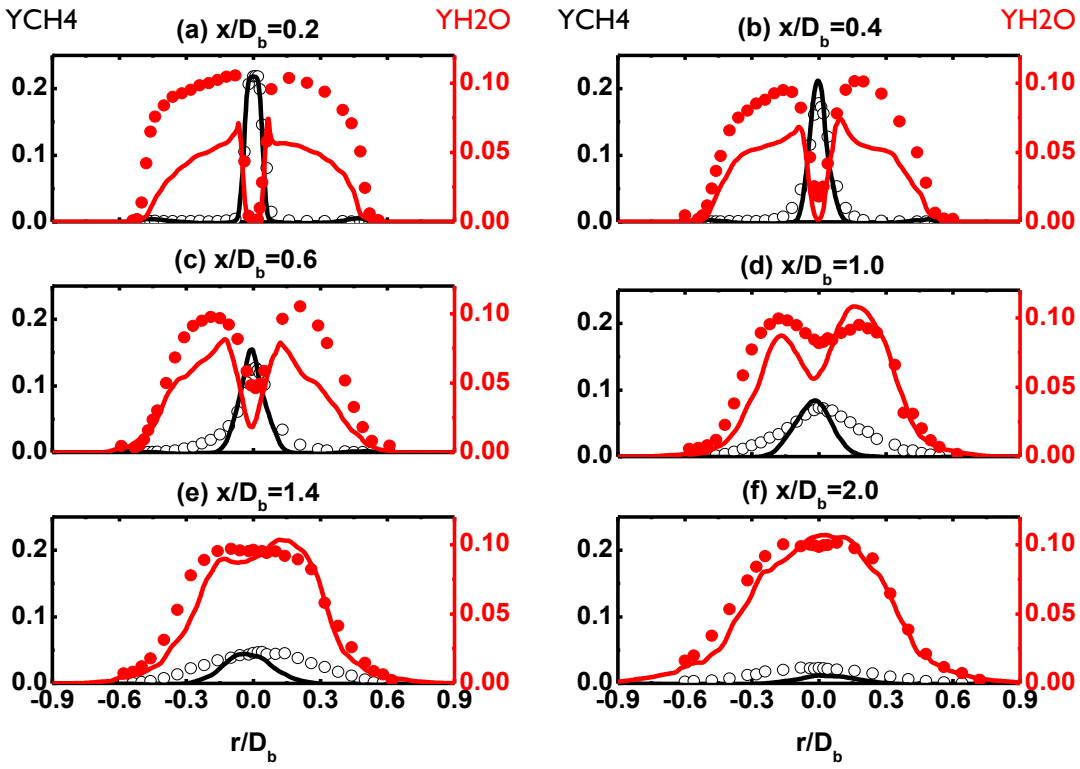

Figure 5.20: Radial profiles of mean mass fractions of CH_4 and H_2O from SMA3 at different streamwise locations. Lines: computational results; symbols: measurements.

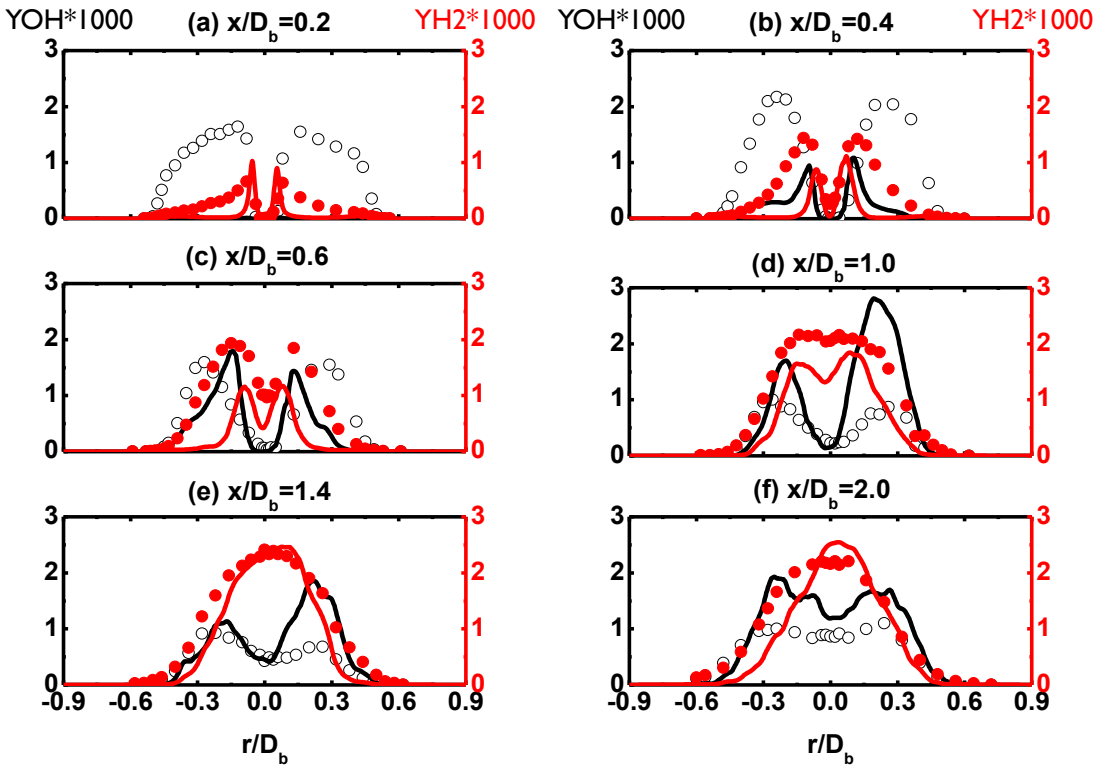

Figure 5.21: Radial profiles of mean mass fractions of OH and H_2 from SMA3 at different streamwise locations. Lines: computational results; symbols: measurements.

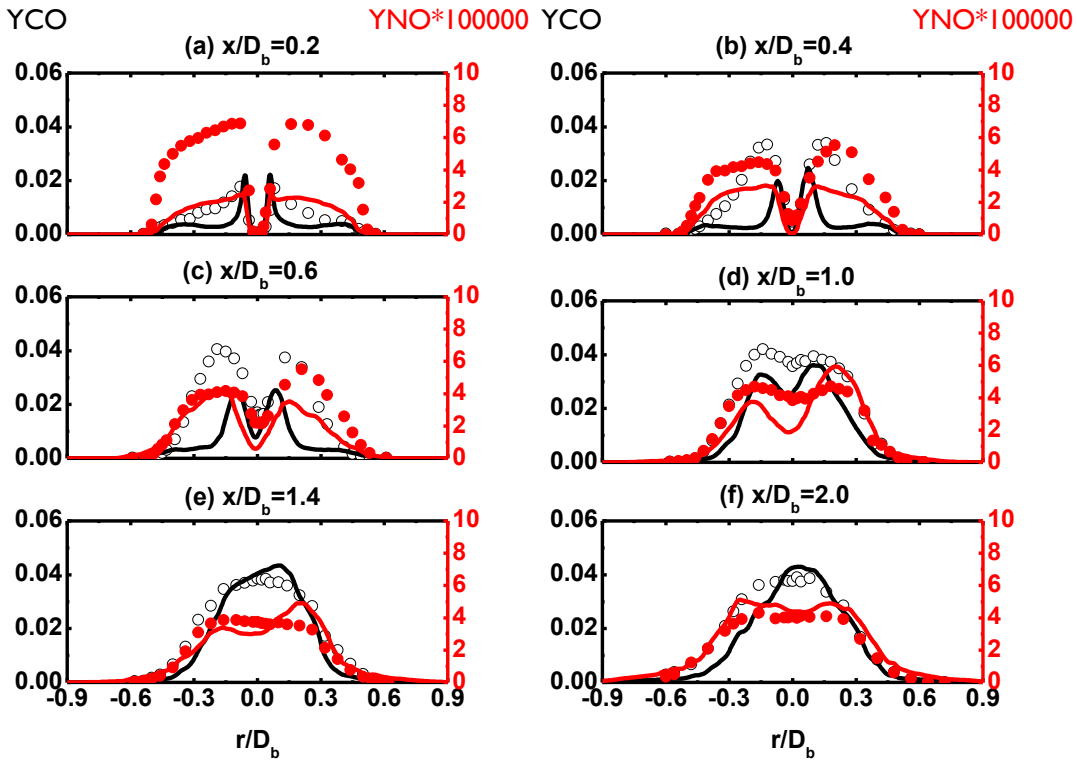

Figure 5.22: Radial profiles of mean mass fractions of CO and NO from SMA3 at different streamwise locations. Lines: computational results; symbols: measurements.

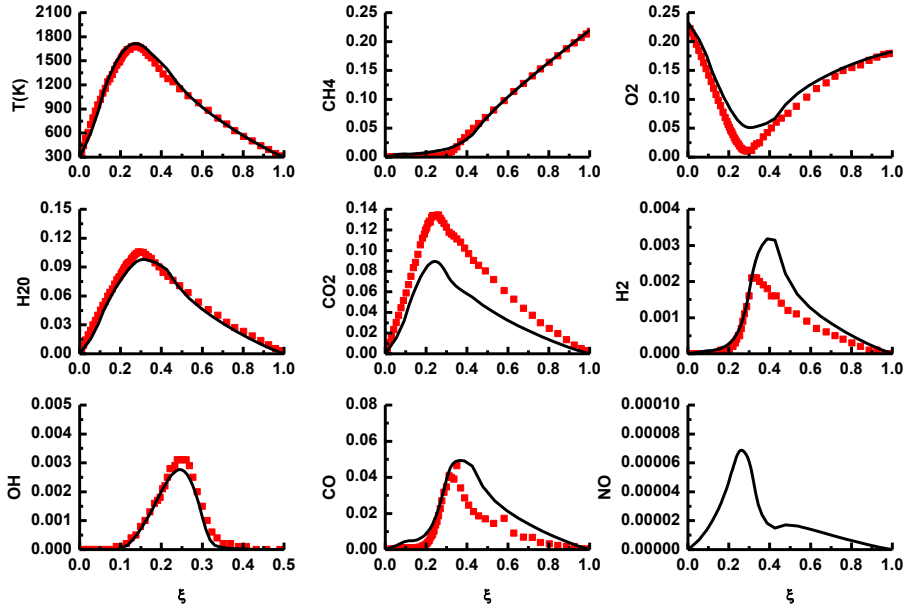

Figure 5.23: Mean conditional temperature and mass fractions at $x/D_b = 0.4$ for SMA3. Lines: computational results; symbols: measurements.

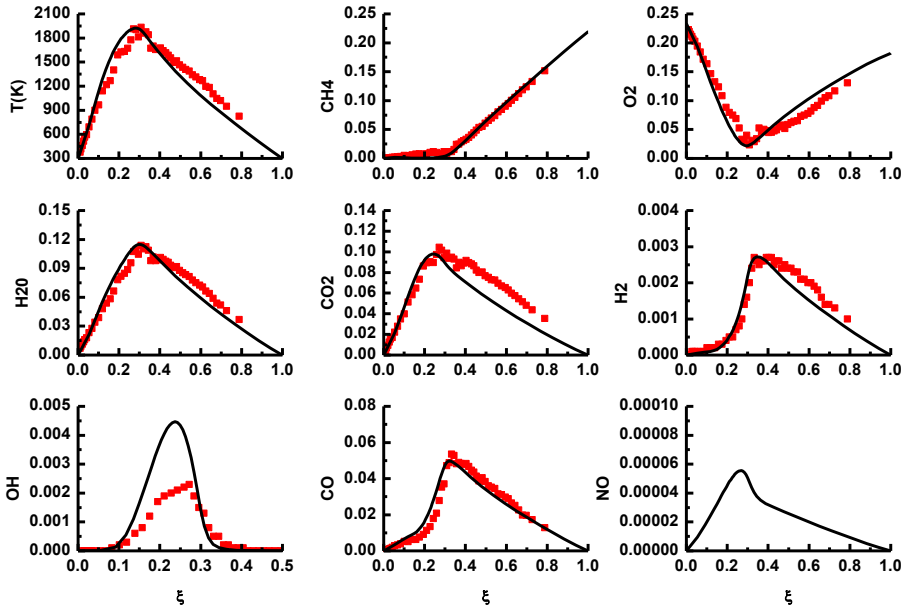

Figure 5.24: Mean conditional temperature and mass fractions at $x/D_b = 1.0$ for SMA3. Lines: computational results; symbols: measurements.

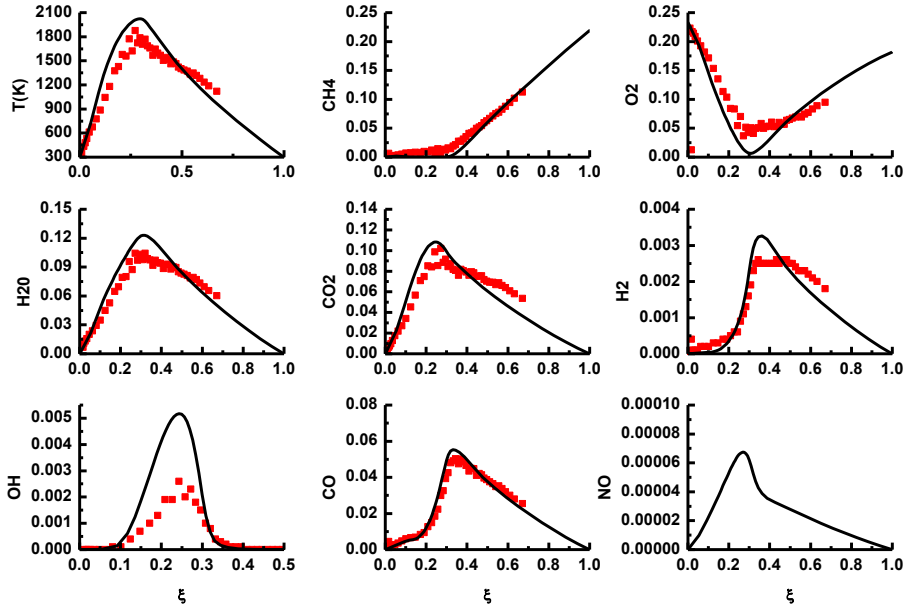

Figure 5.25: Mean conditional temperature and mass fractions at $x/D_b = 1.4$ from SMA3. Lines: computational results; symbols: measurements.

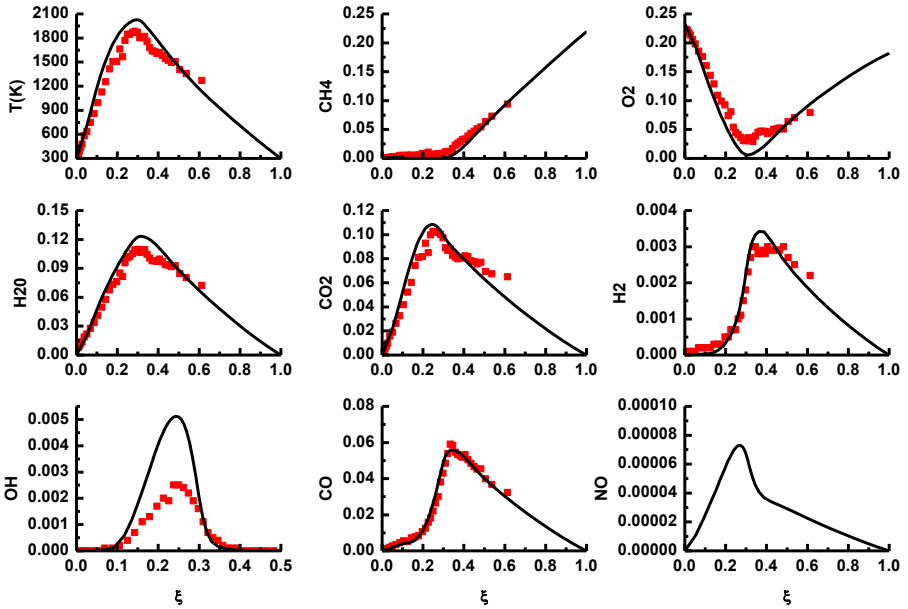

Figure 5.26: Mean conditional temperature and mass fractions at $x/D_b = 2.0$ from SMA3. Lines: computational results; symbols: measurements.

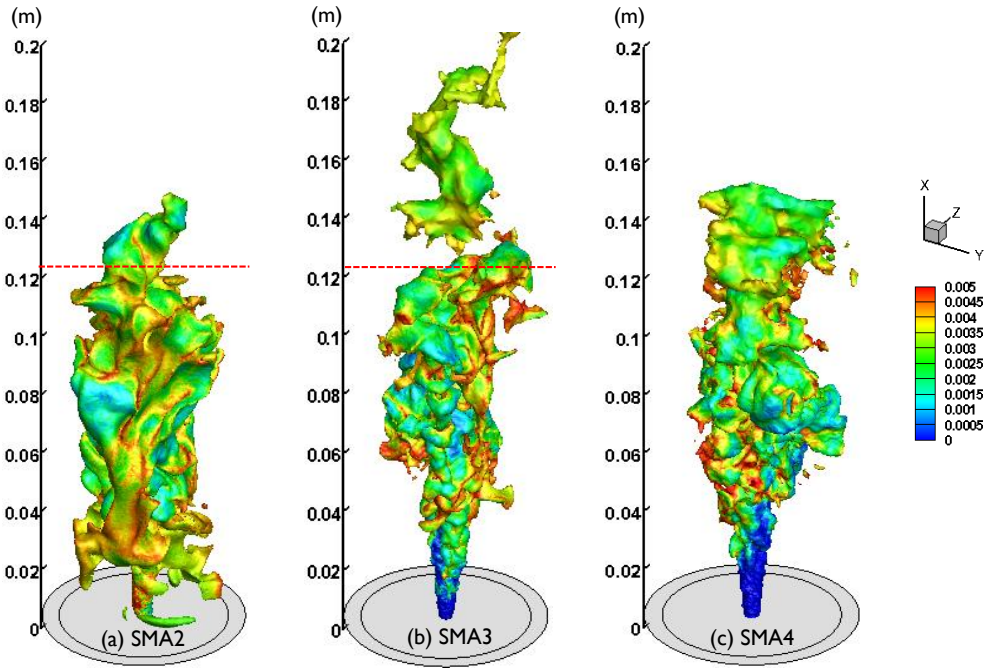

Figure 5.27: Three dimensional iso-surfaces of stoichiometric mixture fraction colored by instantaneous OH mass fraction for (a) SMA2, (b) SMA3 and (c) SMA4 cases. The red lines in (a) and (b) mark the measured mean centerline positions of ξ_{st} [Masri et al., 2004].

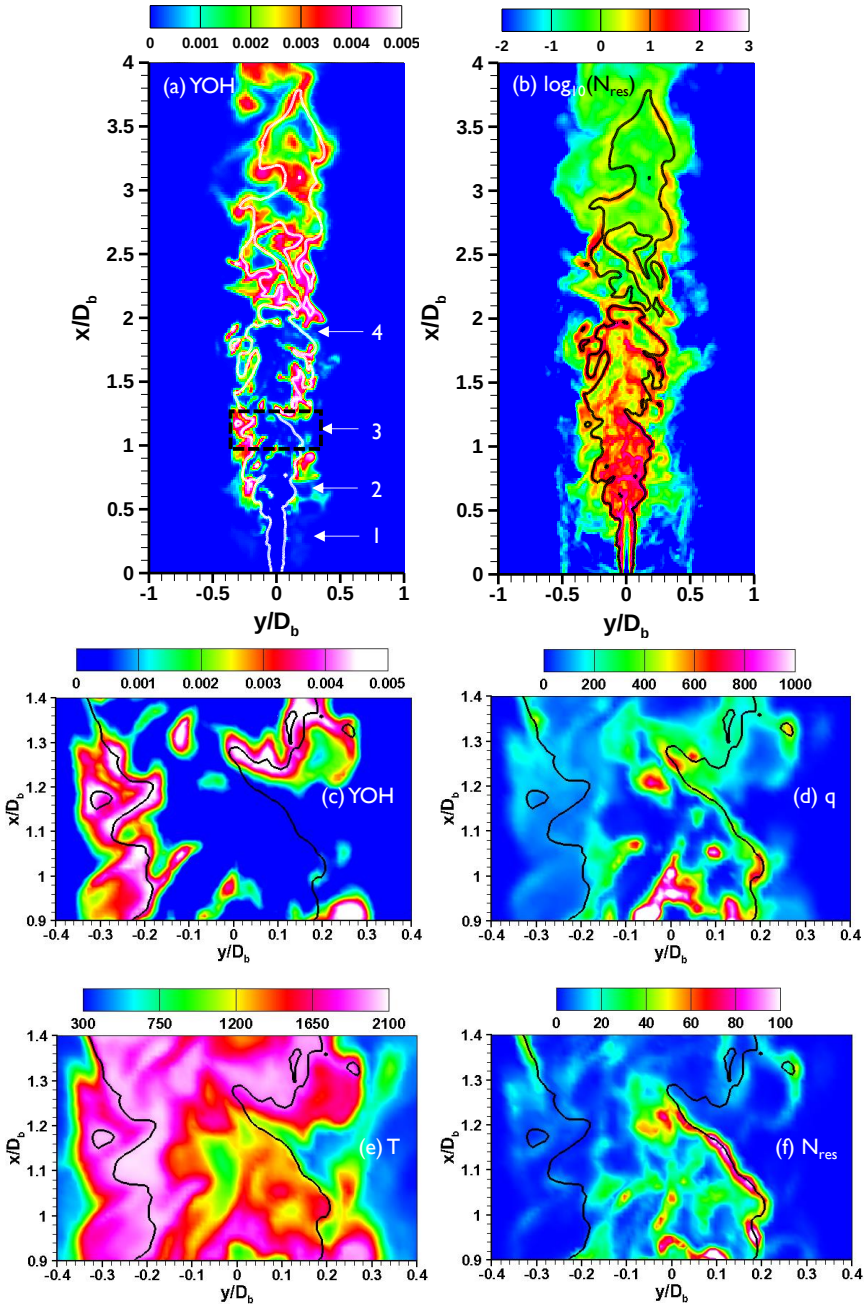

Figure 5.28: (a−b) Contours of instantaneous OH mass fraction and resolved scalar dissipation (in logarithmic scale, in unit of 1/s). (c−d) Contours of instantaneous OH mass fraction, heat release rate (in MJ/m^{3}s), temperature (in K) and resolved scalar dissipation (in 1/s) for the small regions marked with dashed line in (a). Lines: ξ_{st} iso-lines. Numbers 1−4 in (a) mark the low OH mass fraction regions along the ξ_{st} iso-lines.

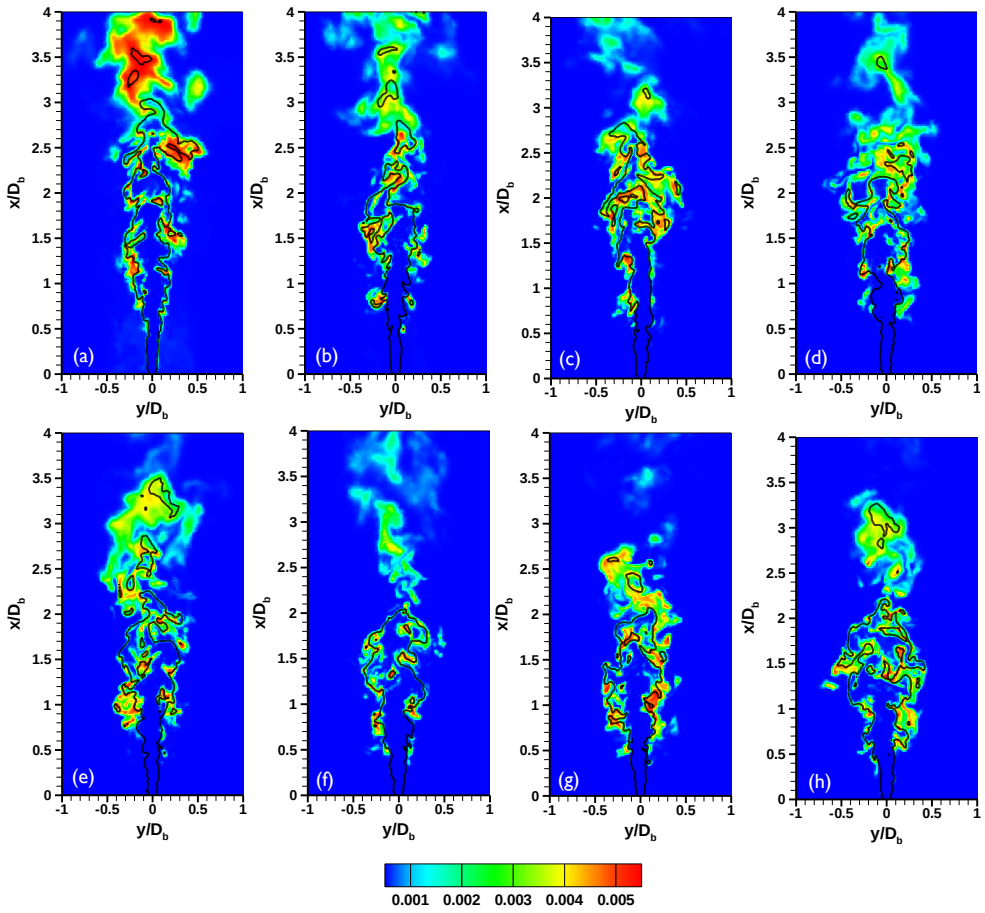

Figure 5.29: Time evolutions of filtered mass fraction of OH at $x-y$ slice for SMA4: (a) $t = 0$ s, (b) $t = 0.0015$ s, (c) $t = 0.003$ s, (d) $t = 0.0045$ s, (e) $t = 0.006$ s, (f) $t = 0.0075$ s, (g) $t = 0.009$ s and (h) $t = 0.0105$ s. Lines: stoichiometric mixture fraction.

Chapter 6

Local Extinction in Cambridge Swirl Flames

6.1 Introduction

Swirl flows are virtually ubiquitous in gas turbines [Gicquel et al., 2012; Gupta et al., 1984; Syred, 2006]. The strong turbulent fluctuations due to the intense shear from the swirling motion can lead to finite-rate chemistry effects [Masri et al., 2006] such as local extinction. As shown in Chapter 4, the Cambridge swirl burner is composed of bluff body, swirler with six guided vanes, quartz enclosure and fuel injection system leading to the central bluff body surface. Therefore, it can be viewed as a simplified configuration of the realistic gas turbine combustor. In terms of the flow establishment, the long IRZ and small CRZ exist in this burner and the entire flame is immersed in the strong recirculating fluid [Cavaliere et al., 2013], which is qualitatively similar to the flow patterns in the gas turbine combustor [Gupta et al., 1984]. The overall flame shape (short and bowl-shaped) in the Cambridge swirl burner is different from that (long and jet-flame-like) of Sydney swirl flames [Masri et al., 2004], but is close to that in the gas turbine combustion [Gupta et al., 1984].

The objective of this Chapter is to apply LES with a three dimensional CMC combustion sub-grid model validated in Chapter 5 to a confined swirl-stabilized non-premixed methane flame in the Cambridge burner [Cavaliere, 2013; Cavaliere

et al., 2013] and to analyze its localized extinction characteristics. The model and numerical implementations are briefly presented in Section 6.2, while the results and discussion are given in Section 6.3, followed by the conclusions in the final Section.

6.2 Modelling

6.2.1 LES and CMC modelling

The filtered velocity and mixture fraction, $\tilde{\mathbf{U}}$ and $\tilde{\xi}$, are solved and their corresponding LES governing equations correspond to Eqs. (3.14b) and (3.14c) in Chapter 3. The Smagorinsky model is applied to close the sub-grid scale stress tensor. Other models for the LES governing equations can be also found in Sub-section 3.1.2. Particularly, the variance of filtered mixture fraction, $\widetilde{\xi''^2}$, is calculated with Eq. (3.23). The filtered scalar dissipation rate $\tilde{N}$ includes two contributions from the resolved and sub-grid parts ($\tilde{N}_{res}$ and $\tilde{N}_{sgs}$), as demonstrated in Eq. (3.22).

The conditionally filtered mass fractions and total enthalpy, Q_α and Q_h, are solved with the three dimensional CMC governing equations, i.e. Eqs. (3.35) and (3.36). The sub-models used for modelling the unclosed terms in the CMC equations are presented in Section 3.2. In this Chapter, the laminar and sub-grid Schmidt numbers are $Sc = 1.0$ and $Sc_t = 0.7$ [Branley and Jones, 2001], respectively.

6.2.2 Problem considered and numerical implementation

The photos of the Cambridge swirl burner have been given in Fig. 4.3, while the schematic and dimensions are shown in Fig. 4.4 and described in Section 4.2.2. The fuel is pure methane in this study. The bulk velocity of air $U_{a,b}$ is 19.1 m/s while that of the methane $U_{f,b}$ is 29.2 m/s. $U_{a,b}$ is roughly 96% of the blow-off air bulk velocity (i.e. 19.9 m/s) for the current fuel bulk velocity $U_{f,b}$. The swirl number S_N is approximately 1.23 calculated following Beer and Chigier's formula [Beer and Chigier, 1971], i.e. Eq. (4.2). The inlet temperatures for both gases

are 298 K. The Reynolds number for the air stream based on the radial distance of annular circular inlet, $D_a - D_b$, and $U_{a,b}$ is about 17,700, while that for fuel jet based on fuel jet exit diameter D_f and fuel bulk velocity $U_{f,b}$ is about 4,500. The stoichiometric mixture fraction is $\xi_{st} = 0.055$. In the experiment by Cavaliere [2013], the velocities were measured with one-component LDA with seeding in the air flow only and used 2000 data points resulting to a statistical uncertainty of 1−3%. Note that the absence of seeding in the fuel jet may cause uncertainty in the reported velocities at positions very close to the fuel nozzle, but the error is expected to be negligible elsewhere due to the dominance of the air flow.

The mixture fraction space is discretized with 51 nodes clustered around the stoichiometric mixture fraction. Concerning the physical space, the computational domains for both LES and CMC are the same and have been shown in Fig. 4.7, which is also used for LES of CSWH1-fl case in Chapter 4. Specifically, the LES domain consists of the annulus/swirler, the chamber, and a hemispherical far-field (not shown in Fig. 4.7). About 10 million tetrahedral cells are generated for LES with a minimum size of 0.0004 m and have been used for the LES of CSWH1-fl in Chapter 4. For the mesh distributions in the rectangular combustion chamber, one can refer to Fig. 4.8. The CMC domain includes the combustor, far-field and partial annulus section without swirler (starting 0.02 m upstream of bluff body). The CMC mesh consists of around 100,000 polyhedral cells reconstructed from LES cells and is refined in the fuel jet and flame regions ($0 < x/D_b < 2.4$) in the chamber.

The contour of the number of LES cells contained by one CMC cell, which can be parameterized by ϱ^{CMC}, is plotted in Fig. 6.1(a). Clearly, ϱ^{CMC} is directly linked to the relative refinement or coarseness of local LES and CMC cells. For instance, it can be seen from Fig. 6.1(a) that near the annulus exit and bluff body ϱ^{CMC} is relatively low (denoted by blue regions in Fig. 6.1a) while the most of region in the combustion chamber ϱ^{CMC} reaches high values (denoted by red regions in Fig. 6.1a). Particularly for the flame region, the distribution of the number of LES cells contained by one CMC cell is plotted in Fig. 6.1(b). The mean of ϱ^{CMC} in the flame region is about 95 for the currently used LES and CMC meshes. Figure 6.1(c) presents the number of CMC faces constituting one CMC cell F^{CMC}. The number of the CMC faces is about 4,800,000 account-

ing for 23% of the LES faces and is roughly 16.5 times the face number (about 300,000) when these CMC nodes are used as cell centroids for generating purely tetrahedral cells. The mean of the CMC face number per CMC cell F^{CMC} is 66. Additionally, in the current CMC mesh, the Euler characteristic $\chi^{CMC} = 2$, calculated with Eq. (3.59), holds for all the reconstructed polyhedral cells, indicating the completeness of all the reconstructed polyhedral CMC cells. This mesh examination is a necessary step before discretizing Eq. (3.35) on the polyhedral cells with finite volume method based on Gauss divergence theorem and is able to ensure the numerical fluxes of the physical terms are correctly calculated.

A preliminary simulation using LES/0D-CMC solver for the above mentioned flow conditions is performed and this provides the initial filtered flow and mixing fields, i.e. $\bar{p}$, $\tilde{\mathbf{U}}$ and $\tilde{\xi}$, for LES/3D-CMC. For the LES boundary conditions, zero pressure gradient is enforced at all inlets. For velocity and mixture fraction, Dirichlet boundary conditions are used. For the air and fuel inlets, random noise with 5% intensity is added to the mean top-hat velocity profiles. At far-field boundaries, the fixed total atmospheric pressure is enforced while for velocities zero gradient extrapolation is applied. At the walls, nonslip condition is enforced for the velocities and zero gradient for the mixture fraction.

In mixture fraction space for the 3D-CMC solver, $\eta = 0$ corresponds to air and $\eta = 1$ to pure fuel, both at 298 K. The fully burning steady solutions with $N_0 = 50$ 1/s from the stand-alone 0D-CMC solver described in Sub-section 3.4.1 are used to initialize all the CMC cells in mixture fraction space. Inert mixing solutions are injected in the air and fuel inlets and zero gradient conditions are applied for all the solid walls in the CMC domain.

The LES/3D-CMC solver introduced in Sub-section 3.4.1 is applied for the computations in this Chapter. The hybrid SIMPLE and PISO algorithm is used for the velocity-pressure coupling and 3 inner PISO loops are used while 5 loops for the outer SIMPLE procedure. A second order implicit Crank−Nicholson scheme is applied for time marching. The time step is $\Delta t = 1.5 \times 10^{-6}$ s. The numerical discreizations for the 3D-CMC solver are presented in Sub-section 3.3.2. The parallel computations were run on 80 2.53 GHz Xeon CPUs with 4 GB RAM for each processor in Stokes Cluster from Department of Engineering, University of Cambridge. Around 24 hours were needed for 0.001 s of physical time and the

total simulated time is about 0.04 s.

6.3 Results and discussion

6.3.1 Flow field and global flame characteristics

Figure 6.2 demonstrates the instantaneous (the upper row) and mean (the lower row) distributions of axial and swirl velocities as well as the z-vorticity in $x-y$ plane. Due to the strong swirling flows with $S_N = 1.23$, no PVCs and dominant frequency in the flow fields are observed based on the LES results not shown here. This is in line with the experimental findings [Cavaliere, 2013]. The recirculation zones are highlighted by the iso-lines of zero axial velocity as the black lines in Fig. 6.2(a). The CRZ and IRZ appear in this investigated swirling flame. The CRZ is formed because of the sudden expansion of chamber and the confinement of the lateral chamber walls. The long IRZ is created by the strong swirling flows and extends from the bluff body surface ($x = 0$) to about $x = 0.18$ m downstream (i.e. beyond the chamber length of 0.15 m). The IRZ here plays a significant role in transporting the hot products back into upstream zones, enhancing the mixing near the bluff body and stabilizing the flame. One can see from Fig. 6.2(b) that the swirling motion exists in the whole chamber although the swirl velocity gradually decays towards downstream. The shearing structures are quantified by the z-vorticity in Fig. 6.2(c). Considerable z-vorticity appears between the fuel jet and IRZ due to the Kelvin−Helmholtz instability. In addition, two shear layers exist: inner layer caused by the swirling air stream and the IRZ, while outer layer by the swirling air and CRZ.

Radial profiles of normalized mean and *r.m.s.* axial velocity at four axial positions (i.e. $x/D_b = 0.4$, 0.6, 2.2 and 4.4) are shown in Fig. 6.3 while those of swirl velocity in Fig. 6.4. The computational statistics were collected spanning 0.032 s; different sampling periods were examined to confirm statistical convergence. It can be seen from Fig. 6.3 that the flow reversals (i.e. negative axial velocity) in both CRZ and IRZ are correctly captured. However, the decay of the fuel jet is over-predicted by the LES and thus its penetration into the IRZ is shorter (see $x/D_b = 2.2$ in Fig. 6.3c) compared to the experiment. Also, from Fig. 6.4, one

can see that in the upstream regions of the IRZ (e.g. $x/D_b = 0.4$ and 0.6) the solid-body rotation is observable and the mean swirl velocity linearly depends on the radius. Meanwhile, the mean swirl velocities are over-predicted in the current LES, which probably results in the above mentioned over-prediction of the fuel jet decay. In both Figs. 6.3 and 6.4, the *r.m.s.* of axial and swirl velocities are consistently over-calculated (see $x/D_b = 0.4$ and 0.6), particularly close to the bluff body. Overall, the distributions of the velocity statistics reasonably follow the experiment and the agreement improves downstream.

Instantaneous contours of selected scalars and scalar dissipation rates are plotted in Fig. 6.5 and the time-averaged heat release rate $\tilde{\dot{q}}$ and OH mass fraction $\tilde{Y}_{OH}$ are compared to experiment in Fig. 6.6. An instantaneous image of OH from the experiment [Cavaliere et al., 2013] is also shown next to the computational $\tilde{Y}_{OH}$ in Fig. 6.6 to show some qualitative performances of the prediction. The white iso-lines showing the stoichiometric mixture fraction are highly distorted due to the strong turbulence. The flame is short ($x < 0.05$ m), severely fragmented and confined at the boundary of the IRZ and therefore is somewhat different from the unconfined Sydney swirl non-premixed flames [Masri et al., 2004]. One can see the flame shape of SMA2 case simulated by LES/3D-CMC, i.e. Figs 5.3 and 5.4. Negligible $\tilde{\dot{q}}$ along the ξ_{st} iso-lines (pointed by arrows in Fig. 6.5b) can occasionally be observed. The mixture fraction decays very quickly due to the fast mixing in IRZ. The fuel CH_4 is almost completely consumed upstream of the IRZ. It can be seen from Fig. 6.6(b) that $\tilde{Y}_{OH}$ is very localized, typically coincides with the ξ_{st} iso-lines, and qualitatively in line with the OH-PLIF image in Fig. 6.6(a), showing breaks along the front (pointed by arrows in Figs. 6.6a and 6.6b). The intermittent lift-off from the corner of bluff body observed in the experiment is also seen in the LES (see the left flame branch in Fig. 6.6b). The time-averaged $\tilde{Y}_{OH}$ and $\tilde{\dot{q}}$ in Figs. 6.6(d) and 6.6(f) show a mean flame shape in reasonable agreement with the experiment. The time-averaged mixture fraction shows effective mixing (Fig. 6.5e) and the average scalar dissipation is high along the fuel jet (Figs. 6.5f and 6.5g), with the resolved higher than the estimated sub-grid in most locations. Immediately downstream of the fuel jet tip along the axis, $\tilde{N}$ is high and thus in most instants the flame is quenched there.

Since the present simulations consider adiabatic wall conditions, we may expect that we do not accurately predict the heat release rate and OH mass fraction near the bluff body surface (see Figs. 6.6d and 6.6f) compared to the experimental results. A more detailed comparison with the measured statistics of lift-off will be presented later once the nature of local extinction is discussed. The influences of convective wall heat loss on the local extinction near the wall will be discussed in depth in Chapter 7. In general, we consider the agreement relatively satisfactory and this helps build confidence for further analysis.

6.3.2 Identification and quantification of local extinction

Three dimensional instantaneous iso-surfaces of stoichiometric mixture fraction $\xi_{st} = 0.055$ colored by the different characterizations of OH mass fraction are plotted in Fig. 6.7. A Comparison between Figs. 6.7(a) and 6.7(b) is made to show the difference of LES/0D-CMC and LES/3D-CMC in extinction prediction. In Fig. 6.7(a), the filtered OH mass fraction $\tilde{Y}_{OH}$ is predicted by Eq. (3.42), replacing $\widetilde{Y_{OH}|\eta}$ with a 0D-CMC solution $Y_{OH}|\eta$ with $N_0 = 50$ 1/s. The FDF $\tilde{P}(\eta)$ is modelled based on the $\tilde{\xi}$ and $\widetilde{\xi''^2}$ (see Eqs. 3.26−3.29) from an LES/3D-CMC instantaneous field. The contour in Fig. 6.7(a) shows some regions with relatively low $\tilde{Y}_{OH}$ as marked by symbol "A". Actually, these regions with low $\tilde{Y}_{OH}$ on the ξ_{st} iso-surfaces in Fig. 6.7(a) correspond to a local FDF $\tilde{P}(\eta)$ not having finite values around ξ_{st} in η-space, which is entirely caused by the local mixing state instead of chemistry. This has been also discussed by Ayache and Mastorakos [2012] and the LES/0D-CMC solver cannot include the turbulence−chemistry interaction, although it is more economical than the LES/3D-CMC solver as discussed in Sub-section 3.4.5. Figure 6.7(b) presents the LES/3D-CMC results of $\tilde{Y}_{OH}$ exactly corresponding to the same instantaneous field used in Fig. 6.7(a) and therefore their FDFs $\tilde{P}(\eta)$ are the same. The large area on the iso-surfaces with very low $\tilde{Y}_{OH}$ can be seen, e.g. the regions also marked by symbol "A". Therefore, the results from 3D-CMC simulations demonstrate the ability to predict the spatial variations of $\widetilde{Y_{OH}|\eta}$ and therefore the instantaneous localized extinction, compared to the results in Fig. 6.7(a). Since in Fig. 6.7(b) $\tilde{Y}_{OH}$ is also calculated with Eq. (3.42), the effects of FDF shape on local extinction prediction

can be indicated if the conditionally filtered OH mass fraction at stoichiometry, $\widetilde{Y_{OH}|\xi_{st}}$, is examined. Figure 6.7(c) presents the distribution of $\widetilde{Y_{OH}|\xi_{st}}$ on the ξ_{st} iso-surfaces which correspond to the same LES and CMC fields as in Fig. 6.7(b). Compared to the low $\tilde{Y}_{OH}$ regions in Fig. 6.7(b), the low $\widetilde{Y_{OH}|\xi_{st}}$ regions as marked by "A" become narrower. This implies that the analysis in 3D-CMC based on filtered quantities, $\tilde{f}$, may over-estimate the level of local extinction compared to that based on $\widetilde{f|\xi_{st}}$.

Figure 6.8 shows the filtered heat release rate $\tilde{\dot{q}}$, OH mass fraction $\tilde{Y}_{OH}$, temperature $\tilde{T}$, and scalar dissipation rate $\tilde{N}_{res}$ on a $y-z$ slice ($x/D_b = 0.59$). Numbers 1−5 mark different positions along the ξ_{st} iso-lines. It can be seen from Fig. 6.8(a) that in Points 1, 4, and 5, $\tilde{\dot{q}}$ is comparatively high, while in Points 2 and 3 it is very low. In instantaneous local extinction, very weak and, more strictly, nearly frozen reactivity should be reached and $\tilde{\dot{q}}$ is indeed negligible in Points 2 and 3. From Figs. 6.8(b)−6.8(d) it can be clearly seen that Point 3 corresponds to low $\tilde{Y}_{OH}$ and $\tilde{T}$ and high $\tilde{N}_{res}$ and thus undergoes localized extinction. Point 2, however, has very low $\tilde{\dot{q}}$ but high $\tilde{Y}_{OH}$ and $\tilde{T}$ and nearly zero $\tilde{N}_{res}$. This state corresponds to very fast chemistry and very low mixing rate (thus very large Damköhler number Da) and so the local heat release rate is very small. It is interesting how, in the same instant, different locations can have such widely different Damköhler numbers. From an extinction identification perspective, exclusively taking the local low heat release rate as the criterion to identify the local extinction could therefore over-predict the degree of extinction. Points 1, 4 and 5 can be considered to be reactive (non-zero $\tilde{\dot{q}}$) although from Fig. 6.8(b) very small $\tilde{Y}_{OH}$ can be seen. It is also seen that very low or medium scalar dissipation $\tilde{N}_{res}$ occurs there. OH-based identification has been widely used for the qualitative or quantitative analysis in both experimental and computational work [Hult et al., 2005; Juddoo and Masri, 2011; Kaiser and Frank, 2009; Prasad et al., 2013; Steinberg et al., 2011], but perhaps a more rigorous criterion for localized extinction is that there is low $\tilde{\dot{q}}$, $\tilde{Y}_{OH}$, $\tilde{T}$, and large $\tilde{N}_{res}$. This is evidenced by the simultaneous imaging of mixture fraction, scalar dissipation, temperature and fuel consumption rate made by Sutton and Driscoll [2007].

To indicate how the conditional reactive scalars Q_α evolve during localized extinction, the time series of conditionally filtered quantities at stoichiometry,

$\widetilde{\dot{q}|\xi_{st}}$, $\widetilde{Y_{OH}|\xi_{st}}$, $\widetilde{T|\xi_{st}}$ and $\widetilde{N|\xi_{st}}$, are plotted in Fig. 6.9. These data spanning about 0.005 s are extracted from one representative CMC cell in the flame region (x/D_b = 0.59, $y/D_b = 0$, $z/D_b = 0.56$; it is marked by the middle solid circle in Fig. 6.5a and termed as *CMC1* hereafter). As a reference, the extinction scalar dissipation rate at $\eta = \xi_{st}$ from the 0D-CMC calculation, $N|\xi_{st,0D} = 18.3$ 1/s, is denoted in Fig. 6.9(d). To quantify the local extinction in η-space, thresholds for $\widetilde{\dot{q}|\xi_{st}}$, $\widetilde{Y_{OH}|\xi_{st}}$, and $\widetilde{T|\xi_{st}}$ are defined as 10%, 10%, and 70% of their corresponding 0D-CMC counterparts from a simulation with $N_0 = 174$ 1/s, which is the extinction value $N_{0,ext}$ shown in Fig. 3.3. The above indicated value of $N|\xi_{st,0D} = 18.3$ 1/s corresponds to $N_0 = 174$ 1/s in the stand-alone 0D-CMC using the AMC shape for the conditional scalar dissipation $N|\eta$. These thresholds are 380 MJ/m^{3}s, 0.00024 and 1245 K, respectively, and are included using dash-dotted lines in Figs. 6.9(a)−6.9(c).

From Figs. 6.9(a) and 6.9(d), initially $\widetilde{\dot{q}|\xi_{st}}$ corresponds to fully burning state and then sharply decreases with gradually increased $\widetilde{N|\xi_{st}}$, which is very close to $N|\xi_{st,0D}$. This period (Period I) lasts about 0.001 s and local extinction occurs (very low $\widetilde{\dot{q}|\xi_{st}}$ and $\widetilde{Y_{OH}|\xi_{st}}$ and low $\widetilde{T|\xi_{st}}$ with relatively high $\widetilde{N|\xi_{st}}$). Then at t = 0.0228 s, $\widetilde{N|\xi_{st}}$ decays far below $\widetilde{N|\xi_{st}}$ and $\widetilde{Y_{OH}|\xi_{st}}$ and $\widetilde{T|\xi_{st}}$ increase. From t = 0.0236 s to $t = 0.0242$ s (Period II), very low heat is liberated locally while the scalar dissipation is nearly zero. Period II has the fully burning composition. At $t = 0.0242$ s, *CMC1* experiences a sharp increase of $\widetilde{N|\xi_{st}}$, and the conditional reactive scalars seem quenched again. This extinction event lasts around 0.0008 s (Period III) during which $\widetilde{N|\xi_{st}} < N|\xi_{st,0D}$. At $t = 0.025$ s, *CMC1* is ignited again and is reactive until $t = 0.0258$ s when a peak $\widetilde{N|\xi_{st}}$ appears. Then *CMC1* is extinguished (Period IV) again. Therefore, local extinction events occur in Periods I, III and IV, while for Period II we have combustion with very high Damköhler number *Da*. For Periods I, III and IV, the quantities, $\widetilde{\dot{q}|\xi_{st}}$, $\widetilde{Y_{OH}|\xi_{st}}$, and $\widetilde{T|\xi_{st}}$, fall below their individual thresholds mentioned above. It should be emphasized that this behavior of *Da* also exists in other positions besides *CMC1* and is directly related to the evolutions of $\widetilde{N|\xi_{st}}$ in the studied swirl-stabilized non-premixed flame presented in Fig. 6.9(d) and the unconditional one $\tilde{N}$ which is not shown here. This feature of *Da* is not observed in the upstream part of the RZ in the Sydney swirl flame SMA2 based on the similar time series analysis not

presented in Chapter 5.

Re-ignition in η-space would not happen automatically as soon as $\widetilde{N|\xi_{st}}$ drops from the critical value, which is also observed in LES/CMC of the Sandia flame F [Garmory and Mastorakos, 2011] and in DNS of planar non-premixed ethylene jet flames [Lignell et al., 2011]. In the studies by Lignell et al. [2011], this delay is attributed to the increased scalar dissipation rate after the onset of local extinction. However, based on the present results (e.g. Period III) and the findings by Garmory and Mastorakos [2011], it can also be caused by the inadequate transport of heat and species from the neighbouring CMC cells and in this sense re-ignition events are affected by both local scalar dissipation and transport. In the DNS studies by Lignell et al. [2011], this mechanism is loosely referred to as re-ignition by premixed flame propagation, while in the present CMC equations, i.e. Eqs. (3.35) and (3.36), such a mechanism is captured by the physical transport terms T_1, T_2 and T_5. To consolidate this argument, the following numerical experiment is conducted: the conditional flame structures Q_α and scalar dissipation rate $\widetilde{N|\eta}$ before re-ignition (e.g. $t = 0.0228$ s) are extracted and used as the initial conditions for the stand-alone 0D-CMC calculation. It is shown that the input conditional flame structures would not be ignited as the calculation proceeds. Since the transient 0D-CMC governing equations do not have the flow transport terms, this confirms that the re-ignition event cannot happen without them.

Further analysis is made to the contributions of the individual terms in the three dimensional CMC governing equations, i.e. Eq. (3.35), to conditionally filtered OH mass fraction, $\widetilde{Y_{OH}|\eta}$, during the local extinction event at $t = 0.024245$ s shown in Fig. 6.9. Figure 6.10 plots the time evolutions of the individual CMC term from $t = 0.024$ s (fully burning) to $t = 0.0243$ s (extinguishment). At $t = 0.024$ s, the contribution from the chemistry, $T_4 = \widetilde{W_\alpha|\eta}$, is intermediate and those from the micro-mixing and sub-grid diffusion terms, $T_3 = \widetilde{N|\eta}\partial^2 Q_\alpha/\partial\eta^2$ and $T_5 = e_f$, are very close to zero. Besides, the conditional convection and dilatation terms, $-T_1 = -\nabla\cdot(\widetilde{\mathbf{U}|\eta}Q_\alpha)$ and $T_2 = Q_\alpha\nabla\cdot\widetilde{\mathbf{U}|\eta}$, basically have the counter-balanced contribution (similar magnitude but sits in LHS and RHS of Eq. 3.35 respectively) to $\widetilde{Y_{OH}|\eta}$. Therefore, this cell still has the reactions to produce $\widetilde{Y_{OH}|\eta}$ in η-space. Then at $t = 0.0242$ s, two pronounced changes: the

chemistry becomes stronger than that at $t = 0.024$ s; the micro-mixing term starts to show finite contribution, mainly appearing in the form of a sink term near $\eta = \xi_{st}$. After that until $t = 0.02425$ s, the contributions from the chemistry terms progressively become weak and at $t = 0.0243$ s, the flame structure in the investigated CMC cell is close to extinction. One can see that the time used for a complete transient localized extinction is $O(0.0001$ s). Furthermore, even if at $t = 0.0243$ s, the chemistry term is not equal to zero and, conversely, it becomes a sink term. This indicates that, for local extinction events, complete termination of the reactions ($\widetilde{W_\alpha|\eta} = 0$) is difficult to be achieved due to the nonlinearity of the reaction system itself, flow transport and local turbulence. During this very short period, the conditional scalar dissipation rate $\widetilde{N|\eta}$ play a significant role as a sink term while the contributions from flow transport related terms are negligible. As such, more strictly, based on the results in Fig. 6.10, transient local extinction from a fully reactive flame structure in η-space corresponds to a state in which the reaction system can not sustain itself due to external factors like high scalar dissipation.

Figure 6.11 presents the contributions of the individual CMC terms corresponding to the re-ignition event at $t = 0.02283$ s demonstrated in Fig. 6.9. At $t = 0.0228$ s in Fig. 6.11(a), the contributions from the CMC terms are similar to those in Fig. 6.10(f), indicating the occurrence of the local extinction in the discussed CMC cell. However, the convection term has the finite effect in Fig. 6.11(a). This is not observed in Fig. 6.10(f). The similar CMC term contributions exist at $t = 0.02281$ s in Fig. 6.11(b) and then at $t = 0.02282$ s in Fig. 6.11(c) the sink term effect of chemistry first decreases at approximately $\eta = 0.04$ in mixture fraction space. At $t = 0.02283$ s and afterwards presented in Figs. 6.11(d)−6.11(f), the contribution from chemistry term dominates, from which one can expect that the reaction system reaches the completely burning state. The time for the onset of re-ignition is similar to that for local extinction, i.e $O(0.0001$ s). Additional attention should be paid to the role of scalar dissipation rate during the re-ignition process. As indicated by Fig. 6.9(d), $\widetilde{N|\xi_{st}}$ has finite values from $t = 0.0228$ s to $t = 0.02285$ s. The contributions from micro-mixing to $\widetilde{Y_{OH}|\eta}$ are always negative (i.e. sink term). Meanwhile, the magnitudes increase with time as presented in Fig. 6.11 and even balance the contribution

from the chemistry term at $t = 0.02285$ s. This argument concerning the role of scalar dissipation during the re-ignition event is different from what was found by Lignell et al. [2011]. This analysis based Fig. 6.11 confirms that in the CMC model the re-ignition transient is triggered by the flow transport in physical space.

As a supplement to Fig. 6.9, Fig. 6.12 presents the full profiles of selected quantities from *CMC1* spanning $t = 0.022-0.025$ s. The evolutions of conditional flame structures during the above discussed local extinction and re-ignition events are clearly shown in Figs. 6.12(a)−6.12(b) and 6.12(d)−6.12(f). During the extinction periods (i.e. before $t = 0.02285$ s and after $t = 0.024245$ s), the pronounced fuel leakage can be seen around ξ_{st} in η-space demonstrated in Fig. 6.12(e). Also, one can see from Fig. 6.12(f) that CH_2O, as the key intermediate from the CH_4 oxidization, has higher mass fraction in the extinction periods than in the fully burning state (e.g. $t = 0.02285-0.024245$ s). This characteristic is different from those of OH demonstrated in Fig. 6.12(d). When local extinction occurs, $\widetilde{Y_{OH}|\eta}$ is almost zero in the whole η-space. As shown in Fig. 6.12(c), the conditional scalar dissipation rate $\widetilde{N|\eta}$ modelled with Eq. (3.60) changes considerably with time, which reflects the strong influence from variations of mixing fields on the localized extinction and re-ignition.

$\widetilde{\dot{q}|\xi_{st}}$, $\widetilde{T|\xi_{st}}$, $\widetilde{Y_{OH}|\xi_{st}}$ and $\widetilde{Y_{CH_4}|\xi_{st}}$ from *CMC1* are plotted in Fig. 6.13 for the whole simulated time. For reference, the 0D-CMC results with high ($N_0 = 170$ 1/s), intermediate ($N_0 = 50$ 1/s), and low ($N_0 = 5$ 1/s) scalar dissipation rates are also shown. A wide scatter (quantified by the large *r.m.s.* in Fig. 6.13) can be observed for all quantities, indicating the frequent transition between burning and frozen conditional distributions. During the extinction event, the conditional profiles of $\widetilde{Y_{OH}|\xi_{st}}$ and $\widetilde{\dot{q}|\xi_{st}}$ are very close to the inert mixing lines (i.e. zero). $\widetilde{T|\xi_{st}}$ and $\widetilde{Y_{CH_4}|\xi_{st}}$ in contrast take time to diffuse to the inert values and therefore very cold temperatures and inert fuel η-space distributions are not reached.

In order to quantify the deviation from the fully burning state and hence the occurence of local extinction in mixture fraction space, the conditional reactedness [Masri et al., 1996] is calculated for each CMC cell by

$$\widetilde{b_\alpha|\eta} = \frac{\widetilde{Y_\alpha|\eta} - Y_{\alpha,m}|\eta}{Y_{\alpha,b}|\eta - Y_{\alpha,m}|\eta} \tag{6.1}$$

where $Y_{\alpha,b}|\eta$ and $Y_{\alpha,m}|\eta$ come from fully burning 0D-CMC solutions with N_0 = 5 1/s (which is about 3% of the extinction value) and inert mixing, respectively. Clearly, $\widetilde{b_\alpha|\eta} = 0$ when the quenching occurs, while it is close to or larger than unity when the conditional solutions are fully burning [Masri et al., 1996]. In particular, $\widetilde{b_\alpha|\eta} > 1$ indicates the super-equilibrium of the conditional flame structures. The PDFs of the conditional reactedness at stoichiometry for temperature and hydroxyl, NO, CO mass fractions for three CMC cells (*CMC1*, *CMC2* and *CMC3* marked by the three white solid circles in Fig. 6.5a) are shown in Fig. 6.14. Most samples of $\widetilde{T|\xi_{st}}$ fall within $0.9 \leq \widetilde{b_T|\xi_{st}} \leq 1.1$, but there are still some data in $\widetilde{b_T|\xi_{st}} \leq 0.6$, indicating that the conditional temperatures in these two cells experience frequent extinction (Fig. 6.14a), consistent with the existence of the peak at 0 for the OH (Fig. 6.14b). The PDFs of $\widetilde{b_{Y_{NO}}|\xi_{st}}$ and $\widetilde{b_{Y_{CO}}|\xi_{st}}$ in Figs. 6.14(c) and 6.14(d) are relatively broad. For NO, two peaks exist at $\widetilde{b_{Y_{NO}}|\xi_{st}} \approx 0.1$ and $\widetilde{b_{Y_{NO}}|\xi_{st}} \approx 0.5$–$0.6$. For CMC1 and CMC2 that lie in the high scalar dissipation rate region (see Figs. 6.5f and 6.5g), the PDFs of stoichiometric reactedness for temperature and OH have obvious bimodality, while for NO and CO this feature is less pronounced. This is likely to be because the chemistry of NO and CO will freeze during an extinction event and hence these species will be evident for some time in η-space. *CMC3* is located in a region with low scalar dissipation (see Figs. 6.5f and 6.5g) and so no local extinction happens and therefore the PDF of $\widetilde{b_T|\xi_{st}}$ is concentrated at high values and $\widetilde{b_{Y_{OH}}|\xi_{st}}$, $\widetilde{b_{Y_{NO}}|\xi_{st}}$ and $\widetilde{b_{Y_{CO}}|\xi_{st}}$ have wide distributions. The conditional mass fractions of OH, NO and CO have large fluctuations in spite of the relatively continuous strong reactivity in *CMC3* due to the fluctuations of the scalar dissipation and the frequent quenching of the neighbouring cells.

6.3.3 Lift-off height

In the present swirl non-premixed flame, lift-off from the bluff-body surface (shown in Figs. 6.5b and 6.6b) is an important dynamic phenomenon caused by local extinction at the flame base. In this Sub-section, the statistics of the lift-off height h_L in the $x-y$ plane are investigated. To be consistent with the experiment [Cavaliere et al., 2013], h_L is defined as the streamwise distance be-

tween the bluff body to the position along the ξ_{st} iso-line where resolved OH mass fraction critically exceeds the 0D-CMC threshold (i.e. 0.00024). 200 samples are extracted equally from both left and right flame branches and 140 samples of those showed lifted flame. We consider here only snapshots with $h_L > 0.0005$ m, which is about one nominal CMC cell size near the bluff body edge.

The PDFs of h_L from the measurement [Cavaliere et al., 2013] and the LES are shown in Fig. 6.15. The mean lift-off height from LES/3D-CMC is 9.75 mm while that from measurement is 5 mm, but the overall shape is consistent and the long tail at large lift-off heights is reproduced. The PDF of lift-off height h_L at about $10-20$ mm is higher in the simulation results than the experimental ones, which may be due to the overprediction of turbulence intensity close to the bluff body as shown in Figs. 6.3 and 6.4, thereby leading to more intensive extinction at those distances. The results in Fig. 6.15 further demonstrate the overall satistifactory capability of LES/3D-CMC in reproducing the local extinction in swirl non-premixed flames.

6.4 Conclusions

The LES/3D-CMC model with detailed chemistry is used to simulate a swirl-stabilised non-premixed flame with local extinction. The LES/3D-CMC simulations reproduce reasonably the flow field and the global flame characteristics (e.g. mean OH-PLIF, OH* chemiluminescence, PDF of lift-off height). The occurrence of localized extinction is typically manifested by low heat release rate and OH mass fraction and low or medium temperature and is accompanied by high scalar dissipation rates. This implies that joint analysis of above quantities are required in extinction investigations for modellers and experimentalists. In mixture fraction space the CMC cells undergoing local extinction have relatively wide scatter between inert and fully burning solutions while for fully burning CMC cells the instantaneous CMC solutions follow closely fully-burning distributions. The reactedness index is analyzed to quantify how far the conditional profiles deviate from the reference fully burning state. The PDFs of reactedness at the stoichiometric mixture fraction demonstrate some extent of bimodality, showing the events of local extinction and re-ignition and their relative occurrence frequency.

6.5 Figures for Chapter 6

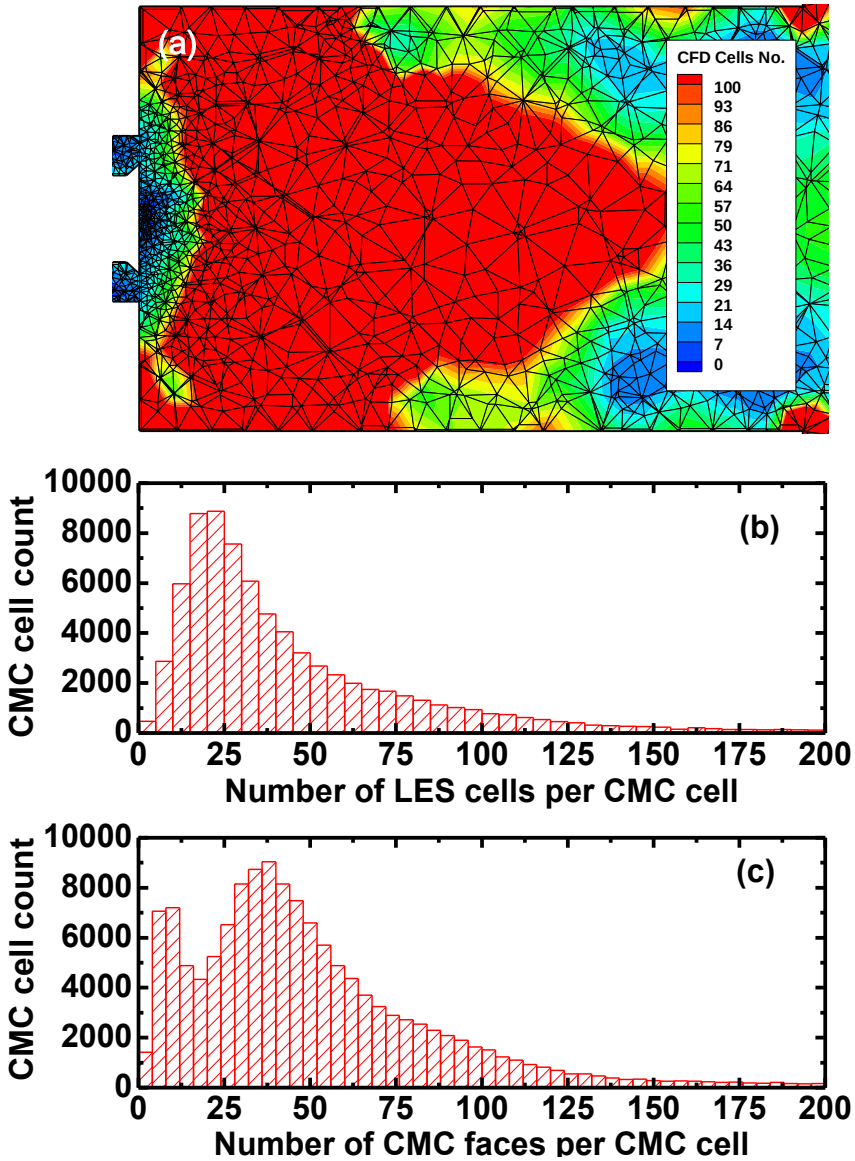

Figure 6.1: (a) Contour of LES cell number for each CMC cell ϱ^{CMC} in the combustion chamber; (b) distribution of LES cell number for each CMC cell ϱ^{CMC} within the flame region ($0 < x/D_b < 2.4$); and (c) distribution of face number for each CMC cell F^{CMC}. The black lines in (a) is for demonstration only but do not represent the real CMC cells.

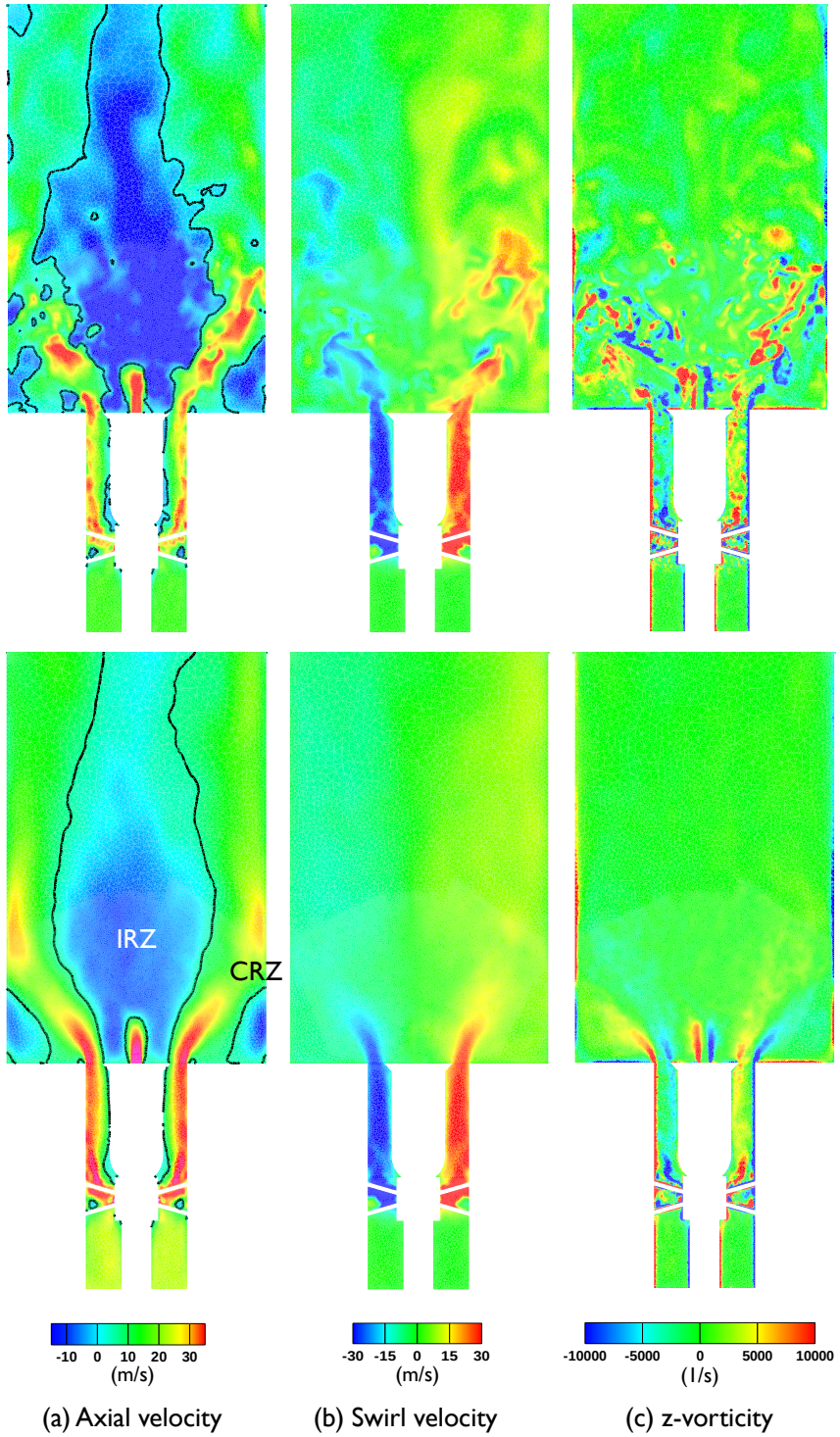

Figure 6.2: Contours of (a) axial velocity, (b) swirl velocity and (c) z-vorticity on the $x-y$ plane. First row: instantaneous; second row: mean. The lines in (a) denote the iso-lines of zero axial velocity. IRZ and CRZ are marked in (a).

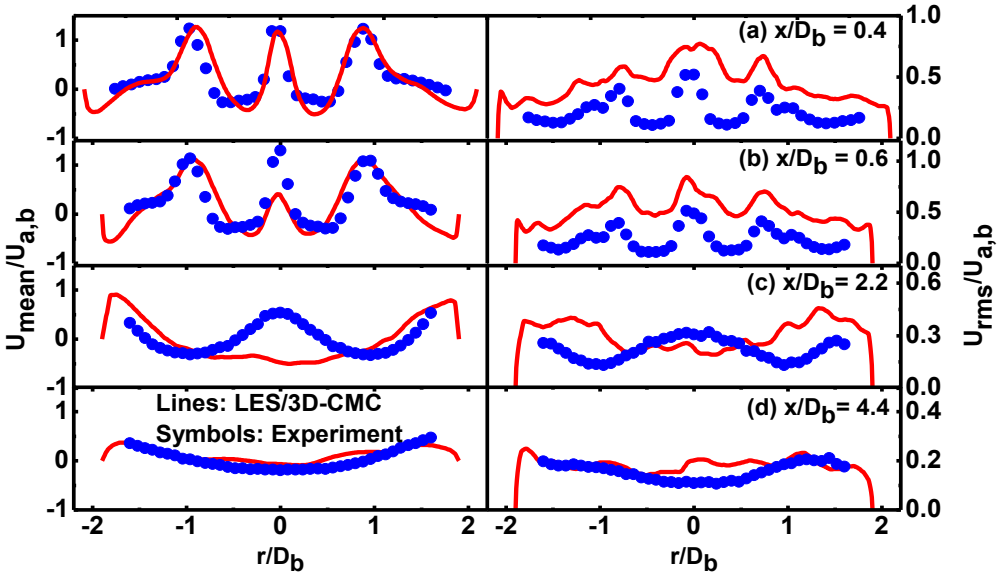

Figure 6.3: Radial profiles of mean and *r.m.s.* axial velocity from the LES (lines) and experiment (symbols).

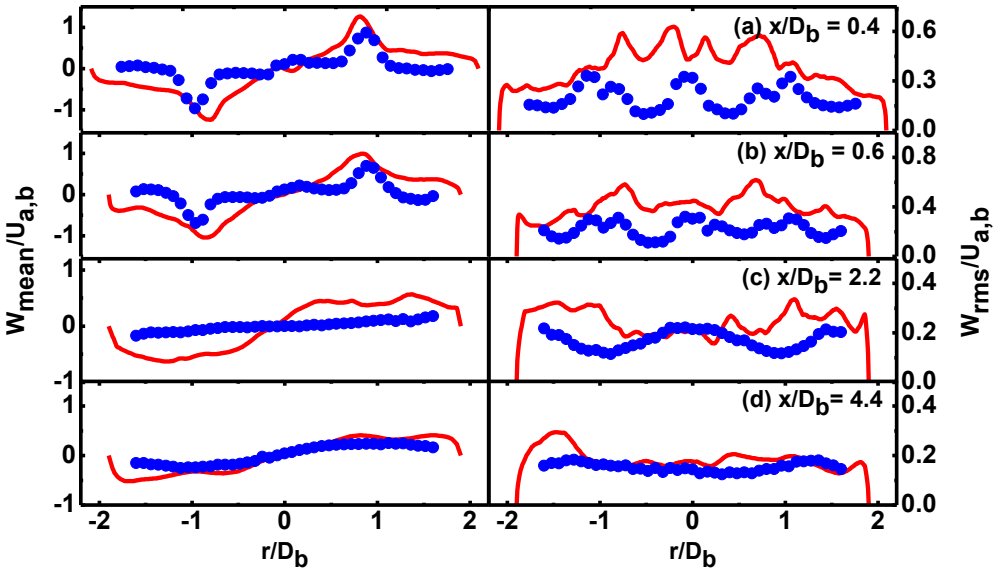

Figure 6.4: Radial profiles of mean and *r.m.s.* swirl velocity from the LES and experiment. The legend is same as that in Fig. 6.3.

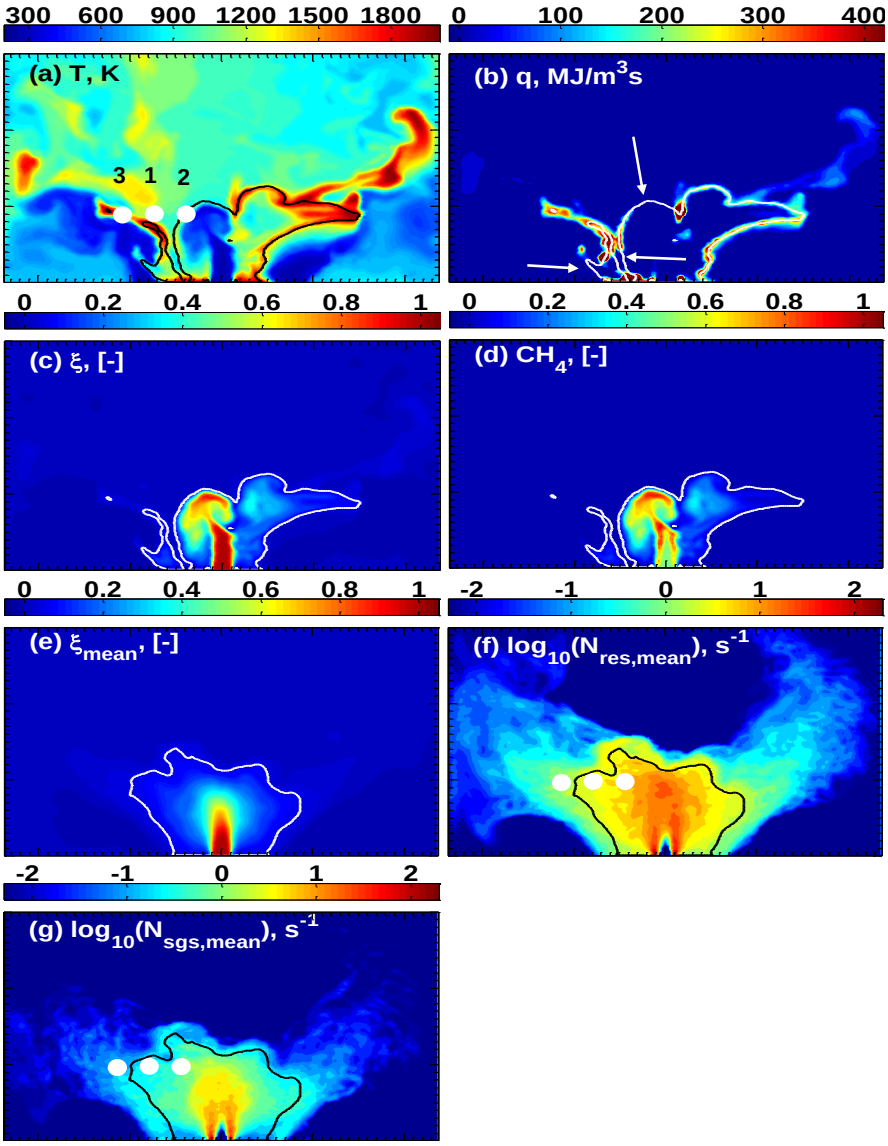

Figure 6.5: Instantaneous (a) temperature, (b) heat release rate, (c) mixture fraction, (d) CH_4 mass fraction, (e) mean mixture fraction, and logarithm of mean (f) resolved and (g) sub-grid scalar dissipation. Images shown are 0.095 m $\times$ 0.06 m. Lines: instantaneous or mean stoichiometric mixture fraction. Solid circles in (a), (f) and (g): Cells *CMC1*, *CMC2* and *CMC3*. Arrows in (b) point to low heat release rate regions along the iso-lines of ξ_{st}.

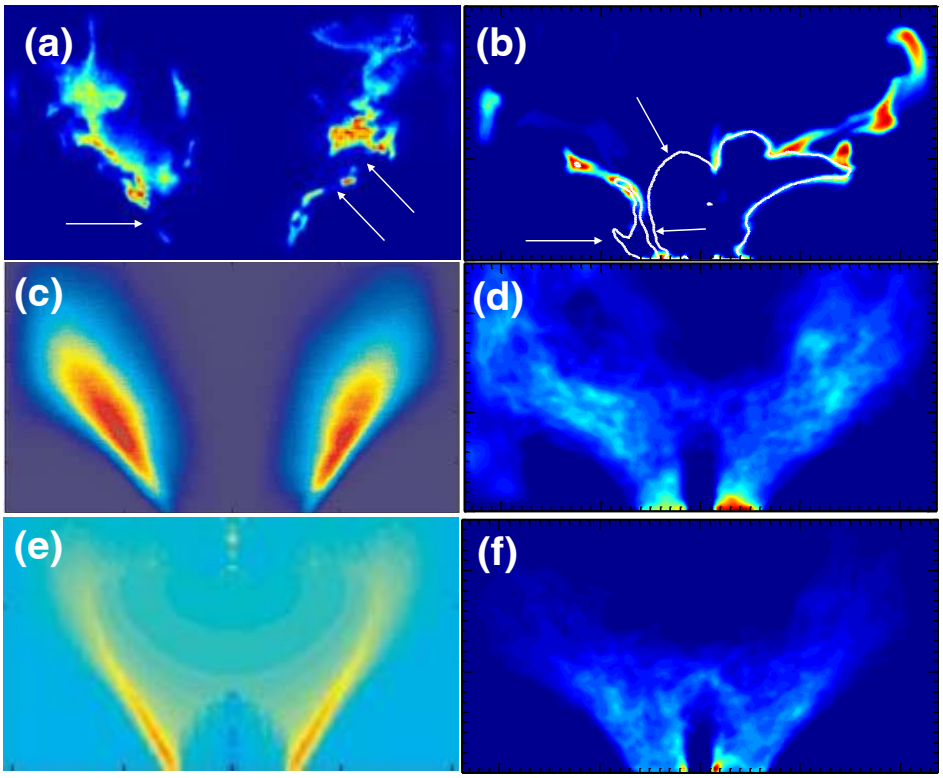

Figure 6.6: Comparisons of the numerical predictions (right column: b, d, f) with experimental data [Cavaliere et al., 2013] (left column: a, c, e): (a, b) instantaneous and (c, d) mean OH-PLIF from the experiment and simulated OH mass fraction, (e) mean OH* chemiluminescence after inverse Abel transform from the experiment and (f) mean heat release rate from the simulation. Images shown are 0.095 m $\times$ 0.06 m. Arrows in (a) and (b) point to low OH regions. Blue: low magnitude; red: strong magnitude.

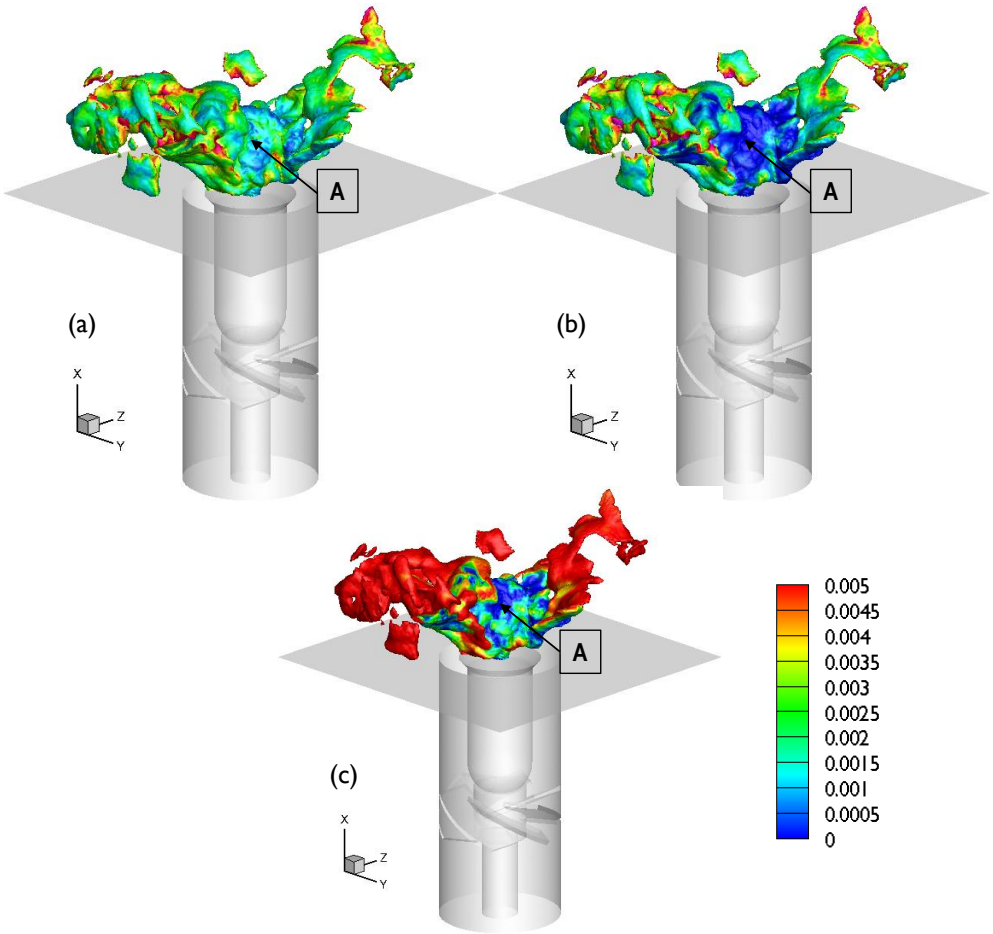

Figure 6.7: Instantaneous iso-surfaces of stoichiometric mixture fraction ξ_{st} colored by instantaneous unconditionally filtered OH mass fraction $\tilde{Y}_{OH}$ calculated respectively from (a) a single constant 0D-CMC solution with $N_0 = 50$ 1/s and (b) instantaneous 3D-CMC solutions and (c) by conditionally filtered OH mass fraction $\widetilde{Y_{OH}|\xi_{st}}$. Regions pointed by symbol "A" have low OH mass fraction.

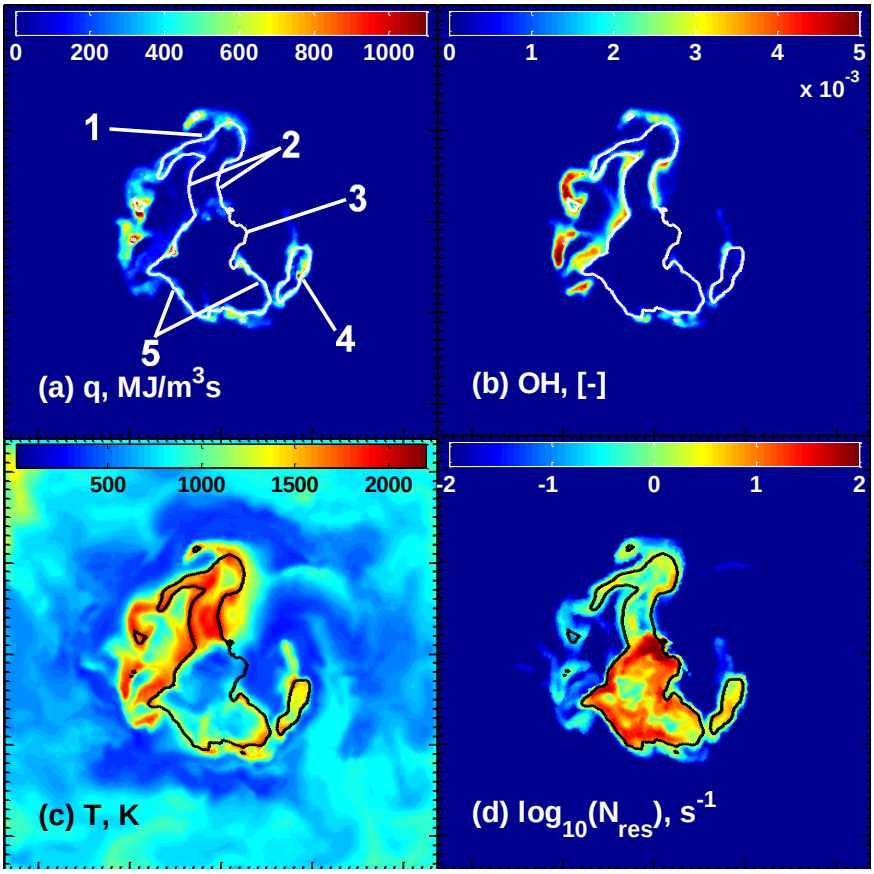

Figure 6.8: Instantaneous contours in the $y-z$ plane ($x/D_b = 0.59$) of (a) $\tilde{\dot{q}}$, (b) $\tilde{Y}_{OH}$, (c) $\tilde{T}$ and (d) logarithm of $\tilde{N}_{res}$. Lines: stoichiometric mixture fraction ξ_{st}.

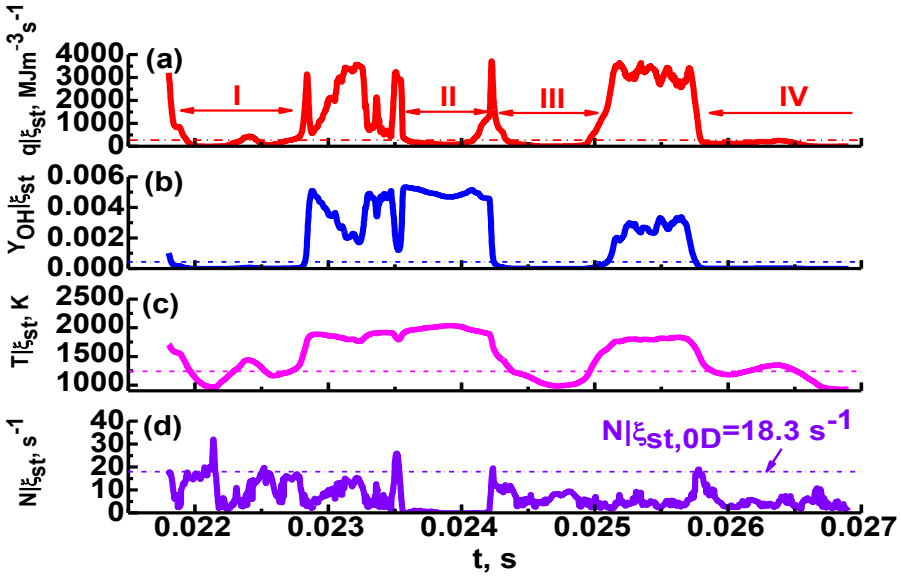

Figure 6.9: Time series of conditionally filtered (a) heat release rate, (b) OH mass fraction, (c) temperature and (d) scalar dissipation rate at $\eta = \xi_{st}$ for *CMC1* (marked in Fig. 6.5a). Dash-dotted lines: the thresholds from 0D-CMC for defining extinction.

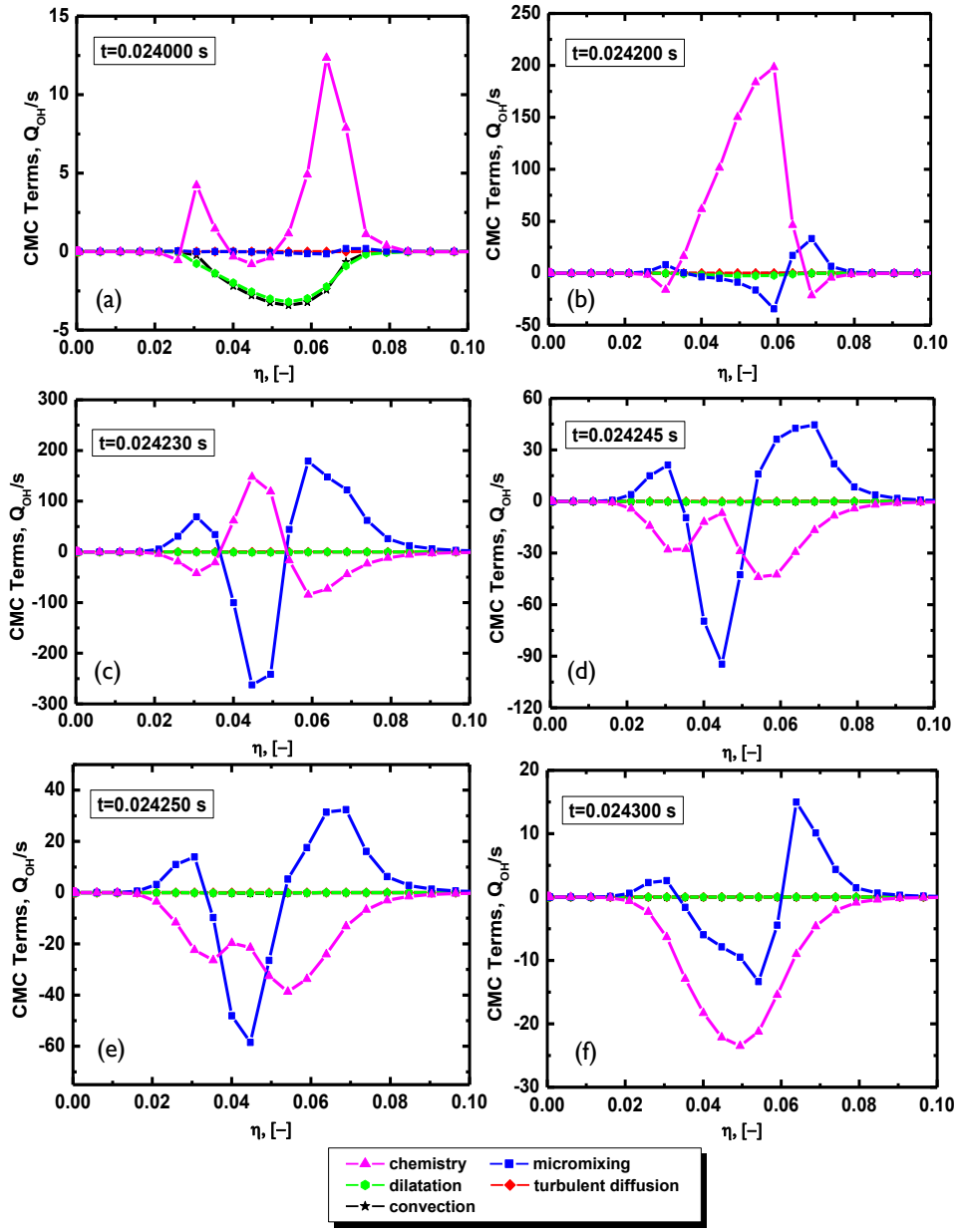

Figure 6.10: Time evolutions of the contributions of the individual terms in the CMC governing equations to conditionally filtered OH mass fraction $\widetilde{Y_{OH}|\eta}$ during the localized extinction event occurring at $t = 0.024245$ s for *CMC1*. The CMC terms correspond to the following terms in Eq. (3.35): convection $=-T_1$, dilatation $= T_2$, micro-mixing $= T_3$, chemistry $= T_4$, sub-grid scale diffusion $= T_5$.

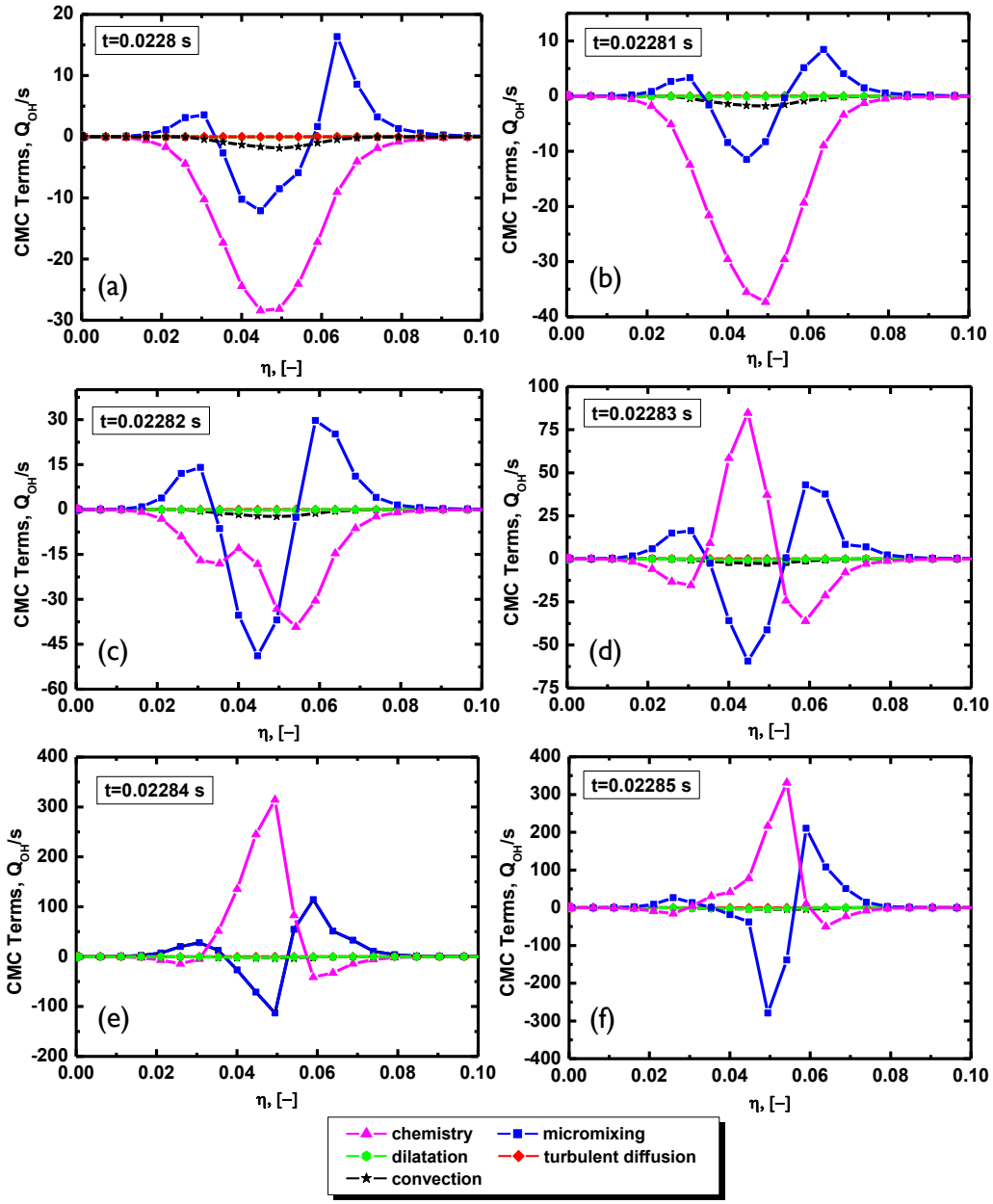

Figure 6.11: Time evolutions of the contributions of the individual terms in the CMC governing equations to conditionally filtered OH mass fraction $\widetilde{Y_{OH}|\eta}$ during the re-ignition event occurring at $t = 0.02283$ s for *CMC1*. The expressions for the CMC terms are the same as those in Fig. 6.10.

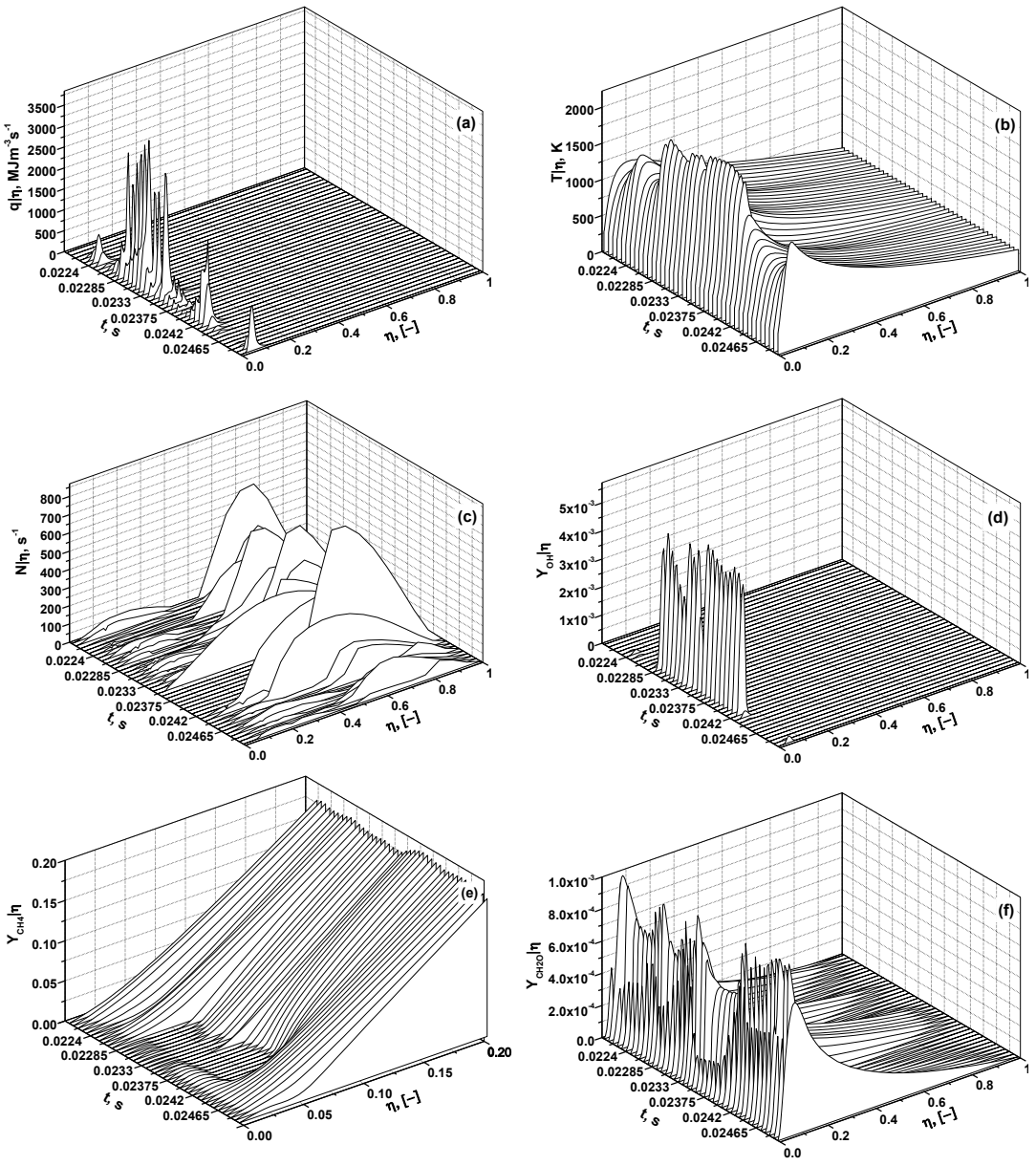

Figure 6.12: Evolutions of conditionally filtered (a) heat release rate $\widetilde{\dot{q}|\eta}$, (b) temperature $\widetilde{T|\eta}$, (c) scalar dissipation rate $\widetilde{N|\eta}$, (d) OH mass fraction $\widetilde{Y_{OH}|\eta}$, (e) CH_4 mass fraction $\widetilde{Y_{CH_4}|\eta}$ and (f) CH_2O mass fraction $\widetilde{Y_{CH_2O}|\eta}$ within $t = 0.022-0.025$ s for *CMC1*.

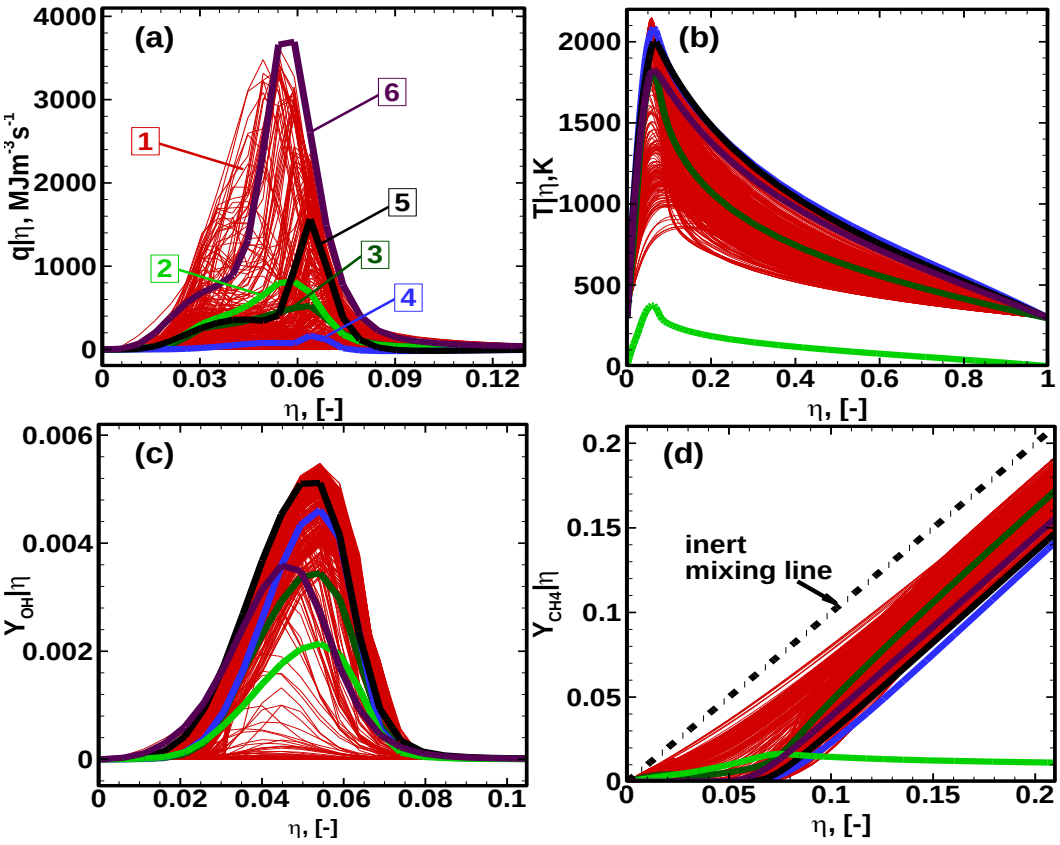

Figure 6.13: Conditional (a) heat release rate, (b) temperature and mass fractions of (c) OH and (d) CH_4 for *CMC1*. Line 1 indicates instantaneous conditional profiles while Lines 2 and 3 their *r.m.s.* and mean, respectively. Lines 4−6 indicate stand-alone 0D-CMC solutions with low, medium and high scalar dissipation rates (N_0 = 5, 50 and 170 1/s), respectively.

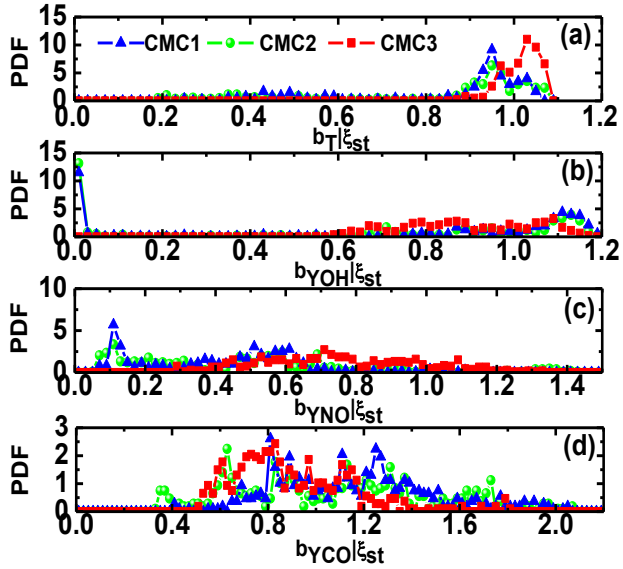

Figure 6.14: Probability density functions of reactedness at $\eta = \xi_{st}$, $\widetilde{b_\alpha|\xi_{st}}$, from (a) temperature, mass fractions of (b) OH, (c) NO and (d) CO for *CMC1* (triangles), *CMC2* (circles) and *CMC3* (squares). *CMC1*, *CMC2* and *CMC3* are marked in Fig. 6.5(a).

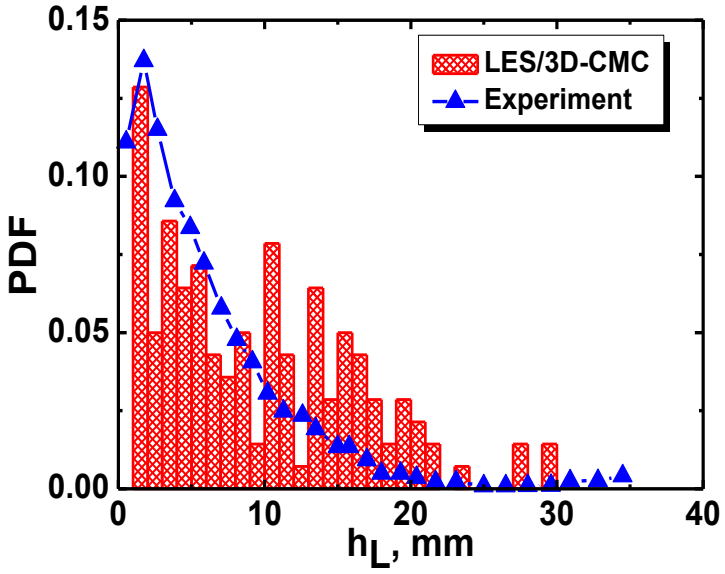

Figure 6.15: Probability density functions of lift-off height. Histogram: LES/3D-CMC, line: experiment [Cavaliere et al., 2013].

Chapter 7

Near-wall Local Extinction

7.1 Introduction

Flame−wall interaction is a physicochemical process in which flames and wall surfaces affect each other through the coupling of chemical kinetics, momentum, and heat transfer [Poinsot and Veynante, 2005]. For instance, when flame fronts approach the vicinity of walls or propagate in tubes, the former are cooled and the latter are heated with strong heat fluxes, accompanied by the variations of near-wall flame reactivity and flow properties like density and viscosity. Flame−wall interactions exist in meso- and micro-scale combustion devices [Ju and Maruta, 2012; Kaisare and Vlachos, 2012], laboratory scale burners [Poinsot and Veynante, 2005], industrial combustion systems such as internal combustion engines and gas turbine combustors [Lefebvre, 2005], and building fires [Drysdale, 1999].

The underlying physics of flame−wall interactions in laminar flows as well as how flame extinction is induced and influenced by walls have been studied extensively in different aspects. As one of the most critical quantities for flame−wall interaction, the quenching distance was investigated theoretically and numerically with one-step global chemistry [Adamczyk and Lavoie, 1978; Carrier, 1979; Hocks et al., 1981; v. Karman and Millan, 1953; Westbrook et al., 1981]. In addition, how the chemical kinetics (e.g. chaining-branching and radical recombination reactions) behave during near-wall flame extinction was studied in terms of temperature dependence [Westbrook et al., 1981] and the radical kinetics [Egolfopoulos

et al., 1997; Hocks et al., 1981]. The strong coupling between the wall and flame also leads to the flame bifurcations with respect to the varying parameters like wall temperature, equivalence ratio and strain rate [Nakamura et al., 2009; Vlachos and Schmidt, 1993; Zhang and Chen, 2013]. The effects of the laboratory scale burner geometries (e.g. curved and slit burners as well as perforated-plates) on the heat exchange and relevant flame dynamics (e.g. flash-back) were examined [Altay et al., 2010; Mallens and Goey, 1998; Oijen and Goey, 2000] and the correlations between wall temperature and heat flux were also reported [Popp and Baum, 1997].

All the above studies contribute to understanding flame−wall interactions for laminar premixed combustion with simplified flame configurations and/or chemical mechanisms. However, investigations for non-premixed flames interacting with walls are quite few and, furthermore, the existence of turbulence in realistic burners renders the interactions more complicated: the turbulence can stretch the flame fronts and the flame can dampen the local turbulence [Poinsot and Veynante, 2005], while the wall would modify the temporal and spatial turbulence scales near the wall [Jiménez, 2013]. Therefore, it is of practical significance to account for the turbulence effects on flame–wall interaction and the incurred flame extinction. This is of particular importance for burners where flames are anchored close to walls such as bluff-body stabilisers, which is the topic studied in this Chapter.

Concerning modelling the flame−wall interactions, the heat transfer between the turbulent flame and chamber wall has been studied in the LES context. For instance, wall functions based on the temperature logarithmic law were used for predicting the wall heat fluxes [Grotzbach, 1987; Schmitt et al., 2007]. However, the inclusion of wall heat loss into advanced combustion models is not straightforward due to the implementations needed to solve the energy equation. The enthalpy defect concept was first proposed by Bray and Peters [1994] and used for defining the enthalpy deviation from the adiabatic profiles in mixture fraction space, caused by volumetric radiation and/or boundary heat loss. It was introduced into the flamelet model for wall heat loss by Hergart and Peters [2001] and a similar approach was adopted by Song and Abraham [2004] to improve the near-wall flame structure calculations in modelling of diesel combustion.

The enthalpy defect approach was also adopted in the CMC modelling for a three dimensional turbulent non-premixed syngas flame with a cooling wall [Kim et al., 2008]. The additional term representing the wall heat loss was included into the governing equations of conditional mean temperature in three dimensional CMC method by De Paola et al. [2008] who simulated combustion in a direct-injection heavy duty diesel engine. The above investigations were based on RANS and therefore could not analyse the unsteady heat transfer between the wall and flame and how the wall heat loss affects the transient flame dynamics. For flames stabilised by bluff body stabilisers approaching blow-off, it has been shown by Kariuki et al. [2012] that flame elements lie very close to the bluff body in a bluff body recirculating premixed flame, and similar observations were made by Cavaliere et al. [2013] for non-premixed flames close to extinction. The effects of the wall heat loss on the local extinction and lift-off of swirl non-premixed flames close to the bluff body need to be examined and to be included in the simulation method.

The goal of the current Chapter is to apply LES with a three dimensional sub-grid CMC combustion model to a swirl-stabilized non-premixed methane flame from the Cambridge swirl burner and the study is focused on the effects of wall heat loss on localized extinction near the bluff body. The wall heat loss is modelled by introducing an additional term in the RHS of conditionally filtered total enthalpy equation. The LES/3D-CMC numerical implementations and the information about the flow investigated are briefly given in Section 7.2 and Section 7.3 presents the main results and discussion, followed by the conclusions in Section 7.4.

7.2 Mathematical formulation and flow considered

7.2.1 LES and CMC modelling

The LES numerics used for this Chapter are identical to those for Chapter 6, which have been mentioned in Section 6.2.1. To include the convective wall heat

loss in the CMC model, an additional term is introduced into the RHS of Q_h governing equation for CMC cells (i.e. Eq. 3.36) adjacent to a wall [De Paola et al., 2008], i.e.

$$\begin{aligned}\int_{\Omega^{CMC}} \frac{\partial Q_h}{\partial t} d\Omega + \int_{\Omega^{CMC}} \nabla \cdot \left(\widetilde{\mathbf{U}|\eta} Q_h\right) d\Omega = \\ \int_{\Omega^{CMC}} Q_h \nabla \cdot \widetilde{\mathbf{U}|\eta} d\Omega + \int_{\Omega^{CMC}} \widetilde{N|\eta} \frac{\partial^2 Q_h}{\partial \eta^2} d\Omega + \\ \int_{\Omega^{CMC}} \nabla \cdot \left(D_t \nabla Q_h\right) d\Omega + \int_{\Omega^{CMC}} \widetilde{q_{W,\Omega}|\eta} d\Omega,\end{aligned} \tag{7.1}$$

in which $\widetilde{q_{W,\Omega}|\eta}$ is the conditionally filtered volumetric heat loss and is only active for the near-wall CMC cells. This term is modelled as

$$\widetilde{q_{W,\Omega}|\eta} = -H \left(Q_T - T_W\right), \tag{7.2}$$

in which T_W is the wall temperature. The heat transfer coefficient H in Eq. (7.2) is predicted through [Hergart and Peters, 2001]

$$H = \frac{\tilde{q}_{W,\Omega}}{\overline{\rho_\eta} \int_0^1 \left(Q_T - T_W\right) \tilde{P}\left(\eta\right) d\eta}. \tag{7.3}$$

The quantity $\tilde{q}_{W,\Omega}$ in Eq. (7.3) (in units of $\mathrm{W/m^3}$) is the filtered volumetric heat loss which is calculated through volume-averaging of the magnitude of the wall surface heat flux $\tilde{q}_{W,S}$ (in units of $\mathrm{W/m^2}$) as

$$\tilde{q}_{W,\Omega} = \frac{\int_{\partial\Omega} \tilde{q}_{W,S} dS}{V^{LES}}, \tag{7.4}$$

where $\partial\Omega$ denotes the faces of the LES cell. Here the surface heat flux magnitude $\tilde{q}_{W,S}$ is estimated from the LES as

$$\tilde{q}_{W,S} = -\tilde{q}^l_{W,S} - \tilde{q}^t_{W,S} = \lambda \nabla_n \tilde{T} + \lambda_t \nabla_n \tilde{T}. \tag{7.5}$$

In Eq. (7.5), $\tilde{T}$ is the filtered temperature and is predicted through

$$\tilde{T} = \int_0^1 Q_T \tilde{P}(\eta)\, d\eta = \int_0^1 \widetilde{T|\eta} \tilde{P}(\eta)\, d\eta \tag{7.6}$$

at the LES cells. In Eq. (7.5), the gradient of the filtered temperature, $\nabla_n \tilde{T}$, is aligned with the wall normal direction. $\tilde{q}^l_{W,S}$ and $\tilde{q}^t_{W,S}$ denote the individual heat fluxes from laminar and sub-grid heat transfer. $\tilde{q}^t_{W,S}$ has been modeled using the classical Reynolds analogy in Eq. (7.5). $\lambda = c_P \mu / Pr$ and $\lambda_t = c_P \mu_{sgs} / Pr_t$ are the laminar and sub-grid scale thermal conductivities, respectively, and c_P is the specific heat capacity at constant pressure. The molecular and sub-grid scale Prandtl numbers are assumed to be $Pr = 1$ and $Pr_t = 0.7$, respectively, over the entire flow.

The data coupling between LES and CMC has been discussed in Sub-section 3.4.3 and will not be repeated here. In particular, filtered volumetric heat loss in the CMC resolution for calculating the heat transfer coefficient H in Eq. (7.3) is obtained through

$$\tilde{q}^{CMC}_{W,\Omega} = \mathscr{L}\left(\tilde{q}_{W,\Omega}\right). \tag{7.7}$$

The operator $\mathscr{L}(\cdot)$ in Eq. (7.7) is defined in Eq. (3.62b) and $\tilde{q}_{W,\Omega}$ is calculated based on Eq. (7.5).

7.2.2 Problem considered and numerical implementation

The burner configuration, flow operating condition and numerical implementations for both LES and CMC in this Chapter are exactly the same as those in Chapter 6 and hence will not be repeated here.

About the wall boundary conditions for the LES solver, nonslip condition for velocity and zero gradient for mixture fraction are enforced. Also, the walls are assumed to be chemically inert and cold ($T_W = 298$ K). It should be emphasized that the assumed wall temperature is below the typical wall temperature values for most hydrocarbon combustion devices, which might be in the region 400−600 K [Poinsot and Veynante, 2005]. However, it is expected that this would not qualitatively affect the conclusions in the present manuscript. $y^+ < 4$ for the near-wall LES mesh is basically satisfied to accurately predict the near-wall tem-

perature gradient. In this Chapter only the bluff body wall heat loss effects are investigated, which are more relevant to the lift-off and local extinction. Figure 7.1 demonstrates the basic configuration and the surface mesh distributions of the bluff body, as a part of the Cambridge swirl burner shown in Fig. 4.3. In addition, the CMC boundary faces are inherited from the LES counterparts as described in Sub-section 3.4.2. Q_α and Q_T for the CMC wall boundaries are assumed to be inert.

7.3 Results and discussion

7.3.1 Velocity statistics

The axial and swirl velocity statistics at four streamwise positions (i.e. $x/D_b = 0.4$, 0.6, 2.2 and 4.4) are compared with the corresponding experimental results [Cavaliere, 2013] in Figs. 7.2 and 7.3. The mean and *r.m.s.* from the simulations reasonably reproduce the main features of the flow (e.g. CRZ, IRZ, as well as the solid-body rotating regions within $-0.8 \leq r/D_b \leq 0.8$ and $x/D_b < 1$ shown in Fig. 7.3). However, the fuel jet penetration is under-predicted in the LES which can be observed by the under-prediction of the central mean axial velocity at $x/D_b = 0.6$ and 2.2 in Fig. 7.2. This may be caused by the fact that the streamwise adverse pressure gradients along the centerline are over-estimated, which is related to the over-prediction of mean swirl velocities at $x/D_b = 0.4$ and 0.6 shown in Fig. 7.3. In addition, the *r.m.s.* of both axial and swirl velocities at $x/D_b = 0.4$ and 0.6 from the LES is over-predicted. The higher *r.m.s.* quantities in LES may be affected by the over-prediction of the turbulence near the annulus exit. Generally, the statistics of axial and swirl velocities from the simulation show reasonable agreement with the experimental results. Furthermore, comparisons are made with the results in Figs. 6.3 and 6.4 which are from the LES/3D-CMC with adiabatic walls and show that the inclusion of wall heat loss in Eq. (7.1) has negligible influence on the velocity statistics.

7.3.2 Wall heat flux and local extinction

Contours of instantaneous and mean temperature overlaid by the stoichiometric mixture fraction and zero axial velocity iso-lines at the $x-y$ plane are demonstrated in Fig. 7.4. The iso-lines of mean and instantaneous ξ_{st} are basically confined within the upstream part of the IRZ ($x/D_b < 1$). Similar to the experimental observations [Cavaliere et al., 2013], the flame base is very close to the bluff body, although lift-off can be observed occasionally near the edge (e.g. the left flame base branch in Fig. 7.4a). The statistics of the lift-off height will be discussed further in Sub-section 7.3.4.

Figure 7.5 demonstrates the distribution of instantaneous surface heat flux, the sum of $\tilde{q}^l_{W,S}$ and $\tilde{q}^t_{W,S}$, on the bluff body surface and the combustor walls. One can find that the circular bluff body top has considerable surface heat flux which is caused by the significant interactions between it and the flames in IRZ. The surface heat flux on the side combustor walls is from the impingement of the flame towards them while that on the bottom of the combustor results from the intermittent engulfment of the hot pockets into CRZ from the impingement. However, both of them are less than heat flux on the bluff body top.

In Fig. 7.6(a), the contour of mean surface heat flux on the entire bluff body is demonstrated. The mean heat flux is approximately symmetrical with respect to the fuel jet exit. Figure 7.6(b) plots radial profiles of the mean heat flux magnitude $q_{w,S}$ and the temperature gradient $\nabla_n \tilde{T}$ on the bluff body surface, i.e. $0.08 \leq r/D_b \leq 0.5$. Here the averaging is performed both in time and in the azimuthal direction. As the radius increases, the mean wall surface heat flux $q_{w,S}$ and temperature gradient sharply increase at $0 \leq r/D_b \leq 0.15$ and reach their individual plateaus at $r/D_b = 0.15$, and eventually decrease at $r/D_b > 0.4$. Clearly, the high values on the middle section of the surface ($0.15 \leq r/D_b \leq 0.4$) are attributed to the contact between the cold surface and the flames as well as recirculating hot gases in IRZ, while the relatively low heat fluxes at low and large radii result from the cold streams of air and fuel jets as shown in Fig. 7.4.

Figure 7.6(b) also presents radial distributions of the mean laminar and sub-grid heat fluxes, i.e. $q^l_{w,S}$ and $q^t_{w,S}$. $q^t_{w,S}$ is much lower than $q^l_{w,S}$ on the whole surface and the fraction of the mean sub-grid heat flux, $q^t_{w,S}/q^l_{w,S}$, monotonically

increases from about 15% at $r/D_b = 0.08$ to about 45% at $r/D_b = 0.5$. The laminar heat flux $q^l_{w,S}$ basically follows the temperature gradient variations while, interestingly, $q^t_{w,S}$ increases monotonically with radius. Clearly, the sub-grid heat flux $q^t_{w,S}$ is directly linked to the sub-grid scale viscosity μ_{sgs} shown in Eq. (3.16) and therefore to the sub-grid kinetic energy k. Since the velocity *r.m.s.* close to bluff body (e.g. $x/D_b = 0.4$ in Figs. 7.2a and 7.3a) is over-predicted, it should be acknowledged that k close to $r/D_b = 0.5$ is accordingly over-predicted.

Figure 7.7 demonstrates the PDF of the instantaneous bluff body surface wall fluxes $\tilde{q}_{w,S}$ based on the whole surface at all simulated time instants. The PDF is close to a Gaussian distribution, although clipped at zero, implying that cold air and fuel streams are occasionally present at the wall. This feature is different from the results reported by Wang and Trouvé [2006] with two dimensional DNS of ethylene/air non-premixed flames near a wall, where the PDF of wall heat fluxes is quite narrow and very few samples can be seen near zero. This discrepancy can be attributed to the existence of the cold air and fuel inlets near the bluff body and also the recirculating fresh gas from downstream in IRZ. Furthermore, the mean and peak heat fluxes in Fig. 7.7 are approximately 1.5×10^5 and 5×10^5 W/m^2, respectively. They show good agreements with the heat flux estimation made by Lataillade et al. [2002], where the order of magnitude of 5×10^5 W/m^2 was obtained from methane/air flames at 1 bar pressure and 300 K wall temperature.

Figure 7.8 shows the variations of the conditionally filtered volumetric heat loss $\widetilde{q_{W,\Omega}|\eta}$ and conditionally filtered total enthalpy Q_h from one CMC cell near the bluff body surface. Each curve is from one instant and in Fig. 7.8(a) large fluctuations of $\widetilde{q_{W,\Omega}|\eta}$ can be seen with respect to its mean profile (denoted as the symbols) in the whole mixture fraction space. The introduction of the volumetric heat loss into the conditionally filtered total enthalpy equations makes Q_h deviate from its adiabatic profile, which is a straight line between $\eta = 0$ and $\eta = 1$, as presented in Fig. 7.8(b). Considerable fluctuations of Q_h occur at about $\eta = \xi_{st}$ resulting from the large fluctuations of $\widetilde{q_{W,\Omega}|\eta}$ there.

The time records of some important conditionally filtered scalars, scalar dissipation rate, and volumetric heat loss at $\eta = \xi_{st}$ from the same CMC cell as that in Fig. 7.8 are presented in Fig. 7.9. Between $t = 0.04$ s and 0.04125 s, the flame is burning based on the values of $\widetilde{\dot{q}|\xi_{st}}$, $\widetilde{Y_{OH}|\xi_{st}}$ and $\widetilde{T|\xi_{st}}$ shown in

Figs. 7.9(a)–(c). However, at around $t = 0.04125$ s, the flame is quenched (low $\widetilde{\dot{q}|\xi_{st}}$, $\widetilde{Y_{OH}|\xi_{st}}$ and $\widetilde{T|\xi_{st}}$ due to the large scalar dissipation as shown in Fig. 10(d). The extinction continues until $t = 0.043$ s when the stoichiometric scalar dissipation $\widetilde{N|\xi_{st}}$ becomes very low and the re-ignition occurs. Based on Fig. 7.9(e) and similar results from other near-wall CMC cells, $\widetilde{q_{W,\Omega}|\xi_{st}}$ roughly follows the evolutions of $\widetilde{T|\xi_{st}}$ but with some high-frequency oscillations. It also shows the pronounced decrease/increase during the onsets of extinction/re-ignition. This can be expected to facilitate the occurrence of these two critical flame behaviors based on the present results.

7.3.3 Near-wall conditional flame structures

In this Sub-section, the influences of convective wall heat loss on the near-wall flame structures in mixture fraction space will be investigated. Comparisons are made between the results from LES/3D-CMC with wall heat loss boundary conditions and those from the same solvers with adiabatic wall. For convenience, the former is termed as heat loss case hereafter. The latter has been investigated in Chapter 6 and is termed as adiabatic case. The adiabatic results in this Sub-section are from the computations in Chapter 6.

Figures 7.10 and 7.11 show the comparisons of mean flame structures in mixture fraction space predicted from heat loss and adiabatic cases. These results are extracted from the same CMC cell as that in Fig. 7.9. The mean conditional mass fractions of reactants (i.e. CH_4 and O_2 in Figs. 7.10a and 7.10b)/products (e.g. H_2O in Fig. 7.10c) are higher/lower in the heat loss case than those in the adiabatic simulation, indicating incomplete reactions when wall heat loss is included. The conditional mass fraction of CH_2O in Fig. 7.10(d) is higher in the heat loss case. The mean profiles of OH mass fraction in η-space, heat release rate and temperature are shown in Figs. 7.11(a)–(c). Compared to the adiabatic results, $\widetilde{Y_{OH}|\eta}$ and $\widetilde{T|\eta}$ in the heat loss case are obviously lower and, conversely, $\widetilde{\dot{q}|\eta}$ is much higher within $0.025 < \eta < 0.075$. In addition, the inclusion of wall heat loss term in Eq. (7.1) leads to a considerable enthalpy defect around $\eta = \xi_{st}$ as shown in Fig. 7.11(d).

Figure 7.12 presents the PDF of conditional reactedness at $\eta = \xi_{st}$, $\widetilde{b_\alpha|\xi_{st}}$,

based on temperature and mass fractions of OH, CO and NO from both heat loss and adiabatic cases. The equation for $\widetilde{b_\alpha|\xi_{st}}$ can be referred to Eq. (6.1). $Y_{\alpha,b}|\eta$ and $Y_{\alpha,m}|\eta$ used to calculate $\widetilde{b_\alpha|\xi_{st}}$ are the fully burning 0D-CMC solutions with $N_0 = 5$ 1/s and inert mixing ones, respectively. $\widetilde{b_\alpha|\eta} = 0$ corresponds to the extinction solutions while $\widetilde{b_\alpha|\eta}$ is close to or larger than unity is fully burning ones. Clearly, in both cases, $\widetilde{b_{OH}|\xi_{st}}$ and $\widetilde{b_T|\xi_{st}}$ in Figs. 7.12(a) and 7.12(b) show the peaks when they are close to unity. However, in the heat loss case, the peaks of $\widetilde{b_{OH}|\xi_{st}}$ and $\widetilde{b_T|\xi_{st}}$ are shifted towards smaller values, which implies weakened reactivity. For $\widetilde{b_{OH}|\xi_{st}}$, another peak appears approaching zero, indicating the instantaneous extinction at the present CMC cell when wall heat loss is considered. However, for $\widetilde{b_{CO}|\xi_{st}}$ and $\widetilde{b_{NO}|\xi_{st}}$ in both cases, the distributions are wide. The PDF of $\widetilde{b_{CO}|\xi_{st}}$ is negligibly affected by the heat loss while that of $\widetilde{b_{NO}|\xi_{st}}$ moves towards smaller values when wall heat loss is included, which is consistent with the variations of the temperature. The results in Figs. 7.10–7.12 only correspond to one selected CMC cell but similar findings can also be obtained from other near-wall CMC cells.

The mean conditional scalar dissipation rates $\widetilde{\langle N|\eta\rangle}$ from the adiabatic and heat loss cases are compared in Fig. 7.13. For all three CMC cells corresponding to different radial positions (i.e. $y/D_b = 0.18$, 0.4 and 0.49) adjacent to the bluff body, $\widetilde{\langle N|\eta\rangle}$ in the heat loss case is always larger than that in adiabatic one. This difference concerning $\widetilde{\langle N|\eta\rangle}$ explains the comparisons of mean flame structures in Figs. 7.10 and 7.11. Also, the difference of $\widetilde{\langle N|\eta\rangle}$ between two cases increases with the increased y/D_b. This implies that the wall heat loss greatly influences scalar dissipation near the outer part (with relatively large radii) of the bluff body surface, where the iso-surfaces of instantaneous ξ_{st} and the flame base are occasionally attached to. However, the peak values of $\widetilde{\langle N|\eta\rangle}$ in these three CMC cells are still well below the critical peak value from 0D-CMC calculations ($N_0 \approx 170$ 1/s). This is consistent with the previous findings from the study by Garmory and Mastorakos [2011] and in Chapter 6 that in LES/CMC the emergence of local extinction is not a simple function of the local and instantaneous scalar dissipation, but also a result of physical transport.

7.3.4 Lift-off height

The streamwise variations of the mean conditional mass fraction of OH, $\langle\widetilde{Y_{OH}|\eta}\rangle$, are shown in Fig. 7.14 through comparing the heat loss and adiabatic results. It can be observed that $\langle\widetilde{Y_{OH}|\eta}\rangle$ in the adiabatic case is higher than in the heat loss case but the difference becomes negligible at $x/D_b = 1.6$. Iso-surfaces of instantaneous mixture fraction ξ_{st} colored by $\widetilde{Y_{OH}|\xi_{st}}$ and $\widetilde{T|\xi_{st}}$ (from the host CMC cells of the local LES meshes) in the heat loss case are plotted in Fig. 7.15. At the iso-surfaces close to the bluff body, large flame holes quantified by low $\widetilde{Y_{OH}|\xi_{st}}$ (< 0.001) and $\widetilde{T|\xi_{st}}$ (< 1200K) can be observed. This explicitly manifests the instantaneous extinction in η-space at the flame base regardless of the local mixing state, which can also be observed in the experiment [Cavaliere et al., 2013].

The localized extinction close to the bluff body surface indicated in Fig. 7.15 is also seen in the adiabatic case as discussed in Chapter 6 where it is attributed to the strong convection approaching the swirling air inlet. To appreciate how the wall heat loss affects the flame reactivity close to the bluff body, Fig. 7.16 presents the PDFs of reactedness at stoichiometry from temperature and OH mass fraction, i.e. $\widetilde{b_T|\xi_{st}}$ and $\widetilde{b_{OH}|\xi_{st}}$. Here the samples include 50 time instants and each instant is extracted from about 3,000 CMC cells enclosing the three dimensional iso-surfaces of the instantaneous stoichiometric mixture fraction near the bluff body, i.e. $0 \leq x/D_b \leq 0.8$ (marked in Fig. 7.15a). In the adiabatic case, $\widetilde{b_T|\xi_{st}}$ has a single peak which is centered at 0.92 with some negative skewness, indicating some degree of instantaneous extinction at the flame base. The extinction is also characterized by the pronounced bimodality in PDF of $\widetilde{b_{OH}|\xi_{st}}$ in Fig. 7.16(b). In the heat loss case, the negative skewness of the PDF of $\widetilde{b_T|\xi_{st}}$ is intensified and the PDF of $\widetilde{b_{OH}|\xi_{st}}$ tends to have a single peak around zero. Both features concerning $\widetilde{b_T|\xi_{st}}$ and $\widetilde{b_{OH}|\xi_{st}}$ statistically indicate the weakened reactivity in the local CMC cells at the flame base when the bluff body heat loss effects are taken into account.

The PDF of the lift-off height h_L extracted from the $x-y$ plane are presented in Fig. 7.17(a). Similarly to the definition in the experiment [Cavaliere et al., 2013] and in Chapter 6, h_L is the streamwise distance between the bluff body surface to the position along the ξ_{st} iso-line where $\tilde{Y}_{OH}$ is critically larger the 0D-

CMC threshold (i.e. 0.00024). 200 samples are extracted equally from both left and right flame branches close to the bluff body edge and 188 samples of those showed lifted flame. Only the snapshots with $h_L > 0.5$ mm are considered here for calculating the PDF of h_L. The counterpart results from the simulations with adiabatic bluff body from Chapter 6 are also given in Fig. 7.17(b) for comparison, which is the same as Fig. 6.15. From Fig. 7.17(a), it can be seen that the PDF of h_L from the simulation agrees reasonably with the measured results. However, an over-prediction around $h_L = 3$ mm and 7mm $< h_L <$ 14mm exist and actually the over-prediction of h_L is also observable for the range 10mm $< h_L <$ 20mm as shown in Fig. 7.17(b). In general, the influence of wall heat loss on the PDF of lift-off height h_L is relatively small, which implies that although heat losses reduces reactivity, the flame stabilisation mechanism is a stronger function of the aerodynamic straining than the heat loss to the bluff body. This is broadly consistent with the measurements made by Kariuki [2012], where the leanest equivalence ratio for blow-off in a premixed flame stabilised on a metal bluff body was smaller by only about 10% compared to the blow-off condition with a ceramic bluff body.

7.4 Conclusions

Large eddy simulation with three dimensional conditional moment closure combustion model is applied to a swirling non-premixed methane flame with local extinction. The convective wall heat loss is included as an additional term in the conditionally filtered total enthalpy equation for the CMC cells adjacent to walls. The mean heat flux is high on the middle bluff body surface but low near its edges. The sub-grid heat flux based on the resolved temperature gradient is relatively low com-pared to the laminar counterpart but increases with the turbulent intensity. For the CMC cells immediately adjacent to the bluff body, the heat loss facilitates the occurrences of extinction and re-ignition. It has a significant influence on the mean flame structures, which is directly linked to the changes of the conditional scalar dissipation near the wall. Furthermore, the degree of local and instantaneous extinction measured by conditional reactedness at stoichiometry is intensified due to the wall heat loss. However, the wall heat loss shows a

small impact on the lift-off near the bluff body surface.

7.5 Figures for Chapter 7

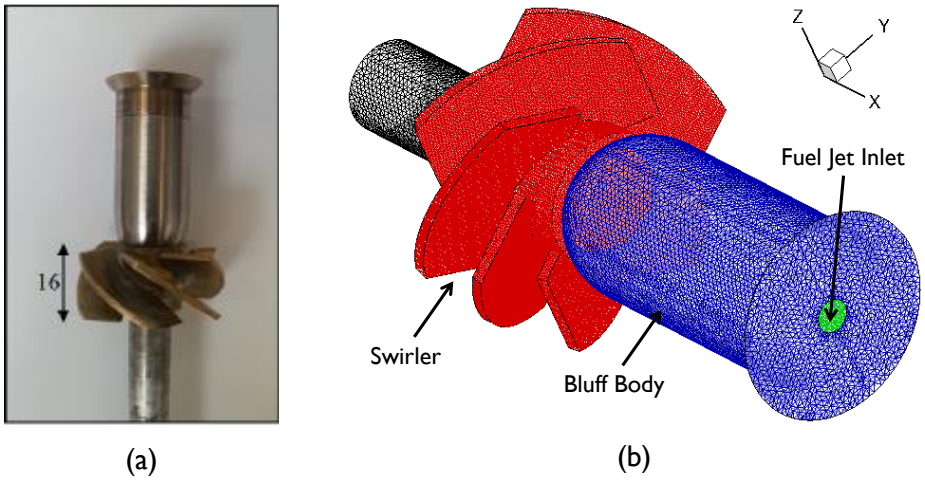

Figure 7.1: (a) Photo [Cavaliere, 2013] and (b) surface mesh distributions of the swirler and bluff body.

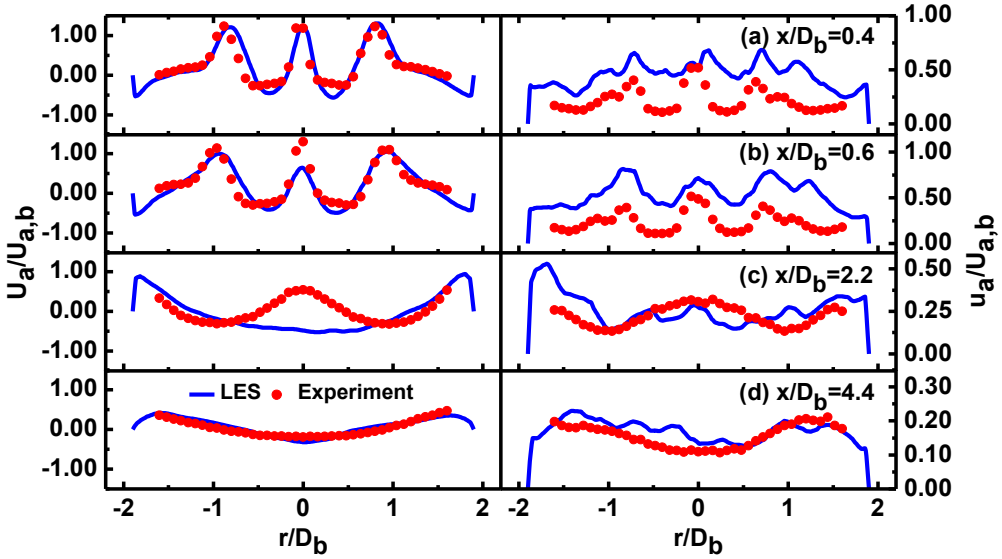

Figure 7.2: Radial profiles of mean (left) and $r.m.s.$ (right) axial velocity at x/D_b = 0.4, 0.6, 2.2 and 4.4.

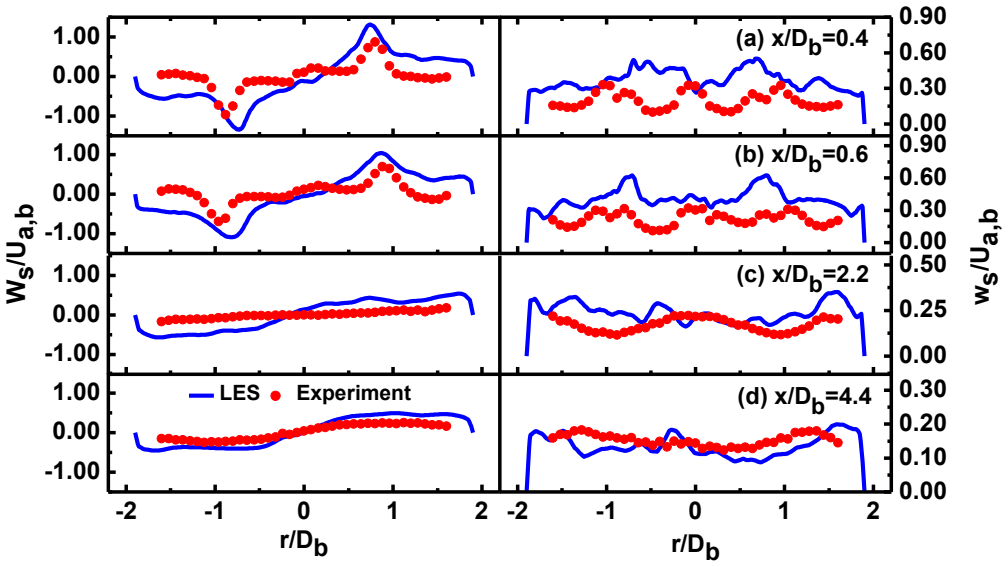

Figure 7.3: Radial profiles of mean (left) and $r.m.s.$ (right) swirl velocity at x/D_b = 0.4, 0.6, 2.2 and 4.4.

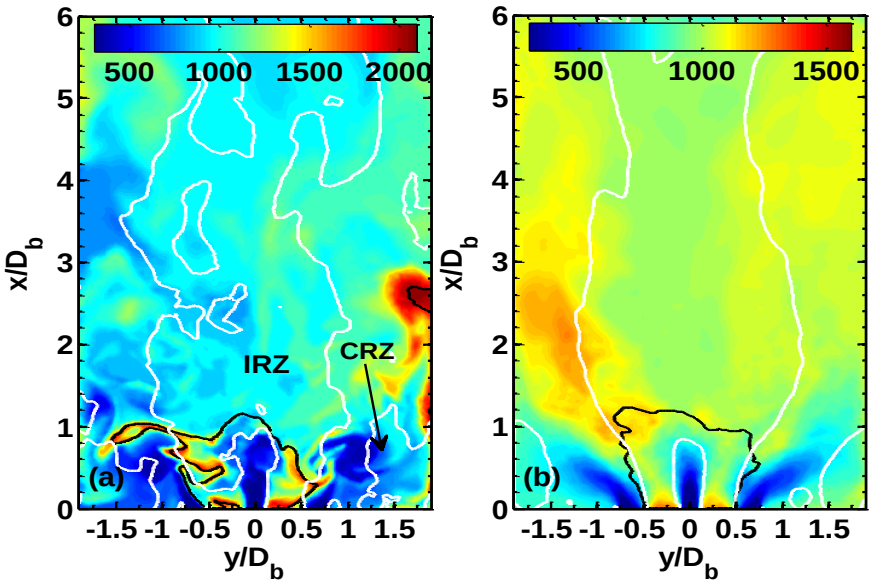

Figure 7.4: Distributions of (a) instantaneous and (b) mean temperature. Black iso-lines: instantaneous or mean stoichiometric mixture fraction. White iso-lines: zero instantaneous or mean axial velocity.

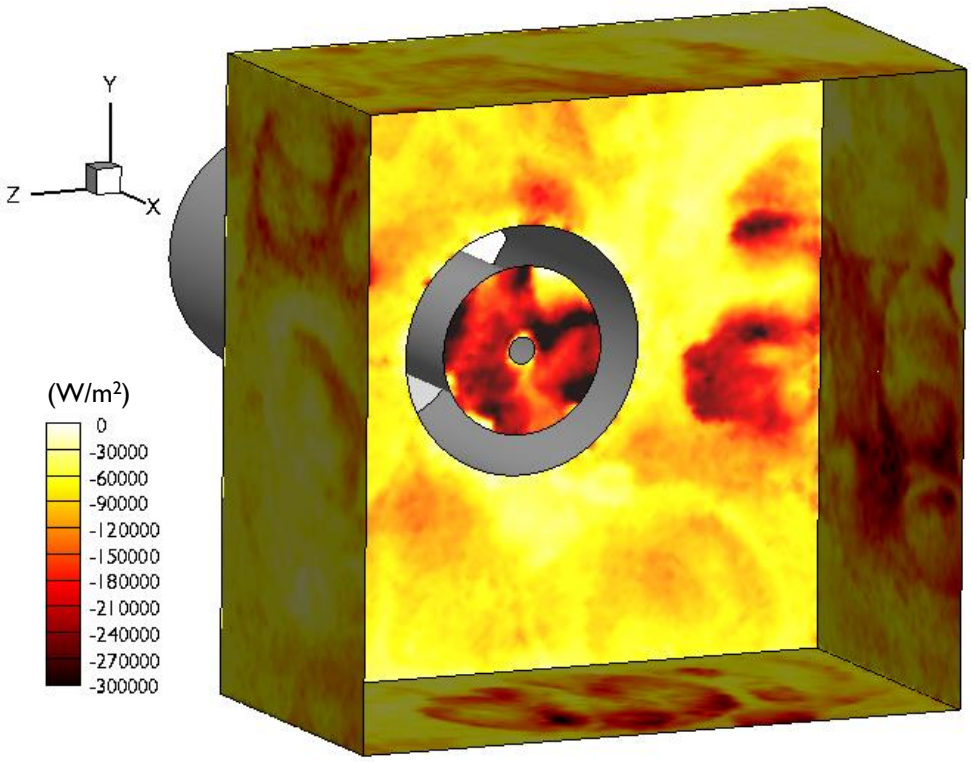

Figure 7.5: Distribution of instantaneous wall heat flux on the bluff body and upstream part (1/3 of the whole chamber length) of the chamber walls.

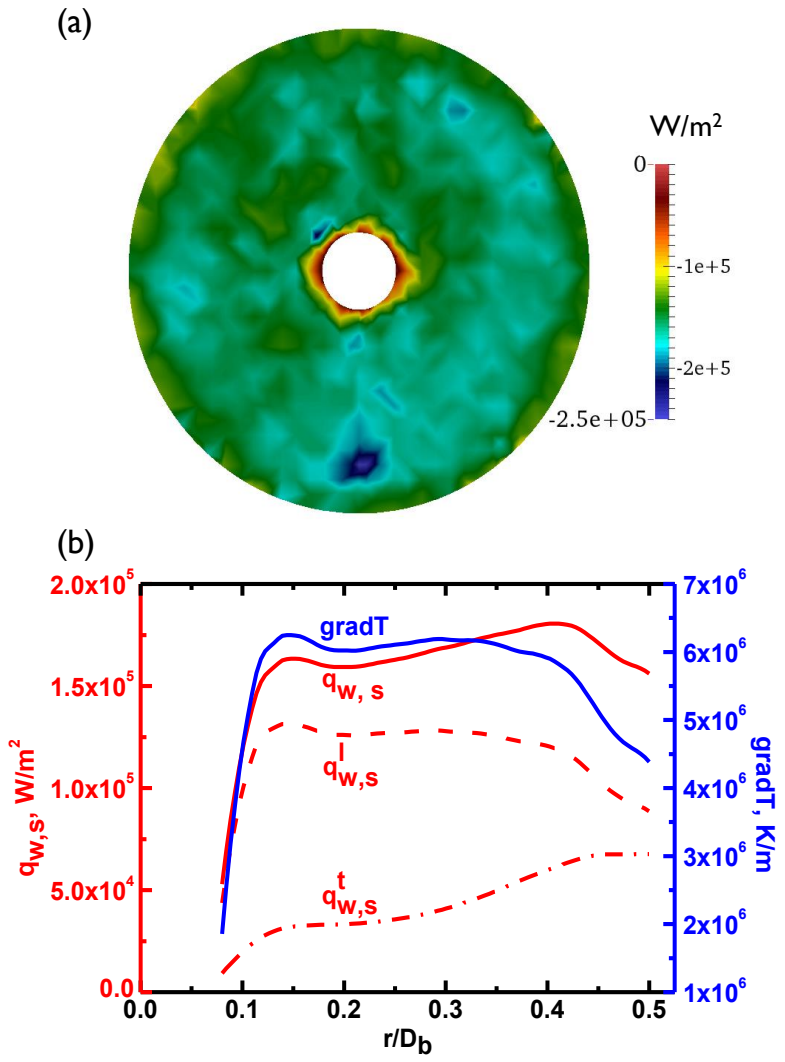

Figure 7.6: (a) Distributions of mean heat flux on the bluff body surface; (b) radial profiles of mean heat flux magnitude and temperature gradient on the bluff body surface ($0.08 \leq r/D_b \leq 0.5$).

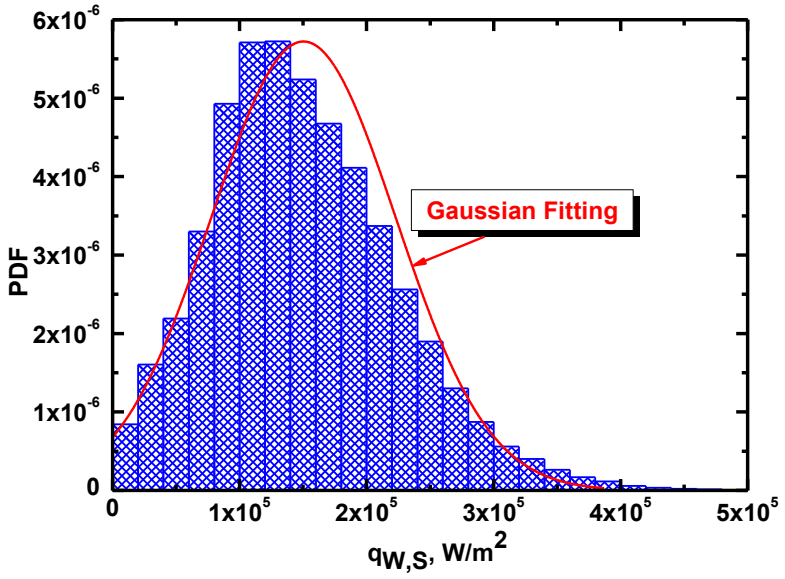

Figure 7.7: Probability density function of the magnitude of the bluff body surface heat flux . The data are extracted both in time and space over the whole bluff body surface.

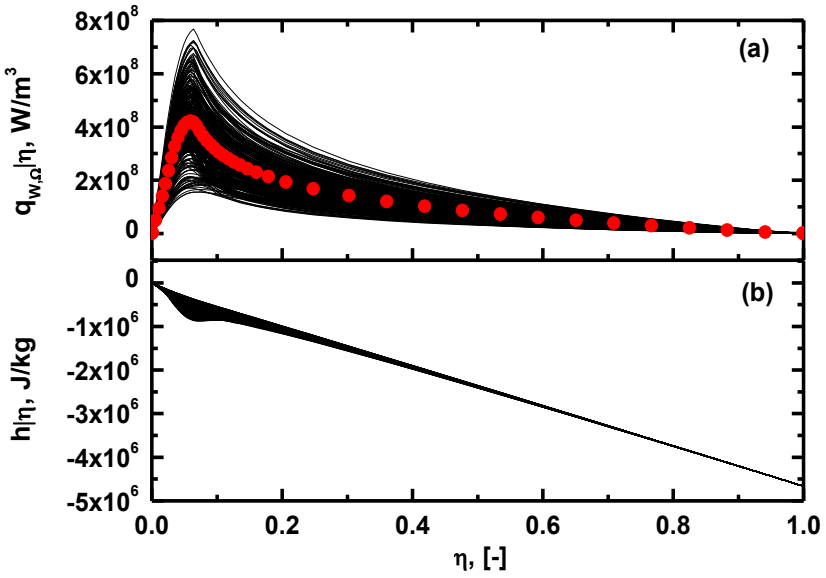

Figure 7.8: Variations of conditionally filtered (a) volumetric heat loss and (b) total enthalpy. Symbols: mean conditional heat flux. The data are from a CMC cell immediately adjacent to the bluff body surface (CMC cell centroid coordinate: $x/D_b = 0.012$, $y/D_b = 0.4$ and $z/D_b = 0$).

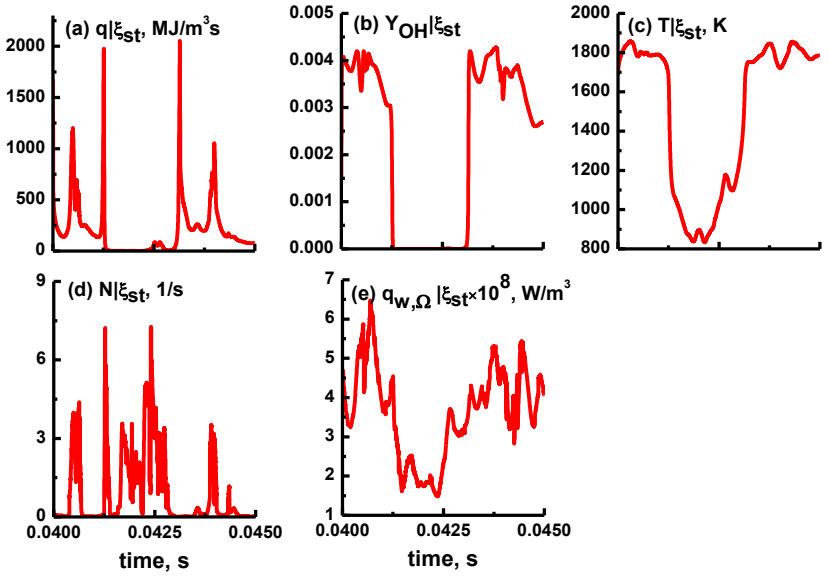

Figure 7.9: Time records of conditionally filtered (a) heat release rate, (b) OH mass fraction, (c) temperature, (d) scalar dissipation and (e) volumetric heat loss at $\eta = \xi_{st}$ from the same CMC cell as in Fig. 7.8.

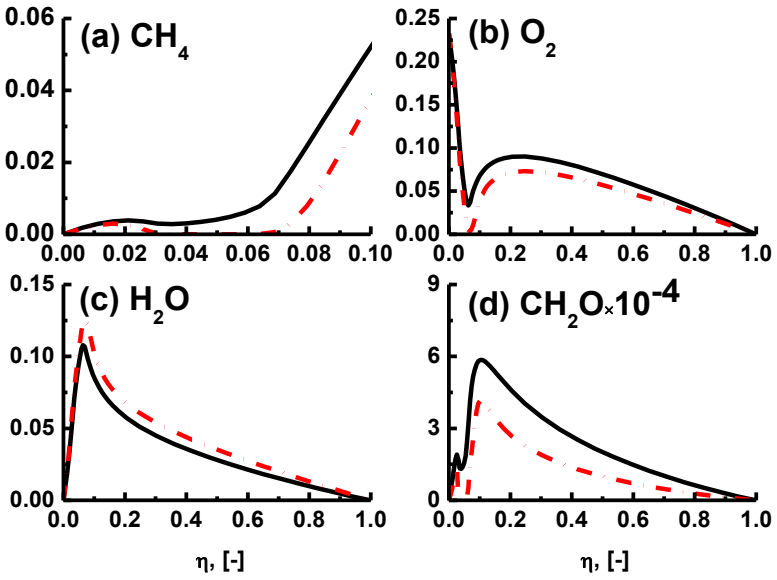

Figure 7.10: Comparisons of the mean conditional mass fractions of (a) CH_4, (b) O_2, (c) H_2O and (d) CH_2O between adiabatic (dash-dot lines) and heat loss (solid lines) cases. The same CMC cell as in Fig. 7.8.

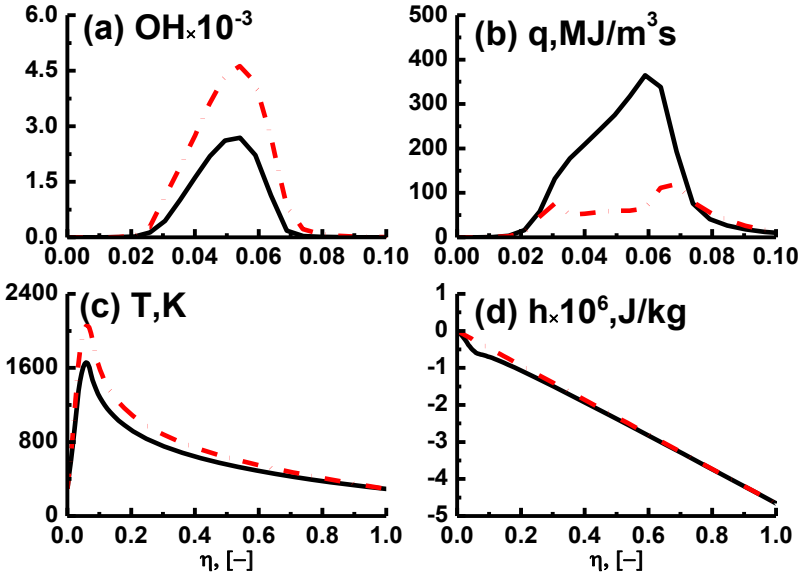

Figure 7.11: Comparisons of the mean conditional (a) OH mass fraction, (b) heat release rate, (c) temperature and (d) total enthalpy between adiabatic (dash-dot lines) and heat loss (solid lines) cases. The same CMC cell as in Fig. 7.8.

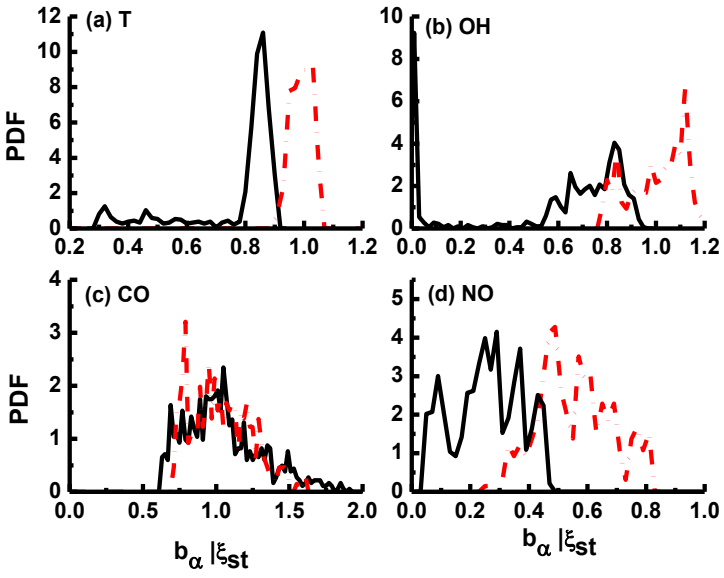

Figure 7.12: Probability density function of reactedness at $\eta = \xi_{st}$ from (a) temperature, mass fractions of (b) OH, (c) CO and (d) NO. Dash-dot lines: adiabatic case, solid lines: heat loss case.

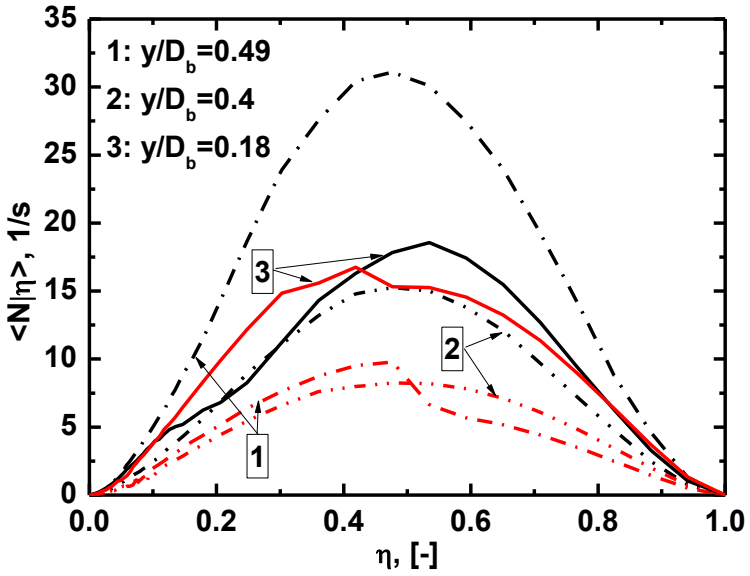

Figure 7.13: The mean conditional scalar dissipation rates of three near-wall CMC cells ($x/D_b = z/D_b = 0$) from adiabatic (red lines) and heat loss (black lines) cases.

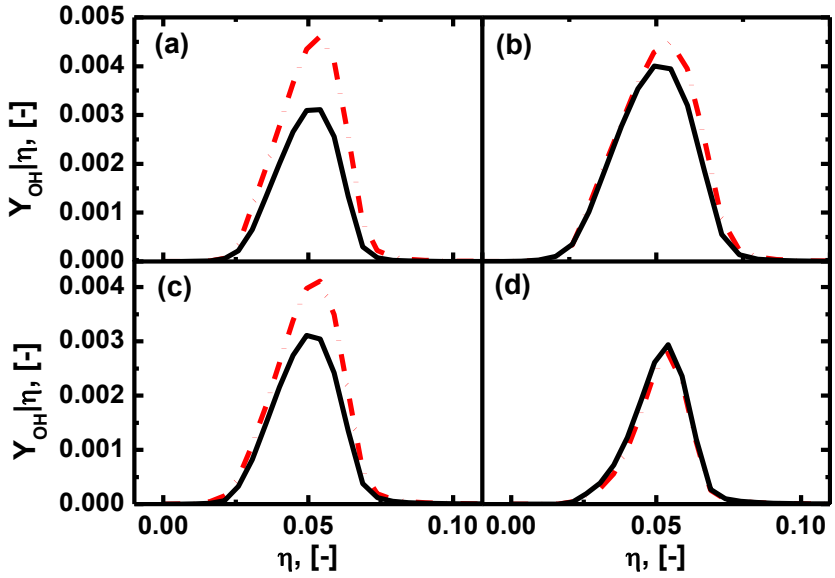

Figure 7.14: Comparisons of mean conditional OH mass fractions between adiabatic (dash-dot lines) and heat loss (solid lines) cases at four streamwise positions $x/D_b =$ (a) 0.03, (b) 0.17, (c) 0.8 and (d) 1.6 with $y/D_b = 0.4$ and $z/D_b = 0$.

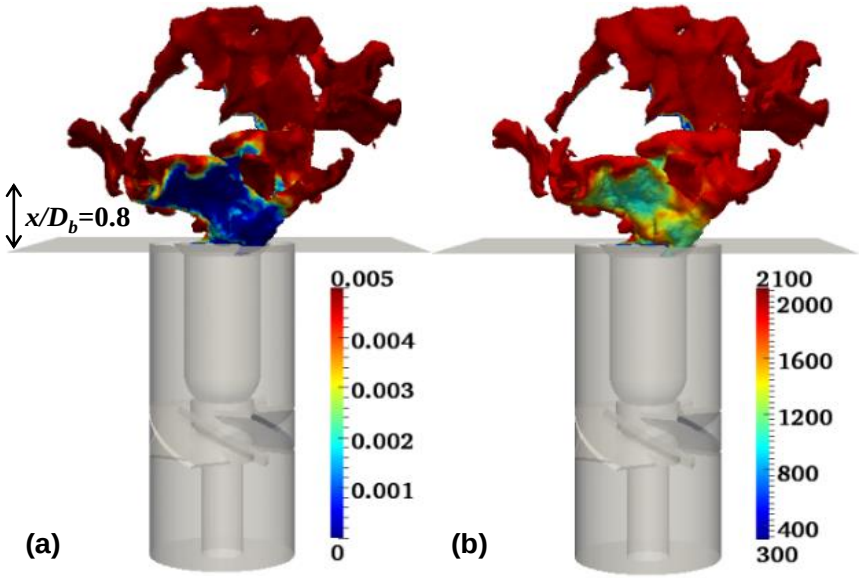

Figure 7.15: Iso-surfaces of instantaneous stoichiometric mixture fraction colored by conditional (a) OH mass fraction and (b) temperature at stoichiometry.

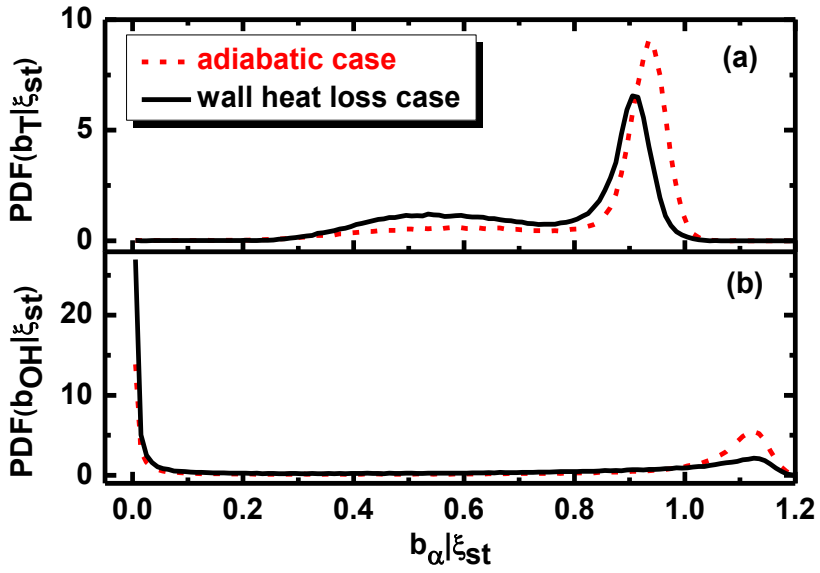

Figure 7.16: Probability density function of reactedness at $\eta = \xi_{st}$ from (a) temperature and (b) OH mass fraction corresponding to the three dimensional stoichiometric iso-surface within $0 \leq x/D_b \leq 0.8$.

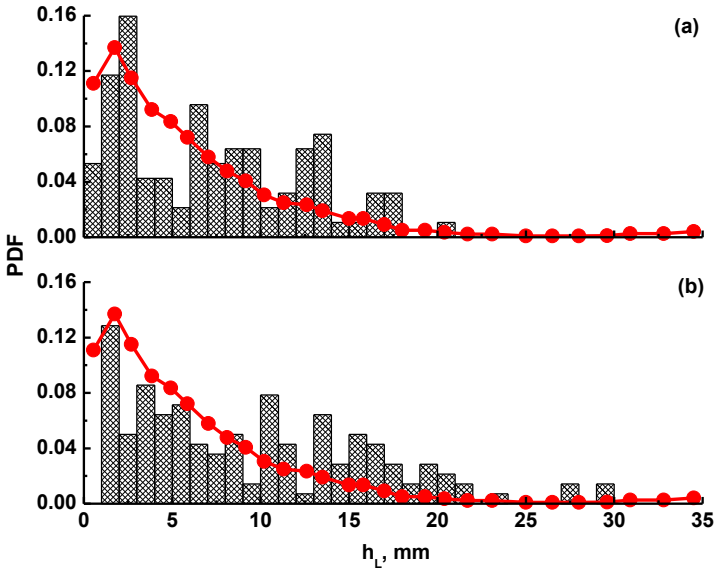

Figure 7.17: Probability density functions of lift-off height from simulations with (a) heat loss and (b) adiabatic walls. Red lines: experimental results [Cavaliere et al., 2013].

Chapter 8

Blow-off of Cambridge Swirl Flames

8.1 Introduction

Blow-off is a transient process in which the localized extinction area on the flame front gradually expands until complete extinction occurs. It has been shown recently [Cavaliere et al., 2013; Chaudhuri et al., 2010; Dawson et al., 2011; Kariuki et al., 2012] that the blow-off transient is long relative to estimates of the residence time in the combustor and that empirical correlations of the blow-off condition do not give very accurate results. Therefore, in the perspective of turbulent combustion modelling, the following question can be posed: does a combustion model that can accurately predict the degree of local extinction also possess the ability to predict the blow-off condition and flame dynamics in a realistic combustor? Tyliszczak et al. [2014] investigated the blow-off dynamics of a swirl-stabilized n-heptane spray flame using LES/3D-CMC and the time evolution of heat release as well as the instantaneous flame behavior were analyzed. Also, for one condition, the simulation predicted an extinguished flame at the experimentally-determined blow-off velocity. However, the blow-off curve has not been studied systematically in that or other combustion modelling work. The ability to predict, from first principles, a wide range of global blow-off operating points would be of huge importance for the reliability of combustion CFD.

The objective of this Chapter is to apply LES with the three dimensional sub-grid CMC model to predict the transient blow-off phenomena and the blow-off curve (i.e. the blow-off conditions) of swirling non-premixed methane flames in the Cambridge swirl burner. The LES/3D-CMC model and flame information are presented briefly in the next Section. The results, findings and discussion are given in Section 8.3 and the conclusions are presented in the final Section.

8.2 Modelling

8.2.1 LES and CMC modelling

The filtered velocity and mixture fraction, $\tilde{\mathbf{U}}$ and $\tilde{\xi}$, are solved and their corresponding LES governing equations are given in Sub-section 3.1.2. The Smagorinsky model is applied to close the sub-grid scale stress tensor. Other models can be also found in Sub-section 3.1.2. The variance of filtered mixture fraction, $\widetilde{\xi''^2}$, is calculated with Eq. (3.23). The filtered scalar dissipation rate $\tilde{N}$ includes two contributions from the resolved and sub-grid parts ($\tilde{N}_{res}$ and $\tilde{N}_{sgs}$), as demonstrated in Eq. (3.22).

The conditionally filtered mass fractions, Q_α, are solved with the three dimensional CMC governing equations, i.e. Eq. (3.35). The sub-models used for modelling the unclosed terms in the CMC equations are presented in Section 3.2. The convective wall heat loss is taken into consideration and the conditional total enthalpy equation with volumetric heat loss, Eq. (7.1), is solved and the models needed have been presented in Sub-section 7.2.1. In this Chapter, the laminar and sub-grid Schmidt numbers are $Sc = 1.0$ and $Sc_t = 0.7$ [Branley and Jones, 2001], respectively.

8.2.2 Flow considered and numerical implementations

The schematic and dimensions of the Cambridge swirl burner have been shown in Fig. 4.4. The blow-off of non-premixed flames is considered in this Chapter and the non-swirling fuel stream (100% methane) is injected through a pipe at the center of bluff body top, whilst the swirling motion of the air stream is generated

by the six vane guided swirler. The temperature for fuel and air is 298 K.

Mixture fraction space is discretised by 51 nodes that are clustered around $\xi_{st} = 0.055$. Both LES and CMC domains include the square combustor as presented in Fig. 4.7 and a downstream hemispherical far-field (not shown in Fig. 4.7). The annulus and the swirler are excluded, which is different from the domain used in Chapters 6 and 7. Around 9 million tetrahedral LES cells are used while the number of the CMC cells is about 140,000. Also, the near-wall cells near the bluff body surface are refined to $y^+ < 4$, to accurately predict the interaction between the flames and bluff body surface resulting from convective heat transfer. For CMC boundaries in mixture fraction space, $\eta = 0$ corresponds to air and $\eta = 0$ to fuel, both at 298 K. For LES boundaries presented in Fig. 4.7, at all the walls, nonslip condition is applied for the velocities and zero gradient for the mixture fraction. The wall temperature T_W was not measured in the experiment but assumed to be 298 K. Zero pressure gradient and Dirichlet velocity and mixture fraction conditions are enforced for the air and fuel inlets which are at the burner exit plane while fixed total atmospheric pressure for the far-field boundaries. About the CMC boundaries in physical space, the inert mixing solutions are specified in the air and inlets as well as at all the walls while zero gradient extrapolation is enforced at the far-field outlet.

The LES/3D-CMC solver introduced in Sub-section 3.4.1 is applied for the computations in this Chapter. The time step here is $\Delta t = 2 \times 10^{-6}$ s and the CFL number, predicted with Eq. (4.3), in the main flow and flame regions is less than 0.5. The simulations are run on Darwin Cluster from the Cambridge High Performance Computing Service and ARCHER Cluster from UK National Supercomputing Service. 80 processors are used for the computations in this Chapter and approximately 0.002 s of physical time can be achieved with 24-hour wall clock time. The whole simulated time is 0.03−0.07 s, depending on the operating conditions.

8.2.3 Blow-off simulation strategy

The flame condition is determined by the fuel and air bulk velocities (i.e. U_f and U_a) and a few pairs of such values that give rise to global blow-off in the

experiment are reproduced in Fig. 8.1 and constitutes the experimental blow-off curve for the non-premixed flames in this burner. A large number of extra (U_f, U_a) conditions are investigated with LES. Most of these runs are done by starting with the identical resolved flow and scalar fields of a stable flame, which follows the procedure in the experiment [Cavaliere et al., 2013]. In the blow-off experiment the fuel flow rate is fixed and the air flow rate is gradually increased in steps of around 2% (0.258 m/s) every 20 s until the blow-off is reached in the fuel-lean condition. The blow-off air bulk velocity, $U_{BO,exp}$, is then recorded for the investigated fuel flow rate. In principle, such operation is also feasible in LES/3D-CMC but in light of the prohibitive computational cost, in this study the air and/or fuel velocities are changed to the required values in one go for each simulation.

To examine the occurrence of blow-off in LES, the quantity of the total heat release rate Q is calculated from volume integration over the entire combustor, i.e.

$$Q = \int_{\Omega^{LES}} \tilde{\dot{q}} dV. \tag{8.1}$$

Here Ω^{LES} represents the whole LES computational domain. The resolved heat release rate $\tilde{\dot{q}}$ is calculated from Eq. (5.1). In this investigation, the blow-off event is assumed to occur when the integrated heat release rate Q reaches below 1% of its initial value that is integrated from the initial field. Accordingly, the duration within which Q evolves from the initial to low (<1%) values is defined as the blow-off time τ_{BO}. If in the whole simulation time (typically 0.05−0.07 s), Q fluctuates with respect to some stable value and never reaches <1%, then no blow-off happens under this operating condition and the flame is assumed to be globally stable.

In the measurements [Cavaliere et al., 2013], the quantification of the individual blow-off transients is based on evolutions of the corresponding area integrated OH* signals taken from the two dimensional images of 5 kHz OH* chemiluminescnece. The reported experimental blow-off time is extracted from the averged time series of area integrated OH* emissions compiled from repeated experiments for the specific operating conditions. The experimental τ_{BO} is defined as the time needed for the OH* emissions reducing from 90% to 10% of the initial value.

Therefore from the LES τ_{BO} only corresponds to a single event but the experimental result by Cavaliere et al. [2013] is in an averaged sense. Theoretically very low or zero heat liberated from turbulent non-premixed flames can be only viewed as a necessary condition for extinction, which is particularly true when highly distributed chemical and mixing time scales exist in strongly turbulent fields like the investigated swirling flows, as discussed in Chapter 6. As such, in the computations the evolutions of key reaction scalars in both mixture fraction and physical space, e.g. $\widetilde{Y}_{OH}$ and $\widetilde{Y_{OH}|\eta}$, are examined as supplements to the Q based criterion.

The flames selected for further analysis are listed in Table 8.1: three (i.e. S1, S2 and S3) are computationally stable, while other three cases (i.e. BO1, BO2 and BO3) result in computational blow-off and hence global extinction. These six cases share the identical fuel bulk velocity (i.e. $U_f = 29.2$ m/s) but have the successively increased air bulk velocity U_a from S1 to BO3. Furthermore, the cases on the experimental blow-off curve that are computationally stable but experimentally blow-off will be discussed as well and correspond to S4, S5, S6 and S7 in Table 8.1. All the above ten cases have been explicitly marked in Fig. 8.1.

Since the velocity statistics at the chamber air inlet are not available from experiment for all these conditions, a non-reacting RANS simulation with the CSWH1 operating conditions investigated in Chapter 4 and complete computational domain (i.e. swirler, annulus, combustion chamber and far-field) presented in Fig. 4.7 is first conducted. The statistics of axial and swirl components from this RANS simulation have been shown in Chapter 4 (see Fig. 4.32) and excellent agreement with measurements is obtained. Then for all the above mentioned LES cases and others in Fig. 8.1, the profiles of three velocity components (axial, swirl and radial velocities) at the air inlet are interpolated and scaled from the non-reacting RANS based on the ratio of the target values (e.g. 19.9 m/s for S2) to the S1 air axial bulk velocity, 19.1 m/s. Thus for all the simulated cases, the swirl number based on Eq. (4.2) is kept constant as $S_N = 1.23$. Top-hat profiles are used at fuel inlets for all the LES cases in Table 8.1. White noise with 5% intensity is applied at both the air and fuel inlets. Simulations of S2−S7 and BO1−BO2 and other conditions in Fig. 8.1 are conducted through being initial-

ized from well-developed LES and CMC fields of S1, which is globally stable in the computations. In addition, the air bulk velocities for S2 and S4−S7 correspond to $U_{BO,exp}$ for the measured fuel bulk velocities, e.g. for S2 case $U_f = 29.2$ m/s, $U_{BO,exp}$ is 19.9 m/s [Cavaliere et al., 2013]. The ratio of axial air velocity to $U_{BO,exp}$, $U_a/U_{BO,exp}$, and momentum ratio of air and fuel axial velocities, $\rho_a U_a^2/\rho_f U_f^2$, are also listed in Table 8.1.

8.3 Results and discussion

8.3.1 Blow-off curve

The critical air axial bulk velocity U_a at blow-off as a function of the fuel jet velocity U_f was measured by Cavaliere et al. [2013] and the data are the squares marked by "*EXP, BO*" in Fig. 8.1. Above the black dashed curve, there is no stable flame in the experiments [Cavaliere et al., 2013] (i.e. blow-off occurs). To obtain the critical air axial bulk velocity in LES, $U_{BO,LES}$, corresponding to the experimental U_f operating conditions, a trial-and-error strategy was performed. In particular, S2 and other four cases (i.e. S4−S7 cases) corresponding to the experimental blow-off curve (i.e. $1.0U_{BO,exp}$ in Fig. 8.1) were first simulated. It turns out that computationally no blow-off was observed. Hence, the current LES/3D-CMC modelling cannot successfully achieve the blow-off in the conditions which exactly correspond to critical blow-off points from the experiments. The curve of $1.0U_{BO,exp}$ is thought of as lower blow-off boundary to locate $U_{BO,LES}$ from LES/3D-CMC. Then, BO3 and other four cases (denoted by blue rhombuses in Fig. 8.1) were run with the air bulk velocities of approximately $1.6U_{BO,exp}$ and the results show that all these five cases result in blow-off (marked by "*LES, BO*" in Fig. 8.1). This means that LES/3D-CMC reproduces the blow-off condition to an accuracy better than 60% for a range of fuel velocities U_f.

Further, a similar effort was done to examine the blow-off likelihood by LES/3D-CMC for air velocities exactly 25% higher than the experimental blow-off velocity. In particular, the cases with (U_f, U_a) = (29.2 m/s, 25 m/s) and (39.5 m/s, 32.5 m/s) demonstrate stable flame features (marked by "*LES, ST*") but possess severe localized extinctions, while the other three with $1.25U_{BO,exp}$ show blow-off

(marked by "*LES, BO*"). Additional simulations show that, for $U_f = 29.2$ and 39.5 m/s, the air bulk velocities that can make the flame undergo global extinction in LES/3D-CMC are 26.5 and 36.0 m/s, respectively. These two points are marked by "*LES, BO*" in Fig. 8.1 and are combined with three blow-off points with $U_a = 1.25U_{BO,exp}$ to constitute the red dashed line (termed as roughly $1.25U_{BO,exp}$ curve hereafter), which is viewed as the upper blow-off boundary from LES/3D-CMC. The trend that increasing the fuel velocity results in a higher air velocity for blow-off is correctly captured. Therefore, the blow-off range in the computations, denoted as the highlighted yellow region in Fig. 8.1, suggests that $U_{BO,LES}$ lies between the $1.0U_{BO,exp}$ (lower boundary) and $1.25U_{BO,exp}$.(upper boundary) curves.

As far as the authors are aware, capturing the global blow-off condition with LES has not been demonstrated yet. This novel result from Fig. 8.1 demonstrates that the present LES/3D-CMC model, using model constants calibrated against the Sandia D flame [Garmory and Mastorakos, 2011], predicts, for a range of fuel jet velocities, an air blow-off velocity within 25% of the experimentally-determined value. This is a new progress confirming the capacity of the sub-grid CMC model in predicting the strong turbulence−chemistry interaction, e.g. global extinction. This accuracy is reasonable and might at present even be considered acceptable from an engineering perspective, considering that there might be also large uncertainties from the experimental blow-off curve ($1.0U_{BO,exp}$ in Fig. 8.1).

8.3.2 Features of S1 stable flame

Since S1 provides one of its filtered LES and CMC fields to initialize all the other simulations, it is of great importance to first confirm the correctness of S1 simulation in terms of flow fields and flame characterization. Therefore, the radial distributions of axial and swirl velocity statistics for S1 case are plotted in Figs. 8.2 and 8.3, respectively. These results are obtained through averaging the data around 0.04 s after the initial transients and different sampling periods are taken for statistics compilation to ensure the convergence. It can be seen from Figs. 8.2 and 8.3 that the current LES correctly captures the mean flow features, e.g. IRZ

and CRZ, central fuel penetration as well as the solid-body rotation region close to the bluff body. However, it is acknowledged that the axial velocity at $x/D_b = 2.2$ is under-predicted, indicating that the fuel length in the LES (about $2D_b$) is shorter than that in the measurement. Furthermore, at $x/D_b = 0.4$ and 0.6, the positions of *r.m.s.* peaks agree well with the experimental results, respectively corresponding to the shear layers along the fuel jet due to Kelvin−Helmholtz instability and the bowl-like double shear layers between the inflowing swirling air and IRZ as well as CRZ in the chamber flows. However, their magnitudes are over-calculated at these two streamwise positions and the peaks of both axial and swirl velocity *r.m.s.* at $r/D_b = 1.25-1.5$ in the computational results are caused by the vortex breakdown from the shear layer between swirl air and CRZ, which is not observed in the experiment. At the downstream, i.e. $x/D_b = 2.2$ and 4.4 in the Figs. 8.2 and 8.3, the *r.m.s.* demonstrates a good agreement with the experimental results.

Figures 8.4(a) and 8.4(c) show the LES results of mean distributions of heat release rate $\tilde{\dot{q}}$ and OH mass fraction $\widetilde{Y}_{OH}$ in $x-y$ plane from S1. For comparison, the mean OH* chemiluminescence after inverse Abel transform and mean OH-PLIF from the experiment [Cavaliere et al., 2013] corresponding to S1 operating conditions are also given in Figs. 8.4(b) and 8.4(d), respectively. From Fig. 8.4(a), one can find that most of the heat is released along the upstream section ($0 < x < 0.03$ m) of mean iso-line of stoichiometric mixture fraction ξ_{st}. Due to the relatively small ξ_{st}, this section of mean ξ_{st} iso-line is basically close to the shear layer between IRZ and swirling air and overlaps with the iso-line of mean axial velocity (not shown in Fig. 8.4a). Instead, at the downstream (0.03 m $<$ $x < 0.06$ m) very low heat release rate $\tilde{\dot{q}}$ can be seen. The above finding indicates that there may be severe extinction along the downstream section of ξ_{st} iso-line, which can be confirmed by the low mean OH mass fraction there as demonstrated in Fig. 8.4(c). Furthermore, based on the results in Fig. 8.4(c), mean OH mass fraction distribution is much broader than mean heat release rate: at the upstream, it is mainly confined by mean ξ_{st} iso-lines to the IRZ, but further downstream ($x > 0.03$ m), finite OH radicals appear outside the mean ξ_{st} iso-line envelope and close to the combustor lateral walls. Compared to Figs. 8.4(b) and 8.4(d), good agreement can be seen between the current S1 simulation and the

experiment. Overall, the results shown in Figs. 8.2−8.4 are able to demonstrate the statistical correctness of S1 computations in terms of both flow field and flame shape, which ensures the ensuing discussion on blow-off dynamics is technically meaningful.

8.3.3 Extinction characteristics of experimental blow-off curve in LES/3D-CMC

Since the present LES/3D-CMC modelling does not successfully predict the blow-off for those cases on the $1.0U_{BO,exp}$ curve that actually constitute the lower boundary of the computational blow-off range as shown in Fig. 8.1, it is of great importance to examine first how far these flames on the $1.0U_{BO,exp}$ curve are from the blow-off in the computations. All the five cases with $U_a = 1.0U_{BO,exp}$ are discussed in this Sub-section and they are S4, S5, S2, S6 and S7 with the successively increased air and fuel bulk velocities. Their relevant information is tabulated in Table 8.1.

The time series of the total heat release for S4, S5, S2, S6 and S7 cases on the $1.0U_{BO,exp}$ curve are presented in Fig. 8.5. For all the five cases, the total heat release rate Q varies around individual stable values with the fluctuations but does not demonstrate the globally decreasing tendency towards zero, which necessarily indicates the onset of global extinction. The time-averaged total heat release rate $\langle Q \rangle$ for S4, S5, S2, S6 and S7 cases are 4.22 kW, 5.06 kW, 6.49 kW, 7.56 kW and 7.59 kW, respectively. They are compiled with the respective time series shown in Fig. 8.5 but excluding the initial period of 0.01 s. For these five cases, the nominal powers estimated by the fuel flow rate times the CH_4 heat of combustion in the standard state [Law, 2006] are 7.93 kW, 10.17 kW, 12.38 kW, 14.12 kW and 16.26 kW, respectively. Therefore, $\langle Q \rangle$ from the current computations accounts for 46%−53% of their nominal values. This is expected to be caused by the strong finite-rate chemistry effects under these five operating conditions on the $1.0U_{BO,exp}$ curve. As such, although in the LES/3D-CMC the blow-off is not reached for S4, S5, S2, S6 and S7 cases, nevertheless, the finite-rate chemistry effects in the simulation results have become considerable on the lower boundary of computational blow-off range (i.e. the experimental blow-off curve).

The above mentioned finite-rate chemistry effects can be further examined through analyzing the extent of instantaneous and localized extinguishment on the stoichiometric mixture fraction ξ_{st} iso-surfaces. In non-premixed combustion, reactions nominally occurs on the ξ_{st} iso-surfaces and hence investigating the evolutions of key reactive scalars on ξ_{st} iso-surfaces is conducive to understanding the flame dynamics. Actually, this technique has been extensively in both experimental and computational studies, such as the reported work by Hult et al. [2005], Juddoo and Masri [2011], Steinberg et al. [2011], Garmory and Mastorakos [2011], Lignell et al. [2011] and Cavaliere et al. [2013], although in the measurements the accurate iso-surfaces of ξ_{st} are not readily available. Phenomenologically, when local extinction occurs flame holes with low temperature and species concentrations (e.g. OH) can be seen within the continuous burning regions. In this study, the conditionally filtered OH mass fraction at stoichiometry on the ξ_{st} iso-surfaces, $\widetilde{Y_{OH}|\xi_{st}}$, is used as the indicator, instead of $\widetilde{Y}_{OH}$, since the former is directly solved from the CMC governing equations, Eq. (3.35). When the local $\widetilde{Y_{OH}|\xi_{st}}$ is below the critical value, say 0.00024, it is supposed that that region is experiencing extinction. The threshold is determined by examining the OH distributions in mixture fraction space during the onset of extinction, which is the same estimation used in Chapter 6. The distribution of $\widetilde{Y_{OH}|\xi_{st}}$ on the ξ_{st} iso-surfaces from S2 case is demonstrated in Fig. 8.6(a). A large fraction of the iso-surface, particularly close to the swirl air ring inlets, experiences the extinction (visualized as blue, i.e. low $\widetilde{Y_{OH}|\xi_{st}}$) although fully reactive regions with high $\widetilde{Y_{OH}|\xi_{st}}$ (red surfaces) still exist. Meanwhile, the extent of transient extinction on the ξ_{st} iso-surfaces change with respect to the time if the similar contours to Fig. 8.6(a) is examined. To quantitatively predict the extinction level on the iso-surfaces, the extinguished fraction is introduced and defined as the area ratio of ξ_{st} iso-surface regions with $\widetilde{Y_{OH}|\xi_{st}} < 0.00024$ to the total ξ_{st} iso-surface, i.e.

$$f_{\Sigma,ext} = \frac{\Sigma\left|\left(\widetilde{Y_{OH}|\xi_{st}} < 0.00024\right)\right.}{\Sigma}. \tag{8.2}$$

Hence $f_{\Sigma,ext} = 1$ means the complete extinction over the entire ξ_{st} iso-surface while $f_{\Sigma,ext} = 0$ fully burning.

Figures 8.6(b) and 8.6(c) present the time evolutions of area of the total ξ_{st} iso-surface, Σ, and the extinguished fraction, $f_{\Sigma,ext}$, for the five cases on the $1.0U_{BO,exp}$ curve. Their areas of ξ_{st} iso-surface change between $0.01-0.03$ m^2 with time and in general Σ of S4 and S5 is slightly higher than that for S2, S6 and S7, probably due to their different flow and mixing characteristics under these operating conditions. It is more interesting when it comes to their extinguished fractions that are shown in Fig. 8.6(b). The initial $f_{\Sigma,ext}$ at $t = 0$ s is around 0.06 and then their $f_{\Sigma,ext}$ starts increasing gradually until $t = 35-40$ s. After $t = 35-40$ s, their respective plateau values are reached and $f_{\Sigma,ext}$ demonstrates the changes around the plateau values. Particularly, for S2 and S7, $f_{\Sigma,ext}$ changes between 0.4 and 0.6 while for others $f_{\Sigma,ext}$ is lower. As such, although all of them are on the $1.0U_{BO,exp}$ curve, however, the extent of local extinction on the ξ_{st} iso-surfaces is quite different. Virtually, the extinguished fraction does not expect to manifest an explicitly regular (e.g. strict monotonicity or, even more loosely, consistent change) variations from the left (i.e. S4) to right (i.e. S7) side of the $1.0U_{BO,exp}$ curve. This anticipation is somewhat groundless; after all, the cases on the $1.0U_{BO,exp}$ curve are parameterized by two quantities, i.e. bulk velocities of air (U_a) and fuel (U_f), and therefore their variations of $f_{\Sigma,ext}$ reflect the combined impacts of varying U_a and U_f. The individual influences of U_a and U_f on the extinction characteristics, flow and mixing fields will be discussed in Sub-section 8.3.4. In general, for the cases on the experimental blow-off curve, although LES/3D-CMC modelling ultimately fails to obtain the global extinction, however, they already demonstrate significant local extinction on the ξ_{st} iso-surface. This ability to capture local extinction has also been confirmed in Chapters 6 and 7. As such, the computational blow-off curve for $U_{BO,LES}$ must be above the $1.0U_{BO,exp}$ curve and selecting the $1.0U_{BO,exp}$ curve as the lower boundary of the computational blow-off range is logically natural.

8.3.4 Bulk velocity effects

In this Sub-section, the effects of air and fuel bulk velocities on the localized extinction characteristics as well as flow and mixing fields in the turbulent swirling non-premixed flames will be discussed separately. The stable flame cases S1, S2

and S3 are selected to examine the increased air bulk velocity effect since their fuel bulk velocity are the same, i.e. $U_f = 29.2$ m/s, but the air bulk velocity is successively increased from S1 ($U_a = 19.1$ m/s) to S3 ($U_a = 25.0$ m/s). The effect of fuel bulk velocity is studied with the cases S1 and S5, both of which have the same air bulk velocity $U_a = 19.1$ m/s but different fuel bulk velocities, i.e. $U_f = 29.2$ m/s for S1 and $U_f = 24.0$ m/s for S5. The other relevant information for these cases is listed in Table 8.1. The reader should be reminded that the swirl number S_N does not change when the bulk velocity varies and hence the swirl number effect is excluded. Here adjusting the bulk velocities U_a or U_f only results in the variations of the injected momentum in the fuel or air streams as well as the global equivalence ratios, which has been demonstrated in Table 8.1.

Although all these cases to be analyzed in this Sub-section represent stable flames in the computations, however, understanding the bulk velocity effects therein is a necessary step towards the following investigations on the blow-off occurrences and dynamics. This is particularly true for the effects of air bulk velocity since as mentioned previously the blow-off in the current computations and the experiments by Cavaliere et al. [2013] is attained through increasing the air flow rates. For the fuel bulk velocity effect, the comparisons made here are based on the S1 and S5, both of which are close to lean blow-off condition. In effect, as an alternative and extensively used approach, the fuel mass flow rate can be increased gradually until the flame blows off, such as in the Sandia piloted jet flame series [Barlow and Frank, 1998] and Sydney swirl flame series [Masri et al., 2004]. More recently, the mixture fraction and scalar dissipation rate in piloted non-premixed CO flames are studied by Sutton and Driscoll [2013] when the fuel mass flow rate is increased towards blow-off. Nevertheless, these flames in the respective series have the increased U_f essentially towards blow-off under fuel rich conditions, which are different from the investigations on the fuel bulk velocity here, which focus on lean blow-off conditions.

8.3.4.1 Air bulk velocity effect

The time records of the volume integrated total heat release rate Q for the S1, S2 and S3 cases are presented in Fig. 8.7. As shown in Fig. 8.7(a), although

the fuel and/or air inlet velocities are changed to the target bulk velocities when the simulation starts, the total heat release rate Q demonstrate the pronounced resistance (lasting roughly 0.02 s for the stable flame cases in Fig. 8.7a) behavior. After $t = 0.02$ s, Q of S1, S2 and S3 cases start to evolve differently due to their different U_a but individually maintain relatively stable values although some low-frequency fluctuations can be found, independent of U_a. Their time-averaged Q values compiled from the time records after $t = 0.02$ s are 7.09 kW, 6.49 kW and 3.65 kW, respectively, well below the nominal 12.38 kW, estimated by the fuel heat of combustion in the standard state [Law, 2006]. Similar to the results in Fig. 8.5, this finding indicates the considerable finite-rate chemistry effects in the investigated swirling flames and also the gradual weakening of flame reactivity with increased air axial bulk velocities from S1 ($U_a = 19.1$ m/s) to S3 ($U_a = 25.0$ m/s).

The time evolutions of areas of total ξ_{st} iso-surfaces Σ and extinguished fraction $f_{\Sigma,ext}$ for cases S1, S2 and S3 are plotted in Fig. 8.8. The change of air bulk velocity in these three cases also leads to the variation of the areas of the ξ_{st} iso-surfaces and one can see from Fig. 8.8(a) that Σ of S3 is lower than the two other cases. In the shown period $t = 0{-}0.05$ s in Fig. 8.8(b), the extinguished fractions $f_{\Sigma,ext}$ consistently become high with respect to the increased U_a from S1 to S3, although initially they are relatively small and close to each other. This directly indicates that on the ξ_{st} iso-surfaces the level of local extinction in mixture fraction space parameterized by $\widetilde{Y_{OH}|\xi_{st}}$ becomes more severe for larger air bulk velocity. In other words, the closer the case to the blow-off, the more local extinction occurs. This demonstrates the ability of the current LES/3D-CMC model to predict the response of the chemistry in mixture fraction space due to changed turbulent flow fields. $f_{\Sigma,ext}$ of S3 case sometimes can reach up to 0.8, which can be expected since S3 case lies fairly close to the upper boundary (i.e. $1.25U_{BO,exp}$ curve as shown in Fig. 8.1) of the computational blow-off range. Furthermore, $f_{\Sigma,ext}$ of S3 demonstrates more fluctuations than that of S2 and S3.

PSDs of filtered axial velocities from S1, S2 and S3 are calculated, which can be found in Fig. 8.9. Their filtered axial velocities are extracted from two probing locations (termed as *LES1* and *LES2* hereafter, denoted by open circles in Fig. 8.25h) and their coordinates are respectively (a) $x/D_b = 0.6$, $y/D_b = 0.72$,

$z/D_b = 0$ and (b) $x/D_b = 2.2$, $y/D_b = 1.28$, $z/D_b = 0$. One can clearly see that in the low-frequency range (i.e. $f < 100$ Hz) for both *LES1* and *LES2*, no dominant frequency exists for S1, S2 and S3 cases. This is in line with the findings from the measurement for S1 made by Cavaliere [2013]. In addition, for *LES1* presented in Fig. 8.9(a), PSDs of S1, S2 and S3 basically show negligible influence over the entire demonstrated frequency domain. Nevertheless, for *LES2*, there are noticeably higher PSD distributed in the high-frequency range (i.e. $f \geq 1000$ Hz) in S3 than those in S2 and S3 cases. The above observations imply that (a) different responses of PSDs exist for different positions caused by the increased air bulk velocity; (b) for *LES2*, more high-frequency turbulence appears in S3 since it is closer to blow-off and would have a significant impact on local scalar mixing and dissipation rate. The comparisons for PSDs of filtered axial velocity in other probing points from S1, S2 and S3 are also made and the PSDs for upstream and downstream regions resemble the representative results in Figs. 8.9(a) and 8.9(b), respectively.

The comparisons for the radial distributions of time and azimuthally averaged mixture fraction $\langle\tilde{\xi}\rangle$ and the *r.m.s.* ξ_{rms} from S1, S2 and S3 cases are made in Figs. 8.10. $\langle\tilde{\xi}\rangle$ and ξ_{rms} are respectively shown in left and right sides of each sub-figure of Figs. 8.10. Four streamwise positions, i.e. $x/D_b = 0.4$, 0.8, 1.2 and 1.6, are selected here for analysis. From Fig. 8.10, one can see that at $x/D_b = 0.4$ and 0.8, the radial distributions of the averaged mixture fraction $\langle\tilde{\xi}\rangle$ are not affected by the increased air bulk velocities from S1 to S3. The exceptional circumstance is along the centerline: for S3 case, the decay rate of $\langle\tilde{\xi}\rangle$ is much faster than that of S1 and S2. Different from the results in $x/D_b = 0.4$ and 0.8, the radial profiles of $\langle\tilde{\xi}\rangle$ at $x/D_b = 1.2$ and 1.6 consistently decrease over the entire shown radius for the cases with increased air bulk velocities, i.e. from S1 to S3. Contrary to the variations of mean mixture fraction, ξ_{rms} of S3 is marginally higher than that of S2 and S3 at $x/D_b = 0.4$ and 0.8 while at $x/D_b = 1.2$ and 1.6 it is significantly reduced and becomes smaller than that of other two cases. The behaviors observed in Fig. 8.10 can be justified by the results in Fig. 8.9. For the intensified high-frequency turbulence at downstream regions for S3, the mixing there is considerably facilitated, thereby leading to lower mixture fraction distribution and the reduced *r.m.s.*

The radial profiles of time and azimuthally averaged scalar dissipation rate $\langle\tilde{N}\rangle$ for S1, S2 and S3 cases at the same four streamwise positions as those in Fig. 8.10 are compared in Fig. 8.11. In the upstream regions such as at $x/D_b = 0.4$, 0.8 and 1.2, the discrepancy of $\langle\tilde{N}\rangle$ in the three cases is very small. However, at $x/D_b = 1.6$ in Fig. 8.11(d), $\langle\tilde{N}\rangle$ decreases as U_a increases from S1 to S3. In the current modelling, the filtered scalar dissipation rates $\tilde{N}$ include two separate contributions from the resolved and sub-grid scale mixing fields, i.e. $\tilde{N}_{res}$ and $\tilde{N}_{sgs}$, as expressed in Eq. (3.22). Therefore, it is important to analyze their individual contributions towards the variations of $\langle\tilde{N}\rangle$ in Fig. 8.11(d). For $\tilde{N}_{res}$, it is directly linked to the gradient of filtered mixture fraction $\nabla\tilde{\xi}$ and the molecular mass diffusivity D. At $x/D_b = 1.6$, with increased air bulk velocity, $\nabla\tilde{\xi}$ decreases appreciably from S1 to S3 based on the results not shown here. In addition, since the molecular mass diffusivity D is modelled as $D = \mu/\bar{\rho}Sc$ and the molecular viscosity μ is from Sutherland's law, D is essentially temperature dependent. Similar to $\nabla\tilde{\xi}$, temperature profiles at $x/D_b = 1.6$ also decrease from S1 to S3, which leads to the fact that D decreases as U_a increases. As such, the joint influences of $\nabla\tilde{\xi}$ and D make $\tilde{N}_{res}$ reduce with increased U_a. For sub-grid scale scalar dissipation $\tilde{N}_{sgs}$, it is affected by the sub-grid mixture fraction variance $\widetilde{\xi''^2}$ and viscosity μ_{sgs}. $\widetilde{\xi''^2}$ is modelled through Eq. (3.23). Based on the results in Fig. 8.10(d), at $x/D_b = 1.6$, the *r.m.s.* of mixture fraction decreases as U_a increases and thus this also can apply for $\widetilde{\xi''^2}$. The sub-grid scale viscosity μ_{sgs} is proportional to $k^{1/2}$, as shown in Eq. (3.16). The sub-grid scale kinetic energy k demonstrates the pronounced increase when U_a is increased from S1 to S3 based on the results not shown here. As such, for $\tilde{N}_{sgs}$, the contribution (leading to reduction of $\tilde{N}_{sgs}$) from sub-grid scale variance of mixture fraction $\widetilde{\xi''^2}$ dominate that (leading to increase of $\tilde{N}_{sgs}$) from sub-grid scale kinetic energy k and hence the net effect is that $\tilde{N}_{sgs}$ decreases with increased U_a, which is the same as that for the resolved scalar dissipation rate $\tilde{N}_{res}$.

The time-averaged conditional temperature and mass fractions of CH_4, O_2, OH and CH_2O in three CMC cells, *CMC1*, *CMC2* and *CMC3*, from S1, S2 and S3 are compared in Fig. 8.12. The positions for these CMC cells are explicitly marked by open squares in Fig. 8.25(h). For clarity, in spite of the same naming, these three CMC cells are different from the probing CMC cells used for analysis

in Chapter 6. For *CMC1* presented in the first column in Fig. 8.12, due to the increased U_a from S1 to S3, the mean conditional temperature $\widetilde{\langle T|\eta \rangle}$ is reduced in the whole mixture fraction space. Meanwhile, mean conditional mass fractions of CH_4 and O_2 are high as the air bulk velocity increases. For S3 cases, the pronounced fuel leakage can be observed for $\eta \leq \xi_{st} = 0.055$. The two key radicals in the methane oxidization, OH and CH_2O, demonstrate quite different behaviors when U_a is increased: the mean conditional mass fraction of OH is decreased with increased U_a while for CH_2O the tendency is opposite. This difference reflects their response due to the variations of local reactivity caused by the change of flow and mixing fields. The similar differences between S1, S2 and S3 also exist for *CMC2* based on the results in the second column of Fig. 8.12. Nevertheless, for *CMC3*, the influence of increased air bulk velocity on the mean conditional flame structures is comparatively small, although one can still see that the mean conditional mass fraction of CH_2O increases as U_a increases. Therefore, the mean flame structures in mixture fraction space for different positions show the different response when the air bulk velocity U_a is adjusted. This is consistent with the variations of axial velocity PSD, mean mixture fractions and their variances as well as the mean scalar dissipation rates in S1, S2 and S3 cases.

8.3.4.2 Fuel bulk velocity effect

Similar to the line of reasoning for the influence of air bulk velocity, the fuel bulk velocity effect will also be discussed in the aspects of extinguished fraction, axial velocity PSD, statistics of mixture fraction and scalar dissipation rate as well as the mean conditional flame structures. First, the time series of extinguished fraction on the stoichiometric mixture fraction iso-surfaces for S1 and S5 are examined. $f_{\Sigma,ext}$ of S1 and S5 extracted from their individual simulated time has been presented in Fig. 8.6(b) and 8.8(b). Clearly, both $f_{\Sigma,ext}$ increases with time and in the whole period, $f_{\Sigma,ext}$ from S5 demonstrates higher value than that from S1, indicating more outstanding level of local extinction on the ξ_{st} iso-surfaces in S5 case. One can find from Table 8.1 that the global equivalence ratios ϕ_g vary roughly between 0.23 and 0.3 for S1 and the cases on the $1.0U_{BO,exp}$ curve and therefore all the cases are operated under the fuel lean conditions. In the

computations, S5 is closer to the computational blow-off range as presented in Fig. 8.1 than S1.

The comparisons of axial velocity PSDs from S1 and S5 cases are made in Fig. 8.13 and the probing locations are exactly same as those in Fig. 8.9, i.e. *LES1* and *LES2*. The reduction of the fuel bulk velocity from S1 to S5 does not lead to the significant change of the PSDs for the axial velocities at these two locations, regardless of high and low frequency domains. This is different from the results in Fig. 8.9, in which case the variations of air bulk velocity results in the pronounced change of PSD in *LES2*.

Figures 8.14 and 8.15 show the radial profiles of statistics of mixture fraction and mean scalar dissipation rate, respectively. Due to the decreased momentum from fuel of S5 compared to that of S1, the mean mixture fraction $\langle\tilde{\xi}\rangle$ of S5 decays much faster. However, close to the centerline at the streamwise locations of $x/D_b = 0.4$, 0.8 and 1.2, ξ_{rms} of S5 is larger than that of S1. For the mean scalar dissipation rate $\langle\tilde{N}\rangle$, at the streamwise locations of $x/D_b = 0.8$ and 1.2, the disparity between S1 and S5 is negligible. At $x/D_b = 0.4$, $\langle\tilde{N}\rangle$ of S5 is higher than that of S1 within $0 < r/D_b < 0.1$, which can be found in Fig. 8.15(b). Furthermore, at $x/D_b = 1.6$, S5 has the lower mean scalar dissipation rate than S1 for the whole radius presented.

The time averaged conditional temperature and mass fractions of CH_4, O_2, OH and CH_2O in *CMC1*, *CMC2* and *CMC3* from S1 and S5 cases are plotted in Fig. 8.16. For *CMC1*, $\langle\widetilde{T|\eta}\rangle$ and $\langle\widetilde{Y_{OH}|\eta}\rangle$ are lower in S5 while $\langle\widetilde{Y_{CH4}|\eta}\rangle$, $\langle\widetilde{Y_{O2}|\eta}\rangle$ and $\langle\widetilde{Y_{CH2O}|\eta}\rangle$ demonstrate the opposite tendency. Instead, at *CMC2* and *CMC3*, the difference is relatively small, except $\langle\widetilde{Y_{CH2O}|\eta}\rangle$. CH_2O shows the influence from the variations of fuel bulk velocity and in S5 $\langle\widetilde{Y_{CH2O}|\eta}\rangle$ is higher than that in S1.

8.3.5 Blow-off characterization

The time records of total heat release rate Q for BO1, BO2 and BO3 are shown in Fig. 8.17. For blow-off case BO1 with $U_a = 26.5$ m/s, the total heat release rate Q gradually decreases, accompanied by the considerable low-frequency fluctuations and also the burst of Q at $t = 0.02$ s, and eventually reaches zero, indicating the

occurrence of the complete blow-off in the LES. The sudden increase and decrease of Q around $t = 0.02$ means that at that time the non-premixed flame is suddenly approaching the extinction in most regions, quantified by large Q, and then large fraction of extinction happens with greatly reduced Q. This trend is explicitly different from those of stable cases in Fig. 8.7, which share the same fuel bulk velocity $U_f = 29.2$ m/s as the blow-off case here. With increased U_a being 30 m/s, BO2 shows the basically similar Q variations to BO1 towards blow-off but faster decay of Q since $t = 0.021$ s. In BO2, relatively low Q with limited increment, corresponding to very weak combustion with fluctuating heat liberation, persists for a long duration, i.e. between $t = 0.03$ s and 0.05 s. The blow-off time obtained from BO1 and BO2 is respectively $\tau_{BO} \approx 0.055$ s and 0.057 s, close to the measured critical result of 0.0466 s. Again, one should be reminded of the fact that this measured critical blow-off time of 0.0466 s is in statistically mean sense and obtained from the experiments with S2 operating conditions, instead of BO1 or BO2 [Cavaliere et al., 2013]. In Fig. 8.17, one can also see that when U_a is increased to 34.5 m/s in BO3, τ_{BO} is decreased to about 0.03 s, a trend consistent with the observations from premixed flame blow-off experiments [Dawson et al., 2011; Kariuki et al., 2012]. Furthermore, three peaks of Q after $t = 0.014$ s are intermittently discernible before BO3 completely extinguishes. Similar to BO1 and BO2, these peaky total heat release rates imply that the flame is suddenly and extensively close to the extinction and based on the results in Fig. 8.17 the flame reactivity is always weakened considerably after these peaks. They are the significant manifestations in blow-off of turbulent non-premixed flames and also observed in the OH* chemiluminescence [Cavaliere et al., 2013]. Based on the results in Fig. 8.7, these variation of total heat release in stable flames, say S1−S3, are not as pronounced as these in BO1−BO3, although Q fluctuations exist.

The time evolutions of three dimensional iso-surfaces of filtered heat release rate ($\tilde{\dot{q}} = 60$ MJ/m^{3}s) overlaid by the filtered temperature $\tilde{T}$ for S3 and BO2 are presented in Figs. 8.18 and 8.19, respectively. Before $t = 0.018$ s in Figs. 8.18(a)−8.18(c), heat release regions are extensive and comparatively continuous in the IRZ near the bluff body and there are also considerable high $\tilde{T}$ areas on the iso-surfaces. Then the heat release regions become small and fragmented as shown

in Fig. 8.18(d) but iso-surfaces always exist near the bluff body until $t = 0.05$ s in Fig. 8.18(g). This is consistent with time history of S3 total heat release in Fig. 8.7. For BO2, similar to the S3 results in Figs. 8.18(a)−8.18(c), the liberated heat is pervasive in the upstream of IRZ presented in Figs. 8.19(a)−8.19(c). Nevertheless, at $t = 0.027$ s in Fig. 8.19(d), the heat release is greatly reduced although at $t = 0.036$ s in Fig. 8.19(e) some degree of recovery appear, caused by the re-ignition in IRZ. Then the $\tilde{\dot{q}}$ iso-surfaces gradually diminish again and basically disappear at $t = 0.061$ s, when BO2 has extinguished based on discussed in Fig. 8.17.

Two additional behaviors from Fig. 8.19 worth noting are: (i) during the BO2 transients towards complete extinction, finite heat release exists very close to the circular bluff body surface for a long period (see Figs. 8.19f and 8.19g) and (ii) due to the essential solid-body rotation in IRZ, the fully burning flame structures are intermittently transported from the IRZ toward the lateral walls (see Figs. 8.19c and 8.19f), where it is accumulated and hence the local $\tilde{\dot{q}}$ increase is expected due to the not high scalar dissipation and reverse flows. These two behaviors can respectively justify the features of total heat release rate demonstrated by BO2 in Fig. 8.17, i.e. the long persistence with low Q and intermittent peaks. They are also seen from the time series of area integrated OH* emissions from the blow-off experiments of CH_4 non-premixed flames [Cavaliere et al., 2013]. So generally the current LES/3D-CMC modelling formulated in Sections 3.2 and 3.3.2 correctly predict the basic transient behaviors of blow-off in swirling non-premixed flames. However, these two behaviors do not appear in the LES/3D-CMC simulations of blow-off of n-heptane spray flames in the same swirl burner [Tyliszczak et al., 2014], which may be attributed to the strong correlations between combustion and evaporation, i.e. weakened reactions leads to cooler recirculation zone and hence weakened evaporation, a process leading to a quicker blow-off event in spray flames compared to the gaseous flames. This discrepancy between non-premixed and spray flames is also indicated by the respective blow-off experiments [Cavaliere et al., 2013].

8.3.6 Localized extinction and re-ignition in blow-off

The time evolutions of conditionally filtered heat release rate, temperature, OH and CH_2O at stoichiometry corresponding to three CMC cells, *CMC1*, *CMC2* and *CMC3*, are presented in Figs. 8.20, 8.21 and 8.22, respectively. The time series are from BO2 case. For *CMC1* in Fig. 8.20, within the initial 0.02 s, the flame structures in mixture fraction space are strongly reactive, which can be manifested by high $\widetilde{T|\xi_{st}}$ and $\widetilde{Y_{OH}|\xi_{st}}$ and fluctuating $\widetilde{\dot{q}|\xi_{st}}$ in Figs. 8.20(a)−8.20(c). Their transient behaviors are similar to the results from the stable flame shown in Fig. 6.9. However, $\widetilde{Y_{CH2O}|\xi_{st}}$ in Fig. 8.20(d) demonstrates the basically opposite variation: when $\widetilde{T|\xi_{st}}$ and $\widetilde{Y_{OH}|\xi_{st}}$ are high (low), $\widetilde{Y_{CH2O}|\xi_{st}}$ is low (high). After $t = 0.02$ s, two features are discernible. First, the frequency at which all these conditional quantities fluctuate becomes large. Second, the flame structures in this CMC cell are gradually quenched with low $\widetilde{T|\xi_{st}}$ and almost zero $\widetilde{\dot{q}|\xi_{st}}$ as well as $\widetilde{Y_{OH}|\xi_{st}}$. Different from $\widetilde{Y_{OH}|\xi_{st}}$, $\widetilde{Y_{CH2O}|\xi_{st}}$ consistently increases compared to itself within $t = 0$−0.02 s.

CMC2 demonstrates the considerably different time evolutions of the same conditionally filtered quantities. In general, this CMC cell is negligibly affected by the blow-off occurrence and always fully burning even when the blow-off point is reached at $t = \tau_{BO} \approx 0.057s$. However, for *CMC3* that lies close to the bluff body surfaces, within the initial 0.03 s period the conditionally filtered reactive scalars are fully burning with few fluctuations. Since $t = 0.03$ s, this CMC cell starts to undergo the instantaneous local extinctions, which leads to the strong variations of the flame structures in mixture fraction space. After $t = 0.05$ s, this CMC cell is exposed to the extinction for a longer period until $t = 0.058$ s when the recovery of the burning flame structures is seen. Therefore, based on the results in Figs. 8.20, 8.21 and 8.22, one can find that, during the blow-off transient, the flame structures in individual CMC cells demonstrate the noticeably evolutions toward extinguishment in mixture fraction space.

Similar to Fig. 8.6(a), the three dimensional ξ_{st} iso-surfaces coloured by $\widetilde{Y_{OH}|\xi_{st}}$ from BO2 case are shown in Fig. 8.23(a). Besides the extinction regions (colored in blue) close to the bluff body edge, one can also see that they are expanded towards downstream over the ξ_{st} iso-surfaces. Meanwhile, some of

the iso-surfaces near the bluff body surface is fully burning with relatively high $\widetilde{Y_{OH}|\xi_{st}}$. The time sequences of the ξ_{st} iso-surface area, Σ, and its extinguished fraction $f_{\Sigma,ext}$ from S3 and BO2 are presented in Figs. 8.23(b) and 8.23(c), respectively. The results for S3 are also available in Fig. 8.8 and shown here for comparison with the blow-off case BO2 since it is very close to the $1.25U_{BO,exp}$ curve but still demonstrates the stable flame characteristics. It can be seen from Fig. 8.23(b) that Σ of S3 fluctuates around a stable value, around 0.012 m^2. This feature is different from the results for the blow-off event BO2 in Fig. 8.23(c), in which case Σ shows a slight decrease with some fluctuations. This trend of BO2 case is contrary to the results from recent DNS of planar, non-premixed ethylene jet flames [Lignell et al., 2011], where the area of instantaneous ξ_{st} iso-surfaces increases as the local extinction degree increases. The extinguished fraction, $f_{\Sigma,ext}$, from BO2 increases from an initially low value to around unity. In addition, a sharp decrease of $f_{\Sigma,ext}$ occurs occasionally (e.g. $t = 0.008$ and 0.02 s in Fig. 8.23c) probably due to the geometrical change (e.g. expansion, fragmentation and corrugation) and/or re-ignition of the ξ_{st} iso-surfaces. The differences in $f_{\Sigma,ext}$ between a stable flame, where $f_{\Sigma,ext}$ stays above zero but below unity, and the blow-off case, where $f_{\Sigma,ext}$ progressively reaches unity, are evident in Fig. 8.23.

For the blow-off event BO2, Fig. 8.24 further shows the time records of the extinguished fraction $f_{\Sigma,ext}$ and ξ_{st} iso-surface area Σ corresponding to different flame sections along the streamwise distance, i.e. flame root ($0 < x \leq 0.015$ m), middle (0.015 m $< x \leq$ 0.03 m) and top ($x >$ 0.03 m), to understand their individual behaviors during blow-off. Here $f_{\Sigma,ext}$ is calculated using Eq. (8.2) but based on the extinguished and total ξ_{st} iso-surface for individual sections. It is seen from Fig. 8.24(a) that at $t = 0$ the flame root has the largest extinguished fraction while the flame top the weakest. The extinguished fraction $f_{\Sigma,ext}$ of the three sections increases until about $t = 0.03$ s and after that all the three extinguished fractions are close to unity, indicating almost complete extinction occurring on the surface. This is consistent with the results in Fig. 8.23(c). Similar to Fig. 8.23, the evolutions of Σ for each section are also shown in Fig. 8.24(b). Σ corresponding to the flame bottom shows negligible variations during the whole time records. As such, its increase (e.g. at $t = 0.03$ s) or decrease (e.g. at $t = 0.035$ s) of $f_{\Sigma,ext}$ is entirely caused by the production or destruction of

OH in mixture fraction space on the iso-surface. However, for the middle section, the strong fluctuations of Σ do not lead to the exactly corresponding change of $f_{\Sigma,ext}$. This is particularly true after $t = 0.035$ s: $f_{\Sigma,ext}$ evolves monotonically towards unity, indicating the gradually severe extinguishment at the middle section. Differently, at the top, Σ fluctuates with comparatively low frequency and the simultaneous low $f_{\Sigma,ext}$ can be seen corresponding to the peak of Σ, e.g. $t = 0.035$ s and 0.041 s. Generally, during the blow-off processes of BO2, local extinction and re-ignition always occur at the bottom and top sections until the onset of complete extinction. This blow-off mode is shared by all the cases marked along $1.25U_{BO,exp}$ and $1.6U_{BO,exp}$ lines in Fig. 8.1 due to the same swirl number S_N. This is different from the Sydney turbulent non-premixed swirling flames with high swirl number in which case the flames completely peel off the burner surface (i.e. base blow-off) when they reach global extinction [Al-Abdeli and Masri, 2003].

8.3.7 Evolutions of species and scalar dissipation during the blow-off transient

The contours of unconditionally filtered temperature $\tilde{T}$ on $x-y$ plane from the BO2 case are plotted in Fig. 8.25. The eight sub-figures correspond to $t = 0-0.061$ s, spanning the whole transient blow-off process. At $t = 0$ s in Fig. 8.25(a), high $\tilde{T}$ appears along the instantaneous ξ_{st} iso-lines as well as in the downstream of the chamber. Within the following around 0.018 s in Figs. 8.25(b) and 8.25(c), $\tilde{T}$ becomes weak in the downstream but along the ξ_{st} iso-lines it is still high, indicating that there are still reactions occurring. As the BO2 flame gradually blows off, the filtered temperature $\tilde{T}$ is considerably reduced and only some pockets near the bluff body still exist, as shown in Figs. 8.25(d)−8.25(g). At $t = 0.061$ s in Fig. 8.25(h) when the blow-off occurs, the flows in the whole chamber are cooled with $\tilde{T}$ basically less than 700 K.

With exactly the same time instants as those in Fig. 8.25, the contours of unconditionally filtered OH mass fraction $\widetilde{Y}_{OH}$ visualized from BO2 as well are plotted in Fig. 8.26. Initially, along the highly convoluted ξ_{st} iso-lines, considerable $\widetilde{Y}_{OH}$ can be observed at $t = 0$ s in Fig. 8.26(a). Meanwhile, regions with low

$\widetilde{Y}_{OH}$ corresponding to instantaneous localized extinction exist around the fuel jet tip as well as the right branch near the bluff body edge. Then the extinction extent gradually increases with time from Fig. 8.26(b) to Fig. 8.26(h). When BO2 blows off at $t = \tau_{BO} \approx 0.057$ s, very little OH exists in Fig. 8.26(h). Furthermore, re-ignition with local increase of OH can be seen in the recirculation zone close to the bluff body, quantified by the localized pockets with high $\widetilde{Y}_{OH}$ in Figs. 8.26(d)−8.26(g). Also, no continuous lift-off near the bluff body surface is seen before complete blow-off, consistent with experiment [Cavaliere et al., 2013] and similar to other findings in blow-out of unconfined swirl-stabilized non-premixed flames [Feikema et al., 1991]. However, this is different from the phenomenological observations of blow-out process in turbulent non-premixed jet fame in which case the flame base is continuously pushed far from the burner and the extinction happens between the flame base and burner exit [Wu et al., 2006]. In general, the blow-off transient in Fig. 8.26 agrees qualitatively well with the experimental results with OH-PLIF [Cavaliere, 2013; Cavaliere et al., 2013].

The time evolution of unconditionally filtered CH_2O mass fraction $\widetilde{Y}_{CH2O}$ from BO2 is demonstrated in Fig. 8.27. CH_2O is a key intermediate from CH_3 oxidization towards CO and CO_2 and therefore viewed as a significant indicator for the underlying chemical kinetics, particularly when the finite-rate chemistry effects become dominant [Böckle et al., 2000; Kariuki et al., 2015; Medwell et al., 2007; Yuan et al., 2015b]. In the present LES of blow-off, initially when the flame has strong reactivity in Fig. 8.27(a), very few localized $\widetilde{Y}_{CH2O}$ peaks appear along the ξ_{st} iso-lines and generally CH_2O distribution is uniform, say $\widetilde{Y}_{CH2O} \approx 0.0002$, within the ξ_{st} iso-lines. As the flame gradually approaches the global extinction, CH_2O is considerably accumulated in IRZ close to the bluff body ($0 < x < 0.02$ m) which can be clearly found from Fig. 8.27(b) to Fig. 8.27(f). In addition, CH_2O is intermittently transported from the IRZ downstream towards the chamber walls, e.g. in Figs. 8.27(c) and 8.27(f). The localized high CH_2O pockets gradually diminish close to the bluff body surface and at $t = 0.061$ s when BO2 is globally extinguished, such pockets basically disappear. However, CH_2O still has finite concentration in most of the chamber. The CH_2O characteristics are different from those of OH shown in Fig. 8.27, which are also found in the measurements by Böckle et al. [2000], Medwell et al. [2007] and Yuan et al. [2015b].

Figures 8.28(a)−8.28(h) shows the evolutions of conditionally filtered OH mass fraction at stoichiometry $\widetilde{Y_{OH}|\xi_{st}}$ in the LES resolution during the blow-off transients and their temporal information exactly corresponds to that in Figs. 8.25−8.27. Compared to Fig. 8.26, one can clearly see that the reactive region in mixture fraction space (i.e. high $\widetilde{Y_{OH}|\xi_{st}}$ in Fig. 8.28) are more distributed than those in physical space (i.e. high $\widetilde{Y_{OH}}$ in Fig. 8.26). Regions with low $\widetilde{Y_{OH}|\xi_{st}}$ only exist in the downstream of central fuel jet and swirling air inlet when $t = 0$ and 0.0009 s in Figs. 8.28(a) and 8.28(b), respectively. This directly results from the convection of inert CMC solutions from both inlets. In contrast, high $\widetilde{Y_{OH}|\xi_{st}}$, indicating the full reactivity in η-space, can be seen in the IRZ close to the bluff body. In Figs. 8.28(c) and 8.28(d), it can be seen that high $\widetilde{Y_{OH}|\xi_{st}}$ regions are disconnected from the downstream reactive regions and become isolated in this two-dimensional slice. Nevertheless, in Figs. 8.28(e) and 8.28(f) the left high $\widetilde{Y_{OH}|\xi_{st}}$ region expands and then coalesces with the downstream zones, leading to the onset of re-ignition there. The extinction regions continuously increase in size in the last stage of blow-off in Figs. 8.28(g) and 8.28(h). When the flame is fully extinguished in physical space, $\widetilde{Y_{OH}|\xi_{st}}$ is zero almost along the whole ξ_{st} iso-lines.

Figures 8.28(i)−8.28(l) correspond to the evolutions of $\widetilde{Y_{OH}|\xi_{st}}$ during the post-extinction stage (approximately 0.03 s more after blow-off). There are always some regions with finite residual $\widetilde{Y_{OH}|\xi_{st}}$, e.g. around the downstream of the air stream and immediately outside the ξ_{st} iso-lines. Complete quenching of OH in mixture fraction space $\widetilde{Y_{OH}|\xi_{st}}$ does not occur, although from Fig. 8.26 $\widetilde{Y}_{OH}$ is zero in the chamber after blow-off. This inconsistency can be analyzed as follows: (i) residual $\widetilde{Y_{OH}|\xi_{st}}$ regions may be never quenched (e.g. around $x = y = 0.04$ m) and/or obtain OH through the neighboring CMC cells, particularly due to the existence of the strong recirculating flows in IRZ (e.g. $0 < y < 0.01$ m close to the bluff body shown in Fig. 8.28i and 8.28l) and (ii) the scalar dissipation in these regions is relatively low so that burning conditional reactive scalars are difficult to reach extinction. After blow-off, another interesting phenomenon in Figs. 8.28(i)−8.28(l) is that the ξ_{st} iso-lines and the enclosed basically have zero $\widetilde{Y_{OH}|\xi_{st}}$, even if the neighboring cells have high values. This ensures the global extinction along the ξ_{st} iso-lines in physical space. However, very localized $\widetilde{Y_{OH}|\xi_{st}}$

would still appear along ξ_{st} iso-lines after blow-off (e.g. $y = -0.01$ m close to the bluff body in Fig. 8.28j) but this would not ignite the whole flame any more. Generally, the above mentioned phenomenon is expected to be related to the evolution of scalar dissipation rate and will be discussed later in this Sub-section.

Essentially, three dimensional flow effects on flame re-ignition exist in turbulent jet flames [Juddoo and Masri, 2011; Steinberg et al., 2011], let alone in swirling flows with strong tangential velocity component. Indeed, they have been observed in the measurements of the current investigated swirl flames [Cavaliere et al., 2013] and also appears in a partially premixed swirl burner [Boxx et al., 2010]. In the context of the CMC model, the three-dimensional flow effects occurring between neighboring CMC cells can be predicted by the conditional convection, dilatation and sub-grid scale diffusion terms as shown in Eq. (3.35). In Subsection 8.3.6, the features of re-ignition during blow-off transients are discussed in the local (in individual CMC cells) and global (over the ξ_{st} iso-surfaces) aspects in Figs. 8.20−8.23. In the results of Fig. 8.28, there are mainly two modes of CMC cell interactions. First, the coalescence of reaction zones with high $\widetilde{Y_{OH}|\xi_{st}}$ (as shown in Fig. 8.28) and appearance of isolated $\widetilde{Y_{OH}|\xi_{st}}$ pockets (not shown in Fig. 8.28) in IRZ are caused by transporting the fully burning conditional profiles between neighboring cells (particularly from downstream cells due to flow reverse). Second, at the downstream of the swirling air streams and close to the chamber walls (spanwise distance $y = \pm 0.04$ m and streamwise distance $x = 0.04$ m), burning profiles in η-space, e.g. high $\widetilde{Y_{OH}|\xi_{st}}$ in Fig. 8.28, are intermittently from IRZ due to the strong shearing between the swirling air stream and IRZ. These two modes are confirmed by the corresponding regions with relatively high mean distributions of $\tilde{\dot{q}}$ and $\widetilde{Y}_{OH}$ as shown in Fig. 8.4. The ability to predict transport effects in physical space by CMC model was also pointed out when the upstream extinction occurring in the Calgary lifted flames [Navarro-Martinez and Kronenburg, 2011] and localized extinction in Sandia flame F [Garmory and Mastorakos, 2011], and TECFLAM [Ayache and Mastorakos, 2013] are investigated.

Figure 8.29 presents the time evolutions of conditional mass fractions and temperature at stoichiometry, $\langle\widetilde{Y_\alpha|\xi_{st}}\rangle_\Sigma$ and $\langle\widetilde{T|\xi_{st}}\rangle_\Sigma$, from the blow-off event BO2. Here the operator "$\langle\cdot\rangle_\Sigma$" denotes the spatial averaging based on the samples extracted from ξ_{st} iso-surfaces Σ for each time instant. During the whole simulated

period, $\widetilde{\langle Y_{OH}|\xi_{st}\rangle_\Sigma}$ gradually decreases toward blow-off at $t = 0.057$ s, as shown in Fig. 8.29(a). This trend is in line with the total heat release rate Q results in Fig. 8.17 and the extinguished fraction $f_{\Sigma,ext}$ in Fig. 8.23(b). However, from Figs. 8.29(b) and 8.29(c), the surface averaged CH_2O and unburned C_2 hydrocarbons (UHC, i.e. ethane C_2H_6, ethylene C_2H_4 and acetylene C_2H_2 included in ARM2 mechanism) concentrations , i.e. $\widetilde{\langle Y_{CH2O}|\xi_{st}\rangle_\Sigma}$ and $\widetilde{\langle Y_{UHC}|\xi_{st}\rangle_\Sigma}$, first increases and after $t = 0.02$ s decrease. At $t = 0.06$ s which is very close to complete blow-off, they are still around 50% of the individual peaks during the time series. The averaged temperature $\widetilde{\langle T|\xi_{st}\rangle_\Sigma}$ in Fig. 8.29(d) presents a similar change to that of $\widetilde{\langle Y_{OH}|\xi_{st}\rangle_\Sigma}$ in Fig. 8.29(a).

The distributions of filtered scalar dissipation rate $\tilde{N}$ in logarithmic scale, $\log_{10}\tilde{N}$, corresponding to the blow-off case BO2 are presented in Fig. 8.30. At $t = 0$ s shown in Fig. 8.30(a), the majority of the high filtered scalar dissipation is spatially confined to thin layers located immediately around the central fuel jet upstream (i.e. $0 < x \leq 0.015$ m) while downstream (i.e. 0.015 m $< x <$ 0.055 m) the layer structures mostly follow the instantaneous ξ_{st} iso-lines. These scalar dissipation distributions resemble those in turbulent jet flames [Frank et al., 2011; Pitsch and Steiner, 2000a; Sutton and Driscoll, 2007]. At $t = 0.018$ s and 0.045 s in Figs. 8.30(b) and 8.30(c), two main features can be observed. First, the layer-like structures there gradually become weak. Second, small pockets with the intermediate $\tilde{N}$ are alternately transported toward the chamber side walls accompanied by the severe disintegration of the ξ_{st} iso-surfaces there. This phenomenon is manifested by the intermittent occurrences of local extinction and re-ignition near the chamber walls, as shown in Figs. 8.28(e), 8.28(g) and 8.28(h). At the blow-off point $t = 0.061$ s in Fig. 8.30(d), the fuel jet penetrates less. If Fig. 8.28(h) is re-visited with Fig. 8.30(d), one can see that, after blow-off, extinction in mixture fraction space occurs almost in the entire regions with finite $\tilde{N}$, which are roughly enclosed by the ξ_{st} iso-lines. However, beyond the ξ_{st} iso-lines where $\tilde{N}$ is small, there are still considerable $\widetilde{Y_{OH}|\xi_{st}}$. Such relation between $\tilde{N}$ and $\widetilde{Y_{OH}|\xi_{st}}$ under blow-off condition is not observed when the flame is strongly reactive if the similar comparison between Figs. 8.30(a) and 8.28(a) is made. The evolutions of the filtered scalar dissipation structures are expected to be affected by the changes in the turbulence when the flame gradually approaches

blow-off and hence the density of the recirculating gases changes.

The averaged unconditionally filtered and conditionally filtered stoichiometric scalar dissipation, i.e. $\langle\tilde{N}\rangle_\Sigma$ and $\langle\widetilde{N|\xi_{st}}\rangle_\Sigma$, on the ξ_{st} iso-surfaces are calculated and their time series are plotted in Fig. 8.31. Here the averaging procedure is same as that used in Fig. 8.29. Figure 8.31(a) presents the time series of surface-averaged $\langle\tilde{N}\rangle_\Sigma$ and $\langle\widetilde{N|\xi_{st}}\rangle_\Sigma$ from the blow-off case BO2. Generally, $\langle\tilde{N}\rangle_\Sigma$ decreases with time. $\langle\widetilde{N|\xi_{st}}\rangle_\Sigma$ is well below the conditional scalar dissipation at extinction from a stand-alone 0D-CMC calculation, which is 18.3 1/s, and shows little change before $t = 0.05$ s. However, when the flame is close to blow-off, (e.g. $t = 0.05{-}0.06$ s in Fig. 8.31a), the peaky fluctuations with high frequency and large magnitudes appear, which is a prominent symptom of the flame close to blow-off. For comparison, the corresponding results of another blow-off case with larger air bulk velocity (BO3) and a stable flame case (S3) are also presented in Figs. 8.31(b) and 8.31(c). One can see that for BO3 the high-frequency fluctuations of $\langle\widetilde{N|\xi_{st}}\rangle_\Sigma$ starts at $t = 0.01$ s, much earlier than BO1 case in Fig. 8.31(a). However, for S3, the fluctuation magnitudes are comparatively small.

8.3.8 Blow-off time

The blow-off time τ_{BO} of BO1, BO2 and BO3 has been demonstrated in Fig. 8.17 based on the time records of total heat release rate Q and it is shown that τ_{BO} for BO1 which is on $1.25U_{BO,exp}$ curve is higher than that for BO3 on $1.6U_{BO,exp}$ curve by around 45%. Figure 8.32 plots the time series of total heat release rate Q of all the cases on both $1.25U_{BO,exp}$ and $1.6U_{BO,exp}$ curves shown in Fig. 8.1. Based on Figs. 8.32(a)$-$8.32(e), basically τ_{BO} of $1.6U_{BO,exp}$ curves is smaller than that of $1.25U_{BO,exp}$ curve. However, the exceptional circumstance can be seen when $U_f = 34.3$ m/s and the blow-off time τ_{BO} for both cases is approximately the same, i.e. $\tau_{BO} \approx 0.04$ s. In addition, the blow-off time of the cases on $1.25U_{BO,exp}$ and $1.6U_{BO,exp}$ curve demonstrates the non-monotonic behaviors with simultaneously increased fuel and air bulk velocities. For example, on $1.25U_{BO,exp}$ curve, τ_{BO} for cases with $U_f = 18.7$ m/s, 29.2 m/s and 39.5 m/s is about 0.07 s, 0.06 s and 0.05 s, but for $U_f = 24$ m/s and 34.3 m/s, it is around 0.04 s. Actually the longer blow-off time is caused by the existence of small flame pockets in the IRZ when

the flame is very close to blow-off, which is quantified by the long-lasting low Q like in Fig. 8.32(a). This phenomenon is not observed in the cases on $1.6U_{BO,exp}$ curve except the one with $U_f = 18.7$ m/s presented in Fig. 8.32(a). It should be highlighted that the evolutions of the total heat release rate in Fig. 8.32 are from a single LES/3D-CMC simulation for the corresponding operating conditions and therefore the blow-off time indicated by Fig. 8.32 does not have statistical sense. To generalize the variations of blow-off time with respect to air and/or fuel bulk velocities, the efforts to predict their mean should be made, which is not conducted in the present investigations due to the prohibitive computational cost. This is not measured by Cavaliere et al. [2013] either and thus further experimental work about blow-off time over a range of conditions is still required. Understanding the correlation between the blow-off time and a range of operating conditions possesses the practical significance for designing the new burner and combustor.

8.3.9 Discussion

In the non-premixed swirling flames like the currently investigated burner [Cavaliere et al., 2013] or other swirl burners [Al-Abdeli and Masri, 2003; Feikema et al., 1990], it is well acknowledged that the existence of the recirculation zones can extend the blow-off limits and the blow-off process takes the finitely long time to complete. Therefore, in perspective of turbulent combustion modelling, accurately predicting the blow-off process means that one needs to correctly capture the key dynamic features in chemistry, flow/mixing fields and their interactions. Specifically, blow-off process is always accompanied by gradually increased level of local extinction along the flame front but this increase is never simply monotonic since the frequent re-ignition can occur globally and locally, particularly in the recirculation zones. This has been observed in the measurement based on OH* chemiluminescence and OH-PLIF [Cavaliere et al., 2013]. As such, the combustion model is expected to have both capacities in simulating the local extinction and re-ignition.

In turbulent non-premixed flames, local extinction is physically caused by the large scalar dissipation [Sutton and Driscoll, 2007] or other fluid structures such as

vortices steepening the local scalar gradient [Masri et al., 2006]. Also, the strong convection would make the immediate downstream of the inlets never ignited. The CMC model in this investigation can predict both situations through the micro-mixing and flow transport related terms in mixture fraction space, which has been discussed previously for globally stable flames with strong turbulence-chemistry interaction, e.g. Sandia flame F [Garmory and Mastorakos, 2011] and also the S1−S7 cases in the current study. Re-ignition occurs after local extinction in stable flames and blow-off transients and it is attributed to the reduced local scalar dissipation after extinction, ignition by the neighboring pockets or auto-ignition. For the turbulent non-premixed flames in this investigation, the CMC model predicts the re-ignition through the interaction between the neighboring CMC cells caused by the convection and sub-grid scalar flux transport in mixture fraction space [Garmory and Mastorakos, 2011; Zhang et al., 2015].

In addition, due to the reversal flow in recirculation zone and its transport effects included in CMC model, another feature of great importance is that the flame cannot be restored to a fully burning state once it reaches blow-off. Based on the present results shown in this Chapter, after the flame blow-off, there are still finite OH mass fraction in mixture fraction space remaining in the downstream of the IRZ and even sometimes the resolved OH mass fraction appears again in the upstream of IRZ close to the bluff body surface. Nevertheless, along the flame front no extensive re-ignition occurs after blow-off.

In terms of the numerical implementations, although the blow-off experiments are mimicked as best as possible in the present LES/3D-CMC simulations, however there are still some approximations and simplifications introduced. First, the approach to obtain blow-off in the LES is to instantly increase the air or fuel velocities in the beginning, instead of gradual adjustment toward the required values. Based on the results shown in Fig. 8.17, within the first 0.015−0.02 s, the evolutions of total heat release rate basically are not influenced by the change of the inlet velocities, indicating that the flame reactivity does not start to show observable variations caused by the change of inlet velocities. Second, the annulus and swirler are not included into the computational domain and the air inlet velocity profiles are obtained through scaling the results from a RANS with the annulus and swirler. The white noise with 5% intensity is superimposed to the

mean profiles and no real turbulence with temporal and spatial correlations is injected. This approximation is used based on the supposition that the turbulence in the combustion chamber is mainly generated by the strong swirling. Third, in discretizing the conditional convection term in the CMC equations, the first order upwind scheme is adopted. This is relatively easy to implement and meanwhile avoids calculating the gradients of conditional reactive scalars, Q_α and Q_h, in mixture fraction space. However, due to the essential diffusivity of first order upwind scheme, this is expected to affect the convection between the neighboring CMC cells and therefore re-ignition or localized extinction. Fourth, the CMC cell size and distribution directly determine the resolution with which the extinction and re-ignition during the blow-off event can be predicted. The CMC cells are refined in the flame active regions ($0 < x < 0.06$ m) but it is not acceptable to make them as fine as the LES cells because of the computational cost. As such, the data transfer from the LES to CMC meshes would bring in some averaging effects, which is specifically important for modelling the conditional scalar dissipation.

Based on the above mentioned modelling and implementation approximations, the critical blow-off air velocity from the LES/3D-CMC, $U_{BO,LES}$, is at most 25% higher than $U_{BO,exp}$ from the measurements for a range of operating conditions. The potential sources responsible for this discrepancy may include the modelling the sub-grid scalar dissipation rate, predicting the numerical fluxes from transport in physical space and the approach to adjust the inlet velocity toward blow-off. These will be topics for the further investigations.

8.4 Conclusions

The LES/3D-CMC model with detailed chemistry is employed to predict the blow-off condition and the blow-off dynamics of swirl-stabilized non-premixed methane flames. The blow-off range from the simulations is obtained and the critical air bulk velocity from the present simulations is larger than the experimental value by around 25%, which shows the good predictive capability of the LES/3D-CMC. The effects of variable fuel and air bulk velocities are examined. The results show that during the blow-off process the total heat release rate

gradually decreases with discernible fluctuations. The predicted blow-off transient lasts finitely long time quantified by the blow-off time, in good agreement with the experimental results. The extinguished fraction is introduced to measure the degree of local extinction occurrence on the iso-surfaces of the filtered stoichiometric mixture fraction. The results also demonstrate that the extinguished fraction gradually increases and reaches unity when the flame approaches the blow-off point. The local extinction characteristics for different sections of the flames are studied to indicate the blow-off mode. The reactive scalars in both physical and mixture fraction space demonstrate the different transient behaviors during blow-off process. When the current swirling flame is close to blow-off, high-frequency and high-amplitude fluctuations of the conditionally filtered stoichiometric scalar dissipation rate on the iso-surfaces of the filtered stoichiometric mixture fraction are evident. The blow-off time from the computations is found to vary with the different operating conditions, but generally the ones for the lower blow-off boundary are larger than those for the upper boundary.

8.5 Tables for Chapter 8

Table 8.1: Selected information of simulated cases

Cases	U_a (m/s)	U_f (m/s)	$U_a/U_{BO,exp}$ (%)	ϕ_g *	$\rho_a U_a^2/\rho_f U_f^2$ †	Blow-off/stable in computations
S1	19.1	29.2	95	0.305	0.82	Stable
S2	19.9	29.2	100	0.293	0.88	Stable
S3	25.0	29.2	126	0.233	1.40	Stable
S4	15.7	18.7	100	0.238	1.28	Stable
S5	19.1	24.0	100	0.251	1.15	Stable
S6	22.6	34.3	100	0.294	0.79	Stable
S7	26.0	39.5	100	0.294	1.15	Stable
BO1	26.5	29.2	133	0.220	1.57	Blow-off
BO2	30.0	29.2	151	0.194	2.01	Blow-off
BO3	34.5	29.2	173	0.169	2.66	Blow-off

* The global equivalence ratio is estimated from $\phi_g = \tau_r \dot{m}_{fuel}/\dot{m}_{air}$ [Cavaliere, 2013], in which $\dot{m}_{fuel}$ and $\dot{m}_{air}$ are the bulk mass flow rates, respectively. τ_r is the stoichiometric fuel-air ratio and for methane/air chemistry $\tau_r = 0.058$.

† The densities for air and pure methane, $\rho_a = 1.18$ kg/m^3 and $\rho_f = 0.65$ kg/m^3, are estimated based on the conditions at air and fuel inlets, respectively.

8.6 Figures for Chapter 8

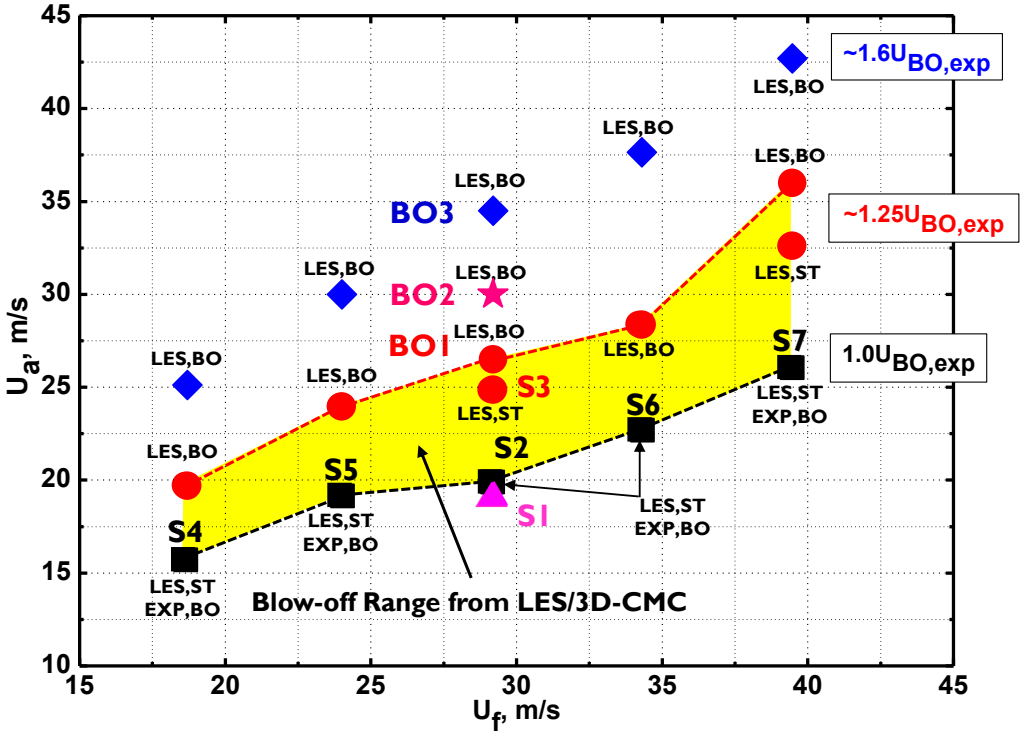

Figure 8.1: Air axial bulk velocity at blow-off as a function of the fuel jet bulk velocity from experiments [Cavaliere et al., 2013] and LES/3D-CMC. *LES, BO*: blow-off in LES, *LES, ST*: stable flames in LES, *EXP, BO*: blow-off in experiments.

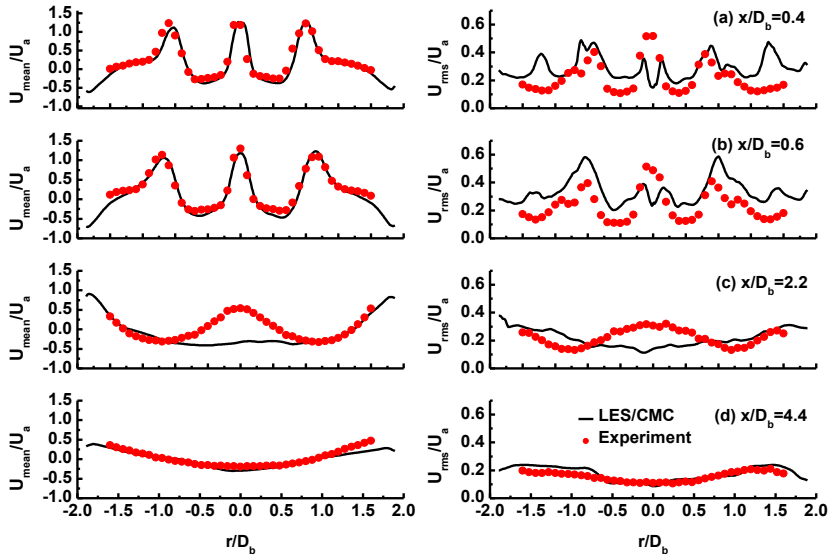

Figure 8.2: Radial profiles of mean and *r.m.s.* axial velocity for four axial positions.

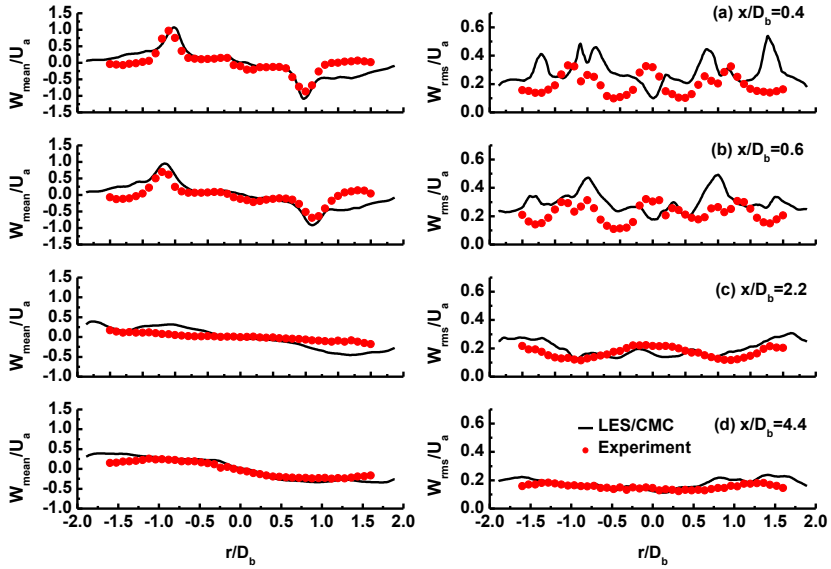

Figure 8.3: Radial profiles of mean and *r.m.s.* swirl velocity for four axial positions.

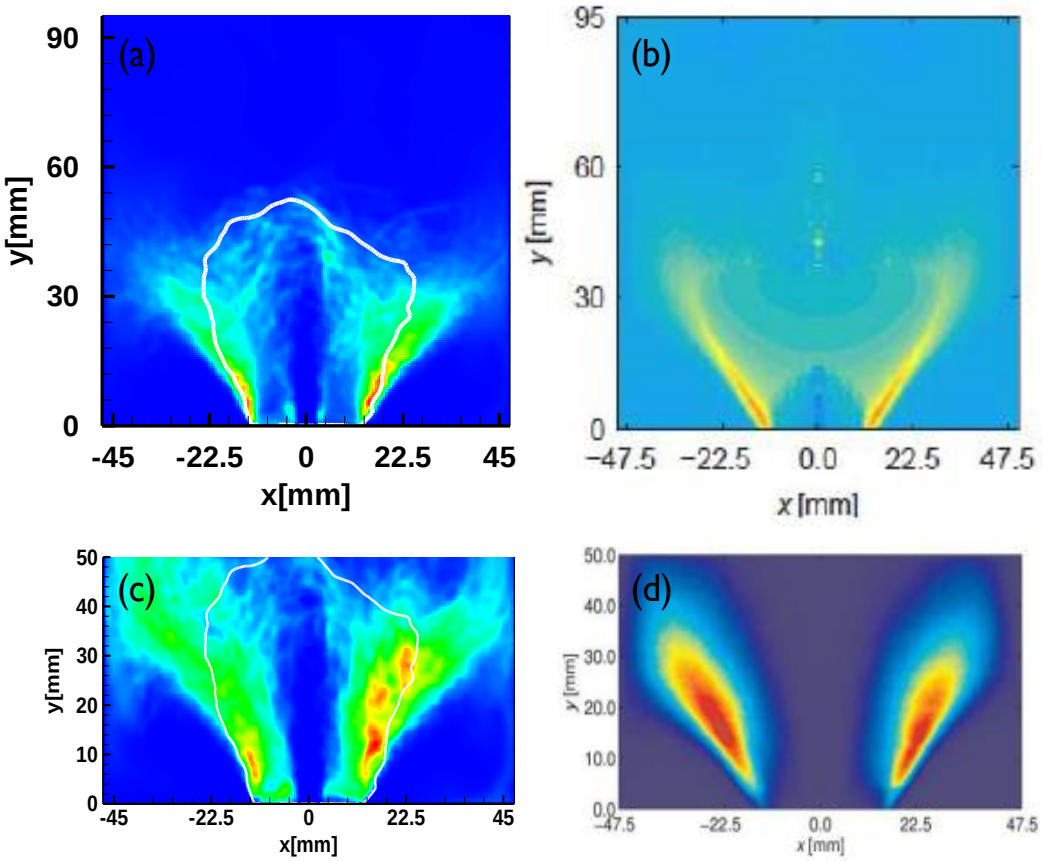

Figure 8.4: Comparisons of the LES results (left column) with experimental data [Cavaliere et al., 2013] (right column): (a) mean heat release rate from the simulation and (b) mean OH* chemiluminescence after inverse Abel transform from the experiment; (c) mean simulated OH mass fraction and (d) mean OH-PLIF from the experiment. White lines: iso-lines of mean stoichiometric mixture fraction $\xi_{st} = 0.055$. Blue: low magnitude and red: red magnitude.

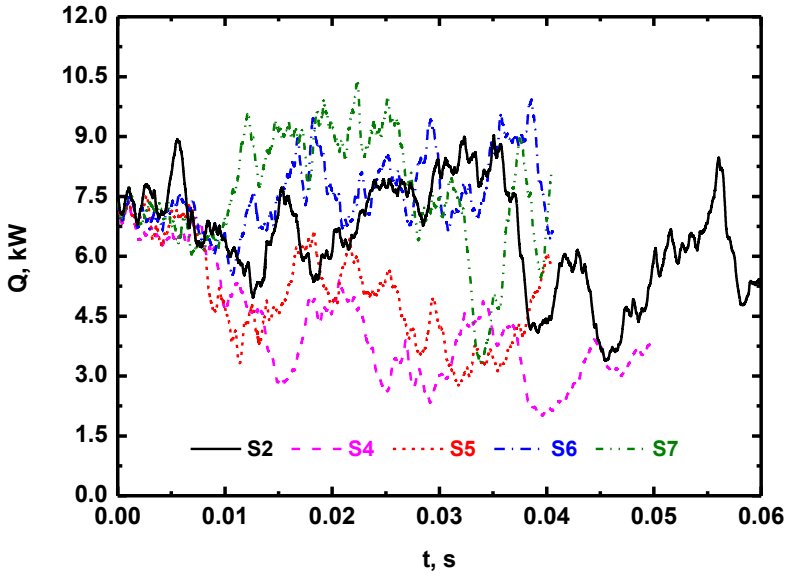

Figure 8.5: Time records of total heat release rate Q from the five cases on the curve of $1.0U_{BO,exp}$ shown in Fig. 8.1.

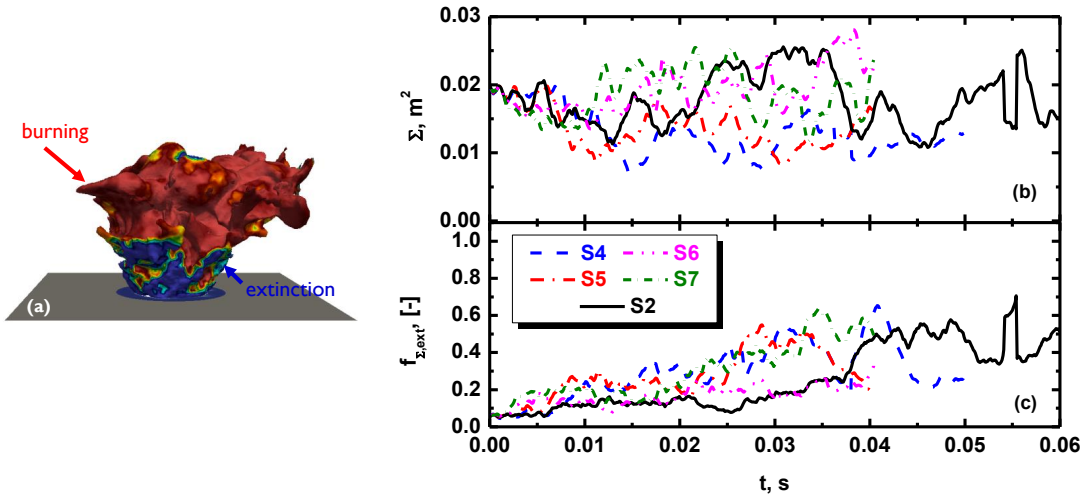

Figure 8.6: (a) Three dimensional iso-surfaces of stoichiometric mixture fraction ξ_{st} coloured by conditionally filtered OH mass fraction at stoichiometry $\widetilde{Y_{OH}|\xi_{st}}$ from S2 case. Blue: extinction with low $\widetilde{Y_{OH}|\xi_{st}}$ and red: burning with high $\widetilde{Y_{OH}|\xi_{st}}$. Time records of (b) ξ_{st} iso-surface area Σ and (c) extinguished fraction $f_{\Sigma,ext}$ from the five cases on the curve of $1.0U_{BO,exp}$ shown in Fig. 8.1.

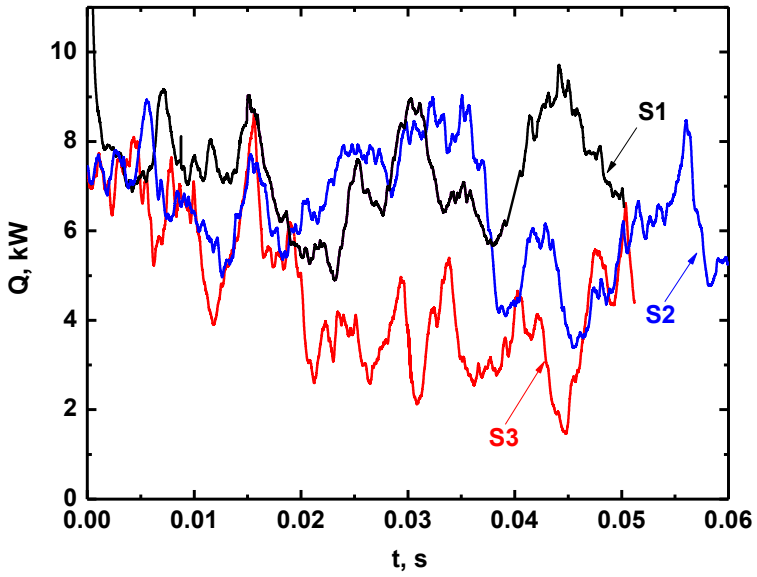

Figure 8.7: Time records of total heat release rate Q from S1, S2 and S3 cases.

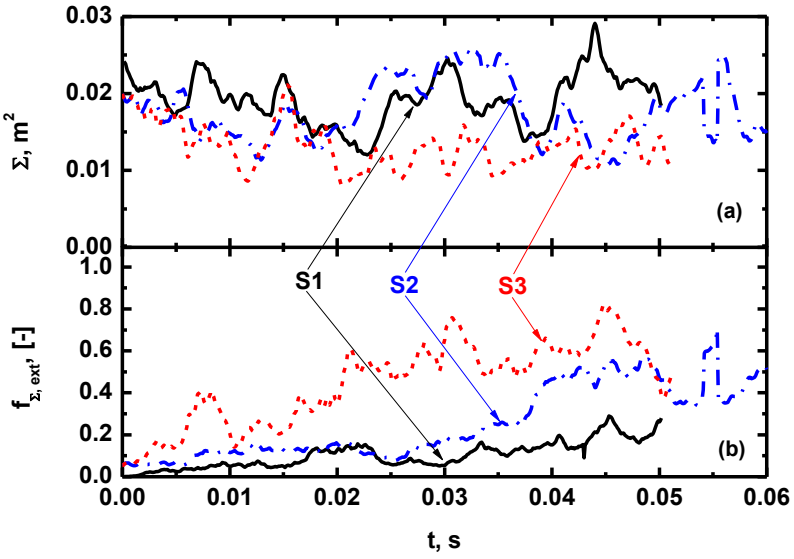

Figure 8.8: Time records of (a) filtered stoichiometric mixture fraction iso-surface area Σ and (b) extinguished fraction $f_{\Sigma,ext}$ from S1, S2 and S3 cases.

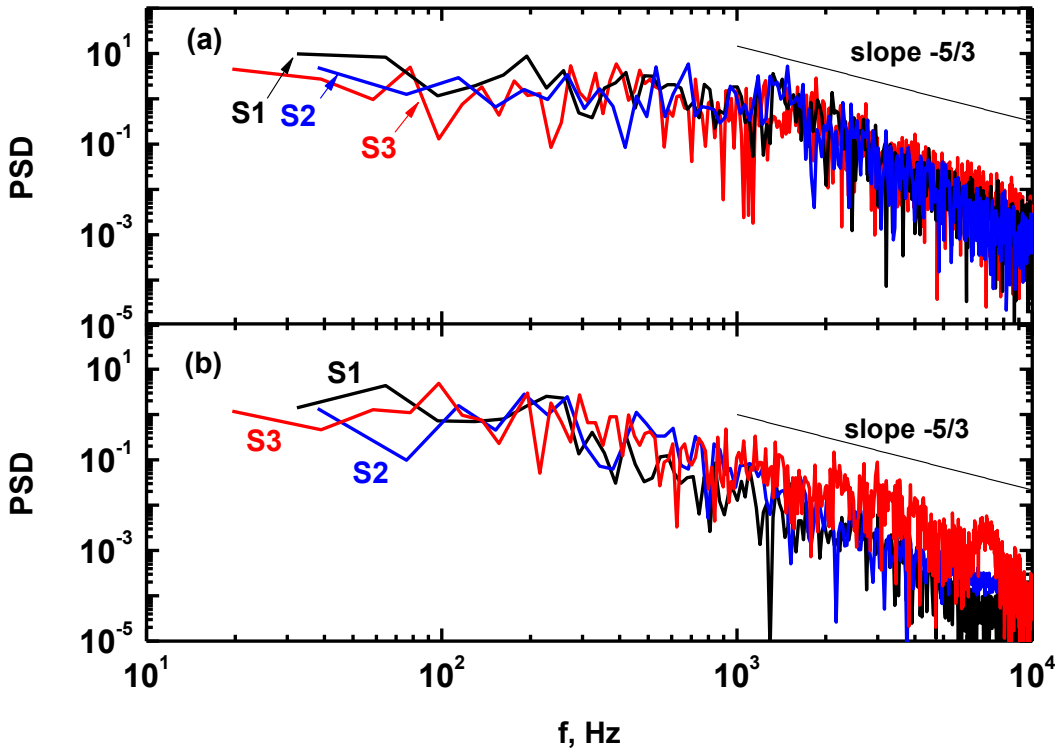

Figure 8.9: Power spectral densities of axial velocity as a function of frequency in two probing locations (a) *LES1* and (b) *LES2* from S1, S2 and S3 cases. The two locations are marked in Fig. 8.25(h) and the coordinates for *LES1* and *LES2* are respectively $x/D_b = 0.6$, $y/D_b = 0.72$, $z/D_b = 0$ and $x/D_b = 2.2$, $y/D_b = 1.28$, $z/D_b = 0$.

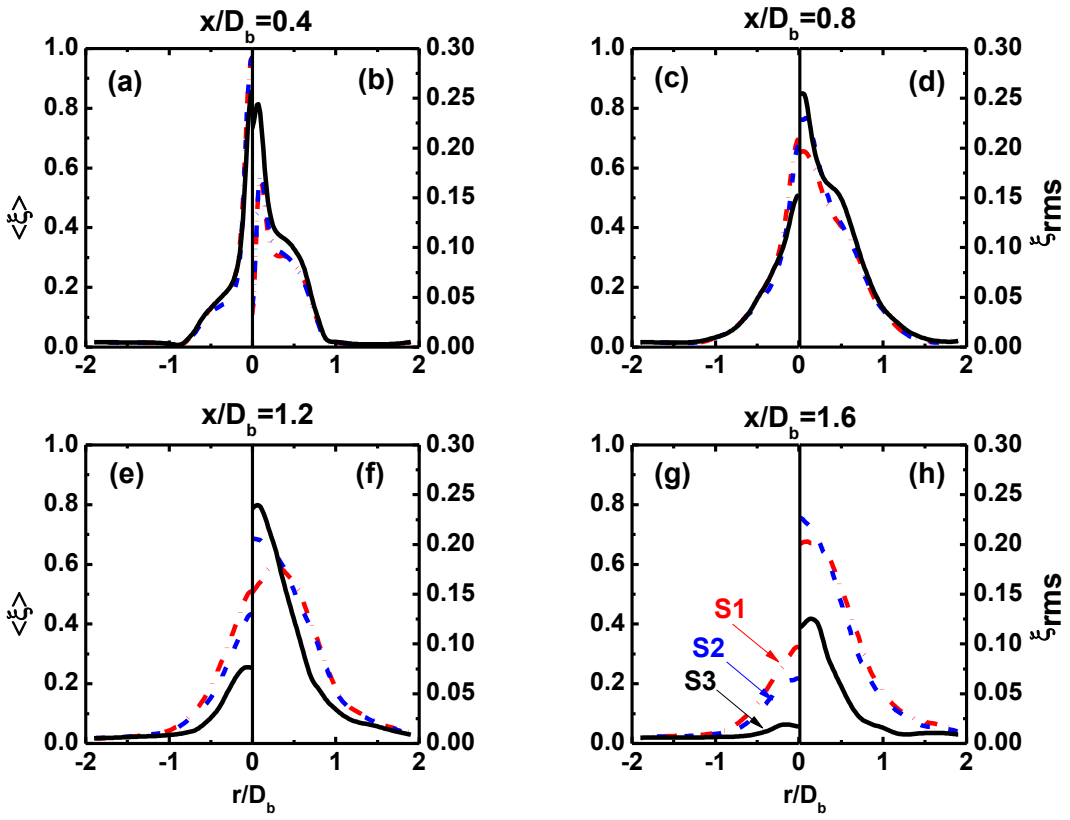

Figure 8.10: Radial profiles of the time and azimuthally averaged mixture fraction and *r.m.s.* at four streamwise positions from S1 (dash-dotted lines), S2 (dashed lines), and S3 (solid lines) cases. The left sub-figures, i.e. (a), (c), (e) and (g), are for the time averaged mixture fraction while the right ones the *r.m.s.*

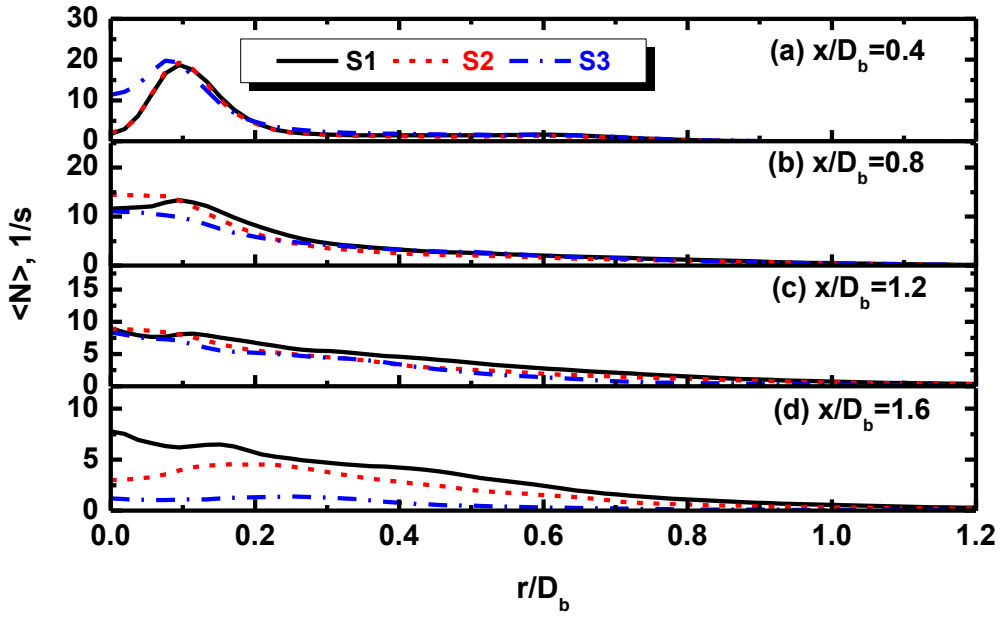

Figure 8.11: Radial profiles of the time and azimuthally averaged scalar dissipation rates at four streamwise positions from S1, S2, and S3 cases.

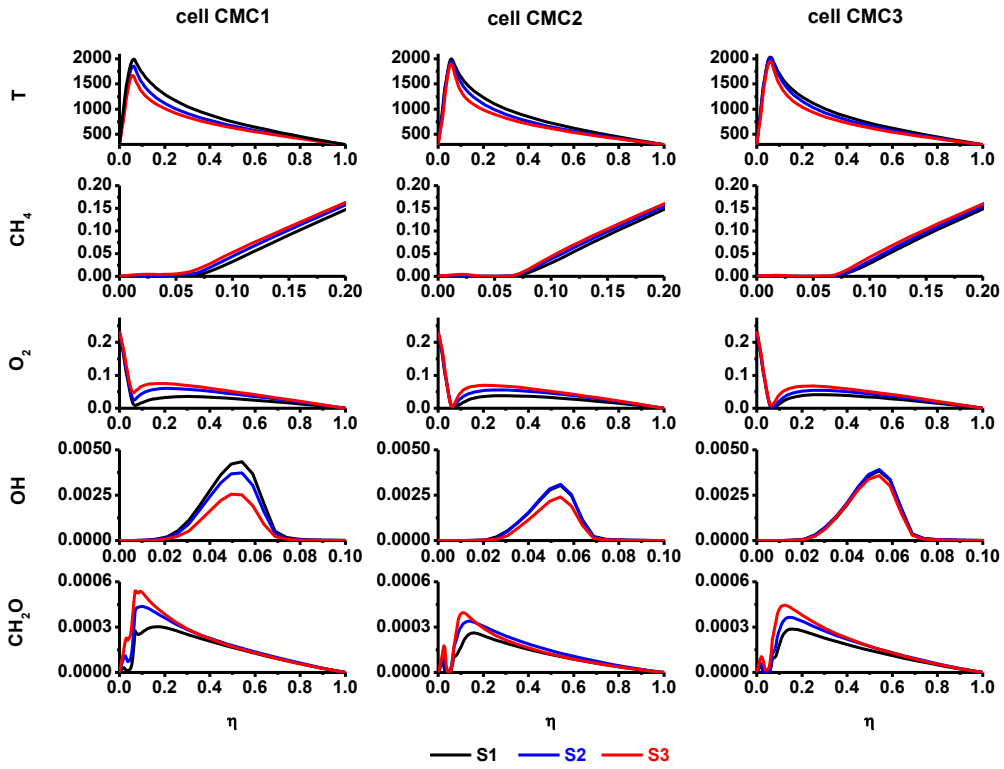

Figure 8.12: Time averaged conditional temperature and mass fractions, $\widetilde{\langle T|\eta\rangle}$ and $\widetilde{\langle Y_\alpha|\eta\rangle}$, from CMC probing cells *CMC1* (left column), *CMC2* (middle column) and *CMC3* (right column) in S1, S2 and S3 cases. The locations of three cells are marked in Fig. 8.25(h).

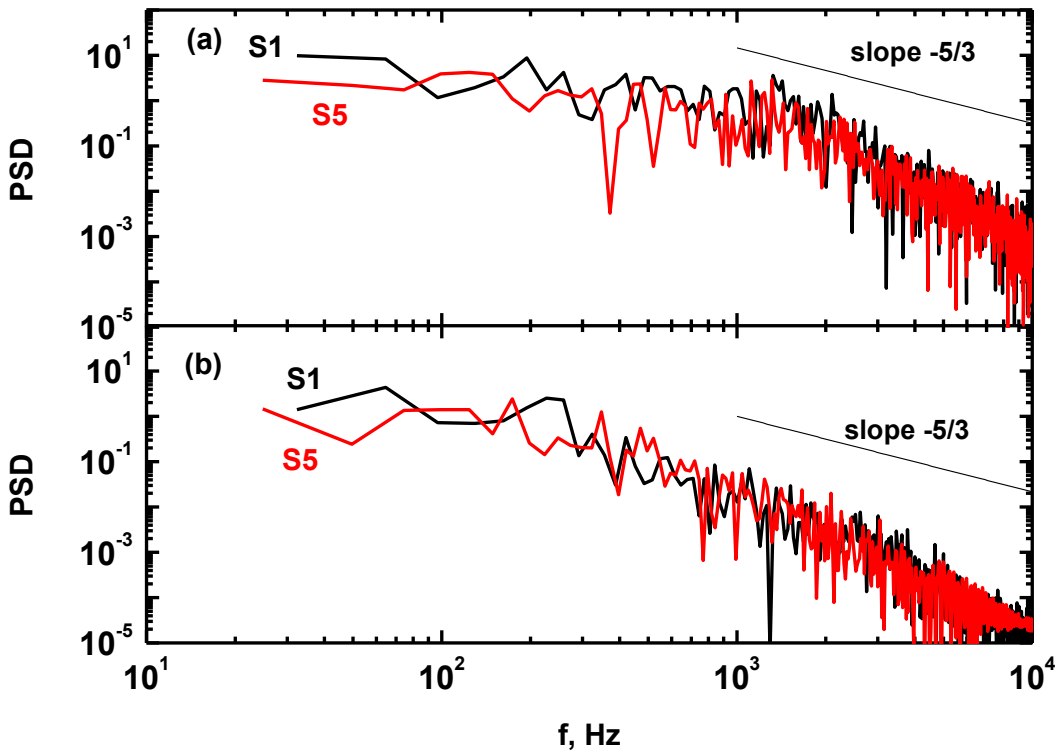

Figure 8.13: Power spectral densities of axial velocity as a function of frequency in two probing cells (a) *LES1* and (b) *LES2* from S1 and S5 cases. The two locations are marked in Fig. 8.25(h).

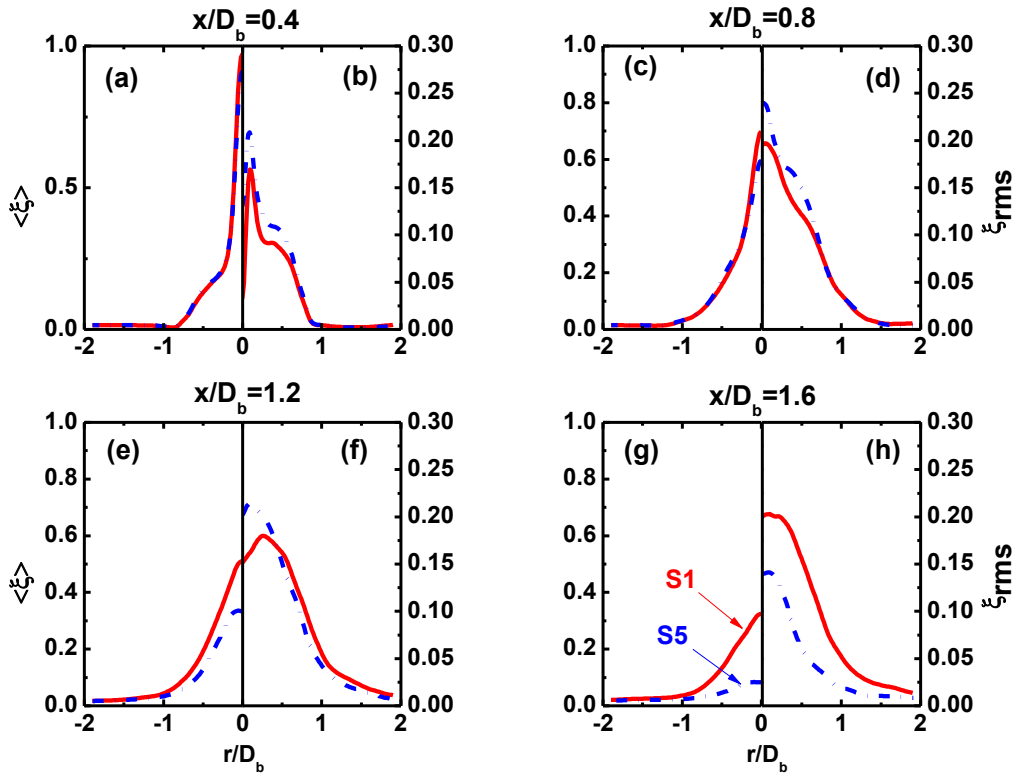

Figure 8.14: Radial profiles of the time and azimuthally averaged mixture fraction and *r.m.s.* at four streamwise positions from S1 (solid lines) and S5 (dash-dotted lines) cases. The left sub-figures, i.e. (a), (c), (e) and (g), are for the time averaged mixture fraction while the right ones the *r.m.s.*

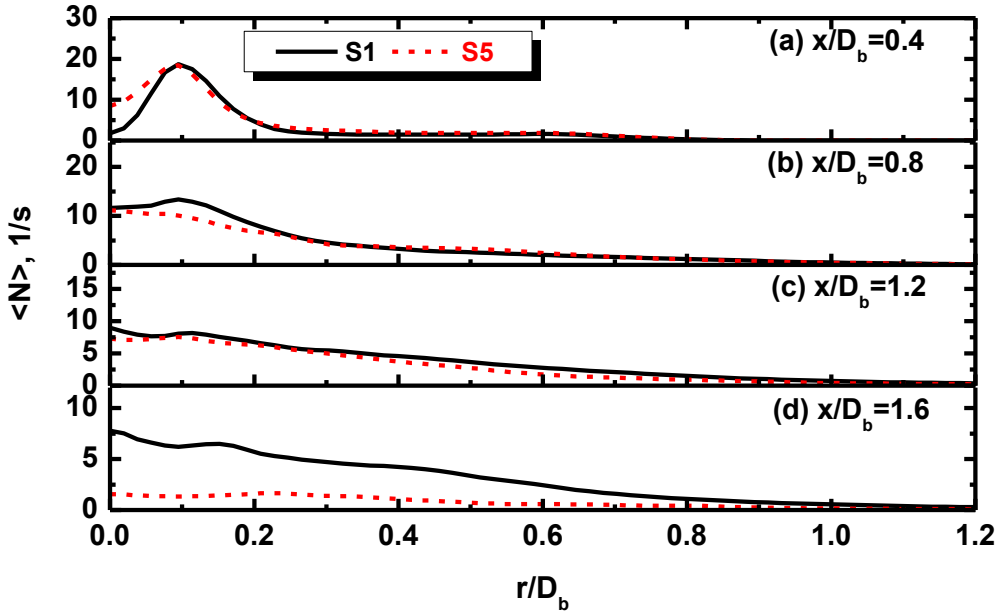

Figure 8.15: Radial profiles of the time and azimuthally averaged scalar dissipation rates at four streamwise positions from S1 and S5 cases.

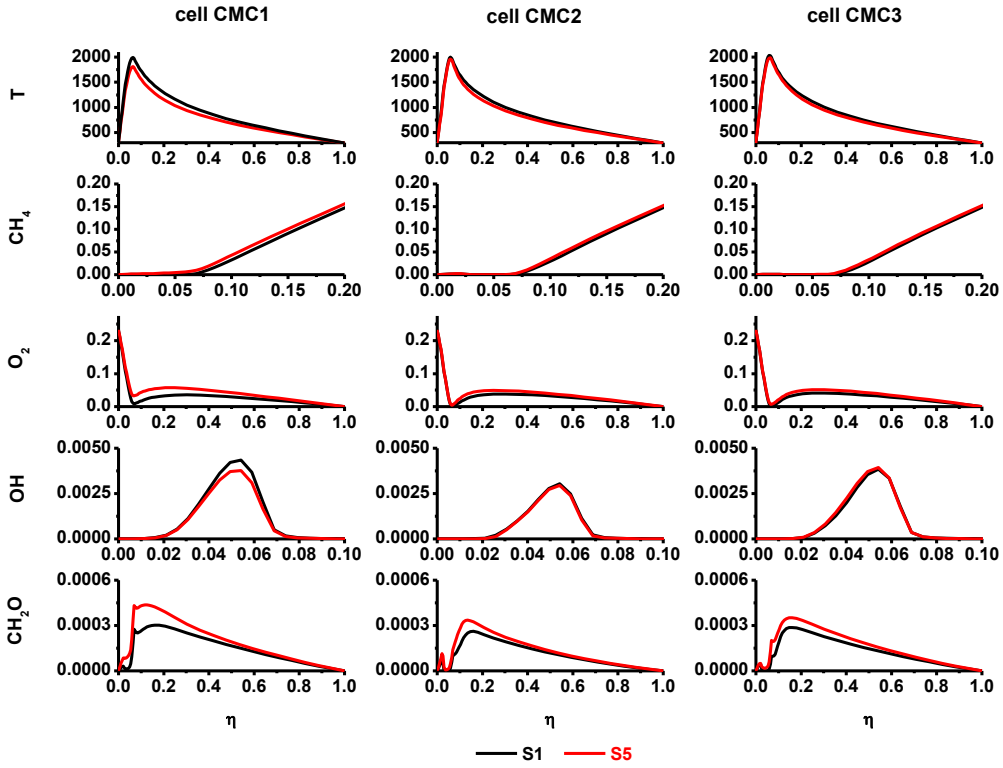

Figure 8.16: Time averaged conditional temperature and mass fractions, $\widetilde{\langle T|\eta\rangle}$ and $\widetilde{\langle Y_\alpha|\eta\rangle}$, from CMC probing cells *CMC1* (left column), *CMC2* (middle column) and *CMC3* (right column) in S1 and S5 cases.

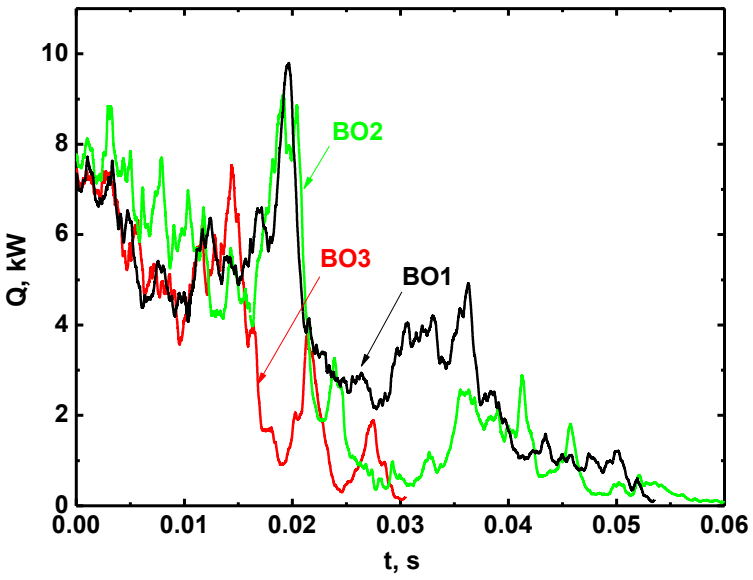

Figure 8.17: Time records of total heat release rate Q from BO1, BO2 and BO3 blow-off cases.

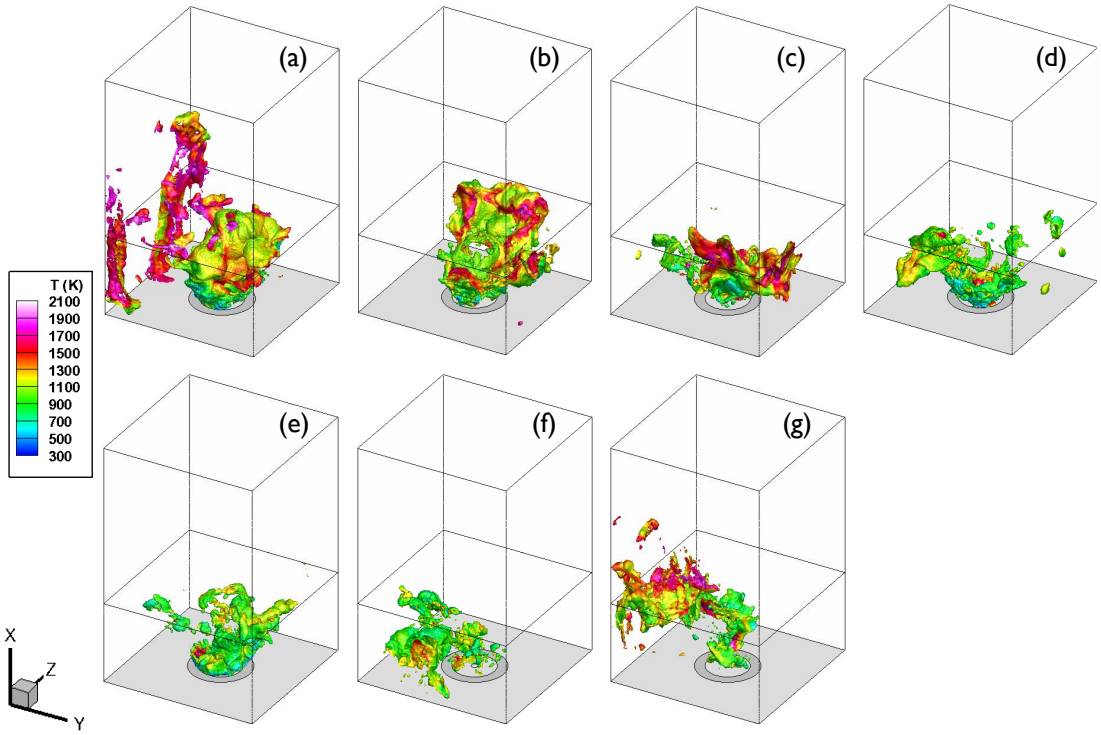

Figure 8.18: Time evolution of iso-surfaces of filtered heat release rate ($\tilde{\dot{q}} = 60$ MJ/m^{3}s) coloured by filtered temperature $\tilde{T}$ in S3: (a) $t = 0$ s, (b) $t = 0.009$ s, (c) $t = 0.018$ s, (d) $t = 0.027$ s, (e) $t = 0.036$ s, (f) $t = 0.045$ s and (g) $t = 0.05$ s. The box edges denote the chamber size.

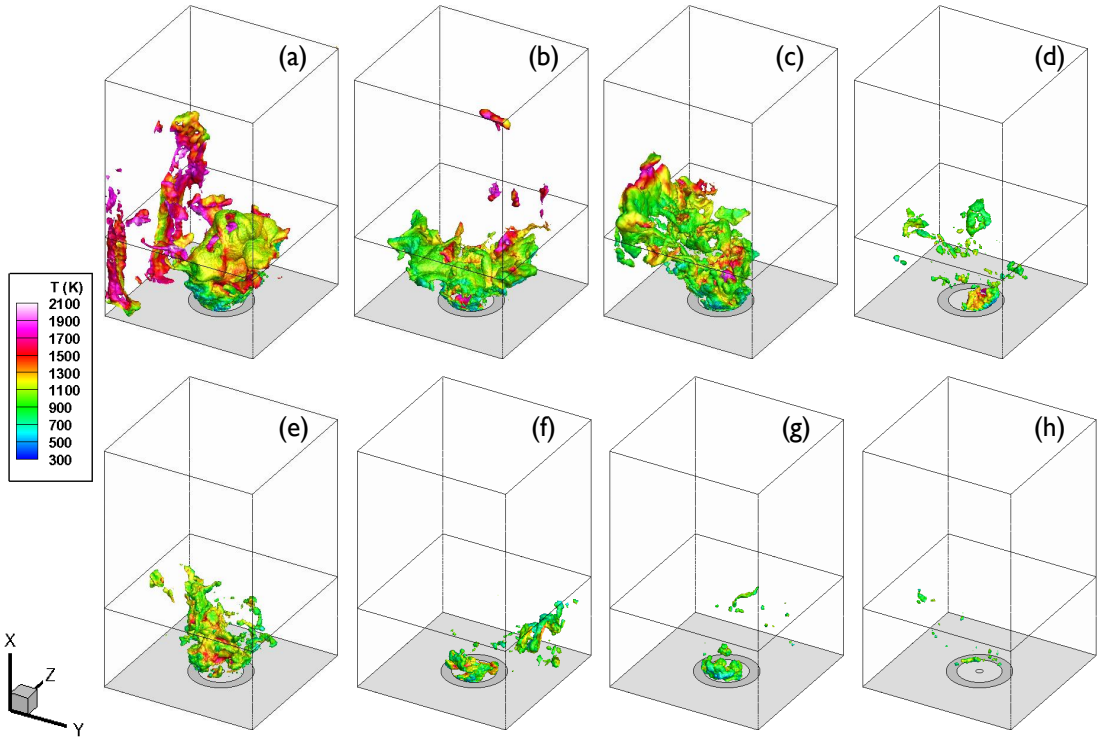

Figure 8.19: Time evolution of iso-surfaces of filtered heat release rate ($\tilde{\dot{q}} = 60$ MJ/m^{3}s) coloured by filtered temperature $\tilde{T}$ in BO2: (a) $t = 0$ s, (b) $t = 0.009$ s, (c) $t = 0.018$ s, (d) $t = 0.027$ s, (e) $t = 0.036$ s, (f) $t = 0.045$ s, (g) $t = 0.054$ s and (h) $t = 0.061$ s. The box edges denote the chamber size.

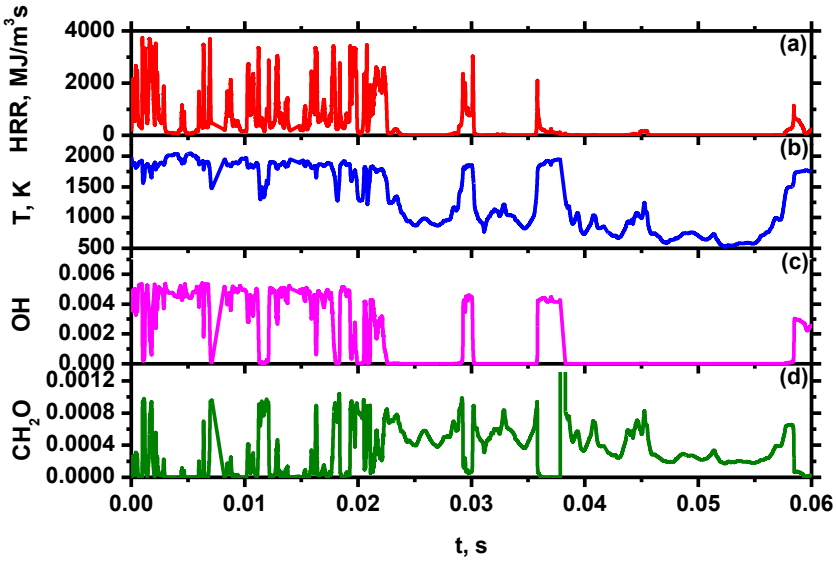

Figure 8.20: Time series of conditional (a) heat release rate, (b) temperature, mass fractions of (c) OH and (d) CH_2O at stoichiometry from probing cell *CMC1* in BO2 case.

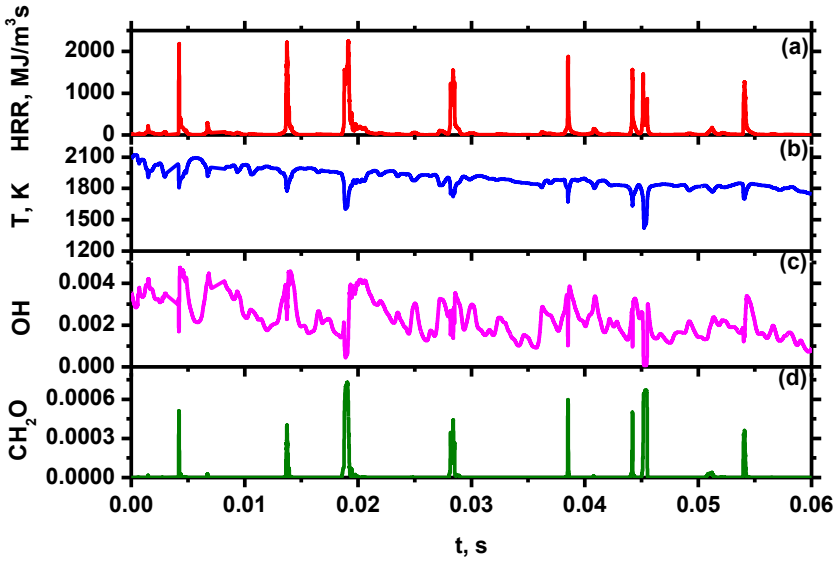

Figure 8.21: Time series of conditional (a) heat release rate, (b) temperature, mass fractions of (c) OH and (d) CH_2O at stoichiometry from probing cell *CMC2* in BO2 case.

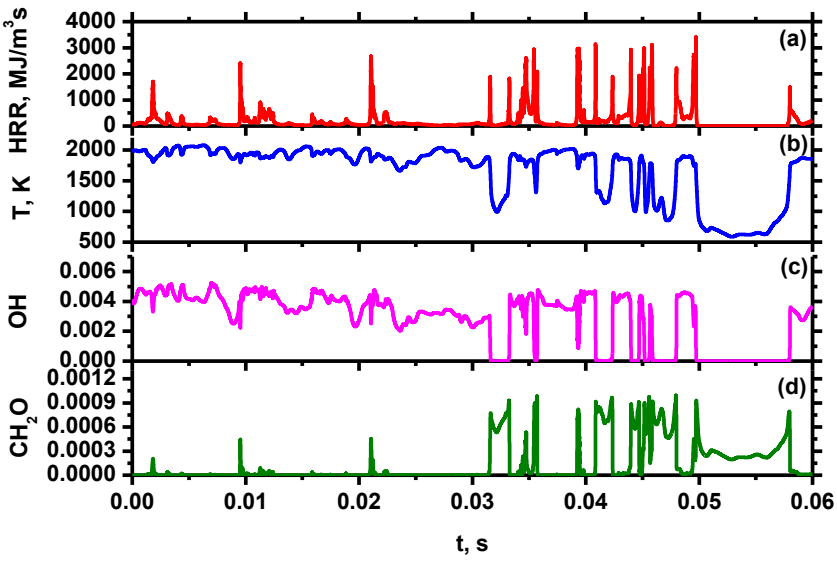

Figure 8.22: Time series of conditional (a) heat release rate, (b) temperature, mass fractions of (c) OH and (d) CH_2O at stoichiometry from probing cell *CMC3* in BO2 case.

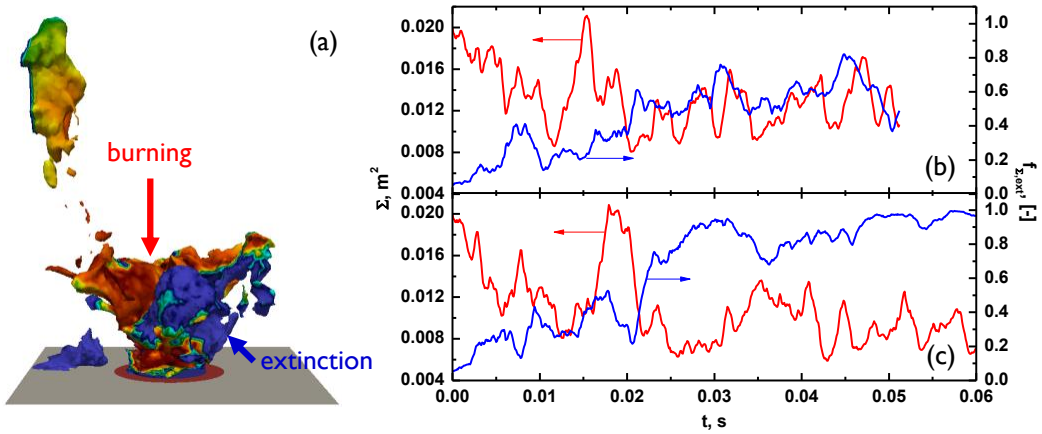

Figure 8.23: (a) Three dimensional iso-surfaces of stoichiometric mixture fraction ξ_{st} coloured by conditionally filtered OH mass fraction at stoichiometry $\widetilde{Y_{OH}|\xi_{st}}$ from BO2 case. Blue: extinction with low $\widetilde{Y_{OH}|\xi_{st}}$ and red: burning with high $\widetilde{Y_{OH}|\xi_{st}}$. Time records of filtered stoichiometric mixture fraction iso-surface area Σ (red lines) and extinguished fraction $f_{\Sigma,ext}$ (blue lines) from (a) S3 and (b) BO2 cases.

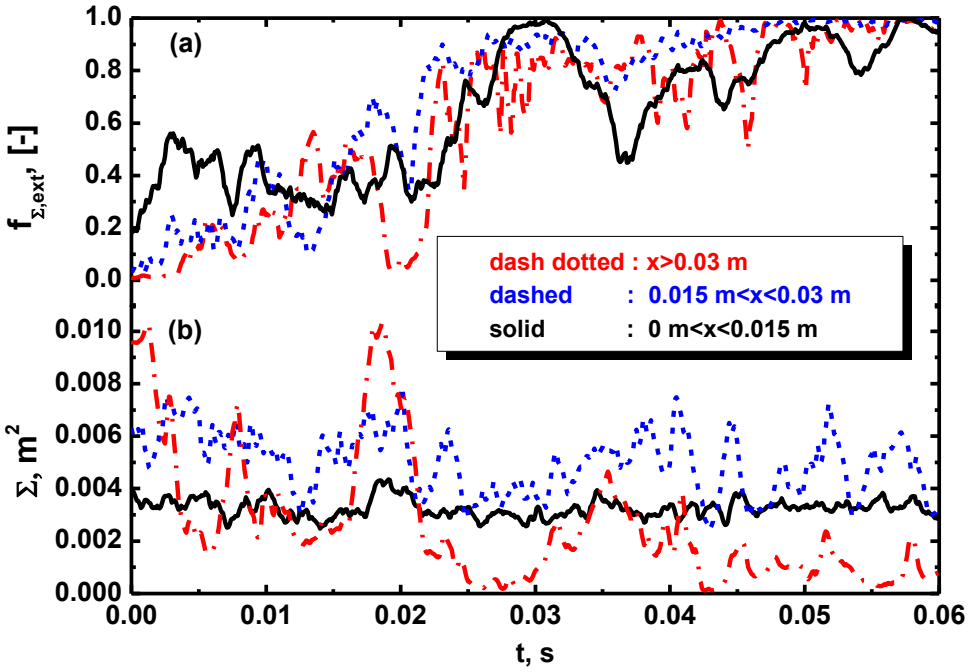

Figure 8.24: Time records of (a) extinguished fraction $f_{\Sigma,ext}$ and (b) ξ_{st} iso-surface area Σ from BO2 case for root ($0 < x \leq 0.015$ m), middle ($0.015\text{m} < x \leq 0.03$ m) and top ($x > 0.03$ m) sections of stoichiometric mixture fraction iso-surfaces.

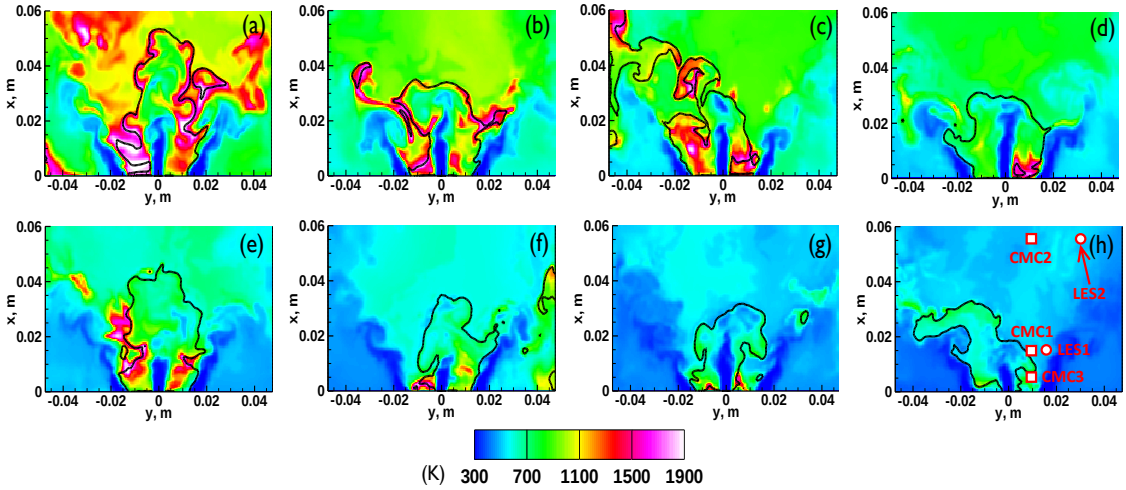

Figure 8.25: Time sequence of distributions of filtered temperature $\tilde{T}$ in $x-y$ plane from BO2: (a) $t = 0$ s, (b) $t = 0.009$ s, (c) $t = 0.018$ s, (d) $t = 0.027$ s, (e) $t = 0.036$ s, (f) $t = 0.045$ s, (g) $t = 0.054$ s and (h) $t = 0.061$ s. Lines: instantaneous stoichiometric mixture fraction $\xi_{st} = 0.055$. The circles in (h) denotes the CMC probing cells (i.e. *CMC1*, *CMC2* and *CMC3*) while the squares the LES probing cells (i.e. *LES1* and *LES2*).

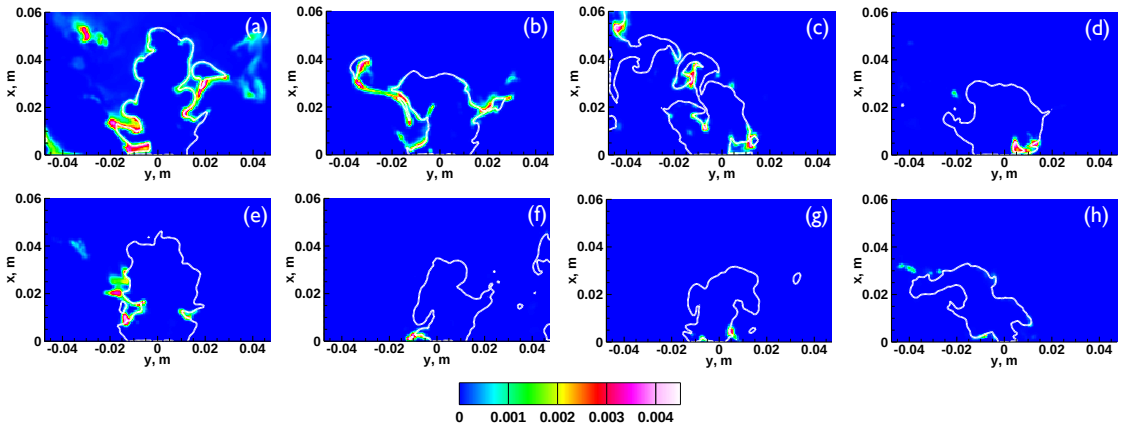

Figure 8.26: Time sequence of distributions of filtered OH mass fraction $\widetilde{Y}_{OH}$ in $x-y$ plane from BO2. The temporal information for (a)−(h) is the same as that in Fig. 8.25. Lines: instantaneous stoichiometric mixture fraction $\xi_{st} = 0.055$.

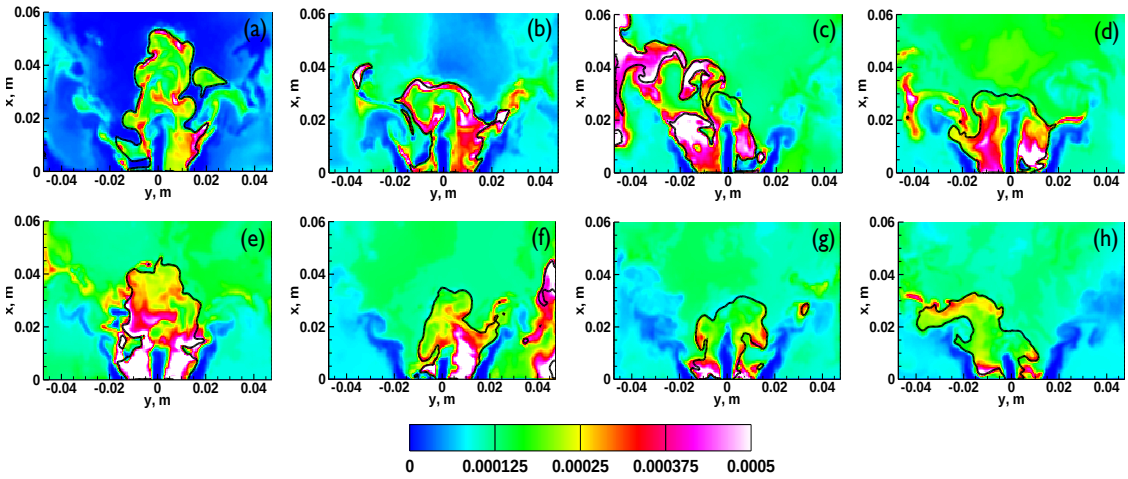

Figure 8.27: Time sequence of distributions of filtered CH_2O mass fraction $\widetilde{Y}_{CH2O}$ in $x-y$ plane from BO2. The temporal information for (a)−(h) is the same as that in Fig. 8.25. Lines: instantaneous stoichiometric mixture fraction $\xi_{st} = 0.055$.

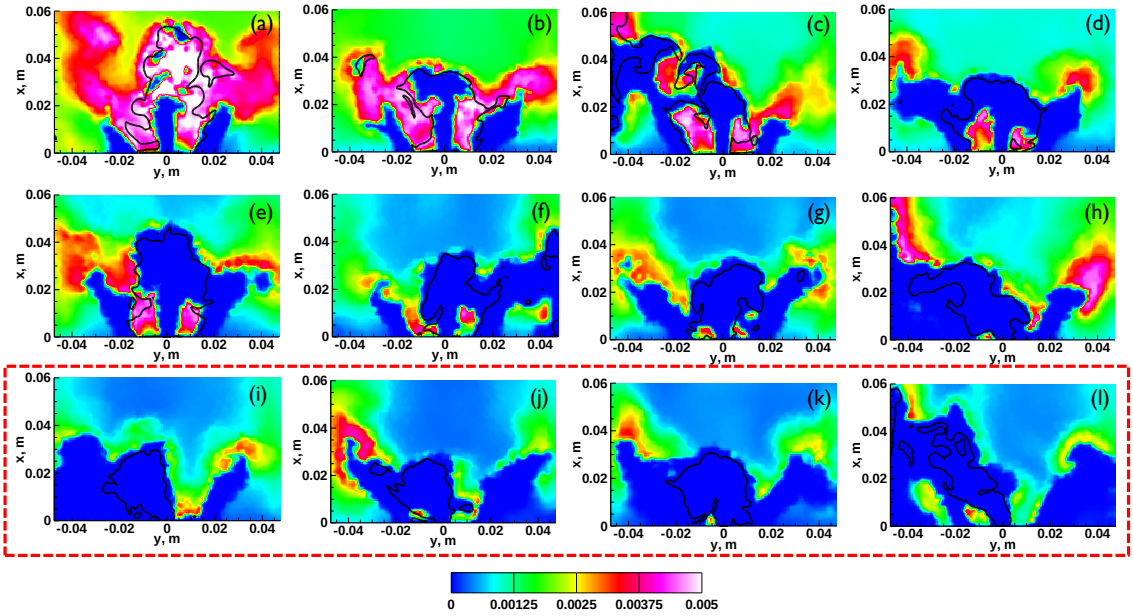

Figure 8.28: Time sequence of distributions of conditionally filtered OH mass fraction at stoichiometry $\widetilde{Y_{OH}|\xi_{st}}$ in $x-y$ plane from BO2. Temporal information for (a)−(h) is same as that for (a)−(h) of Fig. 8.25. The time for (i)−(l) highlighted by the dashed box is $t = 0.063$ s, 0.072 s, 0.081 s and 0.09 s respectively, denoting the evolution of conditionally filtered OH mass fraction in mixture fraction space after the global extinction has been reached in physical space. Lines: instantaneous stoichiometric mixture fraction $\xi_{st} = 0.055$.

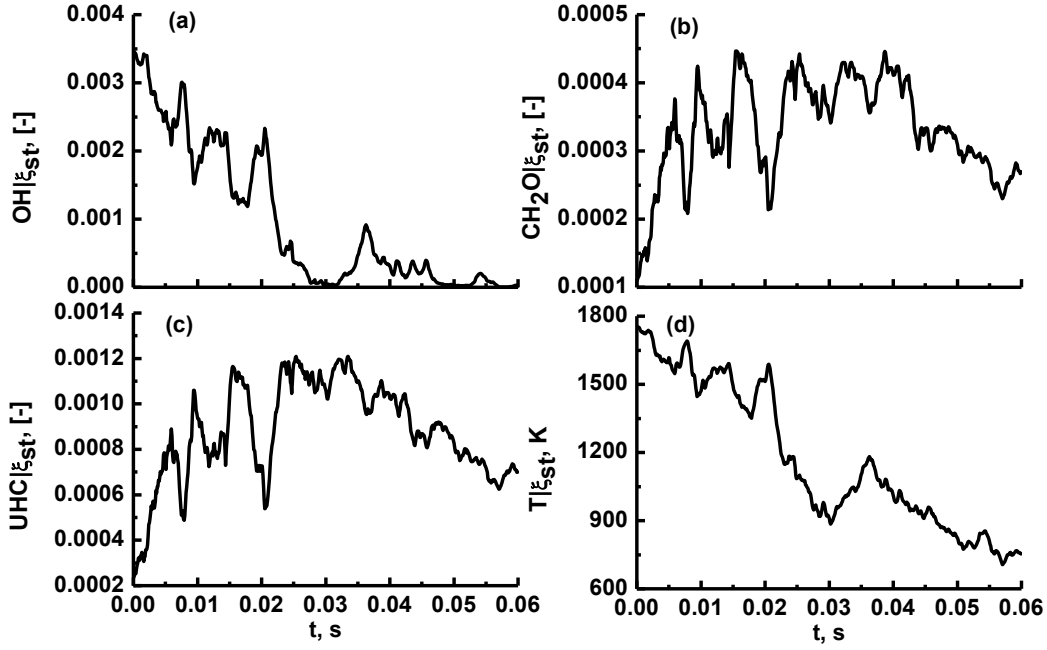

Figure 8.29: Time evolutions of the surface-averaged conditional stoichiometric mass fractions of (a) OH, (b) CH_2O, (c) unburned C_2 hydrocarbons and temperature from BO2. The averaging is performed for each time instant based on the samples on the filtered ξ_{st} iso-surfaces.

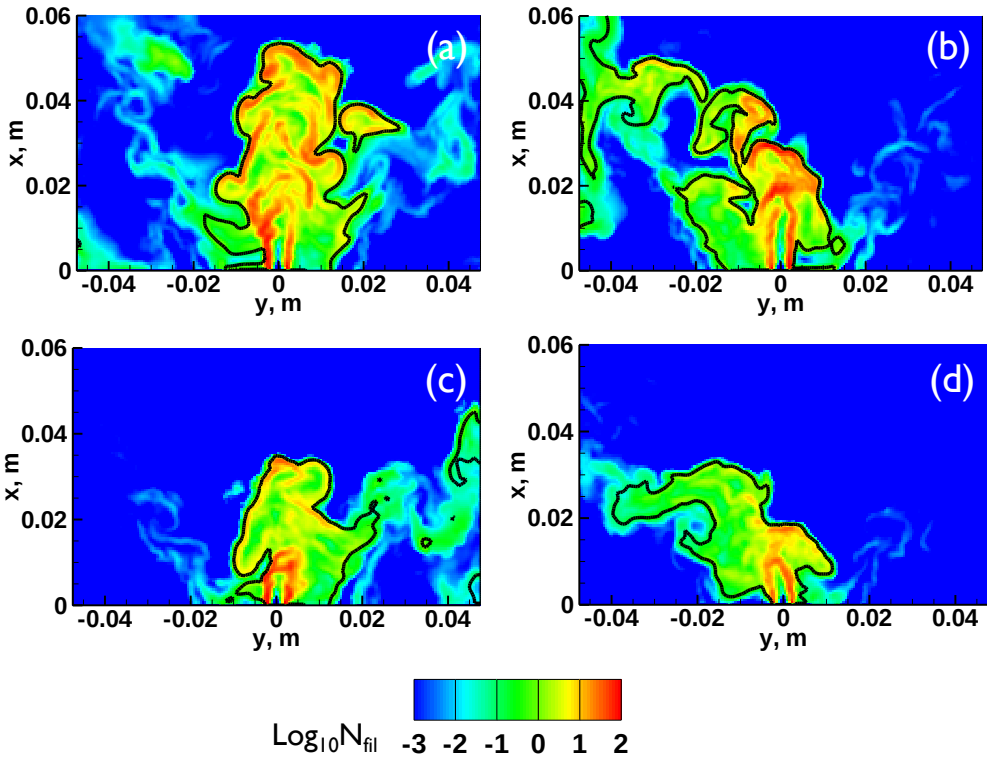

Figure 8.30: Distributions of filtered scalar dissipation at (a) $t = 0$ s, (b) $t = 0.018$ s, (c) $t = 0.045$ s, and (d) $t = 0.061$ s from BO2. Lines: instantaneous stoichiometric mixture fraction $\xi_{st} = 0.055$.

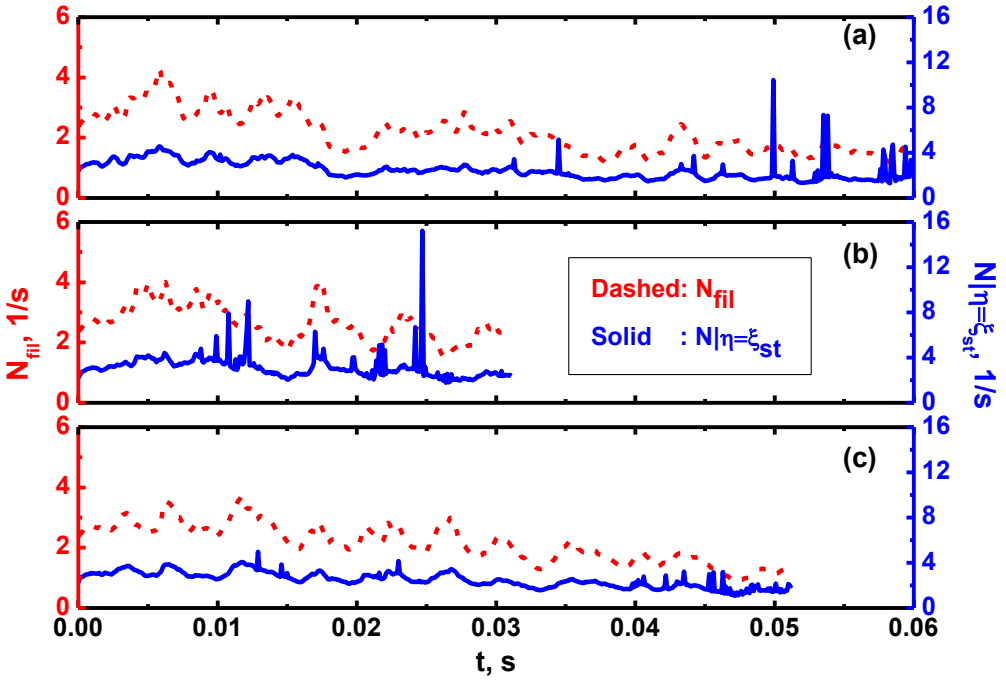

Figure 8.31: Time series of the surface-averaged unconditionally filtered (dashed lines) and conditionally filtered stoichiometric (solid lines) scalar dissipation from cases of (a) BO2, (b) BO3 and (c) S3. The averaging is performed for each time instant based on the samples on the filtered ξ_{st} iso-surfaces.

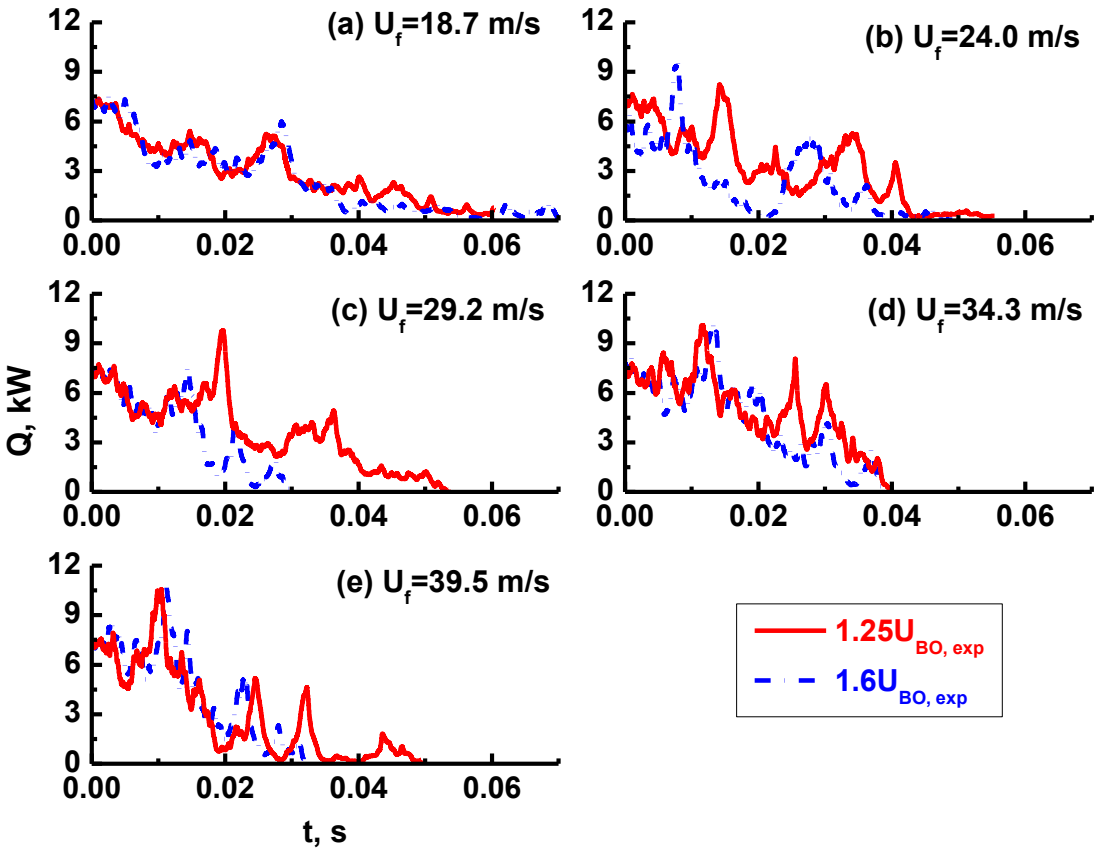

Figure 8.32: Time records of total heat release rate Q from the blow-off cases on the curves of $1.25U_{BO,exp}$ and $1.6U_{BO,exp}$ shown in Fig. 8.1.

Chapter 9

Conclusions and Recommendations for Future Work

Studies on local extinction and blow-off dynamics in turbulent swirling non-premixed flames have been performed with LES and the sub-grid scale multi-dimensional CMC combustion model. The finite volume discretizations for the conservative CMC governing equations are implemented, extending its applicability to combustion problems with complex computational domains. The selected target flames for extinction investigations are from the Sydney and Cambridge swirl burners, with Raman−Rayleigh−LIF and OH-PLIF/OH* chemiluminescence measurements, respectively [Cavaliere et al., 2013; Masri et al., 2004]. The LES/3D-CMC solvers are validated against the Sydney swirl flames (SMA2). The degree of localized extinction in both Sydney and Cambridge swirl flames are predicted reasonably. The blow-off conditions and dynamics are also studied with LES/3D-CMC model and the blow-off critical conditions for Cambridge swirl burner are over-predicted with the error smaller than 25%. The major conclusions from the studies presented in Chapters 4−8 are summarised in the following sections. This chapter closes with some recommendations for further work.

9.1 Conclusions

9.1.1 Implementation and code development

The conservative governing equations for the sub-grid three dimensional CMC model are derived in Chapter 3, which can be discretized on the unstructured meshes with the finite volume method. Based on them, the in-house unstructured 3D-CMC solver is developed. In this implementation, CMC cells are regenerated from the LES cells and can be arbitrarily polyhedral. The numerical flux conservation in physical space is beneficial in predicting the large variations of conditional mass fractions that may exist in such near-limit flame dynamics as extinction. The data transfer interface between the CMC and LES solvers is designed and the MPI based parallelization is employed in the 3D-CMC solver with the round-robin algorithm, ensuring the ideal load balancing among all the processors. The solvers used in the computations of this thesis are also introduced in Chapter 3. The scalability of the solvers is assessed on the ARCHER (Cray XC30) clusters of the UK National Supercomputing Service and, particularly, the LES/3D-CMC solver can have a linear speedup until processor number is close to $O(10^3)$. Through the computational cost analysis, one can see that the MPI communications become the limiting factor for the LES/3D-CMC solver to have a linear speedup with higher processor numbers.

9.1.2 Swirl non-reacting flows

The swirl non-reacting flows from the Sydney and Cambridge swirl burners are simulated with LES solver (isothermal flows) in Chapter 4. The burner configurations and flow information are introduced first. The major features concerning the flow structures, e.g. recirculation zones, are analyzed based on the computational results and the velocity statistics are compared with the measurements. The results show that the non-reacting LES solver and implementations can accurately predict the swirling non-reacting flows in both burners. The influences of mesh refinement, computational domain and turbulent inlet boundary condition on the flow fields are studied. The work in Chapter 4 is a preliminary

preparation for the following chapters on LES/3D-CMC simulations of turbulent non-premixed flames.

9.1.3 Local extinction in Sydney swirl flames

In Chapter 5, three Sydney swirling flames (i.e. SMA2, SMA3 and SMA4) with fixed swirl number but gradually increased central fuel bulk velocity are investigated with LES/3D-CMC. Detailed comparisons are made with SMA2 measurements about the statistics of velocity components and mixture fraction. The temperature and mass fractions of key species in both physical and mixture fraction space are compared as well with the Raman−Rayleigh−LIF data. The above comparisons for SMA2 demonstrate the excellent agreement, which validates the implementations of LES/3D-CMC solvers described in Chapter 3. The flow, mixing and scalar fields are not well predicted for the upstream part of the recirculation zone in the SMA3 case. This may be resulted from the under-prediction of turbulence in the upstream of recirculation zone. The possible causes include the inaccuracy of the turbulent boundary conditions at the fuel exit and not sufficiently fine mesh for SMA3. In addition, the trend of the extinction level from the computations qualitatively agrees with the experimental measurements, i.e. increased local extinction level from SMA2 to SMA4. The current LES/3D-CMC solver and numerical implementations do not achieve the complete extinction in SMA4, which has the experimentally critical blow-off conditions. In the measurements, initial extinction first appears at the flame base and expands from there (i.e. base blow-off), which is reasonably captured in the computations.

9.1.4 Local extinction in Cambridge swirl flames

The local extinction characteristics in a swirl-stabilised non-premixed flame from the Cambridge swirl burner are studied in Chapter 6. The LES/3D-CMC simulation reproduces reasonably the flow field and the global flame characteristics (e.g. mean OH-PLIF, OH* chemiluminescence, PDF of lift-off height). The occurrence of localized extinction is typically manifested by low heat release rate and OH mass fraction, as well as low or medium temperature. Also, it is accom-

panied by high scalar dissipation rates. The considerable temporal and spatial variations of scalar dissipation can be observed in this flame, leading to (temporally) frequent and (spatially) distributed local extinction. In mixture fraction space, the conditional reactive scalars in the CMC cells undergoing local extinction have relatively wide scatter between inert and fully burning solutions while for fully burning CMC cells the instantaneous CMC solutions follow closely fully-burning distributions. A reactedness index is introduced to quantify how far the conditional profiles deviate from the reference fully burning state. The PDFs of reactedness at the stoichiometric mixture fraction demonstrate some extent of bi-modality, showing the events of local extinction and re-ignition and their relative occurrence frequency.

9.1.5 Near-wall local extinction

The wall heat loss effects on the local extinction occurring near the bluff body surface in the Cambridge swirl burner are examined in Chapter 7. The convective wall heat loss is accounted for as a source term in the CMC governing equation for conditionally filtered total enthalpy. The averaged wall heat flux is high on the middle bluff body surface but low near its edges. The sub-grid scale heat flux predicted from the resolved temperature gradient is lower than the laminar counterpart but increases with the turbulent intensity. For the CMC cells adjacent to the bluff body, the heat loss facilitates the occurrence of extinction and re-ignition. It has a significant influence on the mean flame structures, directly associated with the variations of the conditional scalar dissipation rates near the wall. Furthermore, the level of local and instantaneous extinction measured by conditional reactedness at stoichiometry is intensified due to the inclusion of wall heat loss. Nevertheless, the wall heat loss demonstrates a comparatively small influence on the lift-off near the bluff body surface.

9.1.6 Blow-off of Cambridge swirl flames

In Chapter 8, the LES/3D-CMC model is applied for simulating the blow-off conditions and dynamics of swirl-stabilized non-premixed methane flames in the

Cambridge swirl burner. The blow-off range is obtained from the simulations, which covers the same fuel bulk velocities in the measurements. The critical air bulk velocity from the LES/3D-CMC is at most 25% greater than the experimental value, showing the good capability of the LES/3D-CMC in blow-off computations. The effects of variable fuel and air bulk velocities on the change of flow and mixing fields are analyzed. Also, during the blow-off process, the volume integrated heat release rate gradually decreases with discernible fluctuations. The predicted blow-off transient lasts finitely long time and the blow-off duration from the computations is in good agreement with the experimental observations. The extinguished fraction is introduced to measure the degree of local extinction occurrence on the iso-surfaces of the filtered stoichiometric mixture fraction. It is demonstrated that the extinguished fraction gradually increases and reaches unity when the flame is close to complete extinction, i.e. blow-off. The local extinction characteristics for different sections of the flames are studied to indicate the blow-off mode. The reactive scalars in both physical and mixture fraction space present the distinctive transient behaviors during blow-off process. When the flame approaches blow-off, high-frequency and high-amplitude fluctuations of the conditionally filtered stoichiometric scalar dissipation rate on the iso-surfaces of the filtered stoichiometric mixture fraction are evident. The blow-off time from the computations is found to vary with the different operating conditions, but typically the blow-off time corresponding to the cases on the lower blow-off boundary are longer than that for the upper boundary.

9.2 Recommendations for future work

Based on the results of the present thesis, in the following some recommendations for the future work are listed about the understanding and prediction of local extinction and blow-off in turbulent non-premixed flames with the 3D-CMC combustion model.

In this thesis, the first order sub-grid scale CMC model is used, in which the conditional fluctuations are neglected. When the turbulence−chemistry interaction becomes strong (e.g. localized extinction and blow-off), they may be signifi-

cant and would have nonnegligible influence on extinction prediction. Therefore, further studies are needed to examine the effects of higher order closure in the CMC model on modelling the turbulence−chemistry interaction.

The unstructured meshes used for the CMC physical domain in this work provide the flexibility for cell distribution. Meanwhile, the local extinction extent in LES cells is directly determined by the extinction in the host CMC cell. As such, the CMC cell resolution would have a significant effect on local extinction. This effect has not been studied quantitatively yet in this thesis and future efforts need to be spent.

The blow-off curve predicted by the LES/3D-CMC modelling demonstrates the 25% error, although the qualitative correlation between the fuel bulk velocity and the blow-off air velocity is captured. Therefore, it is important to identify the potential causes that result in the above error. In terms of turbulent combustion modelling, further sensitivity analysis can be conducted to assess the effects of numerics, turbulent inlet boundary specifications and the sub-models for CMC. Clearly understanding the error source is indicative for the future model developments for the simulations of turbulent non-premixed combustion.

Blow-off of the Sydney swirl flame case SMA4 in Chapter 5 is not correctly reproduced, although higher level of local extinction appears than that in SMA2 and SMA3. As such, further work is needed to see if computationally it is possible to obtain the blow-off point in this burner and what is the accuracy.

The LES/3D-CMC solvers currently applied for gaseous flames provide a good code framework for the future improvement and development for novel flame regimes. For instance, the flame dynamics in multi-phase combustion can be studied, although more sophisticated models for the interaction between dispersed phase (e.g. droplets and particles) and gas phase are required. Additionally, the unstructured CMC solver has the ability in simulating the combustion in practical burners. Therefore, in the future, studies on the combustion in model or realistic gas turbine combustors with LES/3D-CMC and affordable chemistry are worthy of efforts.

Appendix A Other Conservative CMC Equations

The derivation for other conservative CMC equations is shown as follows and the difference between Eq. (3.35) and the one in this Appendix has been analyzed in Section 3.2.

The transport equation for density weighted FDF, $\tilde{P}(\eta)$, [Klimenko and Bilger, 1999] is

$$\frac{\partial}{\partial t}\left[\overline{\rho_\eta}\tilde{P}(\eta)\right]+\nabla\cdot\left[\overline{\rho_\eta}\widetilde{\mathbf{U}|\eta}\tilde{P}(\eta)\right]=-\frac{\partial^2}{\partial\eta^2}\left[\overline{\rho_\eta}\widetilde{N|\eta}\tilde{P}(\eta)\right]. \tag{A.1}$$

Multiplying Eq. (A.1) by Q_α yields

$$Q_\alpha\frac{\partial}{\partial t}\left[\overline{\rho_\eta}\tilde{P}(\eta)\right]+Q_\alpha\nabla\cdot\left[\overline{\rho_\eta}\widetilde{\mathbf{U}|\eta}\tilde{P}(\eta)\right]=-Q_\alpha\frac{\partial^2}{\partial\eta^2}\left[\overline{\rho_\eta}\widetilde{N|\eta}\tilde{P}(\eta)\right]. \tag{A.2}$$

The two terms in *LHS* of Eq. (A.2) can be expanded respectively as

$$Q_\alpha\frac{\partial}{\partial t}\left[\overline{\rho_\eta}\tilde{P}(\eta)\right]=\frac{\partial}{\partial t}\left[\overline{\rho_\eta}\tilde{P}(\eta)Q_\alpha\right]-\overline{\rho_\eta}\tilde{P}(\eta)\frac{\partial Q_\alpha}{\partial t}, \tag{A.3}$$

$$\nabla\cdot\left[\overline{\rho_\eta}\widetilde{\mathbf{U}|\eta}\tilde{P}(\eta)\right]=\nabla\cdot\left[\overline{\rho_\eta}\widetilde{\mathbf{U}|\eta}\tilde{P}(\eta)Q_\alpha\right]-\overline{\rho_\eta}\widetilde{\mathbf{U}|\eta}\tilde{P}(\eta)\cdot\nabla Q_\alpha. \tag{A.4}$$

Then substituting Eqs. (A.3) and (A.4) into Eq. (A.2) yields

$$\begin{aligned} \frac{\partial}{\partial t}\left[\overline{\rho_\eta}\tilde{P}\left(\eta\right)Q_\alpha\right]-\overline{\rho_\eta}\tilde{P}\left(\eta\right)\frac{\partial Q_\alpha}{\partial t}+ \\ \nabla\cdot\left[\overline{\rho_\eta}\widetilde{\mathbf{U}|\eta}\tilde{P}\left(\eta\right)Q_\alpha\right]-\overline{\rho_\eta}\widetilde{\mathbf{U}|\eta}\tilde{P}\left(\eta\right)\cdot\nabla Q_\alpha= \\ -Q_\alpha\frac{\partial^2}{\partial\eta^2}\left[\overline{\rho_\eta}\widetilde{N|\eta}\tilde{P}\left(\eta\right)\right] \end{aligned} \tag{A.5}$$

Multiply Eq. (3.24) by $\overline{\rho_\eta}\tilde{P}\left(\eta\right)$ yields

$$\begin{aligned} \overline{\rho_\eta}\tilde{P}\left(\eta\right)\frac{\partial Q_\alpha}{\partial t}+\overline{\rho_\eta}\tilde{P}\left(\eta\right)\widetilde{\mathbf{U}|\eta}\cdot\nabla Q_\alpha= \\ \overline{\rho_\eta}\tilde{P}\left(\eta\right)\widetilde{N|\eta}\frac{\partial^2 Q_\alpha}{\partial\eta^2}+\overline{\rho_\eta}\tilde{P}\left(\eta\right)\widetilde{W_\alpha|\eta}+\overline{\rho_\eta}\tilde{P}\left(\eta\right)e_f. \end{aligned} \tag{A.6}$$

Add Eq. (A.5) to Eq. (A.6), and then one can obtain

$$\begin{aligned} \frac{\partial}{\partial t}\left[\overline{\rho_\eta}\tilde{P}\left(\eta\right)Q_\alpha\right]+\nabla\cdot\left[\overline{\rho_\eta}\tilde{P}\left(\eta\right)\widetilde{\mathbf{U}|\eta}Q_\alpha\right]= \\ -Q_\alpha\frac{\partial^2}{\partial\eta^2}\left[\overline{\rho_\eta}\widetilde{N|\eta}\tilde{P}\left(\eta\right)\right]+\overline{\rho_\eta}\tilde{P}\left(\eta\right)\widetilde{N|\eta}\frac{\partial^2 Q_\alpha}{\partial\eta^2}+\overline{\rho_\eta}\tilde{P}\left(\eta\right)\widetilde{W_\alpha|\eta}+\overline{\rho_\eta}\tilde{P}\left(\eta\right)e_f \end{aligned} \tag{A.7}$$

If the gradient model for the turbulent flux e_f, Eq. (3.31), is applied, then Eq. (A.7) becomes

$$\begin{aligned} \underbrace{\frac{\partial}{\partial t}\left[\overline{\rho_\eta}\tilde{P}\left(\eta\right)Q_\alpha\right]}_{T_0}+\underbrace{\nabla\cdot\left[\overline{\rho_\eta}\tilde{P}\left(\eta\right)\widetilde{\mathbf{U}|\eta}Q_\alpha\right]}_{T_1}= \\ \underbrace{-Q_\alpha\frac{\partial^2}{\partial\eta^2}\left[\overline{\rho_\eta}\widetilde{N|\eta}\tilde{P}\left(\eta\right)\right]}_{T_2}+\underbrace{\overline{\rho_\eta}\tilde{P}\left(\eta\right)\widetilde{N|\eta}\frac{\partial^2 Q_\alpha}{\partial\eta^2}}_{T_3}+\underbrace{\overline{\rho_\eta}\tilde{P}\left(\eta\right)\widetilde{W_\alpha|\eta}}_{T_4}+\underbrace{\vec{\nabla}\cdot\left[\overline{\rho_\eta}\tilde{P}\left(\eta\right)D_t\nabla Q_\alpha\right]}_{T_5} \end{aligned} \tag{A.8}$$

The interpretations for Terms T_0 to T_5 are the same as those for Eq. (3.35).

Appendix B List of Publications

Part of the work in this thesis is published or submitted for publication or presented. They include:

Journals

- **Huangwei Zhang**, Epaminondas Mastorakos, Large eddy simulation of local and global extinction in turbulent non-premixed flames (Sydney swirl flames) with conditional moment closure modelling. In preparation.
- **Huangwei Zhang**, Epaminondas Mastorakos, Prediction of the global extinction conditions and dynamics in swirling non-premixed flames using LES/CMC modelling. Submitted to *Flow, Turbulence and Combustion*.
- **Huangwei Zhang**, Andrew Garmory, Davide E. Cavaliere, Epaminondas Mastorakos, Large eddy simulation/conditional moment closure modeling of swirl-stabilized non-premixed flames with local extinction. *Proceedings of the Combustion Institute*, 35 (2015) 1167-1174.

Conferences

- **Huangwei Zhang**, Epaminondas Mastorakos, Prediction of blow-off dynamics of swirl non-premixed flames using LES/CMC modeling. *9th Mediterranean Combustion Symposium*, Rhodes, Greece, 7th-11th June, 2015.
- **Huangwei Zhang**, Andrew Garmory, Epaminondas Mastorakos, Scalable parallel and computationally-conservative implementations of the conditional moment closure model in large eddy simulations. *15th International Conference on Numerical Combustion*, Palais de Papes, Avignon, France, 19th-22nd April, 2015.

- **Huangwei Zhang**, Epaminondas Mastorakos, Effects of wall heat loss on swirl-stabilized non-premixed flames with localized extinction. *10th International ERCOFTAC Symposium on Engineering Turburlent Modelling and Measurements (ETMM10)*, Don Carlos Resort, Marbella, Spain, 17th-19th September, 2014.

- **Huangwei Zhang**, Andrew Garmory, Epaminondas Mastorakos, Predictions of localized extinction and re-ignition in swirl diffusion flames with LES/CMC method. *Joint meeting of the British and Scandinavian-Nordic Sections of the Combustion Institute*, University of Cambridge, 27th-28th March, 2014.

References

A. Adamczyk and G. Lavoie. Laminar head-on flame quenching−a theoretical study. *SAE Technical Paper*, 1978. 186

S. F. Ahmed, R. Balachandran, T. Marchione, and E. Mastorakos. Spark ignition of turbulent nonpremixed bluff-body flames. *Combustion and Flame*, 151:366–385, 2007. 65

Y. M. Al-Abdeli and A. R. Masri. Stability characteristics and flowfields of turbulent non-premixed swirling flames. *Combustion Theory and Modelling*, 7: 731–766, 2003. 3, 19, 63, 64, 70, 73, 74, 116, 118, 120, 121, 122, 128, 133, 231, 237

Y. M. Al-Abdeli and A. R. Masri. Precession and recirculation in turbulent swirling isothermal jets. *Combustion Science and Technology*, 176:645–665, 2004. 62, 63, 64, 75, 78

Y. M. Al-Abdeli, A. R. Masri, G. R. Marquez, and S. H. Starner. Time-varying behaviour of turbulent swirling nonpremixed flames. *Combustion and Flame*, 146:200–214, 2006. xiv, 63, 64, 90

H. M. Altay, K. S. Kedia, R. L. Speth, and A. F. Ghoniem. Two-dimensional simulations of steady perforated-plate stabilized premixed flames. *Combustion Theory and Modelling*, 14:125–154, 2010. 187

S. Ayache and E. Mastorakos. Conditional moment closure/large eddy simulation of the Delft-III natural gas non-premixed jet flame. *Flow, Turbulence and Combustion*, 88:207–231, 2012. 23, 37, 165

S. Ayache and E. Mastorakos. Investigation of the TECFLAM non-premixed flame using Large Eddy Simulation and Proper Orthogonal Decomposition. *Flow, turbulence and combustion*, 90(2):219–241, 2013. 48, 234

R. Balachandran, B. O. Ayoola, C. F. Kaminski, A. P. Dowling, and E. Mastorakos. Experimental investigation of the nonlinear response of turbulent premixed flames to imposed inlet velocity oscillations. *Combustion and Flame*, 143:37–55, 2005. 65

R. S. Barlow and J. H. Frank. Effects of turbulence on species mass fractions in methane/air jet flames. *Symposium (International) on Combustion*, 27:1087–1095, 1998. 14, 122, 221

R. S. Barlow and A. N. Karpetis. Measurements of scalar variance, scalar dissipation, and length scales in turbulent piloted methane/air jet flames. *Flow, Turbulence and Combustion*, 72:427–448, 2004. 125

J. M. Beer and N. A. Chigier. *Combustion Aerodynamics*. Applied Science Publishers Ltd., London, 1971. 65, 160

R. W. Bilger. The structure of diffusion flames. *Combustion Science and Technology*, 13:155–170, 1976. 16

R. W. Bilger. Conditional moment closure for turbulent reacting flow. *Physics of Fluids A: Fluid Dynamics (1989-1993)*, 5:436–444, 1993. 5

S. Böckle, J. Kazenwadel, D.-I. Shin, C. Schulz, and J. Wolfrum. Simultaneous single-shot laser-based imaging of formaldehyde, OH, and temperature in turbulent flames. *Proceedings of the Combustion Institute*, 28:279–286, 2000. 232

M. Bolla, Y. M. Wright, K. Boulouchos, G. Borghesi, and E. Mastorakos. Soot formation modeling of *n*-heptane sprays under diesel engine conditions using the conditional moment closure approach. *Combustion Science and Technology*, 185:766–793, 2013. 28

G. Borghesi, E. Mastorakos, C. B. Devaud, and R. W. Bilger. Modeling evaporation effects in conditional moment closure for spray autoignition. *Combustion Theory and Modelling*, 15:725–752, 2011. 5, 27

G. Boudier, L. Y. M. Gicquel, and T. J. Poinsot. Effects of mesh resolution on large eddy simulation of reacting flows in complex geometry combustors. *Combustion and Flame*, 155:196–214, 2008. 83

I. Boxx, M. Stöhr, C. Carter, and W. Meier. Temporally resolved planar measurements of transient phenomena in a partially premixed swirl flame in a gas turbine model combustor. *Combustion and Flame*, 157:1510–1525, 2010. 234

D. Bradley, P. H. Gaskell, and X. J. Gu. The mathematical modeling of liftoff and blowoff of turbulent non-premixed methane jet flames at high strain rates. *Symposium (International) on Combustion*, 27:1199–1206, 1998. 24

N. Branley and W. P. Jones. Large eddy simulation of a turbulent non-premixed flame. *Combustion and Flame*, 127:1914–1934, 2001. 160, 211

K. N. C. Bray and N. Peters. Laminar flamelets in turbulent flames. In P.A. Libby and F. Williams, editors, *Turbulent Reacting Flows*. Academic, New York, 1994. 187

J. E. Broadwell, W. J. A. Dahm, and M. G. Mungal. Blowout of turbulent diffusion flames. *Symposium (International) on Combustion*, 20:303–310, 1985. 18

P. N. Brown and A. C. Hindmarsh. Reduced storage matrix methods in stiff ODE systems. *Journal of Computational and Applied Mathematics*, 31:40–91, 1989. 46

A. J. M. Buckrell and C. B. Devaud. Investigation of mixing models and conditional moment closure applied to autoignition of hydrogen jets. *Flow, Turbulence and Combustion*, 90:621–644, 2013. 5

W. K. Bushe and H. Steiner. Conditional moment closure for large eddy simulation of nonpremixed turbulent reacting flows. *Physics of Fluids (1994-present)*, 11:1896–1906, 1999. 5, 22

S. Candel, D. Durox, T. Schuller, J.-F. Bourgouin, and J. P. Moeck. Dynamics of swirling flames. *Annual Review of Fluid Mechanics*, 46:147–173, 2014. 3, 66

G. F. Carrier. Nonisenthalpic interaction of a planar premixed laminar flame with a parallel end wall. *SAE Technical Paper*, 1979. 186

D. E. Cavaliere. *Blow-off in gas turbine combustors*. PhD thesis, University of Cambridge, Department of Engineering, 2013. xiv, xvi, xvii, xxii, 3, 62, 65, 67, 71, 72, 81, 92, 93, 109, 114, 159, 161, 163, 191, 199, 223, 232, 241

D. E. Cavaliere, J. Kariuki, and E. Mastorakos. A comparison of the blow-off behaviour of swirl-stabilized premixed, non-premixed and spray flames. *Flow, Turbulence and Combustion*, 91:347–372, 2013. xiii, xxi, xxii, xxiv, 17, 19, 20, 53, 59, 62, 65, 66, 159, 164, 171, 172, 177, 185, 188, 192, 196, 209, 210, 213, 214, 215, 217, 219, 221, 227, 228, 232, 234, 237, 242, 244, 268

C. M. Cha and H. Pitsch. Higher-order conditional moment closure modelling of local extinction and reignition in turbulent combustion. *Combustion Theory and Modelling*, 6:425–437, 2002. 22

C. M Cha, G. Kosály, and H. Pitsch. Modeling extinction and reignition in turbulent nonpremixed combustion using a doubly-conditional moment closure approach. *Physics of Fluids*, 13:3824–3834, 2001. 22

B. H. Chao, C. K. Law, and J. S. T'ien. Structure and extinction of diffusion flames with flame radiation. *Symposium (International) on Combustion*, 23: 523–531, 1991. 13

S. Chaudhuri, S. Kostka, M. W. Renfro, and B. M. Cetegen. Blowoff dynamics of bluff body stabilized turbulent premixed flames. *Combustion and Flame*, 157: 790–802, 2010. 3, 210

H. Chen, S. Chen, and R. H. Kraichnan. Probability distribution of a stochastically advected scalar field. *Physical Review Letters*, 63:2657–2660, 1989. 41

M. K. Chernovsky, A. Atreya, and H. G. Im. Effect of CO2 diluent on fuel versus oxidizer side of spherical diffusion flames in microgravity. *Proceedings of the Combustion Institute*, 31:1005–1013, 2007. 14

M. J. Cleary and J. H. Kent. Modelling of species in hood fires by conditional moment closure. *Combustion and Flame*, 143:357–368, 2005. 5, 26

O. Colin and J.-B. Michel. A simplified CMC approach based on tabulated reaction rates applied to a lifted methane−air jet flame. *Proceedings of the Combustion Institute*, 35:1393–1399, 2015. 25

A. W. Cook and J. J. Riley. A subgrid model for equilibrium chemistry in turbulent flows. *Physics of Fluids*, 6:2868–2870, 1994. 38

W. J. A. Dahm and A. G. Mayman. Blowout limits of turbulent jet diffusion flames for arbitrary source conditions. *AIAA Journal*, 28:1157–1162, 1990. 18

B. B. Dally, A. R. Masri, R. S. Barlow, and G. J. Fiechtner. Instantaneous and mean compositional structure of bluff-body stabilized nonpremixed flames. *Combustion and Flame*, 114:119–148, 1998. 14, 15, 19, 63

J. R. Dawson, R. L. Gordon, J. Kariuki, E. Mastorakos, A. R. Masri, and M. Juddoo. Visualization of blow-off events in bluff-body stabilized turbulent premixed flames. *Proceedings of the Combustion Institute*, 33:1559–1566, 2011. 210, 227

G. De Paola, E. Mastorakos, Y. M. Wright, and K. Boulouchos. Diesel engine simulations with multi-dimensional conditional moment closure. *Combustion Science and Technology*, 180:883–899, 2008. 188, 189

C. B. Devaud, R. W. Bilger, and T. Liu. A new method of modeling the conditional scalar dissipation rate. *Physics of Fluids (1994-present)*, 16:2004–2011, 2004. 25

C. B. Devaud, I. Stanković, and B. Merci. Deterministic Multiple Mapping Conditioning (MMC) applied to a turbulent flame in Large Eddy Simulation (LES). *Proceedings of the Combustion Institute*, 34:1213–1221, 2013. 25

L. di Mare, M. Klein, W. P. Jones, and J. Janicka. Synthetic turbulence inflow conditions for large-eddy simulation. *Physics of Fluids (1994-present)*, 18: 025107–025117, 2006. 68

K. K. J. Ranga Dinesh and M. P. Kirkpatrick. Study of jet precession, recirculation and vortex breakdown in turbulent swirling jets using LES. *Computers & Fluids*, 38:1232–1242, 2009. 70

D. Drysdale. *An Introduction to Fire Dynamics*. John Wiley Sons Ltd, Chichester, England, 1999. 10, 186

F. N. Egolfopoulos, H. Zhang, and Z. Zhang. Wall effects on the propagation and extinction of steady, strained, laminar premixed flames. *Combustion and Flame*, 109:237–252, 1997. 186

P. R. Ehrlich, P. M. Kareivaand, and G. C. Daily. Securing natural capital and expanding equity to rescale civilization. *Nature*, 486:68–73, 2012. 1

H. El-Asrag and S. Menon. Large eddy simulation of bluff-body stabilized swirling non-premixed flames. *Proceedings of the Combustion Institute*, 31:1747–1754, 2007. 116

M. P. Escudier, A. K. Nickson, and R. J. Poole. Influence of outlet geometry on strongly swirling turbulent flow through a circular tube. *Physics of Fluids*, 18: 125103–125120, 2006. 71

M. Fairweather and R. M. Woolley. First-order conditional moment closure modeling of turbulent, nonpremixed methane flames. *Combustion and Flame*, 138: 3–19, 2004. 5

D. Feikema, R.-H. Chen, and J. F. Driscoll. Enhancement of flame blowout limits by the use of swirl. *Combustion and Flame*, 80:183–195, 1990. xiii, 2, 18, 19, 31, 237

D. Feikema, R.-H. Chen, and J. F. Driscoll. Blowout of nonpremixed flames; maximum coaxial air velocities achievable with and without swirl. *Combustion and Flame*, 86:347–358, 1991. 3, 18, 19, 232

F. E. Fendell. Ignition and extinction in combustion of initially unmixed reactants. *Journal of Fluid Mechanics*, 21:281–303, 1965. 12

J. H. Frank, S. A. Kaiser, and J. C. Oefelein. Analysis of scalar mixing dynamics in LES using high-resolution imaging of laser Rayleigh scattering in turbulent non-reacting jets and non-premixed jet flames. *Proceedings of the Combustion Institute*, 33:1373–1381, 2011. 235

C. Fureby. On subgrid scale modeling in large eddy simulations of compressible fluid flow. *Physics of Fluids*, 8:1301–1429, 1996. 34, 35, 36

D. S. Gabriel, G. G. Younger, and W. R. Mickelsen. Experimental study of isothermal wake-flow characteristics of various flame-holder shapes. Technical Reoprt NACA-RM-E51K07, National Advisory Committee for Aeronautics, 1952. 3

A. Garmory and E. Mastorakos. Capturing localised extinction in Sandia flame F with LES-CMC. *Proceedings of the Combustion Institute*, 33:1673–1680, 2011. 6, 23, 24, 37, 52, 116, 128, 168, 195, 216, 219, 234, 238

A. Garmory and E. Mastorakos. Numerical simulation of oxy-fuel jet flames using unstructured LES-CMC. *Proceedings of the Combustion Institute*, 35: 1207–1214, 2015. 26, 46, 48

Y. Ge, M. J. Cleary, and A. Y. Klimenko. A comparative study of Sandia flame series (D–F) using sparse-Lagrangian MMC modelling. *Proceedings of the Combustion Institute*, 34:1325–1332, 2013. 23

L. Y. M. Gicquel, G. Staffelbach, and T. Poinsot. Large eddy simulations of gaseous flames in gas turbine combustion chambers. *Progress in Energy and Combustion Science*, 38:782–817, 2012. 3, 4, 159

S. S. Girimaji. On the modeling of scalar diffusion in isotropic turbulence. *Physics of Fluids A: Fluid Dynamics (1989-1993)*, 4:2529–2537, 1992. 41

G. Grotzbach. Direct numerical and larger eddy simulation of turbulent channel flows. In *Encyclopedia of Fluid Mechanics*, pages 1337–1391. West Orange, 1987. 187

A. K. Gupta, D. G. Lilley, and N. Syred. *Swirl Flows*. Abacus Press, Tunbridge Wells, Kent, 1984. 2, 65, 66, 70, 159

K. Han and K. Y. Huh. First and second order lagrangian conditional moment closure method in turbulent nonpremixed flames. *Proceedings of the Combustion Institute*, 35:1175–1182, 2015. 26

C. Hergart and N. Peters. Applying the representative interactive flamelet model to evaluate the potential effect of wall heat transfer on soot emissions in a small-bore DI diesel engine. *ASME Journal of Engineering for Gas Turbines and Power*, 124:1042–1052, 2001. 187, 189

W. Hocks, N. Peters, and G. Adomeit. Flame quenching in front of a cold wall under two-step kinetics. *Combustion and Flame*, 41:157–170, 1981. 186, 187

F. Holäpfel, B. Lene, and W. Leuckel. Swirl-induced intermittency: A novel effect modifying the turbulence structure of swirling free jets. *Symposium (International) on Combustion*, 26:187–194, 1996. 66

H. C. Hottel, G. C. Williams, W. P. Jensen, A. C. Tobey, and P. M. R. Burrage. Modeling studies of baffle-type combustors. *Symposium (International) on Combustion*, 9:923–935, 1963. 3

J. Hult, U. Meier, W. Meier, A. Harvey, and C. F. Kaminski. Experimental analysis of local flame extinction in a turbulent jet diffusion flame by high repetition 2-D laser techniques and multi-scalar measurements. *Proceedings of the Combustion Institute*, 30:701–709, 2005. 15, 16, 166, 219

IEA. 2014 Key World Energy Statistics. Technical report, International Energy Agency, 2014. 1

M. Ihme and H. Pitsch. Prediction of extinction and reignition in nonpremixed turbulent flames using a flamelet/progress variable model: 2. application in LES of Sandia flames D and E. *Combustion and Flame*, 155:90–107, 2008a. 22

M. Ihme and H. Pitsch. Prediction of extinction and reignition in nonpremixed turbulent flames using a flamelet/progress variable model: 1. a priori study and presumed PDF closure. *Combustion and Flame*, 155:70–89, 2008b. 21

M. Ihme, C. M. Cha, and H. Pitsch. Prediction of local extinction and re-ignition effects in non-premixed turbulent combustion using a flamelet/progress variable approach. *Proceedings of the Combustion Institute*, 30:793–800, 2005. 21

R. I. Issa. Solution of the implicitly discretised fluid flow equations by operator-splitting. *Journal of Computational Physics*, 62:40–65, 1986. 43, 67

S. James, J. Zhu, and M. S. Anand. Large eddy simulations of turbulent flames using the filtered density function model. *Proceedings of the Combustion Institute*, 31:17371745, 2007. 116

S. R. James. Hominid use of fire in the lower and middle pleistocene: A review of the evidence. *Current Anthropology*, 39:1–26, 1989. 1

N. Jarrin, S. Benhamadouche, D. Laurence, and R. Prosser. A synthetic-eddy-method for generating inflow conditions for large-eddy simulations. *International Journal of Heat and Fluid Flow*, 27:585–593, 2006. 68

H. Jasak. *Error Analysis and Estimation for the Finite Volume Method with Applications to Fluid Flows*. PhD thesis, Imperial College of Science, Technology and Medicine, Department of Mechanical Engineering, 1996. 42, 43, 48

C. Jiménez, F. Ducros, B. Cuenot, and B. Bédat. Subgrid scale variance and dissipation of a scalar field in large eddy simulations. *Physics of Fluids (1994-present)*, 13:1748–1754, 2001. 37

J. Jiménez. Near-wall turbulence. *Physics of Fluids*, 25:101302–101330, 2013. 187

W. P. Jones and V. N. Prasad. Large eddy simulation of the Sandia flame series (D−F) using the Eulerian stochastic field method. *Combustion and Flame*, 157:1621–1636, 2010. 21

Y. Ju and K. Maruta. Microscale combustion: Technology development and fundamental research. *Progress in Energy and Combustion Science*, 37:669–715, 2012. 186

Y. Ju and W. Sun. Plasma assisted combustion: Dynamics and chemistry. *Progress in Energy and Combustion Science*, 48:21–83, 2015. 11

M. Juddoo and A. R. Masri. High-speed OH-PLIF imaging of extinction and re-ignition in non-premixed flames with various levels of oxygenation. *Combustion and Flame*, 158:902–914, 2011. 16, 17, 166, 219, 234

N. S. Kaisare and D. G. Vlachos. A review on microcombustion: Fundamentals, devices and applications. *Progress in Energy and Combustion Science*, 38:321–359, 2012. 186

S. A. Kaiser and J. H. Frank. Spatial scales of extinction and dissipation in the near field of non-premixed turbulent jet flames. *Proceedings of the Combustion Institute*, 32:1639–1646, 2009. 16, 166

G. T. Kalghatgi. Lift-off heights and visible lengths of vertical turbulent jet diffusion flames in still air. *Combustion Science and Technology*, 41:17–29, 1984. 18

J. Kariuki. *Turbulent premixed flame stabilization and blow-off*. PhD thesis, University of Cambridge, Department of Engineering, 2012. 3, 197

J. Kariuki, J. R. Dawson, and E. Mastorakos. Measurements in turbulent premixed bluff body flames close to blow-off. *Combustion and Flame*, 159:2589–2607, 2012. 3, 188, 210, 227

J. Kariuki, A. Dowlut, R. Yuan, R. Balachandran, and E. Mastorakos. Heat release imaging in turbulent premixed methane-air flames close to blow-off. *Proceedings of the Combustion Institute*, 35:1443–1450, 2015. 232

A. N. Karpetis and R. S. Barlow. Measurements of flame orientation and scalar dissipation in turbulent partially premixed methane flames. *Proceedings of the Combustion Institute*, 30:665–672, 2005. 17

J. B. Kelman and A. R. Masri. Reaction zone structure and scalar dissipation rates in turbulent diffusion flames. *Combustion science and technology*, 133: 17–55, 1998. 17

A. Kempf, W. Malalasekera, K. K. J. Ranga-Dinesh, and O. Stein. Large eddy simulations of swirling non-premixed flames with flamelet models: A comparison of numerical methods. *Flow, Turbulence and Combustion*, 81:523–561, 2008. 116

G. Kim, S. Kang, Y. Kim, and K.-S. Lee. Conditional moment closure modeling for a three-dimensional turbulent non-premixed syngas flame with a cooling wall. *Energy and Fuels*, 22:3639–3648, 2008. 26, 40, 49, 188

I. S. Kim and E. Mastorakos. Simulations of turbulent lifted jet flames with two-dimensional conditional moment closure. *Proceedings of the Combustion Institute*, 30:911–918, 2005. 5

S. H. Kim and H. Pitsch. Mixing characteristics and structure of a turbulent jet diffusion flame stabilized on a bluff-body. *Physics of Fluids*, 18:75–103, 2006. 38

S. H. Kim, K. Y. Huh, and R. W. Bilger. Second-order conditional moment closure modeling of local extinction and reignition in turbulent non-premixed hydrocarbon flames. *Proceedings of the Combustion Institute*, 29:2131–2137, 2002. 22

M. Klein, A. Sadiki, and J. Janicka. A digital filter based generation of inflow data for spatially developing direct numerical or large eddy simulations. *Journal of Computational Physics*, 186:652–665, 2003. 68

A. Y. Klimenko. Multicomponent diffusion of various admixtures in turbulent flow. *Fluid Dynamics*, 25:327–334, 1990. 5

A. Y. Klimenko and R. W. Bilger. Conditional moment closure for turbulent combustion. *Progress in Energy and Combustion Science*, 25:595–687, 1999. 5, 6, 25, 37, 274

A. N. Kolmogorov. The local structure of turbulence in incompressible viscous fluid for very large Reynolds numbers. *Proceedings of the Royal Society of London A*, 434:9–13, 1991. 4

N. Kornev and E. Hassel. Method of random spots for generation of synthetic inhomogeneous turbulent fields with prescribed autocorrelation functions. *Communications in Numerical Methods in Engineering*, 23:35–43, 2007. 68

L. Krishnamurthy, F. A. Williams, and K. Seshadri. Asymptotic theory of diffusion-flame extinction in the stagnation-point boundary layer. *Combustion and Flame*, 26:363–377, 1976. 13

A. Kronenburg. Double conditioning of reactive scalar transport equations in turbulent nonpremixed flames. *Physics of Fluids*, 16:2640–2648, 2004. 22

A. Kronenburg and M. Kostka. Modeling extinction and reignition in turbulent flames. *Combustion and Flame*, 143:342–356, 2005. 5, 22

A. Kronenburg and E. Mastorakos. The conditional moment closure model. In T. Echekki and E. Mastorakos, editors, *Turbulent Combustion Modeling: Advances, New Trends and Perspectives*. Springer, New York, 2011. 5, 25

A. Kronenburg and A. E. Papoutsakis. Conditional moment closure modeling of extinction and re-ignition in turbulent non-premixed flames. *Proceedings of the Combustion Institute*, 30:759–766, 2005. 22

A. Kronenburg, R. W. Bilger, and J. H. Kent. Second-order conditional moment closure for turbulent jet diffusion flames. In *Symposium (International) on Combustion*, volume 27, pages 1097–1104, 1998. 6

A. De Lataillade, F. Dabireau, B. Cuenot, and T. Poinsot. Flame/wall interaction and maximum wall heat fluxes in diffusion burners. *Combustion and Flame*, 29:775–779, 2002. 193

C. K. Law. *Combustion Physics*. Cambridge University Press, New York, 2006. 10, 11, 35, 127, 218, 222

C. J. Lawn. Lifted flames on fuel jets in co-flowing air. *Progress in Energy and Combustion Science*, 35:1–30, 2009. 18

A. H. Lefebvre. *Gas Turbine Combustion*. Taylor Francis, London, England, 2005. 3, 186

A. Leonard. Energy cascade in large-eddy simulations of turbulent fluid flows. In F. N. Frenkiel and R. E. Munn, editors, *Turbulent Diffusion in Environmental Pollution Proceedings of a Symposium held at Charlottesville*, volume 18, Part A of *Advances in Geophysics*, pages 237–248. 1975. 32

M. Lesieur, O. Métais, and P. Comte. *Large-Eddy Simulations of Turbulence*. Cambridge University Press, New York, 2005. 83

C. Letty, E. Mastorakos, A. R. Masri, M. Juddoo, and W. O'Loughlin. Structure of igniting ethanol and n-heptane spray flames with and without swirl. *Experimental Thermal and Fluid Science*, 43:47–54, 2012. 66

D. Lignell, J. H. Chen, and H. Schmutz. Effects of Damkohler number on flame extinction and reignition in turbulent non-premixed flames using DNS. *Combustion and Flame*, 158:949–963, 2011. 3, 20, 168, 170, 219, 230

D. K. Lilly. On the computational stability of numerical solutions of time-dependent non-linear geophysical fluid dynamics problems. *Monthly Weather Review*, 93:11–25, 1965. 33

A. Liñán. The asymptotic structure of counterflow diffusion flames for large activation energies. *Acta Astronautica*, 1:1007–1039, 1974. 12, 13

J. P. Longwell and M. A. Weiss. High temperature reaction rates in hydrocarbon combustion. *Industrial & Engineering Chemistry*, 47:1634–1643, 1955. 11

T. S. Lund, X. Wu, and K. D. Squires. Generation of turbulent inflow data for spatially-developing boundary layer simulations. *Journal of Computational Physics*, 140:233–258, 1998. 68, 129

K. M. Lyons. Toward an understanding of the stabilization mechanisms of lifted turbulent jet flames: Experiments. *Progress in Energy and Combustion Science*, 33:211–231, 2007. 18

M.-C. Ma and C. B. Devaud. A Conditional Moment Closure (CMC) formulation including differential diffusion applied to a non-premixed hydrogen−air flame. *Combustion and Flame*, 162:144–158, 2015. 25

W. Malalasekera, K. K. J. Ranga-Dinesh, S. S. Ibrahim, and M. P. Kirkpatrick. Large eddy simulation of isothermal turbulent swirling jets. *Combustion Science and Technology*, 179:1481–1525, 2007. 70

R. M. M. Mallens and L. P. H. De Goey. Flame cooling by a curved burner wall. *International Journal of Heat and Mass Transfer*, 41:699–707, 1998. 187

T. Marchione, S. F. Ahmed, and E. Mastorakos. Ignition of turbulent swirling *n*-heptane spray flames using single and multiple sparks. *Combustion and Flame*, 156:166–180, 2009. 65

F. Martinelli, A. Olivani, and A. Coghe. Experimental analysis of the precessing vortex core in a free swirling jet. *Experiments in Fluids*, 42:827–839, 2007. 65

A. R. Masri, R. W. Dibble, and R. S. Barlow. The structure of turbulent nonpremixed flames revealed by Raman-Rayleigh-LIF measurements. *Progress in Energy and Combustion Science*, 22:307–362, 1996. 14, 170, 171

A. R. Masri, S. B. Pope, and B. B. Dally. Probability density function computations of a strongly swirling nonpremixed flame stabilized on a new burner. *Proceedings of the Combustion Institute*, 28:123–131, 2000. 70, 77, 78

A. R. Masri, P. A. M. Kalt, and R. S. Barlow. The compositional structure of swirl-stabilised turbulent nonpremixed flames. *Combustion and Flame*, 137: 1–37, 2004. xiii, xiv, xx, 53, 59, 62, 63, 64, 91, 116, 118, 120, 121, 123, 125, 127, 128, 156, 159, 164, 221, 268

A. R. Masri, P. A. M. Kalt, Y. M. Al-Abdeli, and R. S. Barlow. Turbulence-chemistry interactions in non-premixed swirling flames. *Combustion Theory and Modelling*, 11:653–673, 2006. 15, 159, 238

E. Mastorakos and R. W. Bilger. Second-order conditional moment closure for the autoignition of turbulent flows. *Physics of Fluids*, 10:1246–1248, 1998. 6

F. Mauss, D. Keller, and N. Peters. A Lagrangian simulation of flamelet extinction and re-ignition in turbulent jet diffusion flames. *Symposium (International) on Combustion*, 23:693–698, 1991. 21

P. R. Medwell, P. A. M. Kalt, and B. B. Dally. Simultaneous imaging of OH, formaldehyde, and temperature of turbulent nonpremixed jet flames in a heated and diluted coflow. *Combustion and Flame*, 148:48–61, 2007. 232

W. Meier, R. S. Barlow, Y.-L. Chen, and J.-Y. Chen. Raman/Rayleigh/LIF measurements in a turbulent CH4/H2/N2 jet diffusion flame: experimental techniques and turbulence-chemistry interaction. *Combustion and Flame*, 123: 326–343, 2000. 14, 122

W. Meier, X. R. Duan, and P. Weigand. Investigations of swirl flames in a gas turbine model combustor: II. turbulence chemistry interactions. *Combustion and Flame*, 144:225–236, 2006. xiii, 15, 17, 31

A. Milford and C. B. Devaud. Investigation of an inhomogeneous turbulent mixing model for conditional moment closure applied to autoignition. *Combustion and Flame*, 157:1467–1483, 2010. 25, 41

K. Mills and M. Matalon. Extinction of spherical diffusion flames in the presence of radiant loss. *Symposium (International) on Combustion*, 27:2535–2541, 1998. 13

K. Mobini and R. W. Bilger. Parametric study of the Incompletely Stirred Reactor modeling. *Combustion and Flame*, 156:1818–1827, 2009. 26

M. Mortensen and R. W. Bilger. Derivation of the conditional moment closure equations for spray combustion. *Combustion and Flame*, 156:62–72, 2009. 27

H. Nakamura, A. Fan, H. Minamizono, K. Maruta, H. Kobayashi, and T. Niioka. Bifurcations of stretched premixed flame stabilized by a hot wall. *Proceedings of the Combustion Institute*, 32:1367–1374, 2009. 187

S. Navarro-Martinez and A. Kronenburg. LES-CMC simulations of a lifted methane flame. *Proceedings of the Combustion Institute*, 32:1509–1516, 2009. 5, 27, 37

S. Navarro-Martinez and A. Kronenburg. Flame stabilization mechanisms in lifted flames. *Flow, Turbulence and Combustion*, 87:377–406, 2011. 27, 234

S. Navarro-Martinez, A. Kronenburg, and F. Di Mare. Conditional moment closure for large eddy simulations. *Flow, Turbulence and Combustion*, 75:245–274, 2005. 5, 7, 22, 37, 38, 41, 49

A. M. Oboukhov. Some specific features of atmospheric turbulence. *Journal of Fluid Mech*, 13:77–81, 1962. 41

E. E. O'Brien and T. L. Jiang. The conditional dissipation rate of an initially binary scalar in homogeneous turbulence. *Physics of Fluids*, 3:3121–3123, 1991. 41

J. A. Oijen and L. P. H. Goey. Modelling of premixed laminar flames using flamelet-generated manifolds. *Combustion Science and Technology*, 161:113–137, 2000. 187

C. Olbricht, A. Ketelheun, F. Hahn, and J. Janicka. Assessing the predictive capabilities of combustion LES as applied to the Sydney flame series. *Flow, Turbulence and Combustion*, 85:513–547, 2010. 116

S. V. Patankar. *Numerical Heat Transfer and Fluid Flow*. Hemisphere Publishing Corporation, New York, 1980. 42, 43

Francois Pellegrini. *SCOTCH 4.0 User's guide*. Universite Bordeaux I, 351 cours de la Liberation, 33405 TALENCE, FRANCE, January 2006. 53

C. Pera, J. Réveillon, L. Vervisch, and P. Domingo. Modeling subgrid scale mixture fraction variance in LES of evaporating spray. *Combustion and Flame*, 146:635–648, 2006. 36, 37

N. Peters. Laminar diffusion flamelet models in non-premixed turbulent combustion. *Progress in Energy and Combustion Science*, 10:319–339, 1984. 47

C. D. Pierce and P. Moin. A dynamic model for subgrid-scale variance and dissipation rate of a conserved scalar. *Physics of Fluids*, 10:3041–3044, 1998. 37

C. D. Pierce and P. Moin. Progress-variable approach for large-eddy simulation of non-premixed turbulent combustion. *Journal of Fluid Mechanics*, 504:73–97, 2004. 21, 24

H. Pitsch. Large eddy simulation of turbulent combustion. *Annual Review of Fluid Mechanics*, 38:453–482, 2006. 4

H. Pitsch and S. Fedotov. Investigation of scalar dissipation rate fluctuations in non-premixed turbulent combustion using a stochastic approach. *Combustion Theory and Modelling*, 5:41–57, 2001. 21, 24

H. Pitsch and H. Steiner. Scalar mixing and dissipation rate in large-eddy simulations of non-premixed turbulent combustion. *Proceedings of the Combustion Institute*, 28:41–49, 2000a. 235

H. Pitsch and H. Steiner. Large-eddy simulation of a turbulent piloted methane/air diffusion flame (Sandia flame D). *Physics of Fluids (1994-present)*, 12:2541–2554, 2000b. 117

H. Pitsch, C. M. Cha, and S. Fedotov. Flamelet modelling of non-premixed turbulent combustion with local extinction and re-ignition. *Combustion Theory and Modelling*, 7:317–332, 2003. 21, 24

W. M. Pitts. Assessment of theories for the behavior and blowout of lifted turbulent jet diffusion flames. *Symposium (International) on Combustion*, 22: 809–816, 1989. 18

T. Poinsot and D. Veynante. *Theoretical and Numerical Combustion*. R. T. Edwards, Philadephia, PA, 2005. 10, 33, 34, 35, 186, 187, 190

S. B. Pope. *Turbulent Flows*. Cambridge University Press, New York, 2000. 4, 43

S. B. Pope. Ten questions concerning the large-eddy simulation of turbulent flows. *New Journal of Physics*, 6:35–58, 2004. 76

P. Popp and M. Baum. Analysis of wall heat fluxes, reaction mechanisms, and unburnt hydrocarbons during the head-on quenching of a laminar methane flame. *Combustion and Flame*, 108:327–348, 1997. 187

V. N. Prasad, M. Juddoo, A. R. Masri, W. P. Jones, and K. H. Luo. Investigation of extinction and re-ignition in piloted turbulent non-premixed methane-air flames using LES and high-speed OH-PLIF. *Combustion Theory and Modelling*, 17:483–503, 2013. 166

C. M. Rhie and W. L. Chow. A numerical study of the turbulent flow past an isolated airfoil with trailing edge separation. *AIAA Journal*, 21:1525–1532, 1983. 42, 67

D. S. Richeson. *Euler's Gem: The Polyhedron Formula and the Birth of Topology*. Princeton University Press, Princeton, NJ, 2008. 50

M. R. Roomina and R. W. Bilger. Conditional moment closure modelling of turbulent methanol jet flames. *Combustion Theory and Modelling*, 3:689–708, 1999. 5

M. R. Roomina and R. W. Bilger. Conditional moment closure (CMC) predictions of a turbulent methane-air jet flame. *Combustion and Flame*, 125:1176–1195, 2001. 5

R. N. Roy, S. Kumar, and S. Sreedhara. A new approach to model turbulent lifted CH4/air flame issuing in a vitiated coflow using conditional moment closure coupled with an extinction model. *Combustion and Flame*, 161:197–209, 2014. 27

F. Salehi, M. Talei, E. R. Hawkes, C. S. Yoo, T. Lucchini, G. D'Errico, and S. Kook. A comparative study of conditional moment closure modelling for ignition of *iso*-octane and *n*-heptane in thermally stratified mixtures. *Flow, Turbulence and Combustion*, in press, 2015. 27

K. J. Santa, B. H. Chao, P. B. Sunderland, D. L. Urban, D. P. Stocker, and R. L. Axelbaum. Radiative extinction of gaseous spherical diffusion flames in microgravity. *Combustion and Flame*, pages 665–675, 2007. 14

P. Schmitt, T. Poinsot, B. Schuermans, and K. P. Geigle. Large-eddy simulation and experimental study of heat transfer, nitric oxide emissions and combustion instability in a swirled turbulent high-pressure burner. *Journal of Fluid Mechanics*, 507:17–46, 2007. 187

P. Schmittel, B. Gunther, B. Lenze, W. Leuckel, and H. Bockhorn. Turbulent swirling flames: Experimental investigation of the flow field and formation of nitrogen oxide. *Proceedings of the Combustion Institute*, 28:303–309, 2000. 66

R. Shan and T. Lu. Ignition and extinction in perfectly stirred reactors with detailed chemistry. *Combustion and Flame*, 159:2069–2076, 2012. 11

H. J. Sheen, W. J. Chen, S. Y. Jeng, and T. L. Huang. Correlation of swirl number for a radial-type swirl generator. *Experimental Thermal and Fluid Science*, 12: 444–451, 1996. 66

P. Siwaborworn and A. Kronenburg. Conservative implementation of LES-CMC for turbulent jet flames. In *High Performance Computing in Science and Engineering'12*, pages 159–173, 2013. 26, 40, 49

J. Smagorinsky. General circulation experiments with the primitive equations. *Monthly Weather Review*, 91(3):99–164, 1963. 4, 34

G. P. Smith, D. M. Golden, M. Frenklach, B. Eiteener, M. Goldenberg, C. T. Bowman, R. K. Hanson, W. C. Gardiner, V. V. Lissianski, and Z. W. Qin. GRI-mech 3.0, 2000. URL `http://www.me.berkeley.edu/gri_mech/`. 22

S. H. Sohrab, A. Liñán, and F. A. Williams. Asymptotic theory of diffusion-flame extinction with radiant loss from the flame zone. *Combustion Science and Technology*, 27:143–154, 1982. 13

L. Song and J. Abraham. A wall-modified flamelet model for diesel combustion. *SAE Technical Paper*, 2004. 187

D. B. Spalding. A theory of inflammability limits and flame-quenching. *Proceedings of the Royal Society of London. Series A. Mathematical and Physical Sciences*, 240:83–100, 1957. 12

D. B. Spalding. A single formula for the "law of the wall". *Journal of Applied Mechanics*, 28:455–458, 1961. 70, 71

P. Sripakagorn, S. Mitirai, G. Kosály, and H. Pitsch. Extinction and reignition in a diffusion flame: a direct numerical simulation study. *Journal of Fluid Mechanics*, 518:231–259, 2004. 20

I. Stanković, A. Triantafyllidis, E. Mastorakos, C. Lacor, and B. Merci. Simulation of hydrogen auto-ignition in a turbulent co-flow of heated air with LES and CMC approach. *Flow, Turbulence and Combustion*, 86:689–710, 2011. 5

I. Stanković, E. Mastorakos, and B. Merci. LES-CMC simulations of different auto-ignition regimes of hydrogen in a hot turbulent air co-flow. *Flow, Turbulence and Combustion*, 90:583–604, 2013. 27

A. M. Steinberg, I. Boxx, C. M. Arndt, J. H. Frank, and W. Meier. Experimental study of flame-hole reignition mechanisms in a turbulent non-premixed jet flame using sustained multi-kHz PIV and crossed-plane OH PLIF. *Proceedings of the Combustion Institute*, 33:1663–1672, 2011. 16, 17, 166, 219, 234

M. Stöhr, I. Boxx, C. Carter, and W. Meier. Dynamics of lean blowout of a swirl-stabilized flame in a gas turbine model combustor. *Proceedings of the Combustion Institute*, 33:2953–2960, 2011. 17, 20

L. K. Su and N. T. Clemens. The structure of fine-scale scalar mixing in gas-phase planar turbulent jets. *Journal of Fluid Mechanics*, 488:1–29, 2003. 17

C. J. Sung, C. K. Law, and J. Y. Chen. An augmented reduced mechanism for methane oxidation with comprehensive global parametric validation. *Proceedings of the Combustion Institute*, 27:295–304, 1998. 23, 52

J. A. Sutton and J. F. Driscoll. A method to simultaneously image two-dimensional mixture fraction, scalar dissipation rate, temperature and fuel consumption rate fields in a turbulent non-premixed jet flame. *Experiments in Fluids*, 41:603–627, 2006. 16

J. A. Sutton and J. F. Driscoll. Imaging of local flame extinction due to the interaction of scalar dissipation layers and the stoichiometric contour in turbulent non-premixed flames. *Proceedings of the Combustion Institute*, 31:1487–1495, 2007. 16, 166, 235, 237

J. A. Sutton and J. F. Driscoll. Measurements and statistics of mixture fraction and scalar dissipation rates in turbulent non-premixed jet flames. *Combustion and Flame*, 160:1767–1778, 2013. 16, 17, 221

N. Swaminathan and S. Mahalingam. Assessment of conditional moment closure for single and multistep chemistry. *Combustion Science and Technology*, 112: 301–326, 1996. 41

N. Syred. A review of oscillation mechanisms and the role of the precessing vortex core (PVC) in swirl combustion systems. *Progress in Energy and Combustion Science*, 32:93–161, 2006. 2, 75, 159

G. R. Tabor and M. H. Baba-Ahmadi. Inlet conditions for large eddy simulation: A review. *Computers & Fluids*, 39:553–567, 2010. 68

B. Thornber, R. W. Bilger, A. R. Masri, and E. R. Hawkes. An algorithm for LES of premixed compressible flows using the conditional moment closure model. *Journal of Computational Physics*, 230:7687–7705, 2011. 26, 40

J. S. T'ien. Diffusion flame extinction at small stretch rates: The mechanism of radiative loss. *Combustion and Flame*, 65:31–34, 1986. xiii, 13, 30

A. Triantafyllidis and E. Mastorakos. Implementation issues of the conditional moment closure model in large eddy simulations. *Flow, Turbulence and Combustion*, 84:481–512, 2010. 5, 22, 37, 51, 52

A. Triantafyllidis, E. Mastorakos, and R. L. G. M. Eggels. Large eddy simulations of forced ignition of a non-premixed bluff-body methane flame with conditional moment closure. *Combustion and Flame*, 156:2328–2345, 2009. 5, 27, 37, 52

S. D. Tse, D. Zhu, C.-J. Sung, Y. Ju, and C. K. Law. Microgravity burner-generated spherical diffusion flames: experiment and computation. *Combustion and Flame*, 125:1265–1278, 2001. 14

H. Tsuji. Counterflow diffusion flames. *Progress in Energy and Combustion Science*, 8:93–119, 1982. 13

A. Tyliszczak, D. E. Cavaliere, and E. Mastorakos. LES/CMC of blow-off in a liquid fueled swirl burner. *Flow, Turbulence and Combustion*, 92:237–267, 2014. 6, 23, 28, 37, 210, 228

S. Ukai, A. Kronenburg, and O. T. Stein. LES-CMC of a dilute acetone spray flame. *Proceedings of the Combustion Institute*, 34:1643–1650, 2013. 5, 28

S. Ukai, A. Kronenburg, and O. T. Stein. Simulation of dilute acetone spray flames with LES-CMC using two conditional moments. *Flow, Turbulence and Combustion*, 93:405–423, 2014. 28

S. Ukai, A. Kronenburg, and O. T. Stein. Large eddy simulation of dilute acetone spray flames using CMC coupled with tabulated chemistry. *Proceedings of the Combustion Institute*, 35:1667–1674, 2015. 5

T. v. Karman and G. Millan. Thermal theory of a laminar flame front near a cold wall. *Symposium (International) on Combustion*, 4:173177, 1953. 186

H. K. Versteeg and W. Malalasekera. *An Introduction to Computational Fluid Dynamics. The Finite Volume Method*. Longman Group Ltd., London, 1995. 42

D. G. Vlachos and L. D. Schmidt. Ignition and extinction of flames near surfaces: Combustion of H2 in air. *Combustion and Flame*, 95:313–335, 1993. 187

K. Vogiatzaki, A. Kronenburg, S. Navarro-Martinez, and W. P. Jones. Stochastic multiple mapping conditioning for a piloted, turbulent jet diffusion flame. *Proceedings of the Combustion Institute*, 33:1523–1531, 2011. 23

A. P. Wandel and R. P. Lindstedt. Hybrid multiple mapping conditioning modeling of local extinction. *Proceedings of the Combustion Institute*, 34:1365–1372, 2013. 23, 24

Q. Wang and B. H. Chao. Kinetic and radiative extinctions of spherical burner-stabilized diffusion flames. *Combustion and Flame*, 158:1532–1541, 2011. 13

Y. Wang and A. Trouvé. Direct numerical simulation of nonpremixed flame–wall interactions. *Combustion and Flame*, 144:461–475, 2006. 193

H. G. Weller, G. Tabor, H. Jasak, and C. Fureby. A tensorial approach to computational continuum mechanics using object-oriented techniques. *Computers in Physics*, 12:620–631, 1997. 46

C. K. Westbrook, A. A. Adamczyk, and G. A. Lavoie. A numerical study of laminar flame wall quenching. *Combustion and Flame*, 40:81–99, 1981. 186

F. A. Williams. A review of flame extinction. *Fire Safety Journal*, 3:163–175, 1981. 12

F. A. Williams. *Combustion Theory*. The Benjamin/Cummings Publishing Company, Inc., California, 1985. xiii, 11, 30

C.-Y. Wu, Y.-C. Chao, T.-S. Cheng, Y.-H. Li, K.-Y. Lee, and T. Yuan. The blowout mechanism of turbulent jet diffusion flames. *Combustion and Flame*, 145:481–494, 2006. 18, 232

J. Xu and S. B. Pope. PDF calculations of turbulent nonpremixed flames with local extinction. *Combustion and Flame*, 123:281–307, 2000. 20, 21, 24, 52

Y. Yang and S. K. Kær. Large-eddy simulations of the non-reactive flow in the Sydney swirl burner. *International Journal of Heat and Fluid Flow*, 36:47–57, 2012. 70

R. Yuan, A. Giusti, M. Kotzagianni, and E. Mastorakos. Experimental and numerical investigation of a swirling spray flame with local extinction. In *Ninth Mediterranean Combustion Symposium*, Rhodes, Greece, June 7-11 2015a. 66

R. Yuan, J. Kariuki, A. Dowlut, R. Balachandran, and E. Mastorakos. Reaction zone visualisation in swirling spray n-heptane flames. *Proceedings of the Combustion Institute*, 35:1649–1656, 2015b. 66, 232

H. Zhang and Z. Chen. Effects of heat conduction and radical quenching on premixed stagnation flame stabilized by a wall. *Combustion Theory and Modelling*, 17:682–706, 2013. 187

H. Zhang, A. Garmory, D. E. Cavaliere, and E. Mastorakos. Large eddy simulation/conditional moment closure modeling of swirl-stabilized non-premixed flames with local extinction. *Proceedings of the Combustion Institute*, 35:1167–1174, 2015. 238